

***NMR crystallographic investigations
of defect motifs in high-pressure minerals
of the Earth's deep interior***

Dissertation

zur Erlangung des akademischen Grades einer
Doktorin der Naturwissenschaften
(Dr. rer. nat.)

in der Bayreuther Graduiertenschule für Mathematik und Naturwissenschaften
(BayNAT) der Universität Bayreuth

vorgelegt von

Helen Grüninger
geboren in Darmstadt

Bayreuth, 2018

Die vorliegende Arbeit wurde in der Zeit von Oktober 2014 bis September 2018 in Bayreuth am Lehrstuhl Anorganische Chemie III unter Betreuung von Herrn Professor Dr. Jürgen Senker angefertigt.

Vollständiger Abdruck der von der Bayreuther Graduiertenschule für Mathematik und Naturwissenschaften (BayNAT) der Universität Bayreuth genehmigten Dissertation zur Erlangung des akademischen Grades einer Doktorin / eines Doktors der Naturwissenschaften (Dr. rer. nat.).

Dissertation eingereicht am: 27.09.2018

Zulassung durch die Promotionskommission: 17.10.2018

Wissenschaftliches Kolloquium: 01.02.2019

Amtierender Direktor: Prof. Dr. Dirk Schüler

Prüfungsausschuss:

Prof. Dr. Jürgen Senker (Gutachter)

Prof. Dr. Josef Breu (Gutachter)

Prof. Dr. Roland Marschall (Vorsitz)

Prof. Dr. Tomoo Katsura

Weiterer Gutachter: Prof. Dr. Gerd Buntkowsky

“Think like a proton – always positive!”

Contents

Danksagung	vii
Nomenclature	ix
Abstract	1
Zusammenfassung	3
1. Introduction	7
1.1 Structural studies on defects in high-pressure minerals	9
1.2 NMR crystallography	11
2. Synopsis	17
2.1 Solving ringwoodites OH defect chemistry by NMR crystallography	17
2.2 Structure elucidation of Al defects in bridgmanite by NMR crystallography	31
References	38
3. Index of Publications	45
4. Publications	47
4.1 Hidden Oceans? Unraveling the Structure of Hydrous Defects in the Earth's Deep Interior	47
4.2 Quantitative description of ^1H SQ and DQ coherences for the hydroxyl disorder within hydrous ringwoodite	73
4.3 On the feasibility of ^1H NMR on hydrous defects within nanoliter ringwoodite crystals	95
4.4 Detection of oxygen vacancy ordering in aluminous bridgmanite in the Earth's lower mantle	115

Danksagung

Mein besonderer Dank gilt meinem Doktorvater Prof. Dr. Jürgen Senker für seine Hilfe bei verschiedenen Fragestellungen, seine Gelassenheit und Geduld, und vor allem auch für den Freiraum, den er mir in der Promotion einräumte um mich selbst wissenschaftlich entwickeln zu können.

Weiterhin möchte ich beim Fonds der Chemischen Industrie bedanken für die finanzielle Unterstützung meiner Promotion in Form des Chemiefonds-Stipendiums.

I want to thank my collaboration partners in BGI, Katherine Armstrong and Dr. Zhaodong Liu, for all the efforts they have put in the high-pressure synthesis of the samples. Furthermore, I want to thank Dr. Tiziana Boffa Ballaran and Prof. Dr. Dan Frost for their scientific input, a lot of help organizing our projects and always finding some time for discussions.

I also want to thank my collaboration partners in Nijmegen (Netherlands) Prof. Dr. Arno Kentgens and J. Ole Brauckmann for the opportunity to measure with their unique μ NMR setup and for all the time they spend with the measurements.

Bei Dr. Renée Siegel möchte ich mich herzlich für die Einarbeitung und Unterstützung an den NMR Spektrometern bedanken – nahezu egal zu welcher Uhrzeit!

Außerdem möchte ich mich bei Dr. Maria Jordan (ehemals Mesch), Dominik Greim und Robert Stäglich für die vielen geführten Diskussionen um und neben der Wissenschaft bedanken immer gerne bei Kaffee oder Bier. Ohne euch hätte die Promotion nicht mal halb so viel Spaß gemacht!

Ich möchte mich auch bei allen anderen Kollegen aus der ACIII und der ACI bedanken für die Unterstützung vor allem am Anfang der Promotion, viele gemeinsam erlebte Tagungen, Feiern und sonstige Veranstaltungen.

Mein größter Dank geht an meine Familie – insbesondere an meine Mama und Matthias, die es mir ermöglicht haben eine Familie zu gründen und gleichzeitig zu promovieren, die immer ein offenes Ohr hatten und stets mit Rat und Tat zur Seite standen. Ohne euch wäre dieser Weg nicht möglich gewesen.

Und zuletzt bin ich meinem kleinen Sohn, Levin, dankbar für die Liebe, die Lebensfreude und die vielen lustigen Situationen, die mein Leben so nachhaltig bereichern und zu einer ungeahnten Lebensqualität geführt haben.

Nomenclature

1D	One-dimensional
2D	Two-dimensional
CP	Cross polarization
CC	Charge-coupled
DFT	Density Functional Theory
DQ	Double-quantum
EFG	Electric field gradient
EPMA	Electron probe microanalyzer
FTIR	Fourier transform infrared spectroscopy
MAS	Magic angle spinning
MD	Molecular dynamics
NMR	Nuclear magnetic resonance
OV	Oxygen vacancy
rf	Radio frequency
SEM	Scanning electron microscope
SQ	Single-quantum
XRD	X-ray diffraction

Abstract

In this work NMR crystallography was used to elucidate the defect chemistry of two high-pressure magnesium silicates, namely ringwoodite (γ -Mg₂SiO₄) and bridgmanite (MgSiO₃), which make up major parts of the Earth's mantle. In this way, we focus on understanding the various defect formation mechanisms and provide a framework through which to understand the effects on the mineral properties. The required high-pressure synthesis of the minerals results in low sample yields, which in combination with low defect concentrations renders the structural characterization of the defects challenging.

We have, however, been able to investigate OH defect formation mechanisms within ringwoodite by combining high-resolution multidimensional solid-state ¹H NMR spectroscopy and *Density Functional Theory* (DFT) simulations of multiple model OH defect types. Using these methods, we were able to link experimental and simulated ¹H chemical shifts, and ¹H-¹H connectivities to individual OH defect motifs. The qualitative solution revealed a surprisingly rich OH defect chemistry of ringwoodite's spinel-type structure, including the formation of isolated low-valent Mg²⁺ vacancies charge balanced by two protons ($V''_{Mg} + 2H^{**}$), as well as isolated high-valent Si⁴⁺ defects, either charge balanced by four protons ($V''''_{Si} + 4H^{****}$) or by one Mg²⁺ and two protons ($Mg''_{Si} + 2H^{**}$). Additionally, a coupled defect type with an Mg²⁺ on a Si site coupled to an octahedral vacancy ($Mg_{Si}V''''_{Mg} + 4H^{****}$) makes up a significant proportion. Inherent disorder of hydrogen bonds within the defects prevented a straight-forward quantification of different defect motifs. Therefore, a new approach to model local ¹H disorder within point defects based on molecular dynamics (MD) simulations employing the DFT method and to describe its influence on two complementary ¹H NMR observables was developed. Individual ¹H chemical shift footprints and characteristic ensemble average ¹H-¹H double-quantum (DQ) buildup curves were derived from the modelled OH disorder for each of the four above mentioned OH defect types. These were then used as joint cost function for the refinement of the strongly overlapping experimental ¹H MAS NMR spectrum and ¹H-¹H DQ buildup curves leading to a quantitative determination of the defect motif proportions of ~50% V_{Mg}, 18% V_{Si}, ~13% Mg_{Si} and 20% coupled Mg_{Si}V_{Mg}.

In order to evaluate the OH defect formation mechanisms as a function of the hydration level the feasibility of ¹H NMR spectroscopy on nanoliter hydrous ringwoodite crystals was investigated. For three crystals with hydration levels between an equivalent of 0.3-

2.0 wt% H₂O the 1D ¹H MAS NMR spectra were successfully recorded using a standard MAS NMR setup and a piggy-back μ MAS setup, and were quantitatively refined with the previously determined ¹H chemical shift footprints. The resulting defect type ratios were linked to the experimental unit cell volumes of the same crystals using DFT-predicted unit cell volume trends for each defect motif in order to derive a correlation between defect formation mechanism and hydration level. The ¹H NMR and XRD data suggest that up to ~1wt% H₂O, mainly Si defects ($V_{Si}'''' + 4H^{****}$, $Mg_{Si}'' + 2H^{**}$, $Mg_{Si}V_{Mg}'''' + 4H^{****}$) form, while at higher hydration levels the formation of Mg vacancies seems favoured ($V_{Mg}'' + 2H^{**}$).

This qualitative and quantitative solution of ringwoodite's defect chemistry as a function of hydration level opens up the possibility for modelling the thermodynamics of each hydration mechanism, as well as their interaction. Finally, this could lead to a reasonable model of the impact of ringwoodite's defect chemistry on the transport properties of the transition zone of the Earth's mantle. Furthermore, the NMR spectroscopic investigation of single-crystals, instead of powders, opens up the possibility for a comprehensive characterization of each crystal providing access to unique correlations between quantitative atomic pictures of defect motifs, absolute defect concentrations and their influence on the crystal structure on homogenous samples, which is of fundamental relevance for the investigation of the influence of defects on macroscopic properties. Therefore, the improvement of μ NMR methods to gain sensitivity could pave the way for the routine examination of small crystals.

Al defects in bridgmanite formed by two competing Al substitution mechanisms were investigated by electronprobe micro analysis and ²⁷Al MAS NMR spectroscopy on Al-bearing bridgmanite samples with varying Al contents synthesized in MgO-rich or SiO₂-rich synthesis conditions. These revealed that in MgO-rich systems the oxygen vacancy (OV) mechanism is dominant at low Al contents, while the charge-coupled (CC) mechanism increases linearly with increasing Al content and generally dominates in SiO₂-rich systems. Furthermore, the multidimensional ²⁷Al MAS NMR data in combination with the results of DFT calculations of multiple Al defect models demonstrate the formation of OV clusters probably due to a high mobility of OVs. This surprising OV mechanism leads to a roughly two times larger vacant crystallographic site than formed by an isolated OV. Such sites have been shown to be able to accommodate small noble gas atoms, such as neon, as well as OH groups, and this may therefore greatly change the understanding of the volatile cycling of noble gases and water into the Earth's lower mantle.

Zusammenfassung

In dieser Arbeit wurde mittels NMR Kristallographie die Defektchemie von zwei Hochdruck-Magnesiumsilikaten, Ringwoodit (γ - Mg_2SiO_4) und Bridgmanit (MgSiO_3), die einen Großteil des Erdmantels bilden, aufgeklärt. Auf diese Weise konzentrieren wir uns auf das Verständnis der verschiedenen Mechanismen der Defektbildung und bieten einen Rahmen, um die Auswirkungen auf die Mineraleigenschaften zu verstehen. Die erforderlichen Hochdrucksynthesen der Mineralien führen zu geringen Probenausbeuten, was in Kombination mit niedrigen Defektkonzentrationen die strukturelle Charakterisierung der Defekte anspruchsvoll gestaltet.

Wir waren dennoch in der Lage die Mechanismen der OH Defektbildung in Ringwoodit zu untersuchen, indem wir hochaufgelöste mehrdimensionale Festkörper- ^1H -NMR-Spektroskopie und *Dichte-Funktional-Theorie* (DFT) Simulationen diverser OH-Defekttypen kombinierten. Auf diese Weise verknüpften wir experimentelle und simulierte ^1H chemische Verschiebungen, sowie ^1H - ^1H -Konnektivitäten mit individuellen OH-Defektmotiven. Die qualitative Lösung offenbarte eine überraschend vielfältige OH-Defektchemie innerhalb der Spinell-Struktur von Ringwoodit mit der Bildung isolierter niedervalenter Mg^{2+} Leerstellen ladungsausgeglichen durch zwei Protonen ($V_{\text{Mg}}'' + 2\text{H}^{**}$), sowie isolierter hochvalenter Si^{4+} -Defekte mit einem Ladungsausgleich entweder durch vier Protonen ($V_{\text{Si}}'''' + 4\text{H}^{****}$) oder durch Mg^{2+} und zwei Protonen ($\text{Mg}_{\text{Si}}'' + 2\text{H}^{**}$). Zusätzlich bildete ein gekoppelter Defekttyp mit Mg^{2+} in einer Si-Lücke gekoppelt an eine oktaedrische Leerstelle ($\text{Mg}_{\text{Si}}V_{\text{Mg}}'''' + 4\text{H}^{****}$) einen signifikanten Anteil. Die inhärente Fehlordnung von Wasserstoffbrückenbindungen innerhalb der Defekte verhinderte eine unkomplizierte Quantifizierung verschiedener Defektmotive. Daher wurde ein neuer Ansatz basierend auf Molekulardynamik-Simulationen (MD) auf DFT-Niveau entwickelt, um lokale ^1H -Fehlordnungen in Punktdefekten zu modellieren und deren Einfluss auf zwei komplementäre ^1H NMR Observablen zu beschreiben. Individuelle Abdrücke der ^1H chemischen Verschiebung und charakteristische Ensemble-gemittelte ^1H - ^1H Doppelquanten-(DQ)-Aufbaukurven wurden von der modellierten OH-Fehlordnung für jeden der vier oben erwähnten Defekttypen abgeleitet. Diese wurden dann als gemeinsame Kostenfunktion für die Verfeinerung des stark überlappenden experimentellen ^1H -MAS-NMR-Spektrums und ^1H - ^1H -DQ-Aufbaukurven verwendet, was zur quantitativen

Bestimmung der Defekt-Motive zu $\sim 50\% V_{Mg}$, $18\% V_{Si}$, $\sim 13\% Mg_{Si}$ und 20% gekoppeltes $Mg_{Si}V_{Mg}$ führte.

Um die Mechanismen der OH-Defektbildung als Funktion des Hydratationsgrads zu untersuchen, wurde die Durchführbarkeit der 1H NMR-Spektroskopie an wasserhaltigen Nanoliter-großen Ringwoodit-Kristallen untersucht. Für drei Kristalle mit Hydratationsgraden zwischen einem Äquivalent von $0.3 - 2.0$ Gew.-% H_2O wurden die 1D 1H -MAS-NMR-Spektren unter Verwendung eines Standard MAS-NMR-Setups und eines μ MAS-„Piggy-back“-Designs erfolgreich aufgenommen und mit den zuvor bestimmten charakteristischen Abdrücken innerhalb 1H chemischen Verschiebung quantitativ verfeinert. Die resultierenden Verhältnisse der Defekt-Typen wurden mit den experimentellen Elementarzellen-Volumina der gleichen Kristalle unter Verwendung von DFT-vorhergesagten Trends des Elementarzellen-Volumens für jedes Defekt-Motiv verknüpft, um eine Korrelation zwischen Defektbildungsmechanismus und Hydratationsgrad abzuleiten. Die 1H NMR- und XRD-Daten legen nahe, dass bis zu etwa 1 Gew.-% hauptsächlich Si-Defekte ($V_{Si}'''' + 4H^{****}$, $Mg_{Si}'' + 2H^{**}$, $Mg_{Si}V_{Mg}'''' + 4H^{****}$) entstehen, während bei höheren Hydratationsgraden die Bildung von Mg-Leerstellen begünstigt erscheint ($V_{Mg}'' + 2H^{**}$).

Diese qualitative und quantitative Lösung der Defektchemie in Ringwoodit als Funktion des Hydratationsgrades eröffnet die Möglichkeit die Thermodynamik der Hydratationsmechanismen, sowie deren Wechselwirkung zu modellieren. Schließlich könnte dies zu einem begründeten Modell des Einflusses von der Defektchemie in Ringwoodit auf die Transporteigenschaften der Übergangszone des Erdmantels führen. Darüber hinaus eröffnet die NMR-spektroskopische Untersuchung von Einkristallen anstelle von Pulverproben die Möglichkeit einer umfassenden Charakterisierung von jedem Kristall, die den Zugang zu einzigartigen Korrelationen zwischen quantitativen atomaren Bildern der Defekt-Motive, absoluten Defektkonzentrationen und deren Einfluss auf die Kristallstruktur in homogenen Proben gewährt, was für die Ermittlung des Einflusses der Defekte auf makroskopische Eigenschaften von grundlegender Bedeutung ist. Daher könnte eine Verbesserung von μ NMR-Methoden zur Steigerung der Empfindlichkeit den Weg zur routinemäßigen Untersuchung kleiner Kristalle ebnen.

Al-Defekte in Bridgmanit, die durch zwei konkurrierende Al-Substitutionsmechanismen gebildet wurden, wurden mittels Elektronenstrahl-Mikroanalyse und ^{27}Al -MAS-NMR-Spektroskopie an Al-haltigen Bridgmanitproben mit variierenden Al-Gehalten aus MgO-

reichen oder SiO₂-reichen Synthesebedingungen untersucht. Diese zeigten, dass in MgO-reichen Systemen der Sauerstoff-Leerstellen (engl. oxygen vacancy, OV) Mechanismus bei niedrigen Al-Gehalten dominant ist, während der ladungsgekoppelte (engl. charge-coupled, CC) Mechanismus mit steigendem Al-Gehalt linear zunimmt und generell in SiO₂-reichen Systemen dominiert. Darüber hinaus demonstrieren die mehrdimensionalen ²⁷Al MAS NMR-Daten in Kombination mit den Ergebnissen von DFT-Rechnungen verschiedener Al-Defektmodelle die Bildung von Clustern aus Sauerstoff-Leerstellen wahrscheinlich aufgrund einer hohen Mobilität der Leerstellen. Dieser überraschende OV-Mechanismus führt zu einer etwa zweifach größeren vakanten kristallographischen Lücke als eine isolierte Sauerstoff-Leerstelle. Es wurde gezeigt, dass solche vakanten Lücken in der Lage sind kleine Edelgasatome, wie Neon, sowie OH-Gruppen aufzunehmen, und dies vermag daher das Verständnis für den Kreislauf flüchtiger Stoffe, Edelgase oder Wasser, in den unteren Erdmantel stark zu ändern.

1. Introduction

Disorder within crystalline materials often leads to interesting physical and chemical properties, which has the potential to lead to new functionality. Well-known examples are doping of semiconductors with foreign atoms to tune the electrical conductivity or photovoltaic activity.^[1,2] Furthermore, defects have influence on the chemical, thermal or mechanical stability of materials, in addition to diffusion and ion conductivity. In this context, point defects in the form of cation substitution also play an important role in high-pressure magnesium silicates of the Earth's mantle.^[3-5] Chemical components are exchanged between the Earth's surface and the mantle at subduction zones. One of the most important geochemical exchanges occurs as minerals formed at the surface carry trace amounts of H₂O into the deep interior, where it is ultimately hosted as OH defects in mantle minerals.^[3,6-9] In this respect, defects within the Mg₂SiO₄ polymorphs, forsterite (α -Mg₂SiO₄) in the upper mantle and wadsleyite (β -Mg₂SiO₄) and ringwoodite (γ -Mg₂SiO₄) in the transition zone, as well as within the MgSiO₃ phase bridgmanite in the lower mantle are of great importance (Figure 1), since these minerals are most abundant and together account for more than 62 vol% of the entire Earth.^[10-13]

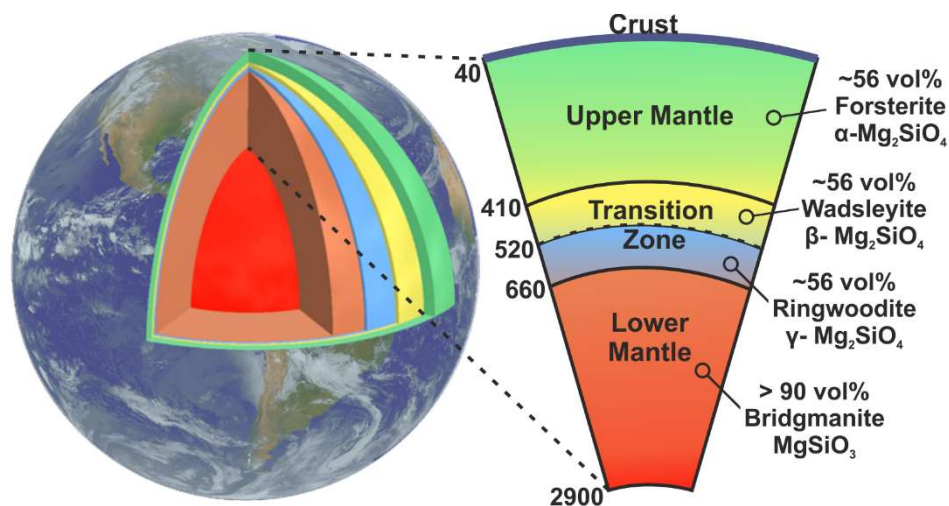


Figure 1. Left: Schematic representation of the layered structure of the Earth's interior. Right: Schematic cross section of the Earth's mantle and its dominant silicate minerals (Mg end members) at various depth.

The three Mg₂SiO₄ polymorphs have been shown to be able to incorporate significant amounts of OH defects charge balanced by cation vacancies. The total amount of equivalent

H₂O hosted in this manner may potentially comprise a large fraction of the Earth's entire water budget, which might even exceed that of all oceans.^[14–19] In the MgSiO₃ phase bridgmanite, that dominates in the lower mantle, Al substitution is known to cause the formation of oxygen vacancies, which can not only accommodate OH defects but may also host atoms of noble gases, such as neon, helium and argon.^[20–22] Therefore, hydrous Mg₂SiO₄, as well as aluminous MgSiO₃ phases are expected to play a crucial role in the deep cycle of volatiles in the Earth's mantle.^[20–23] Furthermore, the nature of the cation substitution mechanisms linked to OH and Al defects is of fundamental significance, since they may influence mineral physical properties, such as elasticity, viscosity and thermal conductivity, which are crucial to the operation of mantle convection.^[24–29]

Despite the importance of the problem, the defect chemistry of ringwoodite and bridgmanite are still open questions. This is mainly due to the necessity of extremely high synthesis pressures ($P > 18$ GPa) for these minerals that results in small sample yields. This further confounds the characterisation of defects which are anyway of low concentration. Furthermore, standard X-ray diffraction (XRD) techniques are impractical due to their focus on long-range order and their inability to resolve hydrogen and to differentiate between Al and Si.^[30,31] The structural investigation of OH and Al defects in high-pressure silicates is therefore a very challenging issue.

Solid-state nuclear magnetic resonance (NMR) spectroscopy combined with diffraction techniques and quantum-chemical calculations, so called NMR crystallography,^[31–33] has proven especially successful for the structural description of disordered materials at the atomic level.^[34–40] Solid-state NMR is independent of long-range order and, therefore, may offer information on local environments. In this context, the NMR data provide access not only to qualitative information concerning inequivalent sites, their local chemical environments, and homo- and heteronuclear connectivities, but also to quantitative data e.g. the ratio of different species and distance relations.^[32,33,36,41,42] Quantum-chemical calculations employing *Density Functional Theory* (DFT) are used to aid the assignment of resonances and to validate structural models.^[34,43–47]

This work therefore is concerned with the qualitative and quantitative structural description of OH disorder in hydrous ringwoodite using an NMR crystallographic approach. We have employed different analysis strategies mainly based on 1D and 2D solid-state NMR spectroscopy, combined with computational methods, to derive a consistent picture of

ringwoodite's defect chemistry. Additionally, we explore the possibility of an NMR spectroscopic approach to measure nanoliter ringwoodite crystals in order to allow for characterizing the defect formation mechanisms as a function of OH concentrations.

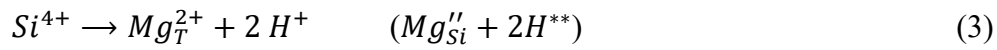
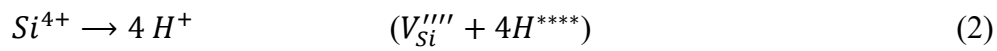
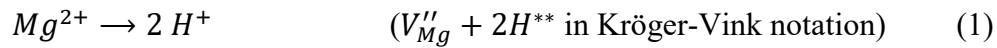
Moreover, the Al substitution mechanisms in bridgmanite are evaluated by NMR crystallography as a function of the Al content on perfectly characterized bridgmanite samples. All hydrous ringwoodite and Al-bearing bridgmanite samples were synthesized using sophisticated high pressure multi-anvil apparatuses at the Bayerisches Geoinstitut, University of Bayreuth.

1.1 Structural studies on defects in high-pressure minerals

After the prediction, based on Pauling bond strength calculations,^[48] that wadsleyite should be able to incorporate high concentrations of water in its structure as hydroxyl defects, unravelling the nature of its OH defect chemistry became the focus of many systematic experimental and analytical studies.^[14,44,45,49–53] Wadsleyite, a high pressure polymorph of olivine with the formula $\beta\text{-(Mg,Fe)}_2\text{SiO}_4$, is the main component of the transition zone region of the Earth's mantle, which encompasses depths between 410 and 520 km. These studies confirmed a maximum water solubility of ~ 3 wt% in wadsleyite and also revealed that the higher-pressure polymorph, ringwoodite, can host comparable quantities of water.^[14–16,18,53] Comprehensive single-crystal XRD, as well as systematic FTIR and multinuclear solid-state NMR spectroscopic investigations of wadsleyite samples containing the equivalent of 0.1 wt% to 3.2 wt% of water revealed a well-defined OH defect formation mechanism.^[14,44,45,51–53] The main hydrogen incorporation mechanism involves the formation of Mg^{2+} (Mg3 site) vacancies and the protonation of the 'underbonded' O1 species, which is not coordinated to Si in the orthorhombic structure of the β -polymorph. Minor amounts of Si-OH signals in ^1H NMR spectra also suggest a partial protonation of O3 and O4 species, which are the non-bridging O atoms of the pyrosilicate (Si_2O_7) building units.^[44,45] This well-defined defect mechanism is also reflected in the polarized FTIR spectra of wadsleyite, where two strong absorption peaks at ~ 3300 cm^{-1} and at ~ 3600 cm^{-1} occur.^[18,51,53]

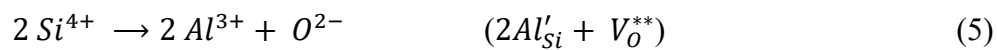
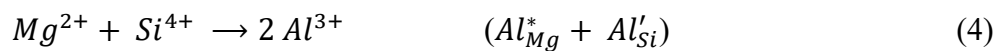
In contrast to wadsleyite, the FTIR spectrum of ringwoodite is difficult to interpret, since it shows very broad and overlapping absorption features in the range of 2400 cm^{-1} to

3800 cm⁻¹.^[18,54–56] The Mg/Si ratio is also barely influenced upon hydration and there seems to be a small degree of Mg/Si disorder.^[15,55] Furthermore, ringwoodite crystalizes in a spinel-type cubic structure consisting of isolated SiO₄ tetrahedra and edge-sharing MgO₆ octahedra.^[57] Therefore, wadsleyite's relatively simple OH defect chemistry involving only Mg vacancies is not applicable to the γ -polymorph. Consequently, high-valent Si⁴⁺ vacancies with and without local cation inversion of the spinel structure in addition to low-valent Mg²⁺ vacancies have been proposed as plausible mechanisms based mainly on computational studies:^[49,50,55,58–62]



In a systematic study Ye *et al.*^[58] correlated the unit cell volume expansion of hydrous ringwoodite to its water concentration between an equivalent of 0 and 2.8 wt% H₂O, whereby they found a discontinuity in the slope at ~2 wt% H₂O. The data were compared to DFT calculations and it was proposed that up to 2 wt% H₂O Mg vacancies (Eq. 1) mainly occur, while at higher water concentrations also high-valent Si defects according to Eq. 2 and 3 are formed.^[58,59] However, experimental data with atomic resolution of the defects to unambiguously verify or falsify this hypothesis are missing.

In the lower mantle the mineral bridgmanite (MgSiO₃) dominates, comprising more than 90 vol% of the mantle rock and, therefore, it is the most abundant mineral in the Earth as a whole.^[10–12] In contrast to the Mg₂SiO₄ polymorphs, the trivalent substitution of Al, besides Fe³⁺, is the main defect forming mechanism in bridgmanite, which crystalizes in an orthorhombic perovskite-type structure with Si in octahedral coordination (B site) and Mg in nominal dodecahedral coordination (A site).^[20,29,63–66] Two competing Al incorporation mechanisms have been proposed for bridgmanite. The first is the charge-coupled (CC) substitution, where Mg and Si are replaced by two Al and thus is charge balanced (Eq. 4).^[64] In the second mechanism only Si is replaced by Al and therefore the formation of oxygen vacancies (OV) is required for charge compensation (Eq. 5).^[20,29]



While vacancy-free bridgmanite can only accommodate minor amounts of water,^[67,68] the OV mechanism was proposed to lead to an increased water uptake ability in the lower mantle by:^[20,22]



The CC mechanism (Eq. 4) is expected for SiO₂-saturated compositions and at higher pressures,^[69,70] while the OV mechanism (Eq. 5) is proposed to be favoured in MgO-saturated compositions and lower pressures.^[20,22,29,71] However, X-ray absorption and solid-state ²⁷Al NMR studies on aluminous bridgmanite to investigate OV and Al defect distributions revealed Al in six-fold or higher coordination indicating that mostly the CC mechanism took place.^[40,72–75] Still, these studies suffered from slightly inhomogeneous samples or SiO₂-rich synthesis conditions, which may have influenced the results or prevented significant formation of OV in bridgmanite, respectively. Systematic investigations as function of Al content are challenging due to the necessity to control the very demanding synthesis conditions, such as control of Mg or Si excesses, high temperatures and especially of high pressures. Due also to difficulties in growing sufficiently big single crystals for X-ray analysis, comprehensive data with atomic resolution to derive a consistent picture of bridgmanites Al defect chemistry are still absent.

1.2 NMR crystallography

Crystal structures are routinely examined by XRD techniques, which depend on the long-range order of atoms and therefore provide information about periodicity. XRD methods may also detect atomic disorder indirectly through differences in electron density mapping, but this only provides average information for each crystallographic site.^[30,31,76] Furthermore, for light atoms such as hydrogen or lithium and for Si/Al disorder, XRD is unable to resolve atom positions due to too low or similar scattering strengths, respectively.^[31–33]

To overcome this problem diffraction techniques have been combined with solid-state NMR spectroscopy and quantum-chemical calculations – so called NMR crystallography^[32,33] – to provide complementary structural information e.g. about dynamics^[77], proton substructures^[38,78] or point defects^[34,40,44]. Solid-state NMR

spectroscopy makes use of the interaction of nuclear spins with an external magnetic field and is able to probe internal spin interactions, whereby the chemical shift, the direct dipole-dipole and the quadrupolar interaction are mostly used.^[41,77,79] These are independent of periodicity and hence can provide local structural information, e.g. chemical environments, symmetries, homo- and heteronuclear connectivities and distances between nuclear spins, for crystalline, as well as amorphous materials.^[32,33,41] Quantum-mechanical calculations are used to calculate the energies and NMR parameters, i.e. chemical shift and electric field gradient (EFG) tensors, of structural models, which can then be compared to experimental data. This may be used to aid the assignment of resonances and to validate different structural models.^[43,44,46,47] Due to its broad applicability and the wide range in information that can be obtained, NMR crystallography has been used for the structure elucidation of, for example, porous materials^[42,80–82], polymer systems^[83–85], glasses^[86–88], proteins^[89–91] and minerals^[92–95].

The chemical shift interaction describes the interaction of the external magnetic field with local fields of the nuclear spins caused by their local electronic and thus chemical environment. The number and intensity ratio of resonances can be used to identify inequivalent crystallographic sites and their multiplicity and can, therefore, be used to deduce information about the asymmetric unit or space groups.^[31,36] Furthermore, chemical shift values are characteristic for chemical groups and thus allow for the determination of functional groups and structural building units.^[31,96] In this context, quantum-mechanical calculations employing *Density Functional Theory* (DFT) are particularly effective for calculating chemical shifts for specific structural models that can then be used as a cost function for evaluating the structure.^[31,43,46,47,97]

The interaction of a quadrupole moment, which is caused by a non-spherical charge distribution in nuclei with a spin $I > \frac{1}{2}$, with the electric field gradient (EFG) is called the quadrupolar interaction. Since the EFG arises from the distribution of the electronic environment around the nuclei, i.e. mostly the coordinating atoms, the quadrupolar interaction is very sensitive to local structural environments, e.g. coordination polyhedra.^[98,99] Similarly to the chemical shifts, the quadrupolar couplings can be simulated by DFT calculations and used for validating structural models.^[43,46,47,100]

The direct dipole-dipole interaction between the magnetic moments of spins in close spatial proximity is a very important interaction in solid-state NMR spectroscopy, since it depends

on the orientation as well as the distances between the spins. Therefore, it allows for determining homo-^[80,101–104] and heteronuclear^[105,106] connectivities and distances^[38,107–111], if the resonances are sufficiently resolved. Magic-angle spinning^[112,113] (MAS) is used to average anisotropic interaction parts in order to gain high resolution spectra allowing for an assignment of individual resonances. In this way, the dipolar interaction is also averaged and must then selectively be recoupled to extract different connectivity and distance information. The recoupling of certain dipolar interaction parts is accomplished by synchronising nuclear spin rotations by radiofrequency (rf) pulses with the MAS sample rotation.^[114–117]

Often double-quantum (DQ) coherences are excited to gain information about homonuclear coupled spins. Since the DQ interaction strength and thus the DQ intensities depend on the internuclear distance proportional to r^{-3} between the coupled spins, it is possible to evaluate not only qualitatively the connectivity of species by two-dimensional (2D) double-quantum-single-quantum (DQSQ) experiments (Figure 2, left), but to quantitatively determine distances between the spins. For this purpose a series of DQ spectra as a function of excitation time of DQ coherences is measured and the DQ signal amplitudes result in DQ buildup curves (Figure 2, right), which contain the quantitative distance information. For isolated spin pairs the distance information can be extracted by fits of buildup curves using analytical expressions, while the buildup curves of extended spin systems are influenced by all dipolar couplings and usually are simulated numerically based on model systems.^[118]

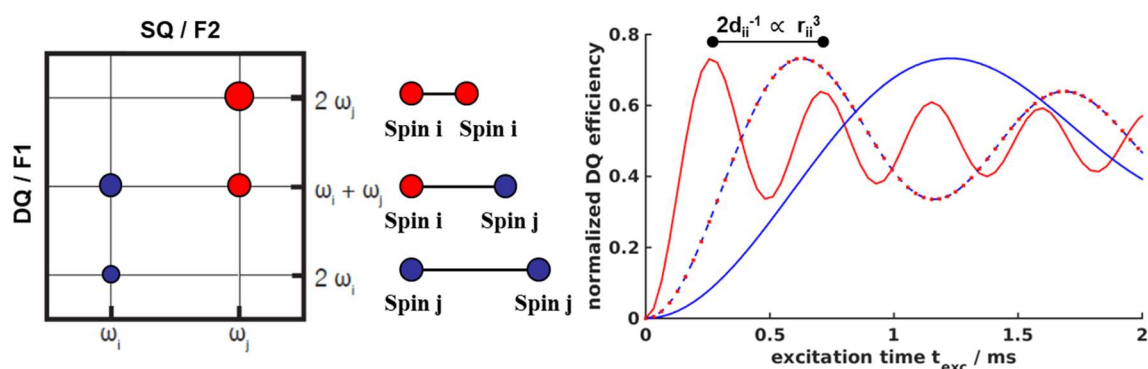


Figure 2. Left: Schematic 2D homonuclear correlation (DQSQ) spectrum of a model spin system containing two different species *i* (red) and *j* (blue) depicting auto-correlation signals on the diagonal and cross correlation at the sum of the two chemical shift frequencies. Right: corresponding symmetric DQ buildup curves of the three isolated spin pairs *i*-*i* (red), *i*-*j* (red and blue dashed) and *j*-*j* (blue) revealing the different internuclear distances.

Due to the high gyromagnetic ratio and a high spin density of ^1H spins a high sensitivity is reached for ^1H solid-state NMR, but the homonuclear dipolar interaction strength between protons gets very strong. This leads to a severe broadening of resonances, which can easily surpass all ^1H chemical shift effects preventing the characterization of inequivalent sites and structural building blocks, which are essential for structure elucidation. Therefore, ultrafast MAS (> 40 kHz) is necessary to narrow the homogeneously broadened lines and to reach a sufficient resolution of ^1H signals.^[113,119] Fast spinning, however, renders the use of dipolar recoupling sequences more difficult due to the necessity to synchronise the timing and power of the rf pulses to the spinning speed.^[114,120] Only recent advances in faster MAS^[113], modern rf consoles, as well as pulse sequence optimizations^[111] allow ^1H NMR experiments to be performed that directly probe proton proton proximities.^[101,108,121–124]

Solid-state NMR is in principal an ideal tool for studying defects in materials due to its local character and ability to resolve the number and type of coordinating atoms. However, disorder often leads to difficulties. Even when high-resolution techniques are used, increasing levels of disorder can cause complicated NMR spectra with heavy spectral overlap, especially in the case of protons, due to small changes in chemical shifts for disordered species. This impedes spectral assignment and the extraction of structural information severely and renders the use of quantum-mechanical calculations of NMR parameters even more important. However, in order to treat the disorder, a large number of initial models with slight changes in their local environments, as well as big supercells are often required. This leads to a large number of possible models and thus to high computational costs. For these reasons often only simplified approaches are possible, which aim at understanding the relative variations in NMR parameters, rather than creating a ‘real’ picture of the structure and exact magnitudes. Consequently, other methods have been developed, such as *ab initio* random structure searching^[125] (AIRSS) or simulated annealing^[126] (SA), the latter based either on classical molecular dynamics (MD) or Monte-Carlo (MC) algorithms, to tightly probe the potential energy surface of the system of interest. These techniques are able to handle virtually random structures and, therefore, can also be used for structure prediction reducing bias in the candidate structures for the disorder model. The main drawbacks of empirical forcefield based techniques, i.e. classical MD and MC runs, are the accuracy of the calculations, that they may easily get stuck in local minima and that the NMR parameters are not directly accessible. AIRSS overcomes

the latter problem since it is based on DFT, but thus is also more limited in the number of atoms.^[125] Recently, AIRSS was combined with a number of structural constraints, such as unit-cell size, bonding environments and prearranged groups of atoms, to enable a detailed investigation of hydrogen disorder in hydrous defects in the high-pressure silicate wadsleyite.^[45]

2. Synopsis

This work consists of two publications and two manuscripts (see chapter 3 & 4) dealing with different aspects of the defect chemistry of high-pressure magnesium silicates of the Earth's deep interior. In all studies an NMR crystallographic approach was applied to investigate qualitatively and quantitatively different defect motifs.

The synthesis of mantle minerals requires similar conditions as in the Earth's mantle, i.e. high pressures and temperatures. Therefore, all defect-bearing mineral samples were synthesized using high-pressure multi-anvil apparatuses at the Bayerisches Geoinstitut, University of Bayreuth.

2.1 Solving ringwoodite's OH defect chemistry by NMR crystallography

The main project within this work is the investigation of ringwoodite's hydrous defect chemistry, which is expected to store H₂O in the Earth's interior in the form of structurally bound OH, in a quantity that may exceed that of the oceans. Perhaps more importantly, the atomic structure of these OH defects will influence the chemical and physical properties of the silicate. Therefore, a structural investigation of the OH defects is essential to understand their impact on the macroscopic properties of the Earth's mantle.

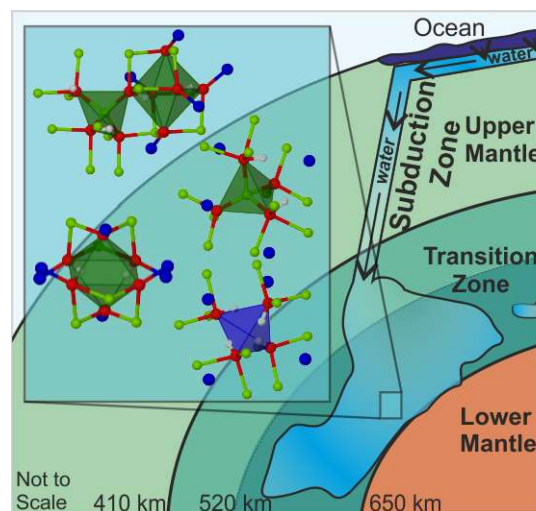


Figure 3. Scheme of the layered structure of the Earth's mantle (not to scale) and the potential formation of an „hidden ocean“ within the transition zone. Possible hydrous defect motifs in ringwoodite's structure are depicted as inset.

Anhydrous ringwoodite (γ - Mg_2SiO_4) crystallizes in a cubic spinel-type structure consisting of isolated SiO_4 tetrahedra and edge-sharing MgO_6 octahedra (Figure 4). Different cation substitution mechanisms are proposed in the literature including Mg and Si vacancies and a partial inversion of the spinel structure (Eq. 1-3, chapter 1.1), but unambiguous experimental data are missing. We therefore investigated multiple OH defect motifs in ringwoodite by a combination of computational methods and ^1H NMR spectroscopy mainly. The first publication “*Hidden Oceans? Unraveling the Structure of Hydrous Defects in the Earth’s Deep Interior*”^[127] is concerned with an NMR crystallographic approach to probe qualitatively different hydrous defect motifs based mainly on using a combination of ^1H chemical shifts and ^1H - ^1H connectivities as cost functions.

The hydrous ringwoodite sample studied in this work was synthesized at the Bayerisches Geoinstitut, University of Bayreuth at 19 GPa and 1150 °C using a large-volume high-pressure multi-anvil apparatus. In order to avoid the formation of MgO-rich dense hydrous impurity phases,^[15] a two step-synthesis was used to reduce pressure and temperature gradients, which arise due to phase transformations and thus volume loss during the synthesis run. We first converted forsterite (α - Mg_2SiO_4) with ~2 wt% liquid water to hydrous wadsleyite (β - Mg_2SiO_4), to which a small amount of SiO_2 was added. The mixture was then converted to hydrous ringwoodite (γ - Mg_2SiO_4) in a second high-pressure run. The phase purity of the recovered products was checked by powder XRD and the water content of ringwoodite was estimated from the b/a lattice parameter ratio of the intermediate wadsleyite to an H_2O equivalence of ~0.1 wt%.

DFT calculations of different OH defect motifs were used to get insight into different defect formation mechanisms. In principle, isolated Mg vacancies charge-balanced by two protons ($V_{\text{Mg}}'' + 2\text{H}^{**}$, Figure 4d), as well as isolated Si vacancies charge balanced either by four protons ($V_{\text{Si}}'''' + 4\text{H}^{****}$, Figure 4e) or one Mg^{2+} and two protons ($\text{Mg}_{\text{Si}}'' + 2\text{H}^{**}$, Figure 4f) are possible.^[59] Furthermore, coupled defects are conceivable, i.e. two coupled octahedral vacancies ($V_{2\text{Mg}}'''' + 4\text{H}^{****}$, Figure 4g) or an Mg_{Si}'' defect coupled to an octahedral void ($\text{Mg}_{\text{Si}}V_{\text{Mg}}'''' + 4\text{H}^{****}$, Figure 4h), which can also be described as local cation inversion in the spinel structure and subsequent Si substitution. Consequently, also a local cation inversion associated with a low-valent Mg defect formation ($V_{\text{Mg}}'' + \text{Mg}_{\text{Si}}'' + \text{Si}_{\text{Mg}}'' + 2\text{H}^{**}$, Figure 4i) has to be considered. Furthermore, multiple proton positions were explored to account for thermal disorder.

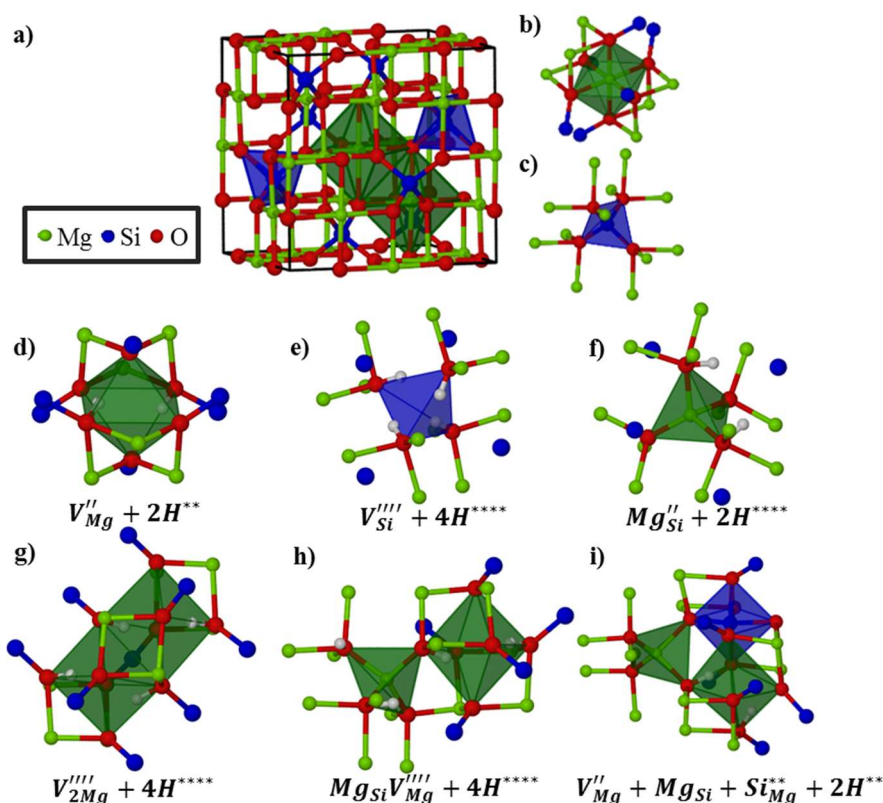


Figure 4. a) Cubic unit cell of the anhydrous ringwoodite crystal structure consisting of edge-sharing MgO_6 octahedra and isolated SiO_4 tetrahedra. The first cation sphere per octahedral and tetrahedral void is shown in b) and c), respectively. d-i) Models of OH defect motifs within hydrous ringwoodite. d) Isolated Mg vacancy charge balanced by two protons resulting in OH groups in mixed Si and Mg environments. e+f) isolated Si vacancies charge balanced by four protons (e) and one Mg^{2+} and two protons (f), respectively. Protons in tetrahedral voids result in OH groups in pure Mg environments. g-i) Coupled defect models: g) coupled Mg vacancies charge balanced by four protons; h) coupled defect with an octahedral vacancy and one Mg^{2+} on a Si site; i) coupled defect with an octahedral vacancy adjacent to local Mg/Si inversion.

Since the calculated energies from DFT simulations of the defect models are difficult to compare, due to the varying stoichiometry, calculated 1H and ^{29}Si isotropic chemical shifts in combination with 1H 1H connectivities are employed as suitable cost functions to determine the defect motifs associated with ringwoodite's defect chemistry. While the isotropic chemical shifts are mainly influenced by the electron density at the nuclei, homonuclear connectivities depend on the direct dipole-dipole interaction. In this way, two different interactions can be used to probe the defect models.

The calculated ^{29}Si and 1H isotropic chemical shifts reveal a clear dependency on the first cation coordination sphere of the nuclei (Figure 5) and are in good agreement with the experimental NMR spectra.

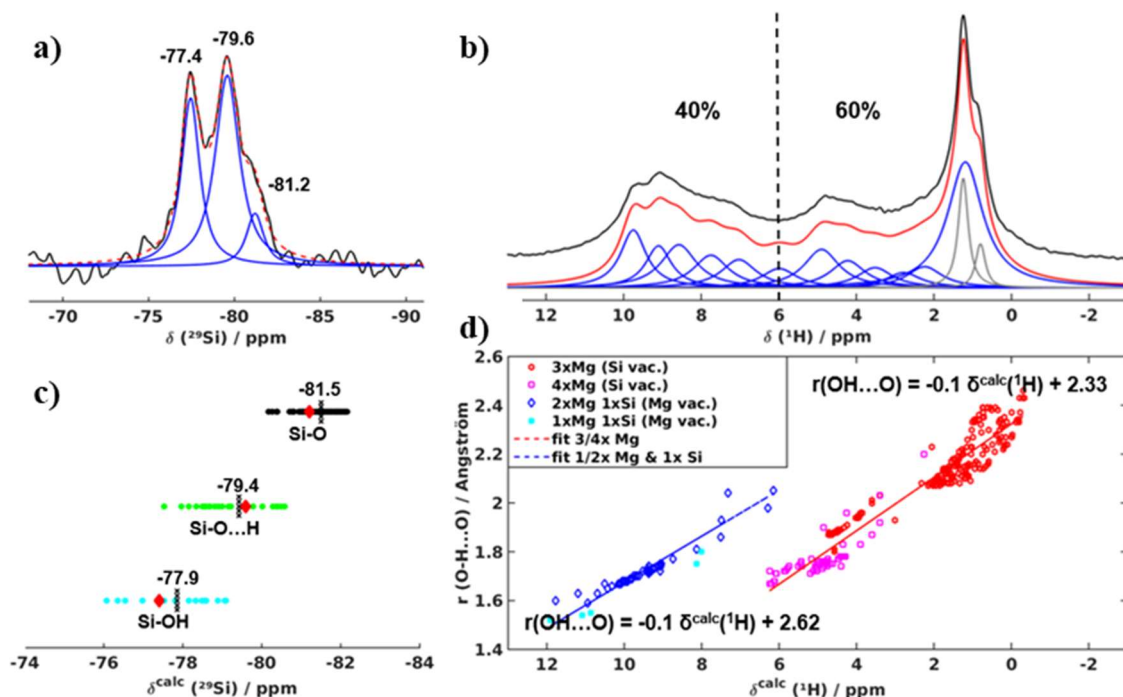


Figure 5. a) Section of the experimental ^1H ^{29}Si CP MAS spectrum revealing three ^{IV}Si species at -77.4, -79.6 and -81.2 ppm. b) Experimental ^1H MAS NMR spin echo spectrum of hydrous ringwoodite. A fit (red) with 14 components (blue and grey) is necessary to reproduce the broad and structured lineshape of the experimental spectrum (black). The resonances depicted in grey are assigned to proton species on the surface. c-d) Calculated isotropic ^{29}Si and ^1H chemical shifts, respectively, of the hydrous defect models shown in Figure 4d-i with multiple OH positions. c) The calculated ^{29}Si chemical shifts are grouped by the closest hydrogen environment of the respective Si species (Si-O: black; SiO...H: green; Si-OH: cyan) Average simulated values are indicated by vertical lines and experimentally observed ^{29}Si chemical shifts are indicated by red diamonds for comparison and allowing for an assignment of experimental resonances to Si-O, SiO...H and Si-OH, respectively. d) Correlation between the calculated ^1H chemical shifts, first cation coordination sphere and hydrogen bond length revealing that the cation environment determines the ^1H shift region of the OH. The hydrogen bond length and ^1H chemical shift show additionally linear correlations for both cation environments.

The experimental ^1H ^{29}Si CP MAS spectrum probes Si species in close proximity to protons and reveals three resonances in the area of ^{IV}Si species at -81.2, -79.6 and -77.4 ppm. The total absence of signals in the region between -150 and -220 ppm rules out the formation of octahedral ^{VI}Si species close to protons and thus exclude any defect models involving full cation inversion such as that shown in Figure 4i.

The ^{29}Si chemical shifts of the SiO_4 tetrahedra show an increasing downfield shift with decreasing proximity to protons in the calculations (Figure 5c), allowing for an assignment of the three experimentally observed ^{29}Si resonances to Si-O, SiO...H and Si-OH species.

The experimental ^1H MAS NMR spectrum of ringwoodite (Figure 5b) exhibits a remarkably broad but structured lineshape with resonances between 0 and 10 ppm. The sharper signals at 1.2 and 0.8 ppm are considered to arise from surface-species, i.e. Si-OH groups.

Our DFT simulations cover the same ^1H chemical shift range and reveal two main influences on ^1H chemical shift: the first cation coordination sphere and the hydrogen bond strength (Figure 5d). The calculated ^1H chemical shift range of OH groups in octahedral vacancies (Figure 4d,g,h,i), and thus in mixed Si and Mg environments, is between 6 and 12 ppm (Figure 5d, blue), while the simulated ^1H chemical shift range for OH in tetrahedral voids (Figure 4e,f,h,i), and thus in pure Mg environments, is between 0 and 6 ppm (Figure 5d, red and pink). Furthermore, if the OH groups are involved in hydrogen bonds, an additional downfield shift proportional to the hydrogen bond strength is observed, which can be described by the following equations:

$$\text{OH in mixed Si and Mg environments:} \quad \delta_{iso}(^1\text{H}) = \frac{r(\text{OH}\cdots\text{O})-2.62}{-0.1} \quad (7)$$

(octahedral voids)

$$\text{OH in pure Mg environments:} \quad \delta_{iso}(^1\text{H}) = \frac{r(\text{OH}\cdots\text{O})-2.33}{-0.1} \quad (8)$$

(tetrahedral voids)

Accordingly, the experimental 1D ^1H MAS NMR spectrum can be divided into a downfield ($\delta_{iso} > 6$ ppm) and a highfield region ($\delta_{iso} < 6$ ppm), revealing that Mg as well as Si defects with hydrogen bond distributions are present.

In order to constrain the defect motifs further, i.e. to differentiate between isolated and coupled models, ^1H ^1H connectivity patterns are identified from 2D ^1H ^1H DQSQ MAS NMR spectra with short DQ excitation times, so that only protons in close proximity up to 3.5 Å and thus within individual defects are highlighted. Hence, the experiments can be directly compared to the simulated connectivities of each defect type (Figure 6) and allow for a qualitative solution of defect motifs. While the strong experimentally observed autocorrelation signals along the diagonal (Figure 6I, blue and red area) are excellently reflected by the three isolated Mg and Si defect types (Figure 6IIa-c), the cross correlation pattern (Figure 6I, green regions) between the previously defined down- and highfield region is only reproduced by the coupled defect $Mg_{Si}V_{Mg}'''' + 4H^{****}$ (Figure 4h) revealing its formation in hydrous ringwoodite. The spread of experimental signals along the diagonal again reflects hydrogen bond distributions caused by orientational disorder of the OH groups.

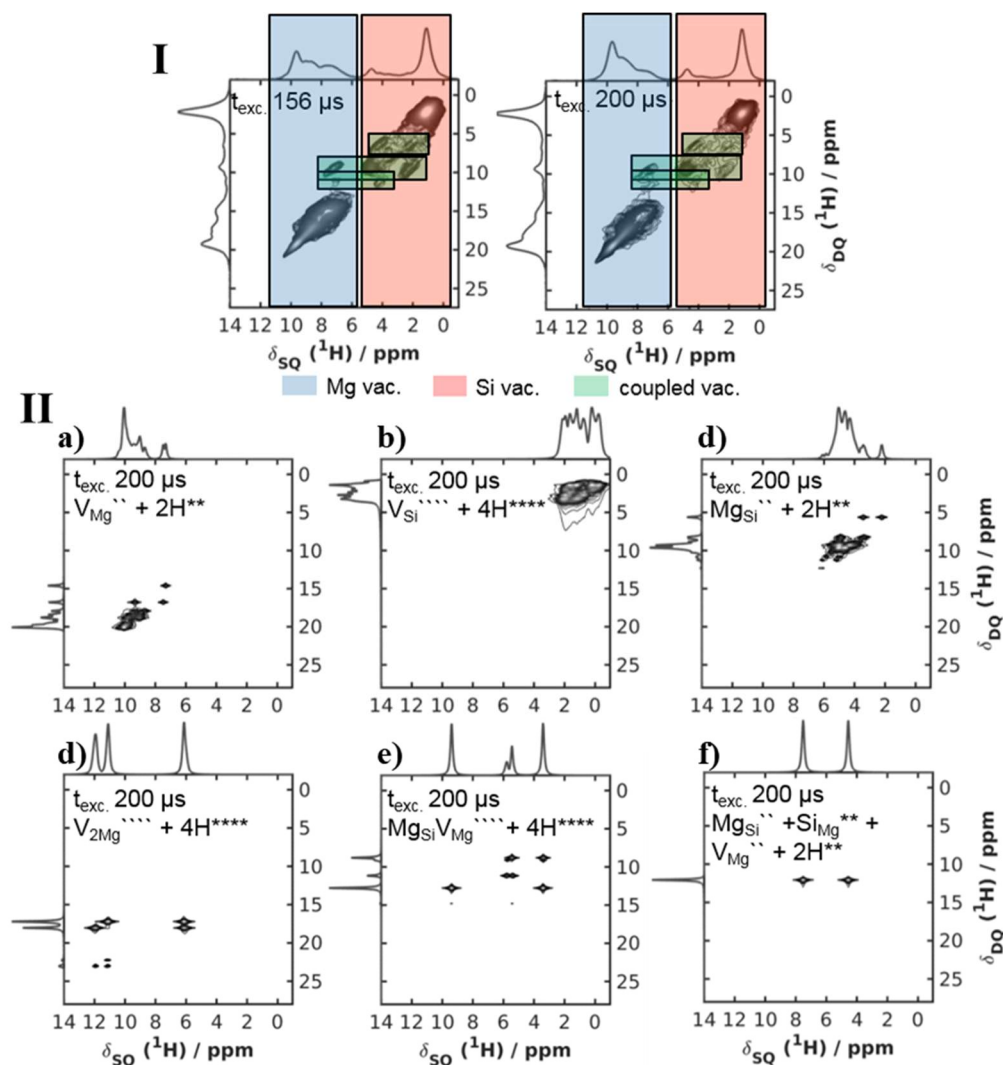


Figure 6. I) Experimentally observed 2D ^1H ^1H DQSQ MAS NMR spectra of hydrous ringwoodite and the assignment of resonances to different vacancy types. II) Simulated 2D ^1H ^1H DQSQ MAS NMR spectra of each defect model shown in Figure 4d-i with multiple OH group positions. The comparison of the experimentally observed to the theoretical connectivity patterns allow for a qualitative determination of hydrous defect types in ringwoodite to isolated Mg and Si vacancies with and without Si/Mg inversion ($V_{\text{Mg}}'' + 2\text{H}^{**}$, $\text{Mg}_{\text{Si}}'' + 2\text{H}^{**}$, $V_{\text{Si}}'''' + 4\text{H}^{****}$, Figure 4d-f), as well as additionally a coupled $\text{Mg}_{\text{Si}}V_{\text{Mg}}'''' + 4\text{H}^{****}$ defect type (Figure 4h).

The 2D ^1H ^1H DQSQ spectra do provide a good resolution, but the spectra cannot be used to extract the defect ratios, since the DQ intensity is not only dependent on the number of contributing ^1H spins, but also on the alignment and distance between the coupled ^1H spins. Therefore, the 1D ^1H MAS NMR spectrum (Figure 5b) has been considered, which suffers from heavy spectral overlap caused by OH \cdots O bond distributions within the four defect types, preventing a straightforward determination of defect ratios by integration, and a reasonable deconvolution of the overlapping 1D spectrum is required.

For this reason we have investigated a new approach to fully model local proton disorder within point defects in the publication “*Quantitative description of ^1H SQ and DQ coherences for the hydroxyl disorder within hydrous ringwoodite*”^[128] in order to gain a quantitative description of defect motifs.

In principle, molecular dynamics simulations employing the DFT method (MD DFT) are used to probe the energy hypersurface around distinct local minima of each defect motif and to model the displacive OH group disorder within each defect type. Since at least two OH groups are in each defect, disorder of these will not only alter the hydrogen bond strength and thus the ^1H chemical shift according to Eq. 7 and 8, but also the ^1H ^1H distances and thus the homonuclear dipolar interaction strength, which can be quantitatively investigated by DQ buildup curves. Therefore, we can use two experimental observables, which rely on different interactions, to probe the OH positions in a joint fashion. It turns out to be advantageous to put the computational effort into the structure prediction at the accuracy of DFT to reproduce the characteristic features of the disorder for both NMR observables and to use our empirical correlations (Eq. 7 and 8) between chemical shift and structural elements to link the proton environment to the ^1H chemical shift interaction.

For each of the four defect types, $V''_{Mg} + 2H^{**}$, $Mg''_{Si} + 2H^{**}$, $V''''_{Si} + 4H^{****}$ and $Mg_{Si}V''''_{Mg} + 4H^{****}$, several thousands of reasonable models with slight changes in the proton configuration representing a model for the OH group disorder were obtained by MD DFT simulation of the minimum structures. In order to translate the position and orientation of the OH groups to experimental observables, the empirical correlations from Eq. 7 and 8 were used to calculate the ^1H shifts from the simulated hydrogen bond length. By summing convoluted individual ^1H signals for each calculated shift over 10.000 MD steps individual footprints within the ^1H lineshape are obtained as the first cost function (Figure 7a). The simulated characteristic ^1H signals for each defect motif show strongly overlapping shift regions, each with a well-defined shape and maxima in the downfield and highfield regions, respectively, corresponding to mixed Si and Mg or pure Mg environments.

The ^1H ^1H distances of the MD run of each defect motif were used to generate the second cost function by simulating the individual ensemble average DQ buildup curves (Figure 7b) and a subsequent comparison to experimental findings (Figure 7b, grey dots).

Experimental curves were recorded using the $R18_8^5$ sequence, a symmetry-based pulse sequence which recouples the homonuclear dipolar interaction and allows for a fast

sampling and a reasonable pulse power, with an S_0S_π supercycle to minimize the influence of chemical shift anisotropy cross terms.^[111,120] The strong overlap of ^1H resonances for different defect types in addition to their inherent OH group disorder with varying ^1H – ^1H distances result in averaging of the experimental DQ buildup curves. Therefore, only curves for the two characteristic down- and highfield chemical shift region were used to measure symmetric integral 1D ^1H – ^1H DQ buildup curves (Figure 7b, grey dots). Comparable simulated DQ buildup curves (Figure 7b) were generated by first calculating the corresponding individual ^1H – ^1H DQ buildup curve for each step of the MD simulations including the full proton chemical shift tensors and all dipolar couplings to account for possible second-order cross terms. Subsequently, these are summed and normalized over all 10.000 MD steps.

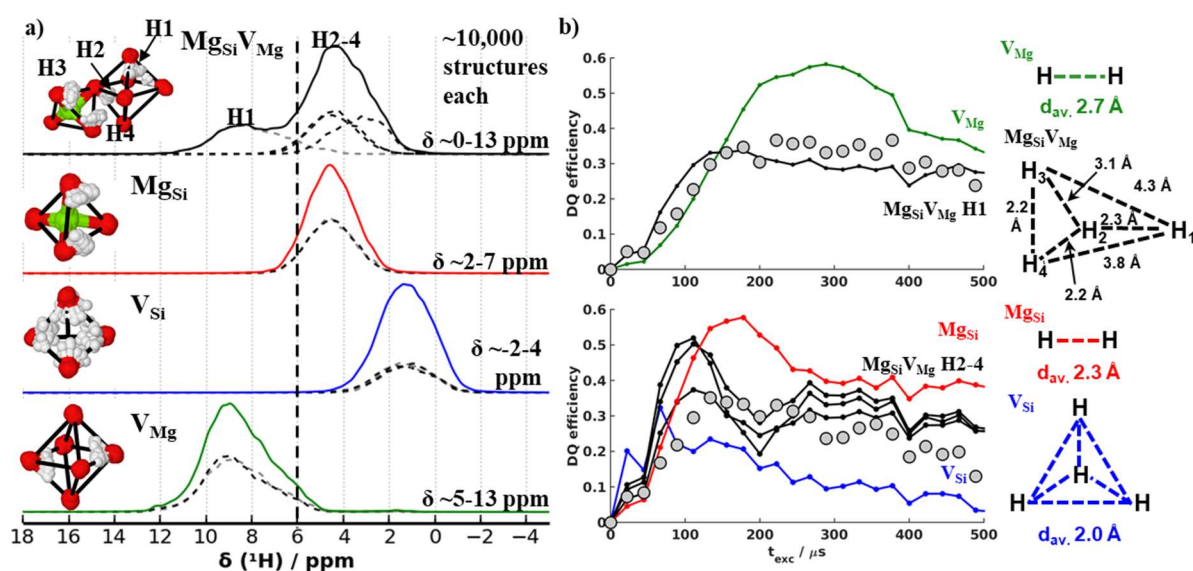


Figure 7. a) Simulated characteristic ^1H signals for all OH groups of each hydrous defect motif in ringwoodite calculated from 10.000 MD steps. The calculated spectra are divided into downfield and highfield regions according to OH groups in mixed Mg and Si and pure Mg environments, respectively. Exemplary proton positions from the MD runs for all OH defect types are depicted on the left side. b) Top: Experimentally measured ^1H – ^1H DQ buildup curves for the downfield shift region ($\delta > 6$ ppm; grey dots) and the corresponding simulated ^1H – ^1H DQ buildup curves of an isolated Mg vacancy (V_{Mg} , green), as well as for the OH group in mixed Si and Mg environments (H1) of the mixed coupled defect (MgSiV_{Mg} , black). Bottom: Experimentally measured ^1H – ^1H DQ buildup curve for the highfield shift region ($\delta < 6$ ppm; grey dots) and the simulated ^1H – ^1H DQ buildup curves of an isolated Si vacancy charge balanced by four protons (V_{Si} , blue), as well as charge balanced by one Mg^{2+} and two protons (MgSi , red) and for the three OH groups in pure Mg environments (H2–H4) of the mixed coupled defect (MgSiV_{Mg} , black). The ^1H connectivities of each defect type and the corresponding ensemble average ^1H – ^1H distances (d_{av}) of the MD runs are additionally depicted on the right side.

Both simulated observables, individual lineshapes within ^1H signals and individual ^1H – ^1H DQ buildup curves, were then combined in one approach to fit the experimental ^1H MAS

NMR spectrum together with the experimental ^1H - ^1H DQ buildup curves using a joint cost function in order to gain a quantitative description of ringwoodite's defect chemistry. In principle, the fit function optimizes the summed lineshape of the four simulated individual ^1H signals and the sum of the simulated ^1H - ^1H DQ buildup curves for each characteristic shift region in a joint fashion by varying the defect ratios to fit the experimental lineshape and both experimental integral buildup curves (Figure 8).

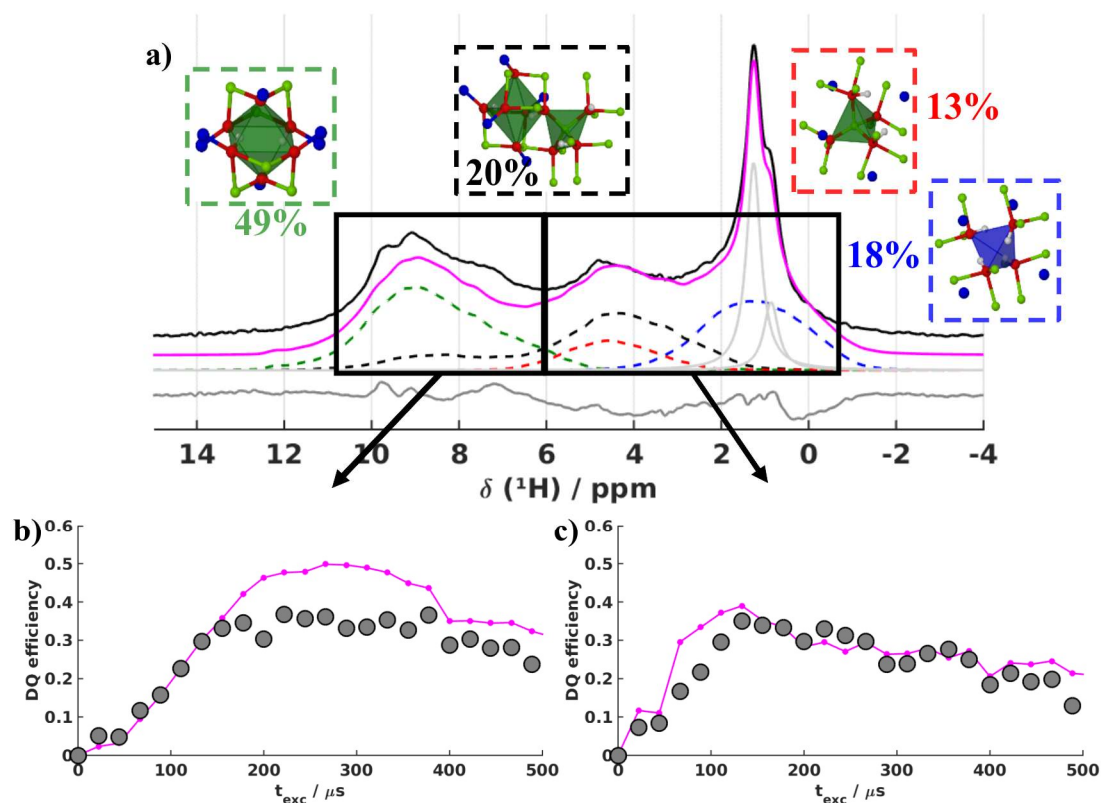


Figure 8. a) Experimentally observed ^1H MAS NMR spin echo of hydrous ringwoodite fitted by the sum of the ^1H signals (pink) calculated of the MD simulations of the defect types V_{Mg} (green dashed), V_{Si} (blue dashed), Mg_{Si} (red dashed) and $\text{Mg}_{\text{Si}}V_{\text{Mg}}$ (black dashed). The two resonances depicted in grey are assigned to proton species on the surface. The difference between experiment and simulation is shown in grey below the spectrum. The areas used for the ^1H - ^1H DQ buildup curves are indicated by black rectangles. b+ c) Combination of the simulated ^1H - ^1H DQ buildup curves of the corresponding models shown in Figure 7b) with the defect ratio observed in the 1D ^1H spectrum (pink) in comparison to the appropriate experimental curve (grey dots). The experimental error of the ^1H - ^1H DQ buildup curves is estimated from the S/N ratio to 5–10%.

The joint refinement resulted in an excellent fit of both experimental observables, the ^1H lineshape as well as the two ^1H - ^1H DQ buildup curves, allowing the quantitative ratio of the defect motifs to be determined with an average accuracy of $\sim 5\%$ for each defect type: isolated Mg vacancies ($V_{\text{Mg}}'' + 2\text{H}^{**}$) account for $\sim 49\%$, while isolated Si defects, $V_{\text{Si}}'''' + 4\text{H}^{****}$ and $\text{Mg}_{\text{Si}}'' + 2\text{H}^{**}$ amount to $\sim 18\%$ and $\sim 13\%$. The contribution of the mixed coupled

defect type $Mg_{Si}V_{Mg}'''' + 4H^{****}$ is ~20%. Furthermore, the excellent agreement between experiment and simulation confirm that our MD DFT calculations are able to scan the full range of orientations and hydrogen bonding for OH groups within constrained defect sites and, therefore, we conclude that MD DFT simulations are well suited for modelling local proton disorder within point defects.

This quantitative assessment of ringwoodite's defect chemistry is the basis to understand its thermodynamic properties, such as the extraction of equilibrium constants or reaction enthalpies of the water incorporation mechanisms, if more hydroxyl concentrations are evaluated. In this instance, the exploration of single crystals instead of a powder sample has several desirable advantages, such as a simplification of the synthesis, since the phase purity within the whole synthesis capsule is no longer an issue, an undoubtable high homogeneity of the sample with respect to water concentration and defect distribution, as well as the possibility to correlate the defect ratios with i.e. changes in the crystal structure measured by XRD and a precise determination of water concentration by FTIR spectroscopy on the same crystals. Therefore, within the manuscript "*On the feasibility of 1H NMR on hydrous defects within nanoliter ringwoodite crystals*" we explore the feasibility of measuring 1H NMR spectra of nanoliter (nL) ringwoodite crystals to study the minerals defect chemistry as a function of water concentration.

We have picked three nL ringwoodite crystals A-C with volumes of ~6-18 nL from two high-pressure synthesis runs with different hydration levels of roughly 0.3(2) wt% H₂O (crystal A) and 2.0(5) wt% H₂O (crystal B+C) estimated by unpolarised FTIR spectroscopy on double-polished thin sections of crystals of the corresponding synthesis runs (Figure 9). Furthermore, we confirmed that the chosen crystals were ringwoodite using preliminary X-ray diffraction patterns recorded in a Debye-Scherrer geometry and we determined the lattice parameters of each crystal by Pawley refinements^[129] of the resulting XRD patterns.

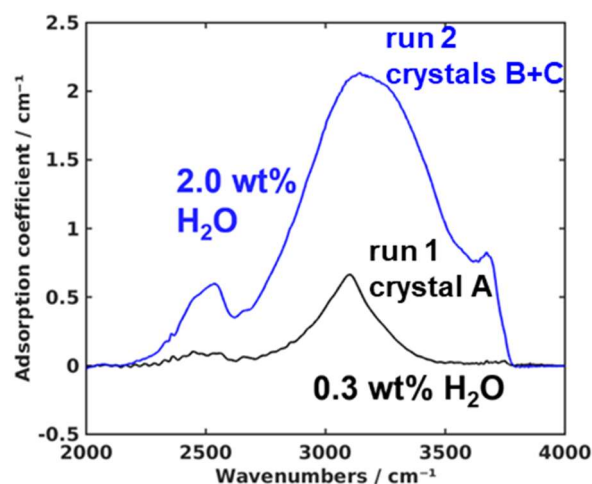


Figure 9. Unpolarised FTIR spectrum (background corrected) of a double-polished hydrous ringwoodite crystal of run 1 (black) and run 2 (blue) normalized to 100 μm thickness. The spectra exhibit the for ringwoodite typical broad OH adsorption features in the range from 2400 cm^{-1} to 3800 cm^{-1} ,^[55,56] arising from the presence of four different defect motifs with additional orientational OH group disorder. From the adsorption coefficient we estimate a hydration level of 0.3(2) and 2.0(5) wt% H_2O for the crystals of run1 and run 2, respectively, by the method of Koch-Müller et al.^[130]

We used the same crystals A-C to investigate the feasibility of ^1H solid-state NMR spectroscopy on such low sample volumes in combination with the low number of spins as OH defects. In this context, two of the ringwoodite crystals, A+C with less than 10 nL volume, were measured using a special piggy-back μMAS setup^[131,132] that employs a micro-coil to enhance the signal as a result of a higher filling factor of the coil. The number of ^1H spins is estimated to $\sim 1 \times 10^{15}$ (crystal A) and $\sim 4 \times 10^{16}$ (crystal C) from their volume and their estimated hydration levels. The other crystal B with a volume of ~ 18 nL (8×10^{16} ^1H spins) was measured using a standard *Bruker* 1.3 mm MAS set-up.

Due to these low numbers of ^1H spins within the crystals long measurement times are necessary even for simple 1D ^1H MAS NMR spectra. Furthermore, the ^1H background originating from the probe and the MAS rotors significantly contribute to the resulting spectra. Therefore, special attention has to be paid to the preparation of the measurements to avoid any small proton-containing contamination of the sample and the NMR rotor. Additionally, the ^1H background signals, which arise intrinsically from the NMR set-up, have to be carefully evaluated and subtracted from the measurements of the crystals (Figure 10).

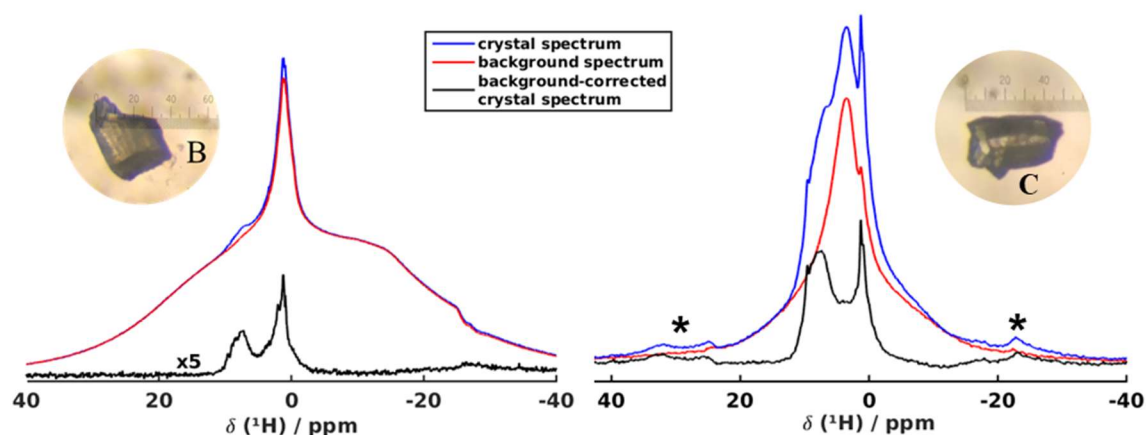


Figure 10. Comparison of the ^1H MAS NMR spectrum (blue) of a 18 nL hydrous ringwoodite crystal (crystal B, left, 62.5 kHz MAS) recorded using a standard Bruker 1.3 mm MAS probe, the ^1H MAS NMR spectrum (blue) of a 9 nL hydrous ringwoodite crystal (crystal C, right, 20 kHz MAS) recorded using a piggyback μMAS probe^[131] and the corresponding ^1H MAS background spectra (red). Subtracting the background from the crystal spectrum yields the background-corrected crystal spectrum (black, left multiplied by factor 5 for crystal B). Small spinning sidebands are observed at 20 kHz MAS (right) and marked by stars.

Despite the difficulties within background correction, we have succeeded to refine the background-corrected ^1H MAS NMR spectra of the three nL hydrous ringwoodite crystals A-C (Figure 11) with the characteristic ^1H chemical shift footprints of the individual defect motifs shown in Figure 7a. The result shows a clear trend in the ratio of defect motifs: for the crystals A-C, i.e. with increasing hydration level, the proportion of isolated Mg vacancies (V_{Mg}) is continuously increasing (Figure 11, green dashed), while the proportion of isolated Si defects (V_{Si} blue dashed, Mg_{Si} red dashed), as well as the coupled defect type ($\text{Mg}_{\text{Si}}V_{\text{Mg}}$, black dashed) decreases.

To link the experimentally observed defect ratios with unit cell volumes of the crystals and their hydration levels, the theoretically predicted unit cell volume expansion for each individual defect motif was used. DFT simulations of each defect motif as a function of hydration level (0 wt%, 1.6 wt% and 3.2 wt% H_2O) revealed linear correlations between unit cell volume and hydration level with varying slopes (Figure 12, solid black lines). From these individual slopes and the defect ratios observed in the ^1H NMR spectra (Figure 8 and 11), the expected slope of the volume expansion for each crystal A-C and the powder ringwoodite sample (Figure 12, data point 9) is extracted. From the expected slopes and the experimental unit cell volumes we can then predict the hydration level, which we would expect from the ratio of ^1H NMR experiments (Figure 12, green dots).

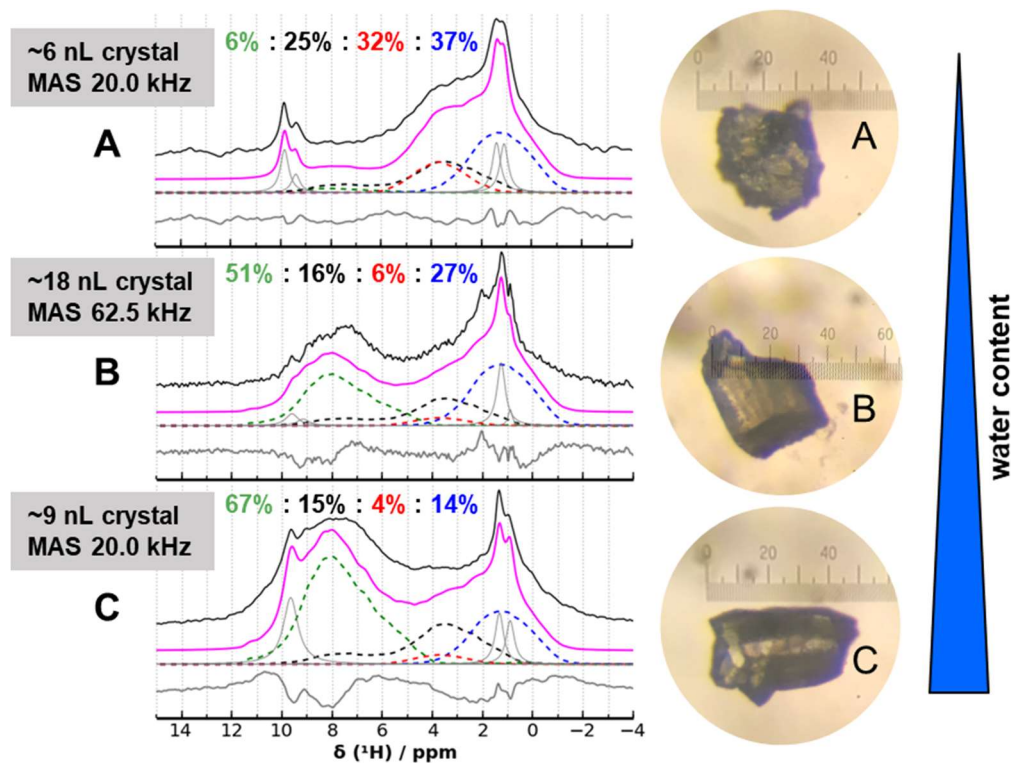


Figure 11. Background-corrected experimental ^1H MAS NMR spectra (black) of hydrous ringwoodite crystals A-C and the corresponding refinements (pink) with the individual ^1H chemical shift footprints for each OH defect motif, V_{Mg} (green dashed), V_{Si} (blue dashed), Mg_{Si} (red dashed) and the coupled $\text{Mg}_{\text{Si}}V_{\text{Mg}}$ (black dashed). The determined defect ratios are indicated for each defect motif by the appropriate colours. Right: Photos of the four crystals A-C with illumination with polarized light from below (transmission). The scale shown can be used to calculate the size of the crystals, whereby 1 digit corresponds to $7\ \mu\text{m}$.

We can fit the data in two different ways in order to extract a trend for a correlation between hydration level, defect formation mechanisms and the unit cell volume of ringwoodite. In principal a linear trend (Figure 12, grey dashed) would fit to our data in addition to recent literature data^[133,134] (Figure 12, pink), which would imply that the defect ratios should stay constant. However, we do observe a different trend in the ^1H NMR spectra of the crystals A-C with a higher proportion of Si defects at low hydration levels and higher proportions of Mg defects at higher hydration levels. For this reason also a discontinuous volume-hydration behaviour would be conceivable with a strong slope (~ 4.1) up to $\sim 1\ \text{wt}\%$ equivalent of H_2O due to the formation of mainly Si defects and a linear trend with a weaker slope (0.63) at higher hydration levels due to the formation of Mg vacancies (Figure 12, green dashed). Both possible trends are considerably different to a previously observed trend^[58] (Figure 12, reproduced in blue).

The predicted hydration levels (Figure 12, green dots) and experimentally estimated hydration levels (Figure 12, red dots) extracted from IR spectroscopy on other crystals of

the same runs agree fairly well, especially since the true hydration level may well vary for different crystals within one run due to temperature and pressure gradients within the synthesis capsule. Anyhow, for unambiguous proof of a hydration – defect formation trend, the water concentrations for each crystal A-C need to be more accurately determined and more data points, especially in the area of 0.7-1.1 wt% water concentration have to be added to the current results.

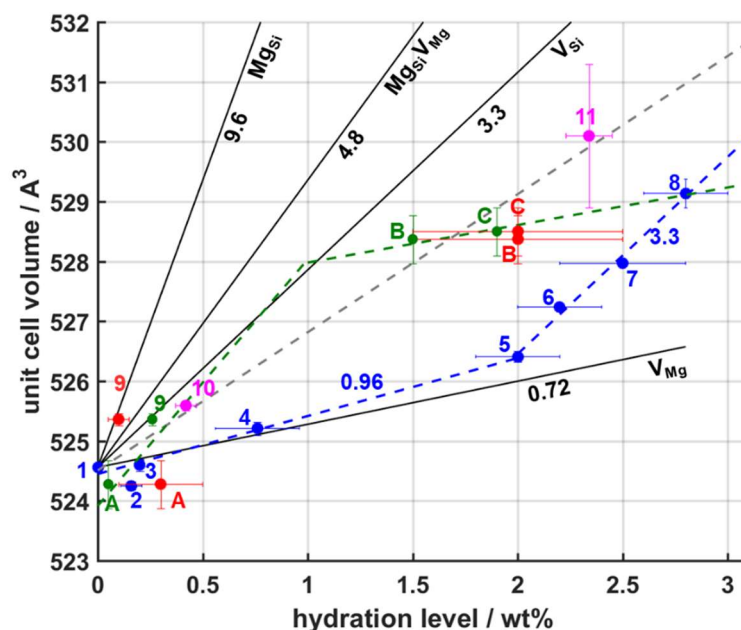


Figure 12. Correlation between unit cell volume and hydration level of hydrous ringwoodite crystals. In blue the correlation published by Ye et al.^[58] is indicated for comparison, while red shows the experimental volumes and estimated water concentrations for the crystals A-C and the powder ringwoodite sample (data point 9)^[127,128]. Pink data points are from the literature^[133,134], which don't agree with the trend observed by Ye et al.^[58] Black solid lines show the volume trends and slopes predicted for the four hydrous defect types by DFT calculations, which are in good agreement with earlier results by Panero^[59]. Green dots represent the experimental volumes and predicted water concentrations of the crystals A-C and the powder ringwoodite sample (data point 9) calculated from the ratios of defect types in ¹H NMR spectra and predicted volume trends from DFT. The two possible hydration-volume trends fitting to our data are depicted in grey dashed and green dashed, respectively. The first would be a linear correlation between hydration level and unit cell volume over the whole range (grey dashed) implying a constant defect ratio. The other possibility is a discontinuous trend with a strong slope (~4.1, dark green dashed) up to 1 wt% H₂O indicating the formation of Si defects and at higher hydration levels a linear trend with a weaker slope (0.63) indicating the formation of Mg vacancies in significant proportions.

These results demonstrate the feasibility of performing a comprehensive study on ringwoodite's defect chemistry using homogeneous single crystal samples and employing ¹H solid-state NMR spectroscopy to perform direct quantitative analysis of defect motifs, X-ray diffraction to extract the influence of the defects on the crystal structure, and FTIR on the same double-polished crystals to accurately quantify the water concentrations in the future.

2.2 Structure elucidation of Al defects in bridgmanite by NMR crystallography

Bridgmanite (MgSiO_3) is, with an abundance of more than 90 vol%, the dominant mineral of the Earth's lower mantle and the presence of Al substitution in its structure has a major impact on its physical and elastic properties.^[135] However, the mechanism of Al substitution is still a matter of debate, since two different mechanisms, the charge-coupled (CC) and the oxygen vacancy (OV) mechanism (Eq. 4 and 5, chapter 1.1), are conceivable. To date the challenging synthesis conditions of extremely high pressures ($P > 25$ GPa) and difficulties in the growth of single-crystals have prevented systematic structural studies. As a result, studies have relied on polycrystalline samples, which often suffer from being inhomogeneous, particularly as a result of very slow diffusion rates. ^{27}Al is a quadrupolar nuclei with 100% natural abundance and therefore ^{27}Al NMR spectroscopy is a very sensitive probe for the local environment of Al species, which influence their EFG tensors and chemical shifts. ^{27}Al NMR spectra thus can provide information about structural building units and their symmetry.

For these reasons, we have systematically investigated Al defects in six bridgmanite samples as function of Al content by electron probe microanalysis (EPMA) and NMR crystallography within the manuscript "*Detection of oxygen vacancy ordering in aluminous bridgmanite in the Earth's lower mantle*" to be submitted to Nature Geoscience. In this study, a NMR crystallographic strategy similar for that employed for ringwoodite was used to identify the defect mechanisms in bridgmanite, with EFG parameters used as cost functions rather than homonuclear distances and connectivities employed for ringwoodite.

Six Al-bearing bridgmanite samples A-F with total Al contents between 0.05 and 0.25 Al p.f.u. have been investigated in this study: three samples were synthesized along the join MgSiO_3 – $\text{MgAlO}_{2.5}$ (sample A, B, C; 5, 10, 20 mol% $\text{MgAlO}_{2.5}$) and two along the join MgSiO_3 – Al_2O_3 (sample D, E; 5, 25 mol% Al_2O_3) of the ternary phase diagram MgO , SiO_2 and Al_2O_3 . All syntheses used vitreous starting materials and were performed at 27 GPa and 2000 K using a multi-anvil apparatus at the Bayerisches Geoinstitut. One additional sample F was synthesized from composition D plus additional 30 wt% MgO in a reversal run. As for ringwoodite, XRD measurements were used to identify the phase compositions of the six aluminous bridgmanite samples A-E in addition to scanning electron microscope

to check the homogeneity of the synthesized products. These revealed that pure bridgmanite was as the only run product for samples A, B and D, whereas additional corundum (Al_2O_3) or periclase (MgO) were found in samples C, F and E. An electronprobe micro analyser (EPMA) was used to determine the chemical compositions of the samples. Using these analyses, the stoichiometry of each sample could be determined. The proportion of the charge-coupled (CC) substitution mechanism, where the stoichiometric Al_2O_3 component forms through the replacement of Mg and Si by two Al, or the oxygen vacancy (OV) mechanism, where a stoichiometric $\text{MgAlO}_{2.5}$ component forms through the substitution of two Si cations by two Al with the formation of an oxygen vacancy for charge compensation, were derived according to the following expression:



Following this stoichiometric model, the compositions show high amounts of the OV component in the Mg-rich synthesis runs (A-C), as well as the reversal run F with additional MgO, proving that MgO excess in the synthesis favors the formation of the OV component. Furthermore, the OV mechanism seems to be favored at lower total Al contents (Figure 13, red), while the CC component linearly increases with increasing Al content (Figure 13, blue).

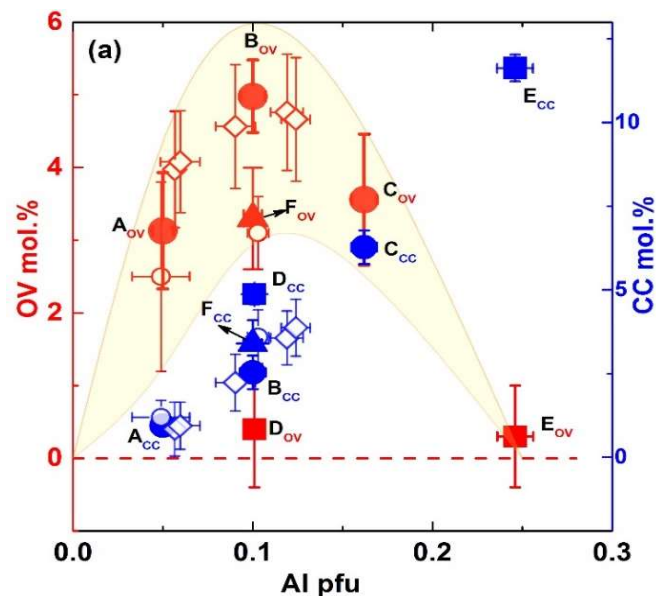


Figure 13. (a) Solubility of OV (red) and CC component (blue) versus Al pfu (per formula units) in bridgmanite in the systems $\text{MgSiO}_3\text{--MgAlO}_{2.5}$ (circles) and $\text{MgSiO}_3\text{--Al}_2\text{O}_3$ (squares,) as well as the reversal run F (triangle), respectively, in the present and previous studies. Solid symbols are the present study, while the open circle and diamond symbols are the data from Kojitani et al.^[136] and Navrotsky et al.^[22]. The yellow shadow area indicates the tendency of OV component. The dashed line represents the reference of zero.

The EPMA analysis, however, provides only indirect evidence for the nature of the defect mechanisms, and gives no insight in the local structure and, for example, short range order of defect motifs within the bridgmanite structure. Furthermore, the determination of the proportion of the different mechanisms is at the limit of the EPMA accuracy and the errors are large. To eliminate ambiguity over the presence of the OV defect mechanism and to investigate potential short range ordering that would have important consequences for the configurational entropy, we have performed ^{27}Al MAS NMR experiments (Figure 14) to probe the local environment of Al^{3+} incorporated into bridgmanite. All spectra show a sharp and a broader ^{27}Al resonance. The former is in the typical chemical shift range for Al in octahedral coordination and is assigned to Al substituted onto the B site, whereas the latter broader resonance has a chemical shift consistent with a larger coordination number and a distorted environment and arises from Al substitution into the nominally dodecahedral A site. The occurrence of both resonances is therefore consistent with the CC substitution mechanism.

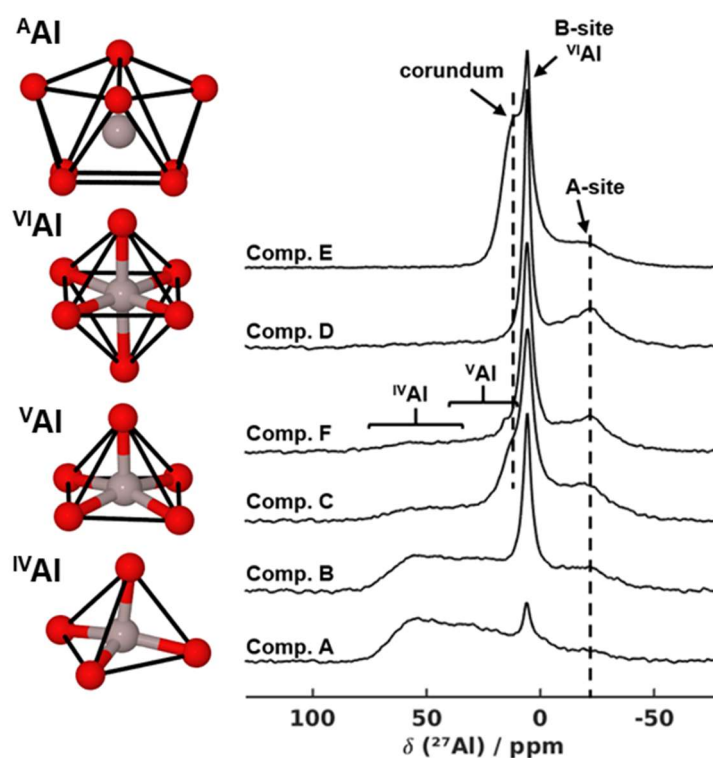


Figure 14. Al coordinations (left) and ^{27}Al MAS NMR spectra (right) of the six Al-bearing bridgmanite samples. Left: Polyhedra of Al in four- and five-fold coordination, as well as in six-fold coordination (B site) and at the distorted A site of the bridgmanite structure, whereby only the eight closest O atoms ($< 2.5 \text{ \AA}$) are shown. Right: The ^{27}Al MAS NMR spectra of the samples A-E exhibit resonances assigned to Al on the A site and B site of the bridgmanite structure, which arise due to the CC mechanism, while the spectra of samples A-C and F exhibit broad signals in the chemical shift region of four- and five-fold coordinated Al sites, which are assigned to the OV mechanism. Corundum impurities are observed in the spectra of sample C and E.

Corundum impurities were observed in the spectra of sample E and C. Additionally, the ^{27}Al MAS NMR spectra of sample A-C and F exhibit broad and overlapping resonances in the typical range for tetra- and penta-coordinated Al species, which can only occur in the bridgmanite structure due to the presence of oxygen vacancies.

Characteristic quadrupolar parameters of six ^{27}Al sites have been obtained by fits of the 1D ^{27}Al MAS NMR spectrum of sample D ($^{\text{VI}}\text{Al}$ and $^{\text{A}}\text{Al}$ signals, CC substitution) and the 2D ^{27}Al STMAS spectrum of sample B ($^{\text{IV}}\text{Al}$, $2\times$ $^{\text{V}}\text{Al}$, $^{\text{VI}}\text{Al}$, OV mechanism, Figure 15a+b), which provides a higher resolution by separating the signals according to their isotropic interaction parts. The resulting characteristic quadrupolar parameters for the different Al environments were then compared to predicted NMR parameters (chemical shift and quadrupolar parameters) from DFT calculations for the various structural Al defect configurations for the CC and the OV mechanisms (Figure 16), in order to support the assignment of experimental resonances and to identify Al defect structures.

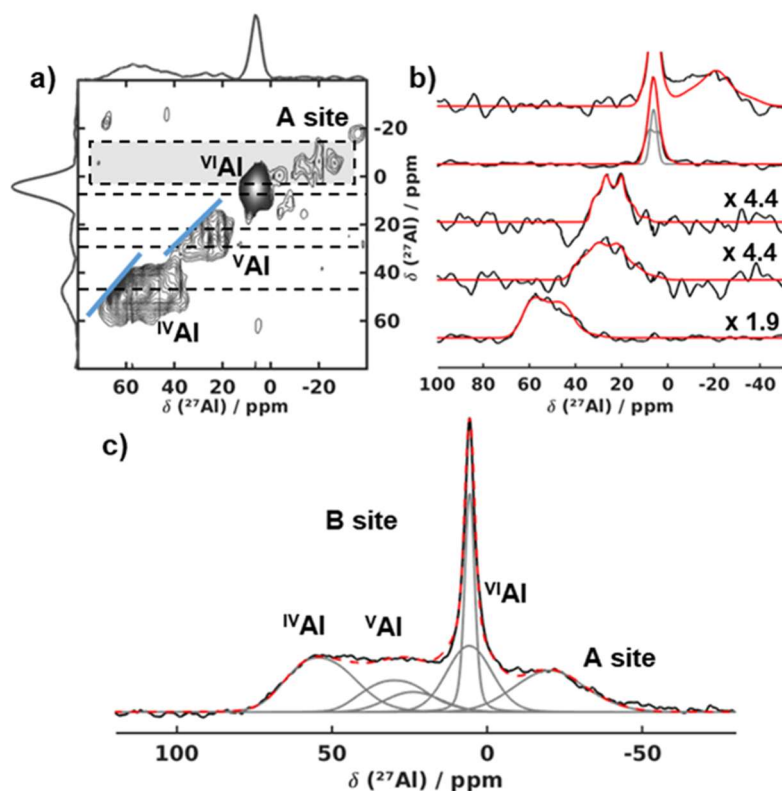


Figure 15. a) 2D ^{27}Al STMAS spectrum of bridgmanite sample B revealing the formation of $^{\text{IV}}\text{Al}$, $^{\text{V}}\text{Al}$, $^{\text{VI}}\text{Al}$ and Al at the A site. The blue lines highlight the effect of the distribution of isotropic chemical shifts. b) Fits of the appropriate horizontal 1D rows of the ^{27}Al STMAS spectrum indicated by dashed lines and the corresponding fits (red) of the quadrupolar parameters. The top spectrum results from the sum of the rows in the area indicated by the translucent grey rectangle to enhance signal-to-noise ratio. c) Exemplary fit of the central transition (red dashed) of the quantitative ^{27}Al MAS NMR spectrum of sample B (black) with six Al sites.

For the CC substitution mechanism two defect models were calculated (Figure 16a, b), in which an Al at the A site is either adjacent or non-adjacent to an Al at the B site. For the OV substitution mechanism isolated oxygen vacancies (Figure 16c), as well as the formation of OV dimers with multiple configurations (Figure 16d-f) were taken into account. In addition, the possibility of one Si at a penta-coordinated site was simulated (Figure 16f) in order to test for the possibility of vacancies not directly associated with the Al coordination.

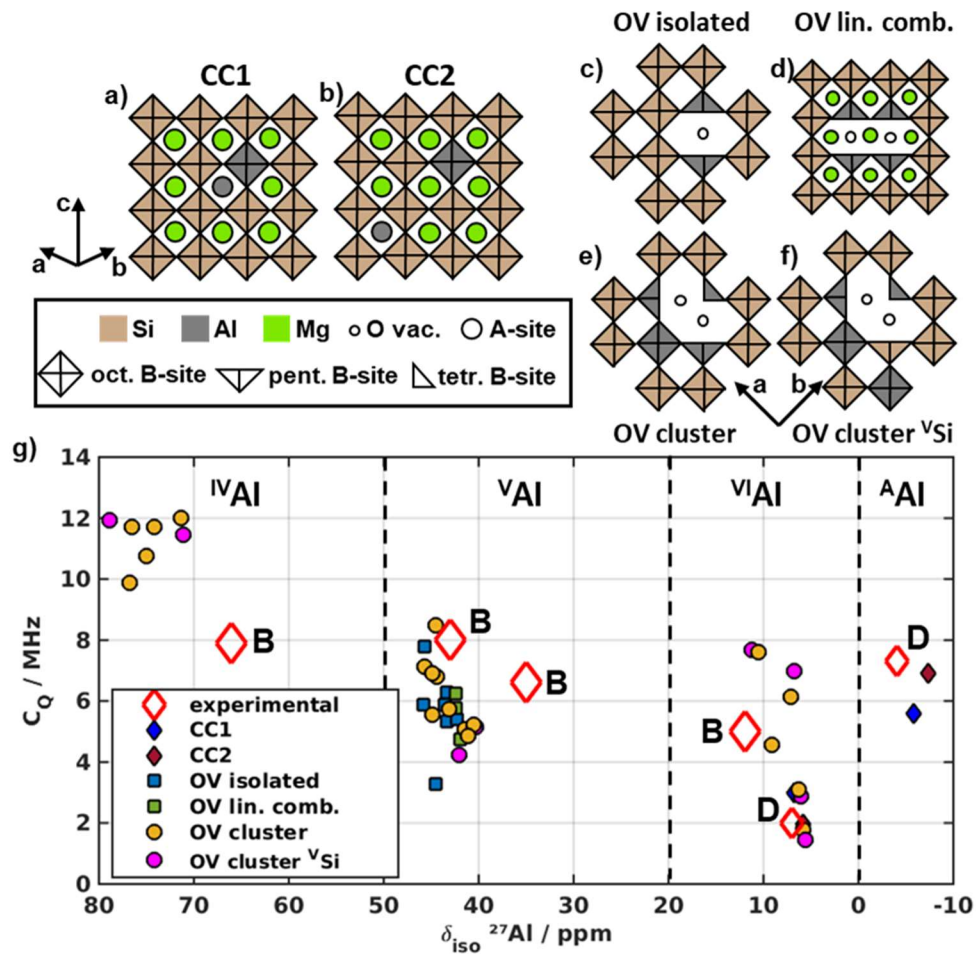


Figure 16. Exemplary Al defect structures in bridgmanite for the CC mechanism (a,b) and the OV mechanism (c-f) and g) corresponding calculated quadrupolar coupling C_Q and isotropic chemical shift δ_{iso} of the Al defect sites in bridgmanite in comparison to the experimental average estimates (red diamonds) of the different Al resonances of sample B and D. For the CC mechanism two models were calculated: a) Al on two adjacent A and B sites (CC1, blue diamonds) and b) two Al on non-neighbouring A and B sites (CC2, dark red diamonds). For the OV mechanism simple oxygen vacancies of O1 and O2 (exemplary for an O2 vac. in c), blue squares), as well as linear combinations of two O1, two O2 and O1 and O2 (exemplary for two O1 vac. in d), green squares) resulting in solely ^VAl sites were considered to investigate possible distortions of the structure. Furthermore, partial clustering of oxygen vacancies as dimers with O2 (exemplary in e, f) and a combination of O1 / O2 vacancies (orange circles) resulting in ^{IV}Al, ^VAl and ^{VI}Al environments were calculated. ^{VI}Al sites in and out of plane with the ^VAl and ^{IV}Al sites were also considered. Additionally, the ^{VI}Al site was put adjacent to (e) and non-neighbouring to other Al defect sites and a partial partitioning between Al and Si on penta-coordinated sites (f, pink) was investigated resulting in a total of 7 models for the OV dimers.

For all considered Al defect models the simulated NMR parameters are of the same order of magnitude compared to the experimental data for ^{IV}Al , ^{V}Al , ^{VI}Al and ^{A}Al environments (Figure 16g). Only Al at the A site of the bridgmanite exhibits a negative isotropic chemical shift (Figure 16g, diamonds) and, therefore, the experimentally broad resonance at negative shift is assigned exclusively to the CC mechanism, whereby comparable energies and NMR parameters for the two CC models (Figure 16a, b, g) render both scenarios plausible.

For the OV models simple oxygen vacancies even when clustering linearly (Figure 16c+d) just lead to five-fold coordinated Al without a significant distortion of the structure and their resulting NMR parameters fit well to the experimental ^{V}Al environments (Figure 16g). Only OV configurations, which have two neighboring oxygen vacancies associated with one octahedron, result in the formation of tetrahedral Al environments in addition to octahedral and pentagonal Al environments (Figure 16e-g) due to the stoichiometry of the OV substitution. In this case, configurations with one Si at a penta-coordinated site result in slightly lower energies. For the tetrahedral Al species a small overestimation of NMR parameters is observed, which is attributed to stronger distortions in the simulations (Figure 16g). In the case of the octahedral Al environments, the NMR parameters of those configurations with some Al not directly associated with the oxygen vacancies fit the experimental data slightly better (Figure 16g), which implies a migration of OVs.

Finally, the ratios between the Al environments were derived from fits of the 1D ^{27}Al MAS NMR spectra for all samples using the characteristic parameters for each Al environment. The relative integral of the A site resonance was used as a measure of the Al incorporated due to the CC mechanism, since it is well separated. According to the nature of this mechanism the same intensity was assigned to the octahedral B site. The DFT results imply that for determining the OV component the intensities of ^{IV}Al , ^{V}Al and the remaining ^{VI}Al environments have to be summed. The resulting OV/CC ratios are in excellent agreement with those obtained from the compositional analysis within the analytical uncertainties.

Independent of the Al content, in all samples from MgO-rich syntheses five- and four-fold coordinated Al species are formed due to oxygen vacancies. The occurrence of tetrahedral Al in combination with the DFT results demonstrates the presence of OV clusters according to Figure 16e, f. For some samples we observed $^{VI}Al : ^{IV}Al$ ratios greater than one, which strongly hints towards a migration of OVs, leading to some ^{VI}Al not directly neighboring the OV defect site. This is consistent with the results of the DFT calculations revealing slightly lower energies for these configurations. However, since the migration of the OVs

changes the intensity ratio between ^{IV}Al , ^{V}Al and ^{VI}Al environments, it is challenging to use these ratios for identifying the cluster configurations unambiguously.

The occurrence of short-range ordered OVs in aluminous bridgmanite means that vacancies are formed from two neighbouring oxygen sites, i.e. with twice the size of a single oxygen vacancy. In the past isolated oxygen vacancies have been demonstrated to be able to accommodate comparable or smaller atomic-sized noble gas, such as neon (1.18 Å), helium (0.90 Å) and argon (1.64 Å), as well as hydroxyl groups.^[11,20,21,137] Therefore, the presence of OV ordering in aluminous bridgmanite under MgO-saturated mantle compositions such as peridotite may greatly change our understanding of bridgmanite's defect chemistry and of the volatile cycling of noble gases and water into the lower mantle. The larger vacancies might now even be able to store xenon with a larger atomic radius than an isolated oxygen vacancy and may explain the strong depletion of xenon relative to argon in the Earth's atmosphere.^[21,138]

References

- [1] J. Li, N. Wu, *Catal. Sci. Technol.* **2015**, *5*, 1360–1384.
- [2] S. B. Zhang, *J. Phys. Condens. Matter* **2002**, *14*, R881–R903.
- [3] H. Keppler, J. R. Smyth, *Rev. Mineral. Geochem.* **2006**, *62*, 1–473.
- [4] R. N. Schock, *Eos, Trans. Am. Geophys. Union* **1985**, *66*, 459.
- [5] A. E. Ringwood, *Composition and Petrology of the Earth's Mantle*, McGraw Hill, New York, **1975**.
- [6] R. J. Stern, *Rev. Geophys.* **2002**, *40*, 1012.
- [7] J. F. Lawrence, M. E. Wyssession, in *Earth's Deep Water Cycle* (Eds.: S.D. Jacobsen, S. van der Lee), Washington, DC, **2013**, pp. 251–261.
- [8] J. R. Smyth, S. D. Jacobsen, in *Earth's Deep Water Cycle* (Eds.: S.D. Jacobsen, S. van der Lee), Washington, DC, **2013**, pp. 1–11.
- [9] T. Irifune, *Nature* **1994**, *370*, 131–133.
- [10] T. Sharp, *Science* **2014**, *346*, 8–10.
- [11] M. Murakami, Y. Ohishi, N. Hirao, K. Hirose, *Nature* **2012**, *485*, 90–94.
- [12] M. Murakami, S. V. Sinogeikin, H. Hellwig, J. D. Bass, J. Li, *Earth Planet. Sci. Lett.* **2007**, *256*, 47–54.
- [13] D. J. Frost, *Elements* **2008**, *4*, 171–176.
- [14] J. R. Smyth, *Am. Mineral.* **1994**, *79*, 1021–1024.
- [15] E. Ohtani, H. Mizobata, H. Yurimoto, *Phys. Chem. Miner.* **2000**, *27*, 533–544.
- [16] T. Inoue, H. Yurimoto, Y. Kudoh, *Geophys. Res. Lett.* **1995**, *22*, 117–20.
- [17] E. Ohtani, *Chem. Geol.* **2015**, *418*, 6–15.
- [18] D. L. Kohlstedt, H. Keppler, D. C. Rubie, *Contrib. Mineral. Petrol.* **1996**, *123*, 345–357.
- [19] D. G. Pearson, F. E. Brenker, F. Nestola, J. McNeill, L. Nasdala, M. T. Hutchison, S. Matveev, K. Mather, G. Silversmit, S. Schmitz, et al., *Nature* **2014**, *507*, 221–4.
- [20] A. Navrotsky, *Science* **1999**, *284*, 1788–1789.
- [21] S. S. Shcheka, H. Keppler, *Nature* **2012**, *490*, 531–534.
- [22] A. Navrotsky, M. Schoenitz, H. Kojitani, H. Xu, J. Zhang, D. J. Weidner, R. Jeanloz, *J. Geophys. Res.: Solid Earth* **2003**, *108*, ECV2-1–11.
- [23] S. D. Jacobsen, S. van der Lee, *Earth's Deep Water Cycle*, American Geophysical Union, Washington, DC, **2013**.
- [24] S.-M. Thomas, C. R. Bina, S. D. Jacobsen, A. F. Goncharov, *Earth Planet. Sci. Lett.* **2012**, *357–358*, 130–136.

- [25] J. Hustoft, G. Amulele, J. I. Ando, K. Otsuka, Z. Du, Z. Jing, S. I. Karato, *Earth Planet. Sci. Lett.* **2013**, *361*, 7–15.
- [26] D. Wang, M. Mookherjee, Y. Xu, S. Karato, *Nature* **2006**, *443*, 977–80.
- [27] K. Regenauer-Lieb, *Rev. Mineral. Geochem.* **2006**, *62*, 451–473.
- [28] S. Karato, in *Earth's Deep Water Cycle*, **2013**, pp. 113–129.
- [29] J. Brodholt, *Nature* **2000**, *407*, 620–622.
- [30] K. D. M. Harris, M. Tremayne, B. M. Kariuki, *Angew. Chemie Int. Ed.* **2001**, *40*, 1626–1651.
- [31] R. K. Harris, *Solid State Sci.* **2004**, *6*, 1025–1037.
- [32] C. Martineau, J. Senker, F. Taulelle, *Annu. Rep. NMR Spectrosc.* **2014**, *82*, 1–57.
- [33] R. K. Harris, R. E. Wasylshen, M. J. Duer, *NMR-Crystallography*, Wiley, Chichester, **2009**.
- [34] R. F. Moran, D. M. Dawson, S. E. Ashbrook, *Int. Rev. Phys. Chem.* **2017**, *36*, 39–115.
- [35] L. Seyfarth, J. Seyfarth, B. V. Lotsch, W. Schnick, J. Senker, *Phys. Chem. Chem. Phys.* **2010**, *12*, 2227.
- [36] F. Taulelle, *Solid State Sci.* **2004**, *6*, 1053–1057.
- [37] X. Xue, M. Kanzaki, *J. Am. Ceram. Soc.* **2009**, *92*, 2803–2830.
- [38] M. B. Mesch, K. Bärwinkel, Y. Krysiak, C. Martineau, F. Taulelle, R. B. Neder, U. Kolb, J. Senker, *Chem. - A Eur. J.* **2016**, *22*, 16878–16890.
- [39] J. Senker, J. Sehnert, S. Correll, *J. Am. Chem. Soc.* **2005**, *127*, 337–349.
- [40] J. F. Stebbins, H. Kojitani, M. Akaogi, A. Navrotsky, *Am. Mineral.* **2003**, *88*, 1161–1164.
- [41] D. D. Laws, H.-M. L. Bitter, A. Jerschow, *Angew. Chemie Int. Ed.* **2002**, *41*, 3096–3129.
- [42] D. H. Brouwer, R. J. Darton, R. E. Morris, M. H. Levitt, *J. Am. Chem. Soc.* **2005**, *127*, 10365–70.
- [43] T. Charpentier, *Solid State Nucl. Magn. Reson.* **2011**, *40*, 1–20.
- [44] J. M. Griffin, A. J. Berry, D. J. Frost, S. Wimperis, S. E. Ashbrook, *Chem. Sci.* **2013**, *4*, 1523.
- [45] R. F. Moran, D. McKay, C. J. Pickard, A. J. Berry, J. M. Griffin, S. E. Ashbrook, *Phys. Chem. Chem. Phys.* **2016**, *18*, 10173–10181.
- [46] C. Bonhomme, C. Gervais, F. Babonneau, C. Coelho, F. Pourpoint, T. Azais, S. E. Ashbrook, J. M. Griffin, J. R. Yates, F. Mauri, et al., *Chem. Rev.* **2012**, *112*, 5733–5779.
- [47] S. E. Ashbrook, D. M. Dawson, *Acc. Chem. Res.* **2013**, *46*, 1964–1974.
- [48] J. R. Smyth, *Am. Mineral.* **1987**, *72*, 1051–1055.

- [49] J. F. Stebbins, J. R. Smyth, W. R. Panero, D. J. Frost, *Am. Mineral.* **2009**, *94*, 905–915.
- [50] J. F. Stebbins, W. R. Panero, J. R. Smyth, D. J. Frost, *Am. Mineral.* **2009**, *94*, 626–629.
- [51] S. D. Jacobsen, S. Demouchy, D. J. Frost, T. Boffa Ballaran, J. Kung, *Am. Mineral.* **2005**, *90*, 61–70.
- [52] S. C. Kohn, R. A. Brooker, D. J. Frost, A. E. Slesinger, B. J. Wood, *Am. Mineral.* **2002**, *87*, 293–301.
- [53] Y. Kudoh, T. Inoue, H. Arashi, *Phys. Chem. Miner.* **1996**, *23*, 461–469.
- [54] J. R. Smyth, C. M. Holl, D. J. Frost, S. D. Jacobsen, F. Langenhorst, C. A. McCammon, *Am. Mineral.* **2003**, *88*, 1402–1407.
- [55] Y. Kudoh, T. Kuribayashi, H. Mizobata, E. Ohtani, *Phys. Chem. Miner.* **2000**, *27*, 474–479.
- [56] W. R. Panero, J. R. Smyth, J. S. Pigott, Z. Liu, D. J. Frost, *Am. Mineral.* **2013**, *98*, 637–642.
- [57] S. Sasaki, C. T. Prewitt, Y. Sato, E. Ito, *J. Geophys. Res.: Solid Earth* **1982**, *87*, 7829–7832.
- [58] Y. Ye, D. A. Brown, J. R. Smyth, W. R. Panero, S. D. Jacobsen, Y.-Y. Chang, J. P. Townsend, S.-M. Thomas, E. H. Hauri, P. Dera, et al., *Am. Mineral.* **2012**, *97*, 573–582.
- [59] W. R. Panero, *J. Geophys. Res.* **2010**, *115*, B03203.
- [60] Y. Kudoh, *Phys. Chem. Miner.* **2001**, *28*, 523–530.
- [61] M. Blanchard, E. Balan, K. Wright, *Am. Mineral.* **2009**, *94*, 83–9.
- [62] M. Blanchard, K. Wright, J. D. Gale, *Phys. Chem. Miner.* **2005**, *32*, 585–593.
- [63] O. Tschauner, C. Ma, J. R. Beckett, C. Prescher, V. B. Prakapenka, G. R. Rossman, *Science* **2014**, *346*, 1100–1102.
- [64] N. C. Richmond, J. P. Brodholt, *Am. Mineral.* **1998**, *83*, 947–951.
- [65] Z. Liu, T. Irifune, M. Nishi, Y. Tange, T. Arimoto, T. Shinmei, *Phys. Earth Planet. Inter.* **2016**, *257*, 18–27.
- [66] C. McCammon, *Nature* **1997**, *387*, 694–696.
- [67] N. Bolfan-Casanova, H. Keppler, D. C. Rubie, *Earth Planet. Sci. Lett.* **2000**, *182*, 209–221.
- [68] N. Bolfan-Casanova, C. A. McCammon, S. J. Mackwell, *Earth's Deep Water Cycle* **2013**, 57–68.
- [69] Z. Liu, T. Ishii, T. Katsura, *Geochemical Perspect. Lett.* **2017**, *5*, 12–18.
- [70] Z. Liu, M. Nishi, T. Ishii, H. Fei, N. Miyajima, T. B. Ballaran, H. Ohfuji, T. Sakai, L. Wang, S. Shcheka, et al., *J. Geophys. Res.: Solid Earth* **2017**, *122*, 7775–7788.

- [71] A. I. Becerro, C. McCammon, F. Langenhorst, F. Seifert, R. Angel, *Phase Transitions* **1999**, *69*, 133–146.
- [72] J. F. Stebbins, *Am. Mineral.* **2006**, *91*, 337–343.
- [73] J. F. Stebbins, S. Kroeker, *Geophys. Res. Lett.* **2001**, *28*, 615–618.
- [74] A. C. Palke, J. F. Stebbins, D. J. Frost, C. A. McCammon, *Am. Mineral.* **2012**, *97*, 1955–1964.
- [75] D. Andrault, D. R. Neuville, A. M. Flank, Y. Wang, *Am. Mineral.* **1998**, *83*, 1045–1053.
- [76] K. D. M. Harris, E. Y. Cheung, *Chem. Soc. Rev.* **2004**, *33*, 526–38.
- [77] M. J. Duer, *Solid-State NMR Spectroscopy - Principles and Applications*, Blackwell Science, Oxford, **2002**.
- [78] L. Seyfarth, J. Senker, *Phys. Chem. Chem. Phys.* **2009**, *11*, 3522.
- [79] M. Mehring, in *Encycl. Magn. Reson.*, John Wiley & Sons, Ltd, Chichester, UK, **2007**.
- [80] J. Wack, R. Siegel, T. Ahnfeldt, N. Stock, L. Mafra, J. Senker, *J. Phys. Chem. C* **2013**, *117*, 19991–20001.
- [81] A. Sutrisno, Y. Huang, *Solid State Nucl. Magn. Reson.* **2013**, *49–50*, 1–11.
- [82] C. Martineau-Corcous, *Curr. Opin. Colloid Interface Sci.* **2018**, *33*, 35–43.
- [83] K. Schmidt-Rohr, H. W. Spiess, *Multidimensional Solid State NMR and Polymers*, Academic Press, London, **1994**.
- [84] M. Schmidt, J. J. Wittmann, R. Kress, D. Schneider, S. Steuernagel, H.-W. Schmidt, J. Senker, *Cryst. Growth Des.* **2012**, *12*, 2543–2551.
- [85] M. Schmidt, J. J. Wittmann, R. Kress, H.-W. Schmidt, J. Senker, *Chem. Commun.* **2013**, *49*, 267–269.
- [86] D. R. Neuville, L. Cormier, D. Massiot, *Geochim. Cosmochim. Acta* **2004**, *68*, 5071–5079.
- [87] H. Eckert, J. P. Yesinowski, L. A. Silver, E. M. Stolper, *J. Phys. Chem.* **1988**, *92*, 2055–2064.
- [88] S. E. Ashbrook, M. E. Smith, *Chem. Soc. Rev.* **2006**, *35*, 718–35.
- [89] F. Castellani, B. van Rossum, A. Diehl, M. Schubert, K. Rehbein, H. Oschkinat, *Nature* **2002**, *420*, 99–102.
- [90] A. Lange, S. Becker, K. Seidel, K. Giller, O. Pongs, M. Baldus, *Angew. Chemie Int. Ed.* **2005**, *44*, 2089–2092.
- [91] A. McDermott, *Annu. Rev. Biophys.* **2009**, *38*, 385–403.
- [92] J. M. Griffin, S. E. Ashbrook, *Annu. Rep. NMR Spectrosc.* **2013**, *79*, 241–332.
- [93] J. F. Stebbins, X. Xue, *Rev. Mineral. Geochem.* **2014**, *78*, 605–653.
- [94] J. F. Stebbins, M. Kanzaki, *Science* **1991**, *251*, 294–298.

- [95] S. E. Ashbrook, D. M. Dawson, in *Nucl. Magn. Reson. Vol. 45*, **2016**, pp. 1–52.
- [96] K. J. D. MacKenzie, M. E. Smith, *Multinuclear Solid-State NMR of Inorganic Materials*, Pergamon, Oxford, **2002**.
- [97] L. B. Casabianca, A. C. de Dios, *J. Chem. Phys.* **2008**, *128*, 052201.
- [98] A. P. M. Kentgens, *Geoderma* **1997**, *80*, 271–306.
- [99] A. P. M. Kentgens, *J. Magn. Reson.* **1991**, *95*, 619–625.
- [100] S. E. Ashbrook, L. Le Pollès, C. J. Pickard, A. J. Berry, S. Wimperis, I. Farnan, *Phys. Chem. Chem. Phys.* **2007**, *9*, 1587–98.
- [101] L. Mafra, R. Siegel, C. Fernandez, D. Schneider, F. Aussenac, J. Rocha, *J. Magn. Reson.* **2009**, *199*, 111–4.
- [102] D. H. Brouwer, P. E. Kristiansen, C. A. Fyfe, M. H. Levitt, *J. Am. Chem. Soc.* **2005**, *127*, 542–543.
- [103] J. Xu, V. V. Terskikh, Y. Chu, A. Zheng, Y. Huang, *Chem. Mater.* **2015**, *27*, 3306–3316.
- [104] G. N. M. Reddy, A. Huqi, D. Iuga, S. Sakurai, A. Marsh, J. T. Davis, S. Masiero, S. P. Brown, *Chem. - A Eur. J.* **2017**, *23*, 2235–2235.
- [105] A. Lesage, L. Emsley, *J. Magn. Reson.* **2001**, *148*, 449–54.
- [106] Y. Jayasubba Reddy, V. Agarwal, A. Lesage, L. Emsley, K. V Ramanathan, *J. Magn. Reson.* **2014**, *245*, 31–7.
- [107] M. Carravetta, M. Edén, O. G. Johannessen, H. Luthman, P. J. Verdegem, J. Lugtenburg, a Sebal, M. H. Levitt, *J. Am. Chem. Soc.* **2001**, *123*, 10628–10638.
- [108] K. Saalwächter, *ChemPhysChem* **2013**, *14*, 3000–3014.
- [109] S. P. Brown, H. W. Spiess, *Chem. Rev.* **2001**, *101*, 4125–4156.
- [110] T. Gullion, *Concepts Magn. Reson.* **1998**, *10*, 277–289.
- [111] P. E. Kristiansen, D. J. Mitchell, J. N. S. Evans, *J. Magn. Reson.* **2002**, *157*, 253–66.
- [112] E. R. Andrew, A. Bradbury, R. G. Eades, *Nature* **1958**, *182*, 1659–1659.
- [113] A. Samoson, T. Tuherm, J. Past, A. Reinhold, T. Anupöld, I. Heinmaa, *Top. Curr. Chem.* **2005**, *246*, 15–31.
- [114] M. Levitt, *eMagRes* **2002**, *9*, 165–196.
- [115] M. H. Levitt, *J. Chem. Phys.* **2008**, *128*, 052205.
- [116] R. Tycko, in *Encycl. Magn. Reson.*, John Wiley & Sons, Ltd, Chichester, UK, **2009**.
- [117] C. P. Jaroniec, in *Encycl. Magn. Reson.*, John Wiley & Sons, Ltd, Chichester, UK, **2009**, pp. 189–212.
- [118] G. Pileio, M. Concistrè, N. McLean, A. Gansmüller, R. C. D. Brown, M. H. Levitt, *J. Magn. Reson.* **2007**, *186*, 65–74.

- [119] I. Schnell, H. W. Spiess, *J. Magn. Reson.* **2001**, *151*, 153–227.
- [120] P. E. Kristiansen, M. Carravetta, J. D. van Beek, W. C. Lai, M. H. Levitt, *J. Chem. Phys.* **2006**, *124*, 234510.
- [121] S. P. Brown, *Prog. Nucl. Magn. Reson. Spectrosc.* **2007**, *50*, 199–251.
- [122] J. P. Bradley, C. Tripon, C. Filip, S. P. Brown, *Phys. Chem. Chem. Phys.* **2009**, *11*, 6941–52.
- [123] J. P. Bradley, C. J. Pickard, J. C. Burley, D. R. Martin, L. P. Hughes, S. D. Cosgrove, S. P. Brown, *J. Pharm. Sci.* **2012**, *101*, 1821–1830.
- [124] S. R. Chaudhari, J. M. Griffin, K. Broch, A. Lesage, V. Lemaury, D. Dudenko, Y. Olivier, H. Siringhaus, L. Emsley, C. P. Grey, *Chem. Sci.* **2017**, *8*, 3126–3136.
- [125] C. J. Pickard, R. J. Needs, *J. Phys. Condens. Matter* **2011**, *23*, 053201.
- [126] S. Kirkpatrick, C. D. Gelatt, M. P. Vecchi, *Science* **1983**, *220*, 671–680.
- [127] H. Grüninger, K. Armstrong, D. Greim, T. Boffa-Ballaran, D. J. Frost, J. Senker, *J. Am. Chem. Soc.* **2017**, *139*, 10499–10505.
- [128] H. Grüninger, A. Schmutzler, R. Siegel, K. Armstrong, D. J. Frost, J. Senker, *Phys. Chem. Chem. Phys.* **2018**, *20*, 15098–15105.
- [129] G. S. Pawley, *J. Appl. Crystallogr.* **1981**, *14*, 357–361.
- [130] M. Koch-Müller, D. Rhede, *Am. Mineral.* **2010**, *95*, 770–775.
- [131] J. O. Brauckmann, J. W. G. (Hans) Janssen, A. P. M. Kentgens, *Phys. Chem. Chem. Phys.* **2016**, *18*, 4902–4910.
- [132] A. Brinkmann, S. K. Vasa, H. Janssen, A. P. M. Kentgens, *Chem. Phys. Lett.* **2010**, *485*, 275–280.
- [133] K. Schulze, H. Marquardt, T. Kawazoe, T. Boffa Ballaran, C. McCammon, M. Koch-Müller, A. Kurnosov, K. Marquardt, *Earth Planet. Sci. Lett.* **2018**, *498*, 9–16.
- [134] J. Wang, S. V Sinogeikin, T. Inoue, J. D. Bass, *Geophys. Res. Lett.* **2006**, *33*, L14308.
- [135] A. Kurnosov, H. Marquardt, D. J. Frost, T. B. Ballaran, L. Ziberna, *Nature* **2017**, *543*, 543–546.
- [136] H. Kojitani, T. Katsura, M. Akaogi, *Phys. Chem. Miner.* **2007**, *34*, 257–267.
- [137] Y. Zhang, Z. Xu, *Am. Mineral.* **1995**, *80*, 670–675.
- [138] E. Anders, T. Owen, *Science* **1977**, *198*, 453–465.

3. Index of Publications

1. H. Grüninger, K. Armstrong, D. Greim, T. Boffa Ballaran, D. J. Frost, J. Senker, Hidden Oceans? Unraveling the Structure of Hydrous Defects in the Earth's Deep Interior, *J. Am. Chem. Soc.*, 139, 10499-10505 (2017).
2. H. Grüninger, A. Schmutzler, R. Siegel, K. Armstrong, D. J. Frost, J. Senker, Quantitative description of ^1H SQ and DQ coherences for the hydroxyl disorder within hydrous ringwoodite, *Phys. Chem. Chem. Phys.*, 20, 15098-15105 (2018).
3. H. Grüninger, Z. Liu, J. O. Brauckmann, T. Martin, T. Boffa Ballaran, R. Siegel, A. P. M. Kentgens, D. J. Frost, J. Senker, On the feasibility of ^1H NMR on hydrous defects within nanoliter ringwoodite crystals, 2018, manuscript to be submitted to Chemical Science.
4. H. Grüninger, Z. Liu, R. Siegel, T. Boffa Ballaran, T. Katsura, J. Senker, D. J. Frost, Detection of oxygen vacancy ordering in aluminous bridgmanite in the Earth's lower mantle, 2018, manuscript to be submitted to Nature Geoscience.

4. Publications

4.1 Hidden Oceans? Unraveling the Structure of Hydrated Defects in the Earth's Deep Interior

This work is the result of a cooperation between the Inorganic Chemistry III and the Bavarian Research Institute of Experimental Geochemistry and Geophysics (BGI) of the University of Bayreuth and will be reprinted with permission from H. Grüninger, K. Armstrong, D. Greim, T. Boffa Ballaran, D. J. Frost, J. Senker, *J. Am. Chem. Soc.* **2017**, *139*, 10499–10505. Copyright 2017 American Chemical Society.

My contributions are:

- conception and main authorship of the article
- implementation of homonuclear DQ recoupling sequences
- conduction and evaluation of all 1D ^1H MAS spin echo, $^1\text{H} \rightarrow ^{29}\text{Si}$ CP MAS spectra, as well as 2D ^1H ^1H DQSQ correlation spectra
- conduction and evaluation of all quantum-chemical simulations including the creation of hydrated defect models
- Simulation and evaluation of all ^1H ^1H DQSQ correlation spectra from structure models

The contribution of all other authors are:

- conception and co-authorship of the article
- high-pressure synthesis of the minerals
- measurement of powder X-ray diffraction patterns
- structure solution from powder X-ray data
- support of quantum-chemical calculations and evaluation

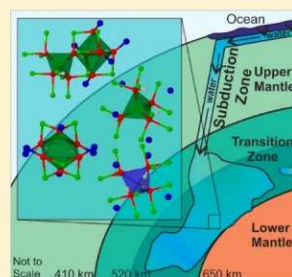
Hidden Oceans? Unraveling the Structure of Hydrous Defects in the Earth's Deep Interior

Helen Grüninger,[†] Katherine Armstrong,[‡] Dominik Greim,[†] Tiziana Boffa-Ballaran,[‡] Daniel J. Frost,^{*,‡} and Jürgen Senker^{*,†}

[†]Anorganische Chemie III and [‡]Bayerisches Geoinstitut, University of Bayreuth, Universitätsstrasse 30, 95447 Bayreuth, Germany

S Supporting Information

ABSTRACT: High-pressure silicates making up the main proportion of the earth's interior can incorporate a significant amount of water in the form of OH defects. Generally, they are charge balanced by removing low-valent cations such as Mg²⁺. By combining high-resolution multidimensional single- and double-quantum ¹H solid-state NMR spectroscopy with density functional theory calculations, we show that, for ringwoodite (γ -Mg₂SiO₄), additionally, Si⁴⁺ vacancies are formed, even at a water content as low as 0.1 wt %. They are charge balanced by either four protons or one Mg²⁺ and two protons. Surprisingly, also a significant proportion of coupled Mg and Si vacancies are present. Furthermore, all defect types feature a pronounced orientational disorder of the OH groups, which results in a significant range of OH...O bond distributions. As such, we are able to present unique insight into the defect chemistry of ringwoodite's spinel structure, which not only accounts for a potentially large fraction of the earth's entire water budget, but will also control transport properties in the mantle. We expect that our results will even impact other hydrous spinel-type materials, helping to understand properties such as ion conduction and heterogeneous catalysis.



■ INTRODUCTION

Thirty years ago it was predicted, on the basis of Pauling bond strength calculations, that the high-pressure mineral wadsleyite (β -Mg₂SiO₄), which dominates the transition zone region of the earth's mantle between 410 and 520 km depth, could incorporate significant concentrations of hydrogen in its structure in the form of hydroxyl defects.¹ Experimental studies confirmed this and also revealed that the higher pressure polymorph ringwoodite (γ -Mg₂SiO₄), which crystallizes in a cubic spinel-type structure with isolated SiO₄ tetrahedra (Q⁰ units) and edge-sharing MgO₆ octahedra (Figure 1),² can also host comparable quantities of water.³ In both cases, charge compensation for the hydroxyl groups is provided by formation of cation vacancies.^{4,5} Experiments under H₂O-saturated conditions show that both minerals contain up to an equivalent of ~3 wt % H₂O.^{3–7} Due to their high abundance in the mantle, this equates to a potential mass of H₂O in the earth's interior that exceeds that of the oceans.^{4,7}

It remained questionable as to whether the transition zone could actually reach this level of hydration, due to a lack of natural samples. However, recently, ringwoodite containing the equivalent of 1 wt % H₂O was identified as an inclusion trapped in a diamond formed in the transition zone.⁸ A critical issue is the nature of the substitution mechanism and the characteristics of the associated cation vacancies. These defect structures will strongly influence transport properties of the mantle, such as viscosity⁹ and thermal conductivity,¹⁰ that are vital for understanding mantle convection. Perhaps more importantly, however, the nature of these defects is of fundamental significance because they form mineral components that may

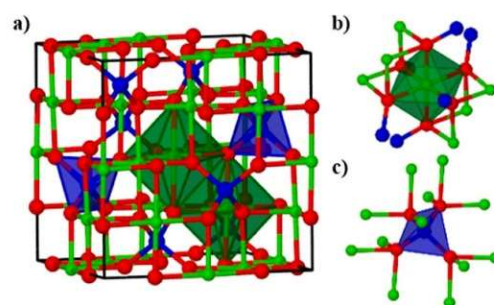


Figure 1. (a) Cubic unit cell of the ringwoodite spinel-type crystal structure (space group $Fd\bar{3}m$). (b, c) Local coordination of the MgO₆ octahedra (b) and SiO₄ tetrahedra (c). Due to the space symmetry, all SiO₄ tetrahedra and MgO₆ octahedra are crystallographically equivalent. Key: Si, blue; Mg, green; O, red.

account for a significant proportion of the earth's entire H₂O budget.

While the defect model associated with hydroxyl group formation in wadsleyite is well understood,^{11,12} the defect chemistry of ringwoodite is still an open question in part due to the difficulty in interpreting the IR spectrum^{13,14} and the challenge of synthesizing suitably large and pure samples for analysis. Several studies on hydrous ringwoodite using methods

Received: May 26, 2017

Published: July 7, 2017

such as single-crystal X-ray diffraction (XRD) and IR/Raman as well as ^{29}Si solid-state NMR (ssNMR) spectroscopy have identified the main hydroxyl sites in magnesium vacancies,^{13–16} as has been demonstrated for wadsleyite,^{4,11,17} whereby the removed Mg^{2+} is charge balanced by two protons (denoted as $V_{\text{Mg}}'' + 2\text{H}^{*}$ according to the Kröger–Vink notation). However, as opposed to wadsleyite, the Mg/Si ratio of ringwoodite is barely influenced upon hydration.⁷ Additionally, there seems to be a small degree of Mg/Si disorder,¹³ and the IR spectrum contains an extremely broad and disordered OH stretching region.^{13,14} Consequently, a simple mechanism involving only Mg vacancies is unlikely to account for all the OH defect structures in hydrous ringwoodite.^{13,14,18}

For these reasons, additional Si vacancies, as well as more complicated, coupled substitutions with and without local inversion of the spinel structure, have been proposed mainly by computational studies.^{13,15,18–21} Si vacancies are well-known from the hydrogarnet substitution in the garnet group at lower pressures, i.e., upper mantle conditions.^{12,22,23} The large volumetric expansion of the tetrahedral sites upon removal of the Si atoms is, nevertheless, considered to be unfavorable under the higher pressure conditions of the transition zone, which renders the formation of Si defects more unlikely.^{12,23} However, to date, experimental data to verify or falsify this hypothesis are missing for ringwoodite.

Here we present a comprehensive study giving unambiguous experimental evidence for a surprisingly large variability of the ringwoodite spinel-type structure to incorporate water in the form of hydroxyl defects. By combining recently developed ultrafast magic angle spinning (MAS) techniques, which provide unique resolution for ^1H ssNMR spectroscopy,²⁴ with quantum chemical calculations and sophisticated multi-anvil synthesis, we have been able to prepare hydrous ringwoodite of high purity and with a controlled water content and are now able to link experimental ^1H chemical shifts, as well as their connectivities to individual OH defect types.

In particular, ssNMR spectroscopy has proven to be a powerful tool for unraveling local and intermediate structural details without depending on long-range order.^{25–29} The high sensitivity for protons together with the unprecedented resolution now provided by ultrafast MAS allows for studying the low proton concentrations, which are typical for the hydroxyl defects. Since the calculated energies of the different vacancies cannot be compared easily, due to differences in the stoichiometry, this is the most promising way to develop a deeper understanding for the hydrous defect chemistry of ringwoodite and the spinel structure.

RESULTS AND DISCUSSION

We synthesized phase-pure hydrous wadsleyite from anhydrous forsterite and H_2O at 19 GPa and 1150 °C in a multi-anvil apparatus. The water content of ~ 0.1 wt % was determined by the b/a lattice parameter ratio obtained by Rietveld refinement ($a = 5.700(1)$ Å, $b = 11.449(2)$ Å, $c = 8.254(0)$ Å, $\alpha = \beta = \gamma = 90^\circ$; Figure S1, Supporting Information).³⁰ The recovered sample with a small addition of 1.5 wt % anhydrous SiO_2 , to suppress MgO-rich dense hydrous magnesium silicate phases or even brucite ($\text{Mg}(\text{OH})_2$) impurities,⁷ was then converted into hydrous ringwoodite at 21 GPa and 1100 °C. This solid-state transformation allows the estimation of the ringwoodite water content based on the intermediate wadsleyite—as water loss is unlikely. The multiphase Rietveld analysis of the PXRD pattern (Figure 2) reveals ~ 98 wt % ringwoodite, ~ 1.4 wt % stishovite

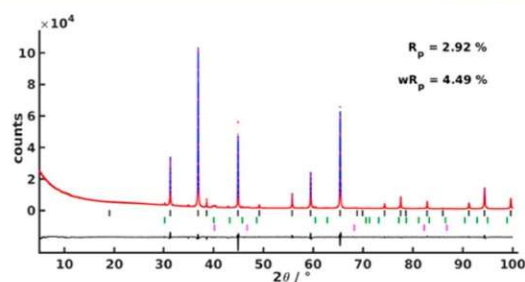


Figure 2. Rietveld profile fit of the PXRD measurement (red) of hydrous ringwoodite. Multiphase refinement (blue) of ringwoodite, stishovite, and platinum results in a weighted profile R -value of 4.49. The positions of the reflections of the individual phases, ringwoodite (black bars), stishovite (green bars), and platinum (pink bars), as well as the difference between experiment and the refinement (black) are shown below the profile fit.

recrystallized from the SiO_2 added to the educts, and a small impurity of ~ 0.6 wt % platinum left from the capsule used during synthesis. As expected on the basis of the synthesis strategy described above, the Rietveld analysis does not provide any hints for the formation of MgO-rich hydrous phases or brucite, which could interfere with the ssNMR experiments. The observed lattice parameter for hydrous ringwoodite ($a = 8.069(1)$ Å; Table S1, Supporting Information) is only slightly larger than that of anhydrous ringwoodite ($a = 8.0649(1)$ Å),² which is in agreement with the relatively low water content. Rietveld refinement parameters are summarized in Table S1.

For a detailed interpretation of the ^{29}Si and ^1H NMR spectra of ringwoodite, quantum-mechanical calculations of the NMR parameters of various hydrous defect models are necessary. Therefore, we explored six different defect types with density functional theory (DFT) calculations (Figure 3). Of the three isolated defects, the first one is based on a Mg vacancy charge balanced by two protons ($V_{\text{Mg}}'' + 2\text{H}^{*}$, Figure 3a). The other two are Si vacancies, charge balanced either by four protons ($V_{\text{Si}}'''' + 4\text{H}^{*}$, Figure 3b) or one Mg^{2+} as well as two protons ($\text{Mg}_{\text{Si}}'' + 2\text{H}^{*}$, Figure 3c). Furthermore, two coupled Si and Mg defects were taken into account: (i) two coupled octahedral Mg vacancies ($V_{2\text{Mg}}'''' + 4\text{H}^{*}$, Figure 3d) and (ii) one Mg^{2+} on a Si site coupled to an octahedral vacancy ($\text{Mg}_{\text{Si}}\text{V}_{\text{Mg}}'''' + 4\text{H}^{*}$, Figure 3e). Finally, also a Mg defect with a local cation inversion of neighboring Mg and Si sites ($\text{Mg}_{\text{Si}}'' + \text{Si}_{\text{Mg}}'' + V_{\text{Mg}}'' + 2\text{H}^{*}$, Figure 3f) was studied.¹⁸ For all defects, multiple OH orientations were considered to account for thermal disorder during synthesis. Detailed descriptions of the extended models and the resulting ^{29}Si and ^1H chemical shifts are given in section S4 of the Supporting Information.

The calculated ^{29}Si chemical shifts show a clear trend in dependence of the proton environment of the isolated SiO_4 tetrahedra (Q^0) (Figure 4a). Without any protons nearby, resonances between -80 and -82 ppm with a center of gravity around -81.5 ppm were found, which agrees well with the results of other DFT and experimental studies,^{16,17} and which is close to the lower boundary of the typical shift range of Q^0 Si species.³¹ SiO_4 tetrahedra involved in O \cdots HO bonds ($\text{SiO}\cdots\text{H}$, Figure 4a) are shifted to higher frequencies (downfield) by roughly 2 ppm, while Si species covalently bound to OH groups ($\text{Si}-\text{OH}$) show the strongest downfield shift by an

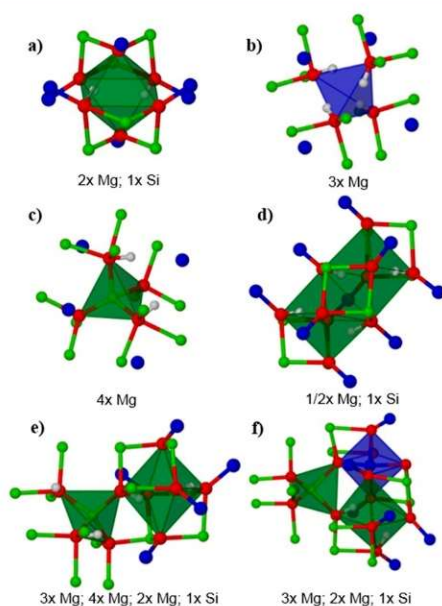
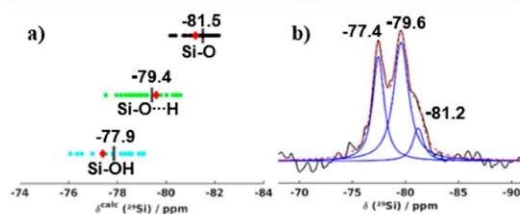


Figure 3. Defect models of hydrous ringwoodite highlighting the cation environments of the hydroxyl groups: (a) isolated Mg vacancy ($V_{\text{Mg}}'' + 2\text{H}^{*\ast}$); (b) isolated Si vacancy charge balanced by four protons ($V_{\text{Si}}'''' + 4\text{H}^{*\ast*\ast}$); (c) isolated Si vacancy charge balanced by one Mg^{2+} and two protons ($\text{Mg}_{\text{Si}}'' + 2\text{H}^{*\ast}$); (d) coupled Mg vacancies ($V_{2\text{Mg}}'''' + 4\text{H}^{*\ast*\ast}$); (e) coupled defect with an octahedral vacancy and one Mg^{2+} on a Si site ($\text{Mg}_{\text{Si}}V_{\text{Mg}}'''' + 4\text{H}^{*\ast*\ast}$), (f) coupled defect with an octahedral vacancy in the neighborhood of local Mg/Si inversion ($\text{Mg}_{\text{Si}}'' + \text{Si}_{\text{Mg}}'' + V_{\text{Mg}}'' + 2\text{H}^{*\ast}$). Key: Si, blue; Mg, green; O, red; H, white.



additional of 1.5–2 ppm. The three experimentally observed ^{29}Si resonances at –81.2, –79.6, and 77.4 ppm (Figure 4b) follow a similar trend and are assigned to Si–O, SiO...H, and Si–OH, respectively. The increasing proximity to protons is also reflected in a faster buildup in ^1H - ^{29}Si cross-polarization (CP) MAS spectra (Figure S2, Supporting Information), which is in good agreement with the results of Stebbins et al.¹⁶ The

total absence of signals between –150 and –220 ppm^{16,32} (Figure S2) rules out the formation of octahedral ^{19}Si species close to protons and thus excludes any defect models involving cation inversion like that shown in Figure 3f.

The experimental 1D ^1H MAS spectrum of ringwoodite (Figure 5a) shows a remarkably broad but structured line

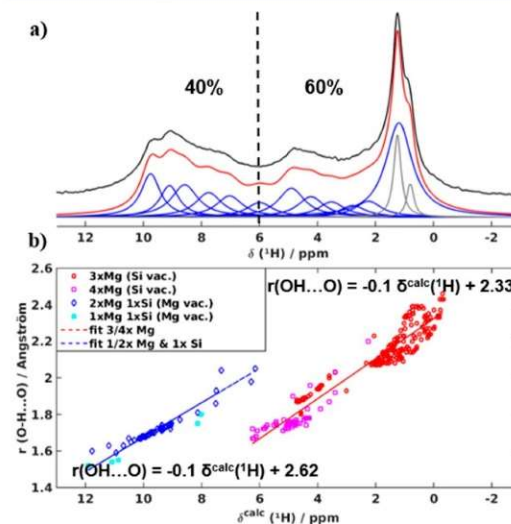


Figure 5. (a) ^1H MAS spin echo spectrum ($\tau = 2\nu_{\text{rot}}^{-1} = 50 \mu\text{s}$) of hydrous ringwoodite (64 scans). A fit (red) with 14 components (blue and gray) is shown below the experimental spectrum (black). The two resonances depicted in gray are assigned to proton species on the surface. A spectrum with a broader spectral range is given in Figure S3 (Supporting Information) to demonstrate that the S/N ratio is good enough for the multicomponent fit. Refinement parameters are given in Table S2 (Supporting Information). (b) Correlation between the hydrogen bond length, cation environment, and calculated ^1H chemical shift for the hydrous defect models in Figure 3. In accordance with the literature,^{33,34} we observe linear correlations between the OH...O bond length and ^1H chemical shift for OH groups in pure Mg environments and mixed Si and Mg environments.

shape, which was fitted by 14 resonances between 0 and 10 ppm. Two of these resonances at 1.2 and 0.8 ppm (gray) exhibit a smaller half-width and have no double-quantum (DQ) intensity (Figure S4, Supporting Information). They are thus considered to arise from surface species, i.e., Si–OH groups.¹² The simulations cover similar ^1H chemical shift regions and reveal two main influences on the ^1H shifts (Figure 5b, Tables S4–S7, Supporting Information). The strongest is the cation environment of the OH groups. If the OH groups are involved in hydrogen bonds, an additional downfield shift proportional to the OH...O bond strength is observed. Similar results were already reported on wadsleyite and silicate glasses.^{33–36} For OH groups in octahedral vacancies (Figures 3a,d–f), one or two Mg atoms and one Si atom form the first coordination sphere, whereas OH groups located around Si vacancies (Figures 3b,c,e,f) are bound to either three or four Mg atoms. While the former leads to a shift range between 6 and 12 ppm, the latter exhibits resonances below 6 ppm (Figure 5b). Accordingly, we divided the experimental spectrum (Figure 5a)

into downfield ($\delta > 6$ ppm) and high-field ($\delta < 6$ ppm) regions with an intensity ratio of 2:3.

2D ^1H - ^1H double-quantum single-quantum (DQSQ) MAS NMR spectra are used to measure protons in close proximity and thus to identify connectivity patterns. We measured several 2D spectra with excitation times t_{exc} between 111 and 244 μs (Figure S4, Supporting Information). Due to the limited t_{exc} experimentally observable ^1H - ^1H correlations depend on the distance between the proton spins and thus on the chosen excitation time of the 2D experiment. From the simulation of DQ buildup curves of ^1H - ^1H spin pairs (Figure 6), we

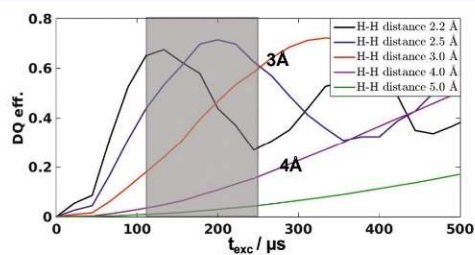


Figure 6. Simulated ^1H - ^1H DQ buildup curves (R18_s^5 sequence with an S_0S_n supercycle) for ^1H - ^1H spin pairs with distances of 2.2, 2.5, 3.0, 4.0, and 5.0 Å. The experimentally used DQ excitation times are indicated by a gray box.

estimate that for excitation times t_{exc} smaller than 250 μs only proton spins in close proximity up to ~ 3.5 Å are highlighted in the 2D spectra. Considering that neighboring oxygen atoms are separated by ~ 3 Å in ringwoodite, all experimentally observed correlations must arise from protons within each individual defect.

The experimental 2D ^1H - ^1H DQSQ MAS NMR spectra (Figure 7, part I) mainly show a wide spread of autocorrelation signals along the diagonal and three cross-correlations at $\delta_{\text{DQ}} = 6.5$ ppm, $\delta_{\text{DQ}} = 9.4$ ppm, and $\delta_{\text{DQ}} = 11.5$ ppm. Due to the chosen experimental excitation times, simulated DQSQ spectra of each defect type (Figure 7, part II) can be directly compared to the experiments and thus used to identify the defects present.

The autocorrelation signals in the downfield region (Figure 7, part I, blue) are only reflected in the DQSQ spectra of the isolated and coupled Mg vacancies (Figure 7, parts IIa and IIc). For the latter, additionally pronounced cross-correlation signals between $\delta_{\text{DQ}} = 15$ ppm and $\delta_{\text{DQ}} = 20$ ppm (Figure 7, part IIc) are expected, which arise from coupling between hydroxyl groups with different OH \cdots O configurations and thus different ^1H shifts. However, these signals are not observed experimentally (Figure 7, part I), and coupled Mg vacancies can thus be excluded. The strong autocorrelation signal between $\delta_{\text{DQ}} = 0$ ppm and $\delta_{\text{DQ}} = 5$ ppm is reproduced only by isolated Si vacancies charge balanced by four protons (Figure 7, part IIb), while the remaining signals between $\delta_{\text{DQ}} = 5$ ppm and $\delta_{\text{DQ}} = 12$ ppm are matched by a combination of the 2D spectra of an isolated Mg vacancy charge balanced by one Mg^{2+} and two protons (Figure 7, part IIc), as well as a mixed coupled defect with one Mg^{2+} on a Si site coupled to an octahedral vacancy (Figure 7, part IIe). The spread of the experimental DQ signals along the diagonal reflects the OH \cdots O bond distributions caused by an orientational disorder of the OH groups.

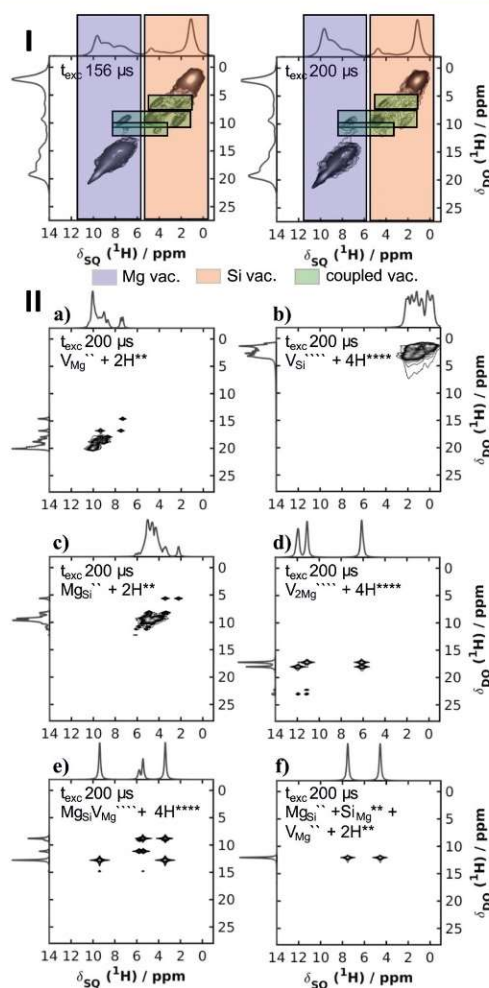


Figure 7. (I) Experimentally observed 2D ^1H - ^1H DQSQ MAS NMR spectra of hydrous ringwoodite at excitation times t_{exc} of 156 and 200 μs and the assignment of the resonances to different vacancy types. (II) Simulated 2D ^1H - ^1H DQSQ MAS NMR spectra at an excitation time t_{exc} of 200 μs of each defect model shown in Figure 3.

The heavy overlap of proton resonances of the various defects within the 1D MAS spectrum (Figure 5a) makes a straightforward determination of defect concentrations by integration difficult. A better resolution is provided within the ^1H - ^1H DQSQ spectra, since they filter for connectivities of neighboring atoms. As a consequence, the DQ intensities depend not only on the number of protons contributing to the resonances but also on their distances and relative alignment. Assuming similar distance relations for all defects, we might estimate the percentage of isolated Mg vacancies ($\text{V}_{\text{Mg}}'' + 2\text{H}^{**}$) to be $\sim 50\%$ and that of isolated Si vacancies charge balanced by four protons ($\text{V}_{\text{Si}}'''' + 4\text{H}^{****}$) to be $\sim 15\%$. The remaining defects—isolated $\text{Mg}_{\text{Si}}'' + 2\text{H}^{**}$ plus mixed coupled defects ($\text{Mg}_{\text{Si}}''\text{V}_{\text{Mg}}'''' + 4\text{H}^{****}$)—exhibit very similar shifts between 2 and 7 ppm (Figure 7, parts IIc and IIe) and thus

could not be distinguished further. Together they amount to ~35%. To derive accurate ratios for the defect types, which is essential to determine, e.g., equilibrium constants, we are currently developing a strategy to predict the full signature of the defects within the ^1H ID spectra on the basis of MD simulations. This work will be the topic of a forthcoming paper.

CONCLUSION

Our results provide a consistent picture of the surprisingly rich OH defect chemistry in ringwoodite explaining the disputed trend of the Mg/Si ratio in combination with a broad variety of OH groups as indicated in IR³⁷ and ^1H MAS NMR spectra already at very low water contents. Correlations between the cation environment, OH...O bond length, and ^1H chemical shift of structurally bound OH groups have been established. Our analysis revealed the formation of roughly 50% isolated low-valent Mg vacancies ($V_{\text{Mg}}'' + 2\text{H}^{**}$), while coupled Mg vacancies ($V_{2\text{Mg}}'''' + 4\text{H}^{****}$) are clearly disfavored. Additionally, we presented unique proof for the formation of three different Si vacancies, which account for the other 50% of defects. These are two types of isolated defects ($V_{\text{Si}}'''' + 4\text{H}^{****}$ and $\text{Mg}_{\text{Si}}'' + 2\text{H}^{**}$) and a mixed coupled vacancy ($\text{Mg}_{\text{Si}}V_{\text{Mg}}'''' + 4\text{H}^{****}$). The replacement of Si by Mg on a tetrahedral site accounts for 35%, while a charge compensation with solely four protons accounts for 15%. This indicates that the high local charge density created by the removal of a Si^{4+} is more effectively compensated by a Mg^{2+} and two protons than just four protons. As such, a Si vacancy is stabilized by migration of a Mg^{2+} from a neighboring octahedral site, creating the mixed coupled vacancy ($\text{Mg}_{\text{Si}}V_{\text{Mg}}'''' + 4\text{H}^{****}$). This octahedral vacancy may diffuse into the bulk, leading to isolated $\text{Mg}_{\text{Si}}'' + 2\text{H}^{**}$ and Mg defects.

While the formation of low-valent cation (Mg^{2+}) vacancies is expected, in particular, the formation of high-valent cation (Si^{4+}) defects, as well as the orientational disorder of the OH groups upon water incorporation, was not observed for other nominally anhydrous high-pressure minerals,^{5,11,12,17} which make up the main proportion of the earth's mantle. As observed, the high local charge density of a Si vacancy can be compensated in two ways: (i) by one Mg^{2+} and two H^+ ions or (ii) by four H^+ ions. This provides a larger flexibility in comparison to the garnet structure type, the only other mineral class with a significant proportion of Si vacancies, where, however, only the latter substitution pattern is found. Additionally, the volume expansion of a vacant tetrahedron in a spinel-type structure ($\Delta V \approx 50\%$) is significantly lower than in garnets ($\Delta V \approx 70\text{--}90\%$).^{38,39} Not only does this highlight the variability of the spinel structure to accommodate various defects, which will alter the silicate's properties, such as rheology and thermal conductivity, and thus impact the transport properties of the whole mantle, but we expect that our results will also have an impact on other challenges in materials sciences, where the spinel structure and hydroxyl defects play an important role. This is true for fields of applications as diverse as (photo)catalysis with ferrites and transition Al_2O_3 ,^{40,41} proton conduction in nonstoichiometric hydrous MgAl_2O_4 ,⁴² and electrode materials in Li ion batteries.⁴³

EXPERIMENTAL DETAILS

Synthesis. Hydrous ringwoodite was synthesized in a two-step process: dry forsterite and liquid H_2O were transformed to hydrated wadsleyite, which was then transformed to hydrated ringwoodite.

Powdered synthetic forsterite was sealed in a 2 mm diameter welded Pt capsule with ~2 wt % liquid H_2O . Two of these sample charges were prepared, and these capsules were pressurized to 19 GPa in a 5000 tonne Kawai-type multianvil apparatus. In each experiment, an 18 mm Cr-doped MgO octahedral pressure medium was compressed with tungsten-carbide cubes with 11 mm truncated edge lengths (a so-called 18/11 assembly). Cylindrical LaCrO_3 heaters were used, and the temperature was measured using a W3%Re–W25% Re (type d) thermocouple. After the attainment of pressure, the sample was heated at 1150 °C for 4 h before the sample was quenched by turning off the electrical power to the furnace. The recovered samples were examined with powder X-ray diffraction (PXRD) and shown to be pure wadsleyite with minor Pt contamination from the capsule. Both wadsleyite samples were ground together with 1.5 wt % reagent-grade SiO_2 under ethanol in an agate mortar and pestle. This powder was again placed into a welded Pt capsule which was compressed as described above to 21 GPa and 1100 °C for 2.5 h using an 18/8 assembly. Further experimental details can be found in ref 44.

Powder X-ray Diffraction. Powder X-ray diffraction measurements were performed in transmission geometry with a STOE STADI P diffractometer with Cu $K\alpha_1$ radiation equipped with a fast, high-resolution silicon strip detector (DECTRIS Mythen1K). The samples were prepared in glass capillaries (diameter 0.3 mm). Instrument parameters for Rietveld refinements were determined by analyzing Si. For Rietveld refinement, the fundamental parameters approach⁴⁵ as implemented in TOPAS Academic⁴⁶ was applied. The background was fitted using a 12th-order Tchebyshev polynomial.⁴⁷ The PO Spherical Harmonics macro⁴⁸ of 12th order as implemented in TOPAS was used to account for the preferred orientation. Crystallite size and strain were fitted for each phase using the implemented macros CS_L, CS_G, STRAIN_L, and STRAIN_G using Lorentzian and Gaussian functions, respectively.

Solid-State NMR. Solid-state NMR spectroscopic experiments were performed using a Bruker Avance III spectrometer operating at a magnetic field strength of 14.1 T, corresponding to a ^1H Larmor frequency of 600.1 MHz and a ^{29}Si Larmor frequency of 119.2 MHz. All experiments were carried out using a Bruker 1.9 mm triple-resonance probe at an MAS frequency of 40.0 kHz, unless otherwise stated. All spectra were referenced with respect to TMS. For ^1H – ^{29}Si CP MAS experiments, ramped (100–50 ramp) contact pulses with lengths of 2.5, 5, 10, and of 15 ms between ^1H and ^{29}Si and a recycle delay of 2.0 s were used.⁴⁹ The radio frequency (rf) field strengths for ^1H ($\nu(^1\text{H}) \approx 90$ kHz) and ^{29}Si ($\nu(^{29}\text{Si}) \approx 70$ kHz), respectively, were directly optimized on the sample. The SPINAL-64 sequence⁵⁰ was used for broad-band proton decoupling, and an MAS frequency of 20 kHz was chosen. For ^1H MAS measurements, an MAS frequency of 40 kHz and a spin echo was used to reduce background signals from the probe. The interpulse distance was adjusted to 50 μs ($2\nu_{\text{rot}}^{-1}$) to suppress probe ringing and the probe background. The recycle delay was set to 3.0 s. 2D homonuclear ^1H correlation spectra were recorded using the double-quantum (DQ) recoupling sequence R18,⁵ ($\nu(^1\text{H}) \approx 90$ kHz) with an S_0S_x supercycle, which maintains γ -encoding of the sequence.^{51,52} The DQ excitation times were set as multiples of one RR' block (22.22 μs) to 111.11, 155.56, 200.00, and 244.44 μs , and a recycle delay of 2.0 s was chosen. Instead of a simple 90° pulse after the DQ block, a spin echo was used again.

DFT Calculations. Calculations of NMR parameters for different proton defect structures in ringwoodite were carried out using the CASTEP DFT code (version 8.0),^{53–56} employing the GIPAW algorithm.⁵⁷ For all calculations, the generalized gradient approximation (GGA) Perdew–Burke–Ernzerhof (PBE)⁵⁸ functional with the semiempirical dispersion correction Grimme06 was employed. Geometry optimizations and NMR parameters were calculated using a planewave energy cutoff of 800 eV and a k -point spacing of 0.015 \AA^{-1} over the Brillouin zone, unless otherwise stated. The calculation of NMR parameters generates the absolute shielding tensor σ in the crystal frame. The isotropic shielding σ_{iso} is given by $1/3\text{Tr}\{\sigma\}$.

The isotropic chemical shift δ_{iso} is given by $-(\sigma_{\text{iso}} - \sigma_{\text{ref}})$, where σ_{ref} is a reference shielding. For ^{29}Si , a reference shielding σ_{ref} of 323.2 ppm was determined by comparison to the experimental spectrum of

anhydrous ringwoodite as a secondary reference to TMS. For ^1H , a reference shielding σ_{ref} of 29.7 ppm was determined by the comparison of the experimental and calculated shifts of superhydrous phase b as a secondary reference to TMS.^{59,60}

Model Building. For anhydrous ringwoodite, the initial atomic positions and unit cell parameters were taken from a publication about the polymorphism of Mg_2SiO_4 .⁶¹ Different hydrous ringwoodite defect structures were introduced by removing Mg or Si atoms from the anhydrous structure and adding the corresponding number of H atoms around the resulting vacancies. To isolate the defects in the models from their periodic images, $2 \times 1 \times 1$ supercells were used. Not only isolated single cation defects, but also combinations of Mg and Si defects with and without cation inversion in the spinel structure were considered, resulting in 11 different defect structures. All structures were fully geometry optimized within space group $P1$ with the cell allowed to vary prior to calculation of the NMR parameters.

To calculate multiple OH orientations and the hydrogen bond strength, the previously optimized structure of isolated single defect structures ($V_{\text{Mg}}'' + 2\text{H}^{*}, V_{\text{Si}}'''' + 4\text{H}^{*} + 2\text{H}$) was reduced to a single unit cell containing one single defect site. The proton positions in the defects were varied manually on a circle, yielding 36 different structures for each defect type. Each of these models was geometry optimized with a fixed cell prior to calculation of the NMR parameters. For these calculations, a planewave energy cutoff of 800 eV and a k -point spacing of 0.03 \AA^{-1} over the Brillouin zone were used.

SIMPSON Simulations. Theoretical ^1H - ^1H DQ buildup curves for isolated spin pairs and theoretical 2D ^1H - ^1H DQSQ MAS NMR spectra of all hydrous defect models were simulated on the basis of the R18_s sequence used experimentally with the program SIMPSON.⁶²⁻⁶⁴ A total of 232 ZCW (α, β) angles and 5 γ angles were found to be sufficient to generate the powder average. For the 2D ^1H - ^1H DQSQ MAS NMR spectra, the full proton chemical shift tensor, including the isotropic shift and the anisotropic part as well as its orientation, was extracted from the DFT calculations of the defect models. For larger spins systems, the 2D ^1H - ^1H DQSQ MAS NMR spectra were constructed from spin pair simulations of the individual dipolar couplings. Other parameters used in the simulations were the same as in the corresponding experiment.

■ ASSOCIATED CONTENT

📄 Supporting Information

The Supporting Information is available free of charge on the ACS Publications website at DOI: 10.1021/jacs.7b05432.

Rietveld analysis of the PXRD data of ringwoodite and wadsleyite, ^1H - ^{29}Si CP MAS spectra with different mixing times, further ^1H MAS NMR spectra and fitting parameter, technical details of the defect models used for DFT, table of simulated ^{29}Si chemical shifts, and tables summarizing the simulated OH...O lengths and calculated ^1H chemical shifts (PDF)

■ AUTHOR INFORMATION

Corresponding Authors

*dan.frost@uni-bayreuth.de

*juergen.senker@uni-bayreuth.de

ORCID

Jürgen Senker: 0000-0002-7278-7952

Notes

The authors declare no competing financial interest.

■ ACKNOWLEDGMENTS

H.G. acknowledges the Fonds der Chemischen Industrie for financial support in the form of the Chemiefonds Fellowship,

and D.F. thanks the Deutsche Forschungsgemeinschaft (DFG) for funding within Grant FR 1555/10-1.

■ REFERENCES

- (1) Smyth, J. R. *Am. Mineral.* **1987**, *72*, 1051.
- (2) Sasaki, S.; Prewitt, C. T.; Sato, Y.; Ito, E. *J. Geophys. Res.* **1982**, *87*, 7829.
- (3) Kohlstedt, D. L.; Keppler, H.; Rubie, D. C. *Contrib. Mineral. Petrol.* **1996**, *123* (4), 345.
- (4) Smyth, J. R. *Am. Mineral.* **1994**, *79* (9–10), 1021.
- (5) Kudoh, Y.; Inoue, T.; Arashi, H. *Phys. Chem. Miner.* **1996**, *23*, 461.
- (6) Inoue, T.; Yurimoto, H.; Kudoh, Y. *Geophys. Res. Lett.* **1995**, *22*, 117.
- (7) Ohtani, E.; Mizobata, H.; Yurimoto, H. *Phys. Chem. Miner.* **2000**, *27* (8), 533.
- (8) Pearson, D. G.; Brenker, F. E.; Nestola, F.; McNeill, J.; Nasdala, L.; Hutchison, M. T.; Matveev, S.; Mather, K.; Silversmit, G.; Schmitz, S.; Vekemans, B.; Vincze, L. *Nature* **2014**, *507* (7491), 221.
- (9) Hustoft, J.; Amulele, G.; Ando, J. I.; Otsuka, K.; Du, Z.; Jing, Z.; Karato, S. I. *Earth Planet. Sci. Lett.* **2013**, *361*, 7.
- (10) Thomas, S.-M.; Bina, C. R.; Jacobsen, S. D.; Goncharov, A. F. *Earth Planet. Sci. Lett.* **2012**, *357*–358, 130.
- (11) Griffin, J. M.; Berry, A. J.; Frost, D. J.; Wimperis, S.; Ashbrook, S. E. *Chem. Sci.* **2013**, *4* (4), 1523.
- (12) Keppler, H.; Smyth, J. R. *Rev. Mineral. Geochem.* **2006**, *62*, v.
- (13) Kudoh, Y.; Kuribayashi, T.; Mizobata, H.; Ohtani, E. *Phys. Chem. Miner.* **2000**, *27*, 474.
- (14) Smyth, J. R.; Holl, C. M.; Frost, D. J.; Jacobsen, S. D.; Langenhorst, F.; McCammon, C. A. *Am. Mineral.* **2003**, *88*, 1402.
- (15) Kudoh, Y. *Phys. Chem. Miner.* **2001**, *28* (8), 523.
- (16) Stebbins, J. F.; Smyth, J. R.; Panero, W. R.; Frost, D. J. *Am. Mineral.* **2009**, *94* (7), 905.
- (17) Griffin, J. M.; Ashbrook, S. E. *Annu. Rep. NMR Spectrosc.* **2013**, *79*, 241.
- (18) Blanchard, M.; Balan, E.; Wright, K. *Am. Mineral.* **2009**, *94*, 83.
- (19) Ye, Y.; Brown, D. A.; Smyth, J. R.; Panero, W. R.; Jacobsen, S. D.; Chang, Y.-Y.; Townsend, J. P.; Thomas, S.-M.; Hauri, E. H.; Dera, P.; Frost, D. J. *Am. Mineral.* **2012**, *97*, 573.
- (20) Blanchard, M.; Wright, K.; Gale, J. D. *Phys. Chem. Miner.* **2005**, *32*, 585.
- (21) Panero, W. R. *J. Geophys. Res.* **2010**, *115* (B3), B03203.
- (22) Ackermann, L.; Cemič, L.; Langer, K. *Earth Planet. Sci. Lett.* **1983**, *62* (2), 208.
- (23) Withers, A. C.; Wood, B. J.; Carroll, M. R. *Chem. Geol.* **1998**, *147* (1–2), 161.
- (24) Samoson, A.; Tuhern, T.; Past, J.; Reinhold, A.; Anupöld, T.; Heinmaa, I. *Top. Curr. Chem.* **2005**, *246* (2004), 15.
- (25) Martineau, C.; Senker, J.; Taulelle, F. *Annu. Rep. NMR Spectrosc.* **2014**, *82*, 1.
- (26) Wack, J.; Siegel, R.; Ahnfeldt, T.; Stock, N.; Mafra, L.; Senker, J. *J. Phys. Chem. C* **2013**, *117* (39), 19991.
- (27) Schmidt, M.; Zehe, C. S.; Siegel, R.; Heigl, J. U.; Steinlein, C.; Schmidt, H.-W.; Senker, J. *CrystEngComm* **2013**, *15* (43), 8784.
- (28) Seyfarth, L.; Seyfarth, J.; Lotsch, B. V.; Schnick, W.; Senker, J. *Phys. Chem. Chem. Phys.* **2010**, *12* (9), 2227.
- (29) Senker, J.; Sehnert, J.; Correll, S. J. *Am. Chem. Soc.* **2005**, *127* (1), 337.
- (30) Jacobsen, S. D.; Demouchy, S.; Frost, D. J.; Boffa Ballaran, T.; Kung, J. *Am. Mineral.* **2005**, *90* (1), 61.
- (31) Engelhardt, G.; Michel, D. *High-Resolution Solid-State NMR of Silicates and Zeolites*; John Wiley & Sons, Ltd.: Chichester, U.K., 1987.
- (32) Stebbins, J. F.; Kanzaki, M. *Science* **1991**, *251*, 294.
- (33) Eckert, H.; Yesinowski, J. P.; Silver, L. A.; Stolper, E. M. *J. Phys. Chem.* **1988**, *92*, 2055.
- (34) Xue, X.; Kanzaki, M. *J. Am. Ceram. Soc.* **2009**, *92* (12), 2803.
- (35) Kohn, S. C.; Brooker, R. A.; Frost, D. J.; Slesinger, A. E.; Wood, B. J. *Am. Mineral.* **2002**, *87*, 293.

- (36) Moran, R. F.; McKay, D.; Pickard, C. J.; Berry, A. J.; Griffin, J. M.; Ashbrook, S. E. *Phys. Chem. Chem. Phys.* **2016**, *18* (15), 10173.
- (37) Panero, W. R.; Smyth, J. R.; Pigott, J. S.; Liu, Z.; Frost, D. J. *Am. Mineral.* **2013**, *98* (4), 637.
- (38) Lager, G. A.; Armbruster, T.; Rotella, F. J.; Rossmann, G. R. *Am. Mineral.* **1989**, *74*, 840.
- (39) Martin, R. F.; Donnay, G. *Am. Mineral.* **1972**, *57*, 554.
- (40) Génin, J. M. R.; Aïssa, R.; Géhin, A.; Abdelmoula, M.; Benali, O.; Ernstsén, V.; Ona-Nguema, G.; Upadhyay, C.; Ruby, C. *Solid State Sci.* **2005**, *7* (5), 545.
- (41) Sohlberg, K.; Pennycook, S. J.; Pantelides, S. T. *J. Am. Chem. Soc.* **1999**, *121* (33), 7493.
- (42) Okuyama, Y.; Kurita, N.; Fukatsu, N. *Solid State Ionics* **2006**, *177*, 59.
- (43) Ammundsen, B.; Islam, M. S.; Jones, D. J.; Rozière, J. J. *Power Sources* **1999**, *81–82*, 500.
- (44) Frost, D. J.; Poe, B. T.; Trønnes, R. G.; Liebske, C.; Duba, A.; Rubie, D. C. *Phys. Earth Planet. Inter.* **2004**, *143–144* (1–2), 507.
- (45) Cheary, R. W.; Coelho, A. J. *Appl. Crystallogr.* **1992**, *25* (Part 2), 109.
- (46) A. A. Coelho, Coelho Software, Brisbane, Australia, 2012.
- (47) Tchebychev, P. L. *Théorie des mécanismes connus sous le nom de parallélogrammes*; Imprimerie de l'Académie Impériale des Sciences: St. Petersburg, Russia, 1853.
- (48) Ahtee, M.; Nurmela, M.; Suortti, P.; Järvinen, M. *J. Appl. Crystallogr.* **1989**, *22* (3), 261.
- (49) Pines, A.; Gibby, M. G.; Waugh, J. S. *J. Chem. Phys.* **1973**, *59*, 569.
- (50) Fung, B. M.; Khitrin, A. K.; Ermolaev, K. *J. Magn. Reson.* **2000**, *142* (1), 97.
- (51) Kristiansen, P. E.; Carravetta, M.; van Beek, J. D.; Lai, W. C.; Levitt, M. H. *J. Chem. Phys.* **2006**, *124* (23), 234510.
- (52) Kristiansen, P. E.; Mitchell, D. J.; Evans, J. N. S. *J. Magn. Reson.* **2002**, *157* (2), 253.
- (53) Clark, S. J.; Segall, M. D.; Pickard, C. J.; Hasnip, P. J.; Probert, M. J.; Refson, K.; Payne, M. C. *Z. Kristallogr. - Cryst. Mater.* **2005**, *220*, 567.
- (54) Pickard, C.; Mauri, F. *Phys. Rev. B: Condens. Matter Mater. Phys.* **2001**, *63* (24), 245101.
- (55) Yates, J. R.; Pickard, C. J.; Mauri, F. *Phys. Rev. B: Condens. Matter Mater. Phys.* **2007**, *76*, 024401.
- (56) Profeta, M.; Mauri, F.; Pickard, C. J. *J. Am. Chem. Soc.* **2003**, *125* (2), 541.
- (57) Charpentier, T. *Solid State Nucl. Magn. Reson.* **2011**, *40* (1), 1.
- (58) Perdew, J. P.; Burke, K.; Ernzerhof, M. *Phys. Rev. Lett.* **1996**, *77* (18), 3865.
- (59) Phillips, B. L.; Burnley, P. C.; Worminghaus, K.; Navrotsky, A. *Phys. Chem. Miner.* **1997**, *24*, 179.
- (60) Xue, X.; Kanzaki, M.; Shatskiy, A. *Am. Mineral.* **2008**, *93* (7), 1099.
- (61) Baur, W. H. *Am. Mineral.* **1972**, *57*, 709.
- (62) Bak, M.; Rasmussen, J. T.; Nielsen, N. C. *J. Magn. Reson.* **2000**, *147* (2), 296.
- (63) Tosner, Z.; Vosegaard, T.; Kehlet, C.; Khaneja, N.; Glaser, S. J.; Nielsen, N. C. *J. Magn. Reson.* **2009**, *197* (2), 120.
- (64) Tošner, Z.; Andersen, R.; Stevnsso, B.; Edén, M.; Nielsen, N. C.; Vosegaard, T. *J. Magn. Reson.* **2014**, *246*, 79.

Supporting Information

for

Hidden Oceans? Unraveling the Structure of Hydrous Defects in the Earth's Deep Interior

Helen Grüninger,^[a] Katherine Armstrong,^[b] Dominik Greim,^[a] Tiziana Boffa-Ballaran,^[b]

Daniel J. Frost,^{*[b]} and Jürgen Senker^{*[a]}

^a Anorganische Chemie III, Universitätsstrasse 30, University of Bayreuth,
95447 Bayreuth, Germany,

^b Bayerisches Geoinstitut, Universitätsstrasse 30, University of Bayreuth,
95447 Bayreuth, Germany.

*To whom correspondence should be addressed;

Email: juergen.senker@uni-bayreuth.de; dan.frost@uni-bayreuth.de.

Contents

S1.	Powder X-ray diffraction of ringwoodite and wadsleyite	S2
S2.	^1H ^{29}Si CPMAS ssNMR	S3
S3.	^1H ssNMR	S3
S4.	Hydrous defect structures in ringwoodite used for DFT calculations	S5
S5.	References	S17

S1. Powder X-ray diffraction of ringwoodite and wadsleyite

Table S1: Lattice parameters after the multi-phase Rietveld refinement parameters of the PXRD of ringwoodite ($R_{wp} = 4.49$). The starting cell parameters and symmetry were taken from published crystallographic data of anhydrous ringwoodite, anhydrous stishovite and platinum.¹⁻³ An initial Pawley fit resulted in a R_{wp} value of 4.33, lattice parameter of $a = 8.068 \text{ \AA}$ (ringwoodite) and a similar quality for the profile plot as observed for the Rietveld refinement (Figure 2).

Phase	$a / \text{\AA}$	$b / \text{\AA}$	$c / \text{\AA}$	$\alpha=\beta=\gamma / ^\circ$	phase ratio	space group	Est. H_2O content / wt%
Ringwoodite	8.0686(7)	8.0686(7)	8.0686(7)	90	97.94 %	$Fd\bar{3}m$	0.05-0.1
Stishovite	4.180(3)	4.180(3)	2.667(0)	90	1.42 %	$P4_2/mnm$	-
Platinum	3.884(0)	3.884(0)	3.884(0)	90	0.64 %	$Fm\bar{3}m$	-

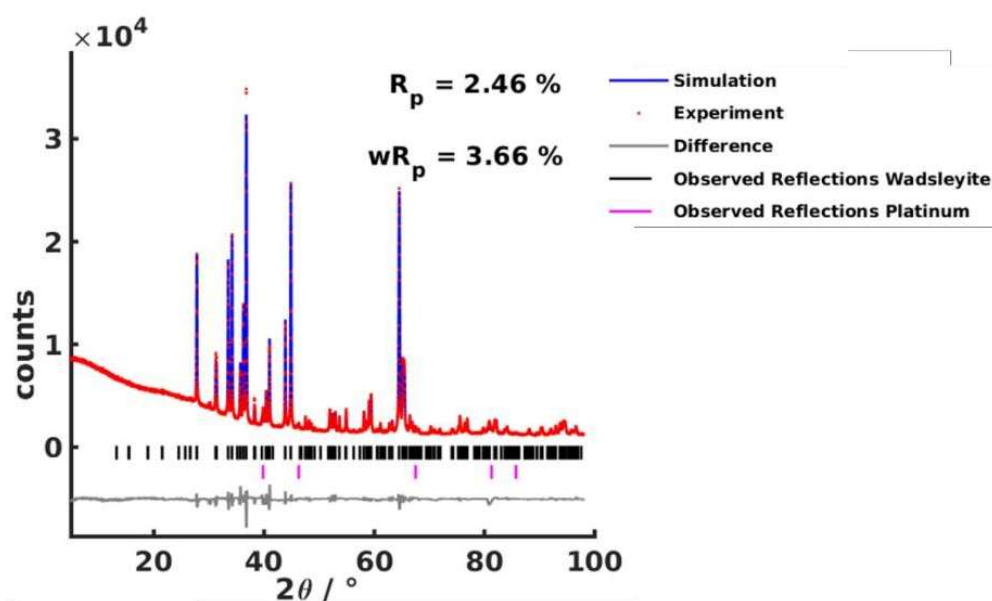


Figure S1: PXRD measurement of the hydrous wadsleyite sample (red) and the Rietveld refinement of wadsleyite and platinum (blue), respectively. The positions of the reflections of the individual phases, wadsleyite (black bars) and platinum (pink bars) are shown below the PXRD pattern. The refinement with a weighted profile R -value of 3.66% gave a ratio of ~99.4% to ~0.6% between wadsleyite and a minor platinum impurity left from the capsule used in the synthesis. The determined lattice parameters for wadsleyite (space group $Imma$) are $a=5.700(1) \text{ \AA}$; $b=11.449(2) \text{ \AA}$; $c=8.254(0) \text{ \AA}$ with $\alpha=\beta=\gamma=90^\circ$ and for platinum (space group symmetry $Fm\bar{3}m$) $a=b=c=3.921(8) \text{ \AA}$ with $\alpha=\beta=\gamma=90^\circ$. An initial Pawley fit resulted in a R_{wp} value of 2.92 and lattice parameters of $a=5.700(1) \text{ \AA}$, $b=11.449(3) \text{ \AA}$, $c=8.254(0) \text{ \AA}$.

S2. ^1H ^{29}Si CPMAS ssNMR

The recorded ^1H - ^{29}Si CPMAS spectra of ringwoodite with varying contact times of (2.5, 5.0, 10, 15 ms) are shown in Figure S2.

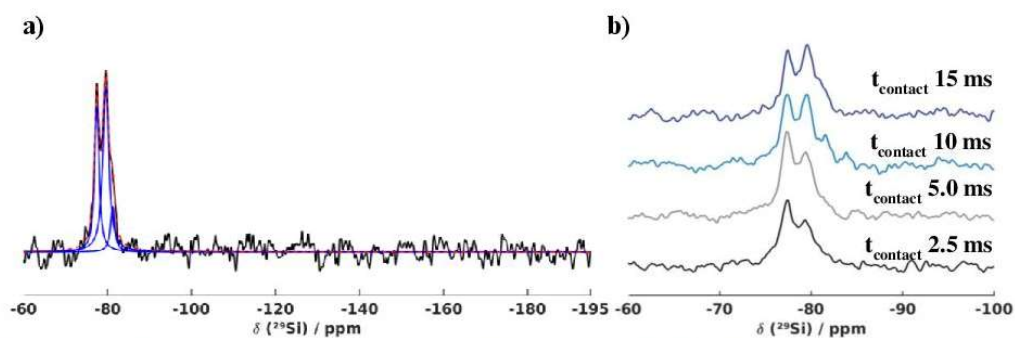


Figure S2: a) ^1H - ^{29}Si CPMAS spectrum of ringwoodite resulting from coadding 32768 transients separated by a recycle interval of 2.0 s. The contact pulse duration was set to 15 ms to make sure that also Si-species further away from protons would be excited. b) Comparison of the ^1H - ^{29}Si CP MAS spectra of ringwoodite with different contact times.

S3. ^1H ssNMR

The parameters used for the fit of the 1D ^1H MAS spin echo (Figure 5a) are given in Table S2.

Table S2: Parameters of the fit of the 1D ^1H MAS spin echo shown in Figure 5a.

Signal	δ_{iso} / ppm	FWHM / ppm	Relative integrals	Percentage / %	Assignment
1	9.7	0.8	0.33	8.7 %	Si-OH
2	9.1	0.8	0.24	6.3 %	Si-OH
3	8.6	1.1	0.34	8.9 %	Si-OH
4	7.75	1.1	0.26	6.7 %	Si-OH
5	7.1	1.1	0.22	5.8 %	Si-OH
6	6.0	1.1	0.15	3.4 %	Si-OH / Mg-OH
7	4.9	1.1	0.30	7.9 %	Mg-OH
8	4.2	1.1	0.21	5.6 %	Mg-OH
9	3.5	1.1	0.16	4.2 %	Mg-OH
10	2.8	1.1	0.12	3.1 %	Mg-OH
11	2.2	1.1	0.17	4.4 %	Mg-OH
12	1.2	0.3	0.24	6.2 %	surface OH-species
13	1.2	1.1	1.00	25.9 %	Mg-OH
14	0.8	0.3	0.09	2.4 %	surface OH-species

The MAS spin echo spectra recorded with a MAS rate of 40 kHz and 62.5 kHz are almost identical (Figure S3), demonstrating that not the homonuclear dipolar coupling but the chemical shift distribution is the dominating factor.

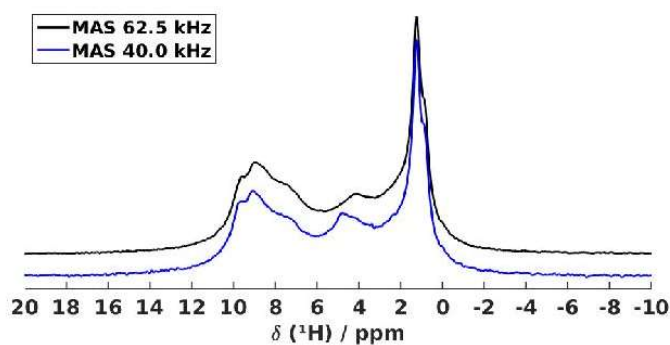


Figure S3: Comparison of ^1H MAS spin echos recorded at a MAS rate of 62.5 kHz (black) and 40.0 kHz (blue), respectively. The spectra are each the result of coadding 64 transients separated by a recycle interval of 3.0 s.

Four rotor-synchronised 2D ^1H ^1H DQSQ MAS NMR spectra of our ringwoodite sample are shown in Figure S4. The spread along the diagonal ($\delta_{\text{DQ}} = 2 \delta_{\text{SQ}}$) indicates a distribution of different hydroxyl proton environments. In addition to the autocorrelation signals along the diagonal, cross correlation signals at $\delta_{\text{DQ}}=6.5$ ppm, $\delta_{\text{DQ}}=9.4$ ppm and $\delta_{\text{DQ}}=11.5$ ppm were observed (Figure S4, dashed lines).

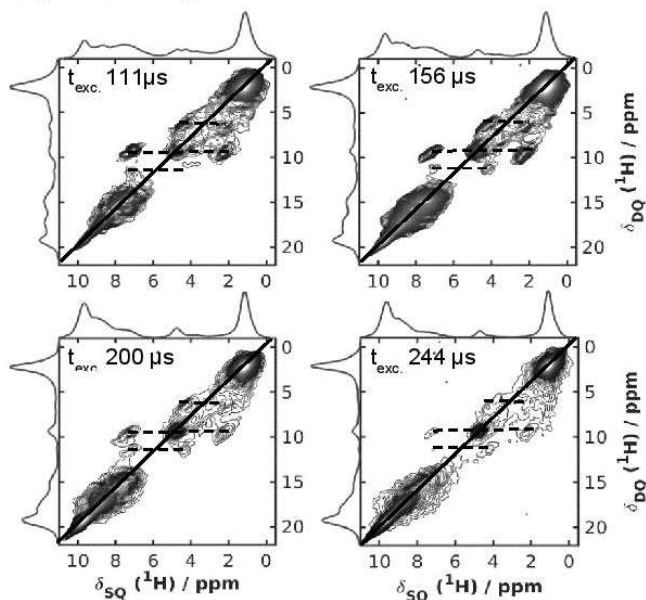


Figure S4: Rotor-synchronised ^1H ^1H DQSQ MAS NMR spectra were recorded using the $R18g^2$ sequence with a S_0S_π supercycle.^{4,5} The RR' Blocks were incremented to yield the excitation times t_{exc} of 111.11 μs , 155.56 μs , 200.00 μs (corresponding to one full $R18g^2$ cycle) and 244.44 μs . DQ cross correlations are indicated by dashed lines. The ^1H ^1H DQSQ MAS NMR spectra are the results of sampling 256 transients separated by a recycle interval of 2.0 s for each of the 132 t_1 increments of 50.00 μs . The spectra were recorded at a MAS rate of 40.0 kHz.

S4. Hydrous defect structures in ringwoodite used for DFT calculations

In the following a structural description of the six different hydrous defect types shown in Figure 3 with multiple proton configurations is given.

Isolated defects of the type $V_{Mg}'' + 2H^{**}$, $V_{Si}'''' + 4H^{****}$ and $Mg_{Si}'' + 2H^{**}$ are shown in Figures 3a-c and S5. For the case of the $V_{Mg}'' + 2H^{**}$ defect (Mg1) one Mg atom was removed from the octahedral 16d site and two protons were placed in the resulting vacant octahedron on opposite O atoms which was shown to be energetically favoured.⁶ The resulting hydroxyl groups are in a mixed cation environment of two Mg and one Si cation and form hydrogen bridges (2.04 Å) along the shorter O-O edge shared by the 16d with its neighbor 16c octahedron which is vacant in the normal spinel structure (Figure S5a).

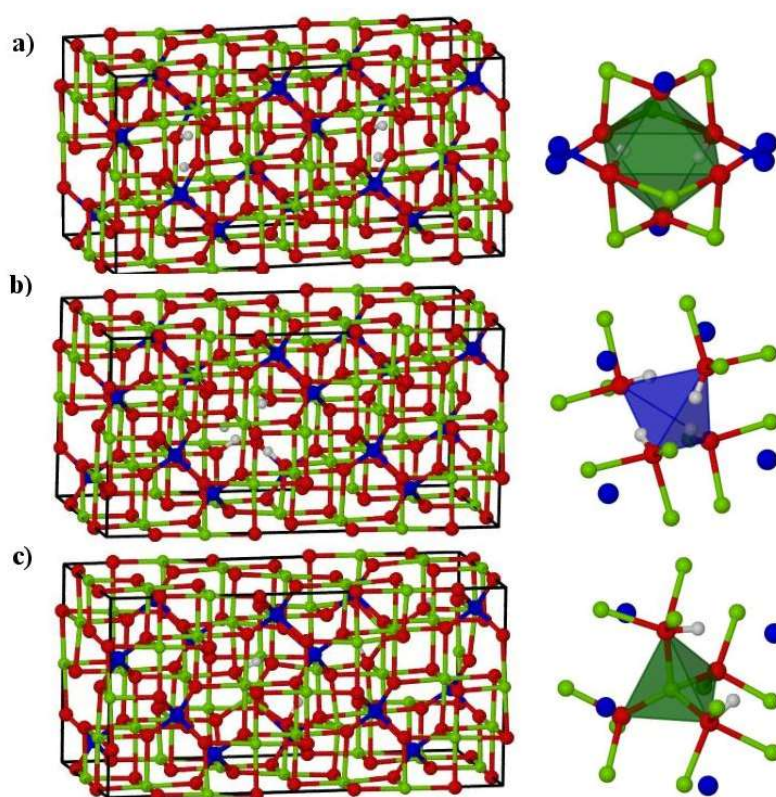


Figure S5: Isolated defects of the type a) $V_{Mg}'' + 2H^{**}$ (Mg1), b) $V_{Si}'''' + 4H^{****}$ (Si1) and c) $Mg_{Si}'' + 2H^{**}$ (MgSi1). The geometry-optimized structure is shown left, while the local coordination of the defect site is shown on the right side.

Multiple proton configurations (Figure S6) with various hydrogen bond length between ~ 1.65 and 2.04 Å, all located along the edge between the 16d and 16c octahedra, were found to be stable with a maximum energy difference of about 3.6 kJ/mol to the most stable structure with two hydrogen bonds of 1.67 Å and 1.68 Å.

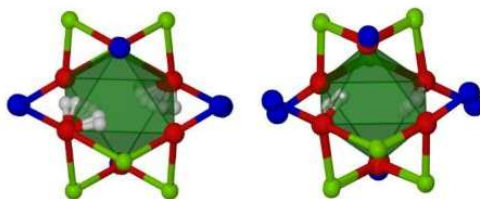


Figure S6: Left: multiple starting hydrogen positions of the hydroxyl group for the defect type $V_{Mg}^{''} + 2H^{**}$. Right: geometry-optimized positions of the hydroxyl group forming hydrogen bonds along the edge between the 16d and the 16c octahedra.

Isolated defects of the type $V_{Si}^{''''} + 4H^{****}$ (Si1, Figures 3b and S5) were created by removing one Si atom of the 8a tetrahedral site and placing four protons in the vacancy. The resulting hydroxyl groups, which are non-silicate, thus solely coordinated to Mg atoms, form hydrogen bonds close to the tetrahedral edge with the oxygens acting as donor and acceptor. The length of the hydrogen bond is between 2.08 Å and 2.46 Å.

36 $V_{Si}^{''''} + 4H^{****}$ defect structures with different hydrogen bond strengths were simulated with energy differences up to max. ~1.8 kJ/mol (Figure S7). Hereby the hydrogen bond is always located along the tetrahedral edge with varying bond length between 2.05 and 2.43 Å.

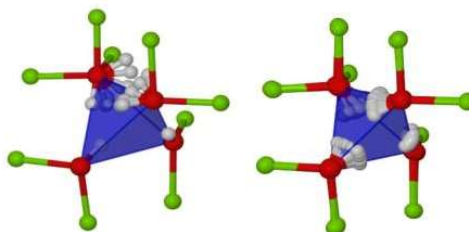


Figure S7: Left: multiple starting hydrogen positions of the hydroxyl group for the defect type $V_{Si}^{''''} + 4H^{****}$ Right: geometry-optimized positions of the hydroxyl group forming hydrogen bonds along the tetrahedral edges.

Another kind of Si defect was introduced by the $Mg_{Si}^{''} + 2H^{**}$ defect type ($Mg_{Si}1$, Figures 3c and S5). Here, one Si located on the 8a tetrahedral site was replaced by a Mg atom and two protons. In contrast to the simple Si defect ($V_{Si}^{''''} + 4H^{****}$) the hydroxyl groups of the $Mg_{Si}^{''} + 2H^{**}$ defect type are forming hydrogen bonds (1.73 Å - 1.77 Å) along the edges shared by the 16d and 16c octahedra.

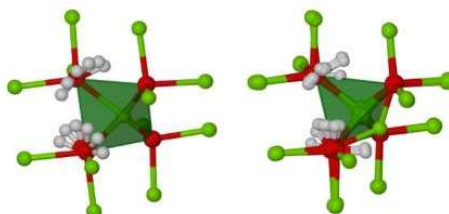


Figure S8: Left: multiple starting hydrogen positions of the hydroxyl groups for the defect type $Mg_{Si}^{''} + 2H^{**}$. Right: geometry-optimized positions of the hydroxyl group forming hydrogen bonds along between the 16d and the 16c octahedra.

In the case of the $Mg_{Si}^{''} + 2H^{**}$ defect type multiple hydrogen bond patterns with energy differences up to ~30 kJ/mol were simulated (Figure S8). Hereby three different types of hydrogen bonding could be clearly distinguished. In the first and energetically favoured case

the hydrogen bond is along the edges shared by the 16d and 16c octahedra and has a length of 1.71-1.78 Å. In the second case the hydrogen bond itself is also along these edges, but is less linear and almost bifurcated between two oxygens forming hydrogen bond lengths of about 1.83-2.03 Å. Here, the energy difference is between 3 kJ/mol and 13 kJ/mol depending not only on the orientation of the bifurcated hydrogen bond but also of the second hydroxyl group. In the third case the hydrogen bond of the hydroxyl group is along the tetrahedral edge. As a result the Mg atom is moving out of the center of the tetrahedron towards the vacant 16c octahedron. The hydrogen bond length along the tetrahedral edge is about 2.14 to 2.20 Å and the energy difference to the most stable structure simulated is about 9 kJ/mol and thus under the synthesis conditions easily accessible.

Three different coupled Mg defects of the type $V_{2Mg} + 4H$ were created by the removal of two neighboring Mg atoms and adding four protons around the resulting vacancies (Figures 3d and S9). Hereby always two protons were placed close to the oxygen atoms of the sharing edge between the vacancies since a higher partial charge of those oxygen atoms is expected. By variation of the other two protons in the vacant 16d and 16c octahedra around the vacancies three different models were evaluated. In all three cases the hydroxyl groups form hydrogen bonds along the O-O edge between the 16d and 16c octahedra, as in the case of isolated vacancies ($V_{Mg} + 2H$). Hereby the hydrogen bond lengths is varying between 1.52 and 2.05 Å. One extremely short hydrogen bond of 1.38 Å does not seem to be realistic and was no further taken into account. The slightly shorter hydrogen bonds in comparison to the isolated Mg defect can be explained by greater distortions in the structure being possible due to the coupled defects.

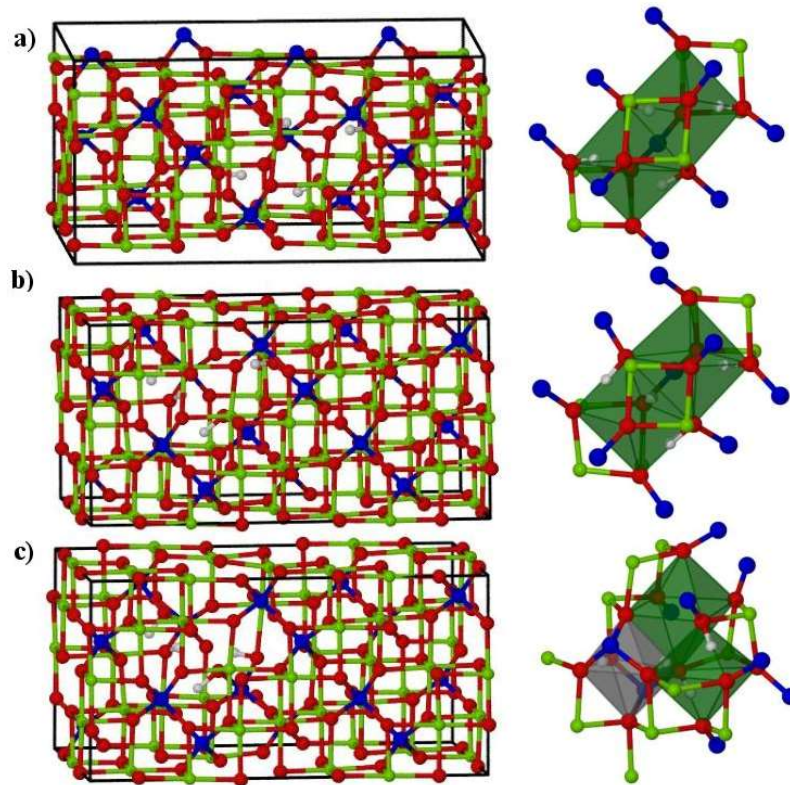


Figure S9: Coupled Mg defects of the type $V_{2Mg}^{4-} + 4H^{2+}$ with three different proton configurations (a) Mg2_1; b) Mg2_2; c) Mg2_3). The geometry-optimized structure is shown left, while the local coordination of the defect site is shown on the right side. The vacant 16d octahedra are shown in green, while the vacant 16c octahedron is shown in grey.

Furthermore, five coupled and mixed defect structures with Si and Mg vacancies were considered. This way hydroxyl groups with significantly different cation environment and thus chemical shift in one single defect can be realized and investigated. Here, models with six-coordinated Si atoms ($Mg_{Si}^{2-} + Si_{Mg}^{2+} + V_{Mg}^{2-} + 2H^{2+}$, $Mg_{Si}-Si_{Mg}-Mg_{1-2}$, Figures 3f and S11), according to models of previous work of Blanchard et al.⁶ and without ^{VI}Si atoms ($Mg_{Si}V_{Mg}^{4-} + 4H^{2+}$; $Mg_{Si}-Mg_{1-3}$, Figures 3e and S10) can be differentiated.

The latter can be described by local cation disorder with a four-coordinated Mg cation on the 8a site directly connected to a vacant 16d site which is normally occupied by magnesium. This nominally corresponds to a Si defect. The oxygen atom connecting the defects is carrying the highest partial charge in these models and is therefore always forming a hydroxyl group. The configuration of the other three protons needed for charge balance, was varied (Figure S10) resulting in three different models.

All hydroxyl groups of these models, both of the $V_{Mg}^{2-} + 2H^{2+}$ type, as well as the $Mg_{Si}^{2-} + 2H^{2+}$ type, are forming hydrogen bonds along the edges between the 16d and 16c octahedra. The hydrogen bond length is varying between 1.71 and 1.81 Å for the hydroxyl groups located in the Mg vacancy (2x Mg and 1x Si cation environment), 1.72 and 1.83 Å for the hydroxyl groups of the $Mg_{Si}^{2-} + 2H^{2+}$ type (4x Mg cation environment) and between 1.81 and 2.03 Å for the hydroxyl group located on the connecting oxygen atom (3x Mg cation environment).

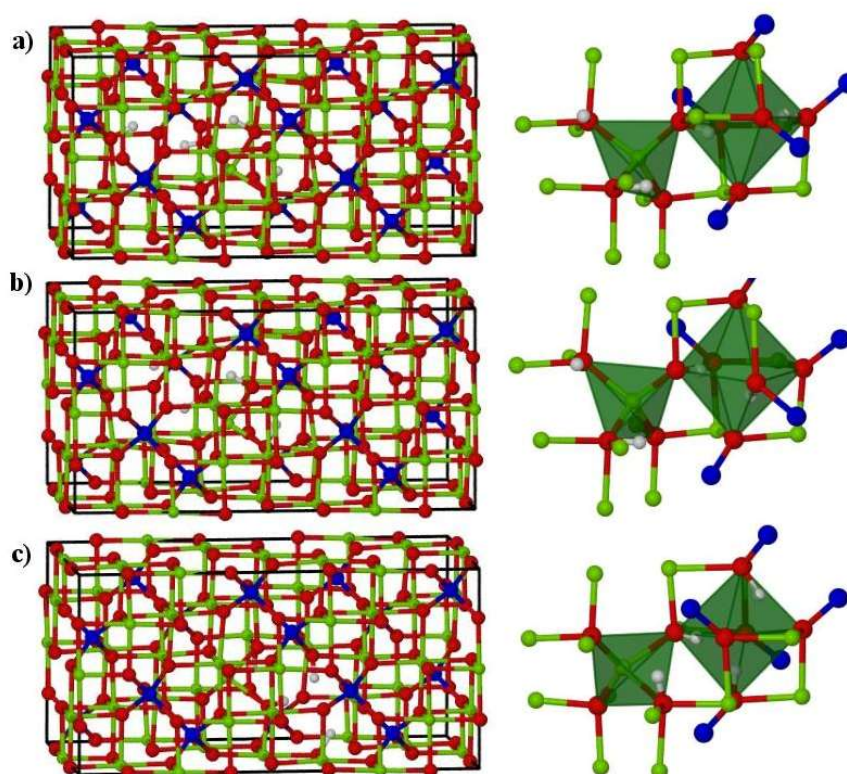


Figure S10: Coupled mixed defects of the type $Mg_{Si}V_{Mg} + 4H^{*}$ with three different proton configurations (a) $Mg_{Si}-Mg_1$; b) $Mg_{Si}-Mg_2$; c) $Mg_{Si}-Mg_3$). The geometry-optimized structure is shown left, while the local coordination of the defect site is shown on the right side.

Models with a local cation disorder with VI Si species ($Mg_{Si} + Si_{Mg} + V_{Mg} + 2H^{*}$) are shown in Figures 3f and S11. Here cation disorder between Mg and Si (16d and 8a site) connected to a Mg vacancy, thus a vacant 16d octahedron, was modelled. Again the cornersharing oxygen connecting the Mg_{Si} site with the vacant 16d site, is protonated because of its high partial charge. The other proton is located in the vacant 16d site. Both hydroxyl groups of each model form hydrogen bonds along the edge shared by the 16d and 16c octahedra with bond lengths between 1.63 and 1.93 Å, whereby the local cation environment doesn't seem to influence the bond length significantly.

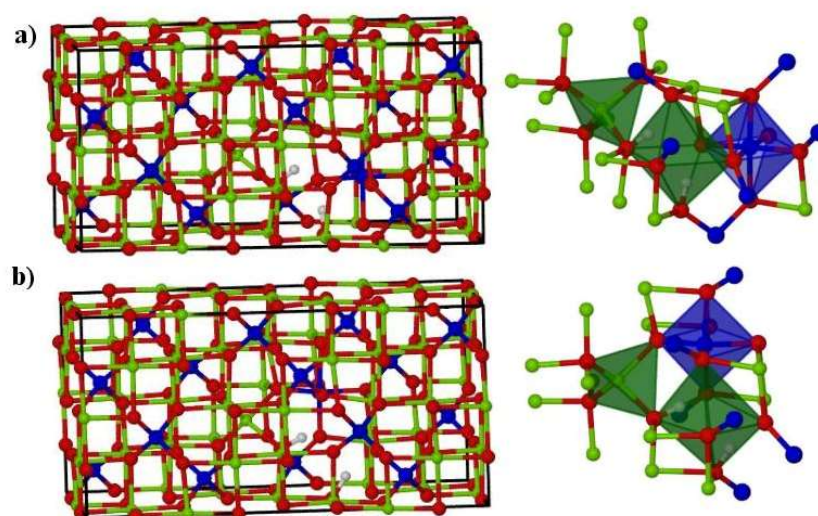


Figure S11: Coupled mixed defects of the type $Mg_{Si}'' + Si_{Mg}'' + V_{Mg}'' + 2H^{**}$ in two different configurations (a) $Mg_{Si}-Si_{Mg}-Mg_1$; b) $Mg_{Si}-Si_{Mg}-Mg_2$). The geometry-optimized structure is shown left, while the local coordination of the defect site is shown on the right side.

The calculated ^{29}Si chemical shifts grouped by the nearest hydrogen environment and the calculated 1H chemical shift, hydrogen bond length and cation environment of the hydroxyl groups of all the different fully geometry-optimized models are summarized in Tables S3 and S4, respectively.

The calculated 1H chemical shifts, the respective $OH \cdots O$ bond length and the energy difference of multiple proton configurations of the isolated models $V_{Mg}'' + 2H^{**}$, $Mg_{Si}' + 2H^{**}$ and $V_{Si}'''' + 2H^{****}$, shown in Figures S6-8, are listed in Tables S5-7, respectively.

Table S3: Calculated ^{29}Si chemical shift grouped by the closest hydrogen environment for the fully geometry-optimized hydrous defect models (Figure 3a-f).

<i>model</i>	<i>Defect type</i>	$\delta (^{29}\text{Si-OH})$ / ppm	$\delta (^{29}\text{Si}\cdots\text{OH})$ / ppm	$\delta (^{29}\text{Si-O})$ / ppm	$\delta (^{29}\text{Si-O})$ / ppm	
<i>Mg1</i>	$\text{V}_{\text{Mg}}'' + 2\text{H}^{**}$		-80.38			
				-80.38		
			-78.89	-80.39	-81.53	
			-78.89	-80.37	-81.53	-
			-78.89	-80.38	-81.52	
			-78.89	-80.39	-81.52	
<i>Si1</i>	$\text{V}_{\text{Si}}'''' + 4\text{H}^{****}$			-80.38		
				-80.38		
					-81.11	
					-81.77	
					-81.87	
					-81.28	
					-81.99	
					-82.06	
					-81.86	
					-81.94	
					-81.51	
					-80.79	
			-81.30			
			-81.98			
			-81.91			
			-82.08			
			-82.00			
<i>Mg_{Si}1</i>	$\text{Mg}_{\text{Si}}'' + 2\text{H}^{**}$			-81.14		
				-81.67		
				-81.72		
				-81.21		
				-81.69		
				-82.17		
				-81.85		
				-81.01		
				-80.38		
				-81.21		
				-82.03		
				-81.68		
		-81.89				
		-81.85				
<i>Mg2_1</i>	$\text{V}_{2\text{Mg}}'''' + 4\text{H}^{****}$			-80.99		
				-81.59		
			-78.60	-78.91	-81.61	
			-78.49	-79.22	-81.87	
			-77.53	-78.67	-81.07	
			-76.98	-78.5	-81.66	
			-81.64			
			-81.51			
<i>Mg2_2</i>	$\text{V}_{2\text{Mg}}'''' + 4\text{H}^{****}$			-81.73		
				-81.46		
				-81.77		
			-78.32	-78.68	-81.85	
			-78.56	-77.96	-81.02	
			-76.36	-78.15	-81.59	
	-76.54		-81.29			
			-81.51			
			-81.53			

<i>model</i>	<i>Defect type</i>	$\delta (^{29}\text{Si-OH})$ / ppm	$\delta (^{29}\text{Si}\cdots\text{OH})$ / ppm	$\delta (^{29}\text{Si-O})$ / ppm	$\delta (^{29}\text{Si-O})$ / ppm
<i>Mg2_3</i>	$\text{V}_{2\text{Mg}}^{\text{---}} + 4\text{H}^{\text{---}}$	-78.15 -76.08	-78.56 -77.53	-81.42 -81.72 -82.08 -81.67 -81.97 -81.29 -81.75 -81.48 -81.23 -81.36 -81.44	-
<i>Mg_{Si}⁻ Mg_1</i>	$\text{Mg}_{\text{Si}}\text{V}_{\text{Mg}}^{\text{---}} + 4\text{H}^{\text{---}}$	-79.09	-80.48 -80.28 -78.57	-80.71 -81.35 -80.78 -81.30 -81.62 -81.97 -82.03 -81.04 -81.15 -81.84 -80.39	-
<i>Mg_{Si}⁻ Mg_2</i>	$\text{Mg}_{\text{Si}}\text{V}_{\text{Mg}}^{\text{---}} + 4\text{H}^{\text{---}}$	-78.48	-79.78 -80.58	-80.81 -81.75 -81.45 -81.40 -81.78 -82.11 -81.90 -81.02 -81.64 -81.63 -80.18	-
<i>Mg_{Si}⁻ Mg_3</i>	$\text{Mg}_{\text{Si}}\text{V}_{\text{Mg}}^{\text{---}} + 4\text{H}^{\text{---}}$	-79.06 -77.81	-79.00 -78.34 -79.16	-81.55 -81.62 -81.40 -80.27 -81.97 -81.17 -80.94 -81.20 -80.98 -81.79 -81.94	-
<i>Mg_{Si}⁻-Si_{Mg}⁻ Mg_1</i>	$\text{Mg}_{\text{Si}}^{\text{--}} + \text{Si}_{\text{Mg}}^{\text{--}} + \text{V}_{\text{Mg}}^{\text{--}} + 2\text{H}^{\text{--}}$	-81.47	-80.87 -85.61	-81.30 -81.59 -80.83 -81.62 -82.68 -82.03 -81.94 -82.29 -83.84 -83.06 -85.09 -85.61 -82.55 -81.47	-173.57

<i>model</i>	<i>Defect type</i>	$\delta (^{IV}Si-OH)$ / ppm	$\delta (^{IV}Si\cdots OH)$ / ppm	$\delta (^{IV}Si-O)$ / ppm	$\delta (^{VI}Si-O)$ / ppm
<i>Mg_{Si}-Si_{Mg}⁻</i> <i>Mg_2</i>	$Mg_{Si}^{\cdot\cdot} + Si_{Mg}^{**}$ $+ V_{Mg}^{\cdot\cdot} + 2H^{**}$	-78.91	-78.79	-81.66	-166.83
				-80.93	
				-81.47	
				-80.49	
				-81.45	
				-82.19	
				-81.73	
				-81.93	
				-82.09	
				-84.41	
				-83.71	
				-85.17	
-78.91					
-82.62					

Table S4: Calculated ^1H chemical shift, hydrogen bond length and cation environment of the hydroxyl groups of the different fully geometry-optimized hydrous defect models in the structure of ringwoodite.

<i>model</i>	<i>Defect type</i>	<i>N (H)</i>	<i>Cat.env.</i> δH_1 (<i>OH...O length</i>)	<i>Cat.env.</i> δH_2 (<i>OH...O length</i>)	<i>Cat.env.</i> δH_3 (<i>OH...O length</i>)	<i>Cat.env.</i> δH_4 (<i>OH...O length</i>)
<i>Mg1</i>	$V_{\text{Mg}}^{\prime\prime} + 2\text{H}^{**}$	4	2x Mg; 1x Si 7.32 ppm (2.04 Å)			
<i>Si1</i>	$V_{\text{Si}}^{\prime\prime\prime} + 4\text{H}^{*****}$	4	3x Mg -0.31 ppm (2.46 Å)	3x Mg 1.76 ppm (2.14 Å)	3x Mg 1.46 ppm (2.15 Å)	3x Mg 1.77 ppm (2.10 Å)
<i>Mg_{Si}1</i>	$Mg_{\text{Si}}^{\prime\prime} + 2\text{H}^{**}$	4	4x Mg 5.48 ppm (1.73 Å)	4x Mg 5.19 ppm (1.75 Å)	4x Mg 4.98 ppm (1.76 Å)	4x Mg 4.65 ppm (1.77 Å)
<i>Mg2_1</i>	$V_{2\text{Mg}}^{\prime\prime\prime} + 4\text{H}^{*****}$	4	1x Mg; 1x Si 8.13 ppm (1.75 Å)	1x Mg; 1x Si 8.02 ppm (1.80 Å)	2x Mg; 1x Si 11.77 ppm (1.60 Å)	2x Mg; 1x Si 10.51 ppm (1.67 Å)
<i>Mg2_2</i>	$V_{2\text{Mg}}^{\prime\prime\prime} + 4\text{H}^{*****}$	4	2x Mg; 1x Si 11.20 ppm (1.63 Å)	1x Mg; 1x Si 11.09 ppm (1.54 Å)	1x Mg; 1x Si 11.92 ppm (1.52 Å)	2x Mg; 1x Si 6.14 (2.05 Å)
<i>Mg2_3</i>	$V_{2\text{Mg}}^{\prime\prime\prime} + 4\text{H}^{*****}$	4	1x Mg; 1x Si 10.86 ppm (1.55 Å)	1x Mg; 1x Si 15.30 ppm (1.38 Å)	2x Mg; 1x Si 10.95 ppm (1.59 Å)	2x Mg; 1x Si 6.28 ppm (1.98 Å)
<i>Mg_{Si}-Mg_1</i>	$Mg_{\text{Si}}V_{\text{Mg}}^{\prime\prime\prime\prime} + 4\text{H}^{*****}$	4	3x Mg 3.4 ppm (2.03 Å)	4x Mg 5.43 ppm (1.76 Å)	4x Mg 5.75 ppm (1.74 Å)	2x Mg; 1x Si 9.40 ppm (1.73 Å)
<i>Mg_{Si}-Mg_2</i>	$Mg_{\text{Si}}V_{\text{Mg}}^{\prime\prime\prime\prime} + 4\text{H}^{*****}$	4	3x Mg 4.71 ppm (1.88 Å)	2x Mg; 1x Si 8.14 ppm (1.81 Å)	4x Mg 5.42 ppm (1.74 Å)	4x Mg 6.25 ppm (1.72 Å)
<i>Mg_{Si}-Mg_3</i>	$Mg_{\text{Si}}V_{\text{Mg}}^{\prime\prime\prime\prime} + 4\text{H}^{*****}$	4	2x Mg; 1x Si 9.37 ppm (1.71 Å)	2x Mg; 1x Si 9.52 ppm (1.72 Å)	4x Mg 4.26 ppm (1.83 Å)	3x Mg 4.57 ppm (1.81 Å)
<i>Mg_{Si}-Si_{Mg}-Mg_1</i>	$Mg_{\text{Si}}^{\prime\prime} + \text{Si}_{\text{Mg}}^{**} + V_{\text{Mg}}^{\prime\prime} + 2\text{H}^{**}$	2	3x Mg 4.57 ppm (1.80 Å)	2x Mg; 1x Si 7.51 ppm (1.86 Å)	-	-
<i>Mg_{Si}-Si_{Mg}-Mg_2</i>	$Mg_{\text{Si}}^{\prime\prime} + \text{Si}_{\text{Mg}}^{**} + V_{\text{Mg}}^{\prime\prime} + 2\text{H}^{**}$	2	3x Mg 3.00 ppm (1.93 Å)	2x Mg; 1x Si 10.69 ppm (1.63 Å)	-	-

Table S5: Calculated hydrogen bond length and ^1H chemical shift of the hydroxyl groups, as well as relative energies of the multiple proton configurations of the model Mg1 ($V_{\text{Mg}}^{2+} + 2\text{H}^{*}$). The cation environment of all the hydroxyl groups is 2x Mg and 1x Si.

Proton conf. No.	$r(\text{OH}\dots\text{O})$ H1 / Å	δ (H1) / ppm	$r(\text{OH}\dots\text{O})$ H2 / Å	δ (H2) / ppm	ΔE / kJ/mol
1	1.75	9.04	1.69	9.81	2.32
2	1.74	9.06	1.72	9.36	2.25
3	1.73	9.22	1.77	8.74	2.40
4	1.72	9.33	1.93	7.49	3.59
5	1.67	10.14	1.68	9.99	0.02
6	1.70	9.61	1.70	9.62	0.25
7	1.72	9.31	1.73	9.22	2.17
8	1.73	9.27	1.70	9.68	2.21
9	1.74	9.10	1.69	9.85	2.28
10	1.70	9.70	1.75	9.07	2.28
11	1.68	10.03	1.68	10.04	0.03
12	1.68	10.02	1.67	10.11	0.00
13	1.68	9.94	1.69	9.84	0.05
14	1.68	9.97	1.67	10.09	0.00
15	1.69	9.82	1.65	10.43	0.14
16	1.68	10.06	1.68	10.04	0.07
17	1.72	9.38	1.72	9.43	2.17
18	1.93	7.49	1.72	9.33	3.60
19	1.68	9.92	1.68	10.01	0.04
20	1.70	9.69	1.68	9.92	0.12
21	1.68	9.92	1.68	9.92	0.10
22	1.66	10.33	1.68	9.93	0.07
23	1.72	9.44	1.72	9.37	2.16
24	1.77	8.74	1.73	9.23	2.39
25	1.70	9.76	1.67	10.12	0.15
26	1.70	9.76	1.70	9.75	0.17
27	1.68	9.92	1.70	9.69	0.12
29	1.67	10.11	1.68	10.01	0.02
30	1.74	9.37	1.72	9.07	2.25
31	1.67	10.10	1.67	10.10	0.12
32	1.67	10.12	1.70	9.75	0.15
33	1.68	10.01	1.68	9.92	0.04
34	1.69	9.84	1.68	9.93	0.06
35	1.73	9.22	1.72	9.34	2.16
36	1.69	9.81	1.75	9.04	2.32

Table S6: Calculated hydrogen bond length and ^1H chemical shift of the hydroxyl groups, as well as relative energies of the multiple proton configurations of the model $\text{Mg}_{\text{Si}1}$ ($\text{Mg}_{\text{Si}1}^{2+} + 2\text{H}^{**}$). The cation environment of all the hydroxyl groups is $4x$ Mg.

Proton conf. No.	$r(\text{OH}\dots\text{O})$ H1 / Å	δ (H1) / ppm	$r(\text{OH}\dots\text{O})$ H2 / Å	δ (H2) / ppm	ΔE / kJ/mol
1	1.75	4.62	1.75	5.43	11.20
2	1.74	4.84	1.77	5.17	11.56
3	1.73	5.04	1.72	5.86	10.61
4	1.73	4.89	1.72	5.85	10.74
5	1.67	6.24	1.68	6.11	29.59
6	1.68	6.14	1.67	6.19	29.53
7	1.75	4.84	1.78	4.39	3.42
8	1.76	4.82	1.87	3.61	3.93
9	1.76	4.83	1.76	4.79	0.07
10	1.76	4.77	1.76	4.80	0.06
11	1.72	5.84	1.72	5.12	10.55
12	1.71	6.08	1.71	5.19	10.56
13	1.75	4.86	1.77	4.48	3.39
14	1.75	4.85	1.92	3.39	4.13
15	1.76	4.83	1.76	4.89	0.10
16	1.76	4.82	1.76	4.76	0.12
17	1.73	5.79	1.72	5.02	10.58
18	1.71	6.07	1.71	5.20	10.69
19	1.74	5.02	1.78	4.36	3.43
20	1.76	4.82	1.76	4.88	0.00
21	1.76	4.90	1.76	4.80	0.14
22	1.76	4.85	1.76	4.83	0.00
23	1.74	4.40	1.9	4.85	12.74
24	1.96	4.26	1.73	5.00	13.03
25	1.77	4.74	1.76	4.89	0.00
26	1.83	3.90	1.75	4.97	3.57
27	1.78	4.29	1.75	4.99	3.44
28	1.78	4.32	1.76	4.82	3.30
29	1.75	5.44	1.75	4.68	11.14
30	1.74	5.50	1.74	4.77	11.35
31	1.75	4.80	1.74	5.08	2.61
32	1.75	4.81	1.75	5.00	2.58
33	1.77	4.46	1.75	4.87	3.34
34	1.78	4.42	1.75	4.96	3.40
35	2.03	3.39	2.2	2.25	9.00
36	1.74	5.51	1.75	4.74	11.23

Table S7: Calculated hydrogen bond length and ^1H chemical shift of the hydroxyl groups, as well as relative energies of the multiple proton configurations of the model $\text{Si1} (\text{V}_{\text{Si}}'''+4\text{H}^{***})$. The cation environment of all the hydroxyl groups is $3x \text{Mg}$.

Proton conf. No.	$r(\text{OH}\dots\text{O})$ H1 / Å	$\delta(\text{H1})$ / ppm	$r(\text{OH}\dots\text{O})$ H2 / Å	$\delta(\text{H2})$ / ppm	$r(\text{OH}\dots\text{O})$ H3 / Å	$\delta(\text{H3})$ / ppm	$r(\text{OH}\dots\text{O})$ H4 / Å	$\delta(\text{H4})$ / ppm	$\Delta E /$ kJ/mol
1	2.16	0.86	2.14	0.73	2.09	1.99	2.33	0.94	0.41
2	2.22	0.21	2.11	1.29	2.08	2.02	2.22	1.28	0.07
3	2.37	-0.22	2.15	1.38	2.08	1.81	2.13	1.76	0.35
4	2.34	-0.19	2.18	1.35	2.08	1.62	2.10	1.95	0.31
5	2.24	0.10	2.10	1.22	2.08	1.33	2.23	2.05	0.12
6	2.16	0.61	2.30	1.02	2.16	0.94	2.08	1.97	0.28
7	2.22	0.63	2.14	0.81	2.09	1.91	2.34	0.91	0.76
8	2.27	-0.01	2.09	1.46	2.08	2.03	2.19	1.38	0.15
9	2.43	-0.29	2.12	1.63	2.09	1.74	2.10	1.90	0.40
10	2.33	-0.19	2.15	1.61	2.10	1.51	2.07	2.03	0.27
11	2.24	0.16	2.21	1.35	2.16	1.09	2.08	1.87	0.30
12	2.21	0.42	2.26	1.13	2.23	0.70	2.09	1.80	0.76
13	2.30	0.30	2.14	0.94	2.13	1.64	2.39	0.73	1.12
14	2.43	-0.21	2.08	1.64	2.10	1.88	2.16	1.43	0.26
15	2.43	-0.34	2.12	1.70	2.12	1.57	2.10	1.66	0.29
16	2.34	-0.14	2.14	1.75	2.15	1.37	2.07	1.85	0.32
17	2.27	0.15	2.18	1.45	2.20	1.05	2.08	1.76	0.67
18	2.26	0.30	2.21	1.26	2.30	0.59	2.11	1.51	1.14
19	2.24	0.49	2.14	1.34	2.23	1.05	2.38	0.50	1.79
20	2.28	-0.02	2.07	1.95	2.18	1.50	2.12	1.36	0.22
21	2.33	-0.12	2.10	1.91	2.20	1.24	2.08	1.55	0.34
22	2.37	0.00	2.13	1.77	2.23	1.02	2.08	1.62	0.49
23	2.33	0.12	2.17	1.55	2.29	0.77	2.10	1.53	0.90
24	2.33	0.30	2.18	1.36	2.39	0.63	2.15	1.09	1.58
25	2.13	1.18	2.14	1.62	2.37	0.73	2.35	0.18	1.57
26	2.17	0.59	2.07	2.15	2.33	1.00	2.11	1.13	0.08
27	2.27	0.24	2.10	1.90	2.34	0.83	2.10	1.18	0.55
28	2.31	0.26	2.13	1.68	2.39	0.73	2.12	1.16	0.88
29	2.38	0.35	2.16	1.45	2.35	0.74	2.17	0.92	1.48
30	2.39	0.53	2.15	1.21	2.23	1.15	2.28	0.39	1.88
31	2.12	1.20	2.14	1.69	2.35	0.71	2.32	0.21	1.33
32	2.15	0.67	2.08	2.14	2.34	0.97	2.11	1.10	0.00
33	2.25	0.33	2.11	1.91	2.36	0.84	2.10	1.21	0.44
34	2.34	0.29	2.14	1.60	2.39	0.75	2.14	0.94	1.16
35	2.39	0.42	2.16	1.38	2.32	0.78	2.20	0.74	1.70
36	2.39	0.61	2.15	1.15	2.20	1.25	2.33	0.33	1.79

S5. References

- (1) Sasaki, S.; Prewitt, C. T.; Sato, Y.; Ito, E. *J. Geophys. Res.* **1982**, *87*, 7829.
- (2) Ross, N. L.; Shu, J.-F.; Hazen, R. M.; Gasparik, T. *Am. Mineral.* **1990**, *75* (7–8), 739.
- (3) Kahler, H. *Phys. Rev.* **1921**, *18*, 210.
- (4) Kristiansen, P. E.; Carravetta, M.; van Beek, J. D.; Lai, W. C.; Levitt, M. H. *J. Chem. Phys.* **2006**, *124* (23), 234510.
- (5) Kristiansen, P. E.; Mitchell, D. J.; Evans, J. N. S. *J. Magn. Reson.* **2002**, *157* (2), 253.
- (6) Blanchard, M.; Balan, E.; Wright, K. *Am. Mineral.* **2009**, *94*, 83.

4.2 Quantitative description of ^1H SQ and DQ coherences for the hydroxyl disorder within hydrous ringwoodite

This work is the result of a cooperation between the Inorganic Chemistry III and the Bavarian Research Institute of Experimental Geochemistry and Geophysics (BGI) of the University of Bayreuth and will be reproduced from H. Grüninger, A. Schmutzler, R. Siegel, K. Armstrong, D. J. Frost, J. Senker, *Phys. Chem. Chem. Phys.* **2018**, 20, 15098-15105, with permission from the PCCP Owner Societies.

H. Grüninger and A. Schmutzler contributed equally.

My contributions are:

- conception and main authorship of the article
- implementation and measurement of homonuclear ^1H DQ buildup curves
- calculation and evaluation of MD DFT simulation runs
- simulation of all ensemble average ^1H DQ buildup curves
- evaluation of all NMR data and simulations

The contribution of all other authors are:

- conception and co-authorship of the article
- high-pressure synthesis of the sample
- conception and implementation of the joint cost function for the refinement
- support of NMR measurements



PCCP

PAPER

View Article Online

View Journal | View Issue



Cite this: *Phys. Chem. Chem. Phys.*,
2018, 20, 15098

Quantitative description of ^1H SQ and DQ coherences for the hydroxyl disorder within ringwoodite[†]

Helen Grüninger,^a Adrian Schmutzler,^a Renée Siegel,^a Katherine Armstrong,^b Daniel J. Frost^b and Jürgen Senker^{b,*}

Proton-containing point defects in solid materials are important for a variety of properties ranging from ionic transport over thermal conductivity up to compressibility. Ultrafast magic-angle spinning techniques nowadays offer high-resolution solid-state NMR spectra, even for ^1H , and thus open up possibilities to study the underlying defect chemistry. Nevertheless, disorder within such defects again leads to heavy spectral overlap of ^1H resonances, which prevents quantitative analysis of defect concentrations, if several defect types are present. Here, we present a strategy to overcome this limitation by simulating the ^1H lineshape as well as ^1H – ^1H double-quantum buildup curves, which we then validate against the experimental data in a joint cost function. To mimic the local structural disorder, we use molecular dynamics simulations at the DFT level. It turned out to be advantageous for the joint refinement to put the computational effort into the structural optimisation to derive accurate proton positions and to use empirical correlations for the relation between isotropic and anisotropic ^1H chemical shifts and structural elements. The expressiveness of this approach is demonstrated on ringwoodite's ($\gamma\text{-Mg}_2\text{SiO}_4$) OH defect chemistry containing four different defect types in octahedral and tetrahedral voids with both pure Mg and mixed Si and Mg cation environments. Still, we determine the ratio for each defect type with an accuracy of about 5% as a result of the minimization of the joint cost function. We expect that our approach is generally applicable for local proton disorder and might prove to be a valuable alternative to the established AIRSS and Monte Carlo methods, respectively.

Received 6th February 2018,
Accepted 2nd May 2018

DOI: 10.1039/c8cp00863a

rsc.li/pccp

Introduction

Weak secondary interactions, such as hydrogen bonds, significantly influence structural and thus chemical and physical properties of materials. They are especially important for chemical and biological processes like folding of proteins,^{1,2} self-assembly in supramolecular chemistry,³ or proton conducting materials.^{4,5} Inherently hydrogen bond patterns often exhibit a high degree of disorder, which impacts on the material properties.

Crystal structures are routinely examined by X-ray diffraction techniques, for which localizing hydrogen atoms is usually difficult, in particular, if no single crystals are available or if the hydrogen atoms are disordered.^{6,7} Complementary information might be provided by spectroscopic methods, like IR or Raman spectroscopy,^{8,9} which allow one to probe the strength of hydrogen bonds.

Alternatively, diffraction techniques have been combined with solid-state NMR spectroscopy (ssNMR).^{10–13} In particular, for hydrogen bond interactions this appears to be promising, since ^1H chemical shifts are easy to measure and sensitive to local environments. ssNMR is independent of long-range order, and thus provides complementary information about disorder compared to diffraction techniques. ^1H NMR data give access to the number of inequivalent sites, homo- and heteronuclear connectivities, as well as distances, if an assignment of the resonances was achieved in advance.^{10,11,14–18} The assignment usually is aided by quantum-mechanical (QM) calculations of NMR parameters of structural models at the DFT level.^{10,11,19–24} The combination of these techniques was very successful and the term NMR crystallography was introduced.^{10–13,25–27}

For ^1H ssNMR very strong dipolar couplings and a small spread of chemical shifts lead to heavy overlap of ^1H resonances, which makes an unambiguous assignment challenging. Even with the use of ultrafast magic-angle spinning (MAS) and high power decoupling, which effectively average anisotropic broadening of resonances in order to yield better resolution,^{16,28–30} the ^1H lineshape of high-resolution spectra often show a strong overlap due to disorder.^{19–21} In such cases, QM calculations

^a *Anorganische Chemie III, University of Bayreuth, Universitätsstr. 30, 95447 Bayreuth, Germany. E-mail: juergen.senker@uni-bayreuth.de*

^b *Bayerisches Geo-Institut, University of Bayreuth, Universitätsstr. 30, 95447 Bayreuth, Germany*

[†] Electronic supplementary information (ESI) available. See DOI: 10.1039/c8cp00863a

become even more important to model the observed spectral lineshape. However, in order to treat the disorder, multiple initial models with slight changes in their local environment have to be considered. This leads to a large number of possible models and thus to high computational costs. Therefore, other methods have been developed, such as *ab initio* random structure searching³¹ (AIRSS) or simulated annealing³² (SA), the latter using the Monte Carlo (MC) algorithm.³³ Both techniques probe the potential energy surface of the system of interest. At fundamental level they provide the global minimum structure, but may also be used to gain information about local minima. Both approaches can handle virtually random structures and are particularly useful for unknown systems, since they can be used for structure prediction due to their large degrees of freedom. Main drawbacks of the MC runs are the accuracy of the calculations since they usually rely on empirical potentials, they may easily get stuck in local minima, and NMR parameters are not directly accessible. Since the AIRSS method is based on DFT, it overcomes the latter problem, and has a much higher accuracy, but without restraints is restricted to a few tens of atoms.³¹ Introducing structural restraints, such as unit cell sizes, bonding environments or prearranged groups of atoms or molecules, significantly decreases the dimension of the energy surface and thus allows for a more accurate investigation of the local structural disorder of complex systems in a decent time frame.^{19,31} Such restraints within AIRSS enabled a detailed study of the hydrogen substructure of hydrous defects in the high-pressure silicate wadsleyite.¹⁹

For cases, like hydrous ringwoodite, where the OH defect types are already known,²¹ we here explore an alternative approach to model the influence of displacive proton disorder on the spectral lineshapes of NMR spectra, finally leading to a quantification of defect concentrations. In such cases, only parts of the energy hypersurface around distinct local minima of the defects need to be probed, which represents such a confined variable space that random AIRSS or MC runs are not beneficiary, but MD DFT simulations might be better suited. The resulting structures are validated by two complementary cost functions: ¹H–¹H distances and ¹H chemical shifts. While the latter is used to model footprints of the ¹H MAS NMR lineshape, proton distance relations allow for predicting ¹H–¹H DQ buildup curves. We explore the possibility to combine both NMR observables in a joint fashion. To keep the computational cost at a reasonable level and still sample the energy hypersurface finely enough to reproduce the characteristic features of the disorder for both NMR observables, we calculated the structure at the DFT level and then used well-established empirical correlations between chemical shifts and structural elements^{19,21,34–38} to link proton environments to the ¹H chemical shift interaction.

The starting point of our investigations are DFT optimized minimum structures of the defect models. In order to account for expected disorder due *e.g.* to thermal fluctuations, we run *ab initio* molecular dynamics simulations at the DFT level (MD DFT). This method offers the possibility of chemical bond-breaking and forming events during the simulation run. Furthermore, it allows one to start from one initial state, which

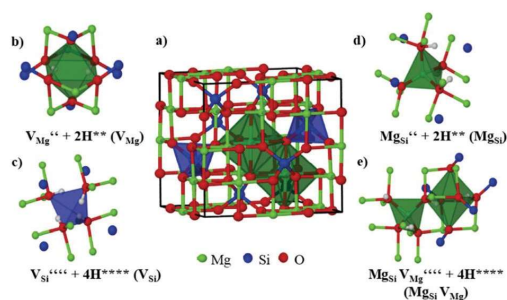


Fig. 1 (a) Spinel-type crystal structure (space group $Fd\bar{3}m$) of anhydrous ringwoodite consisting of isolated SiO_4 tetrahedra and edge-sharing MgO_6 octahedra and (b–e) different defect types in hydrous ringwoodite. (b) Isolated Mg vacancy; (c) isolated Si vacancy charge balanced by four protons; (d) isolated Si vacancy charge balanced by one Mg^{2+} and two protons; (e) coupled defect with an octahedral vacancy and one Mg^{2+} on a Si site.

then evolves according to the basic laws of physics without the need of further experimental inputs.³⁹ Another advantage of the MD runs is that the resulting structures are inherently weighted by Boltzmann's factor, which in principal allows us to directly compare the results to experimental data by adjusting the simulation temperature to the energy spread of the explored hypersurface. The applicability of MD DFT simulations for proton disorder was already shown for the exploration of the hydrogen sublattice in $\text{Mg}(\text{OH})_2$ and $\text{Ca}(\text{OH})_2$ under external pressure,⁴⁰ and the radiation-induced formation of H_2^* defects in crystalline silicon.⁴¹

We demonstrate this approach on the hydroxyl disorder within hydrous ringwoodite, $\gamma\text{-Mg}_2\text{SiO}_4$ (Fig. 1), for which we previously studied its OH defect chemistry.²¹ Although we were able to distinguish four different defect types including isolated and coupled Mg and Si vacancies ($V_{\text{Mg}}^{2+} + 2\text{H}^{**}$, $V_{\text{Si}}^{4+} + 4\text{H}^{****}$, $\text{Mg}_{\text{Si}}^{2+} + 2\text{H}^{**}$ and $\text{Mg}_{\text{Si}} V_{\text{Mg}}^{2+} + 4\text{H}^{****}$, Fig. 1b–e), the heavy overlap of the ¹H resonances on the 1D NMR spectra prevented the determination of defect concentrations.²¹

Experimental

Synthesis

The synthesis of the hydrous ringwoodite sample studied in this work is given in ref. 21.

Solid-state NMR spectroscopy

Solid-state NMR spectroscopic experiments were performed using a Bruker Avance III spectrometer operating at a magnetic field strength of 14.1 T, corresponding to a ¹H Larmor frequency of 600.1 MHz. All experiments were performed using a Bruker 1.9 mm triple resonance probe spinning the sample at an MAS frequency of 40.0 kHz, unless otherwise stated.

For ¹H measurements spin-echoes were used to reduce the background signals from the probe. The interpulse delay was adjusted to 25 μs ($1 \nu_{\text{rot}}^{-1}$), 50 μs ($2 \nu_{\text{rot}}^{-1}$) and 75 μs ($3 \nu_{\text{rot}}^{-1}$) to suppress probe ringing and background. The recycle delay was

set to 3.0 s. 1D ^1H double-quantum (DQ) buildup curves were recorded using the DQ recoupling sequence R18_8^5 with an S_0S_π supercycle ($\nu(^1\text{H}) \sim 90$ kHz), which maintains γ -encoding of the sequence.^{42,43} The excitation time was incremented in steps of 22.22 μs , corresponding to one RR' block, until a maximum excitation time of 511 μs was reached. The recycle delay was set to 2.5 s. The DQ buildup curves were recorded following the symmetric protocol with a complementary spin echo after the DQ block in order to reduce the background effects of the probe ("DQ excitation–DQ reconversion–spin echo–acquisition"). Zero-quantum (ZQ) reference measurements were used for a normalisation of the DQ buildup curves (eqn (1)).⁴⁴

$$\text{DQeff.} : I_{\text{DQ}}^{\text{norm.}}(t_{\text{exc.}}) = \frac{I_{\text{DQ}}(t_{\text{exc.}})}{I_{\text{ZQ}}(t_{\text{exc.}}) + I_{\text{DQ}}(t_{\text{exc.}})} \quad (1)$$

Computational methodology

MD DFT calculations. Molecular dynamics (MD) DFT calculations were carried out using the CASTEP DFT code (version 8.0),^{45–48} employing the GIPAW algorithm.²³ For all calculations, the generalized gradient approximation (GGA) PBE⁴⁹ functional with the semi-empirical dispersion correction Grimme06 was employed. The MD simulations were calculated using a planewave energy cut-off of 800 eV and a k -point spacing of 0.07 \AA^{-1} (Monkhorst–Pack grid, $2 \times 2 \times 2$) over the Brillouin zone, which is a good trade-off between accuracy and calculation time. The NVT ensemble with the Nosé–Hoover thermostat (MD_ion_t 1 ps), a temperature of 315 K and a time increment of 1 fs for each of the MD steps were used. For each model $\sim 10\,000$ MD steps were calculated in order to yield multiple defect models with varying hydrogen bond configurations. Initial atomic positions of the four hydrous defect models (Fig. 1), including isolated $V_{\text{Mg}}'' + 2\text{H}^{**}$, $V_{\text{Si}}''' + 4\text{H}^{****}$ and $\text{Mg}_{\text{Si}}'' + 2\text{H}^{**}$ defects, as well as coupled $\text{Mg}_{\text{Si}}V_{\text{Mg}}''' + 4\text{H}^{****}$, were taken from a previous study on hydrous ringwoodite.²¹ The corresponding defects were placed in one single unit cell of ringwoodite.

Simulation of ^1H – ^1H DQ buildup curves. All ^1H – ^1H DQ buildup curves were simulated on the basis of the R18_8^5 supercycle with an S_0S_π supercycle ($\nu(^1\text{H}) \sim 90$ kHz) at a spin rate of 40 kHz, used experimentally, with the program SIMPSON.^{50–52} 232 ZCW (α , β) angles and 5 γ angles were found to be sufficient to generate the powder average. Hereby the chemical shift and anisotropy (Haeberlen–Mehring–Spiess convention as defined in SIMPSON^{50–52}) of the hydrogen atoms, as well as the dipolar coupling between all protons was taken into account resulting in two-spin systems ($V_{\text{Mg}}'' + 2\text{H}^{**}$; $\text{Mg}_{\text{Si}}'' + 2\text{H}^{**}$) and four-spin systems ($V_{\text{Si}}''' + 4\text{H}^{****}$; $\text{Mg}_{\text{Si}}V_{\text{Mg}}''' + 4\text{H}^{****}$). A representative SIMPSON input file is provided in the ESI† (Section 6).

Joint refinement. The fit of the simulated ^1H signals and the simulated ^1H – ^1H DQ buildup curves to the experimental findings using a joint cost function described by eqn (5) to (13) was implemented as a function in MatLab R2017b. The function was optimized using the MatLab tool lsqcurvefit based on the trust-region-reflective algorithm, with the weighting factors v_i (eqn (5)) as variable coefficients. lsqcurvefit minimizes the squared 2-norm of the residuals, *i.e.* the value m_{tot} in eqn (13). To provide error values,

we first obtained the covariance matrix for the optimized coefficients based on the output of lsqcurvefit. Then, uncertainty propagation through eqn (6) and (7) was performed, finally obtaining error margins for the defect ratios.

Results and discussion

To allow for a quantitative description of ringwoodite's defect chemistry, the OH group disorder within the four hydrous defect types, V_{Mg} , V_{Si} , Mg_{Si} and $\text{Mg}_{\text{Si}}V_{\text{Mg}}$ (Fig. 1b–e), has to be modelled, since it is responsible for the strong superposition of resonances of the different defect types observed in the 1D ^1H MAS NMR spectrum of ringwoodite.²¹

By using MD DFT simulations of the previously determined minimum structures of the defect types (Fig. 1b–e), we obtain several thousands of reasonable models with slight changes in the proton configuration, *i.e.* different hydrogen bond strength and thus also varying ^1H – ^1H distances. While the hydrogen bond strength will strongly influence the electron density at the OH group and thus the isotropic chemical shift,²¹ varying ^1H – ^1H distances alter the homonuclear dipolar interaction and can quantitatively be investigated by double-quantum (DQ) buildup curves.^{53–55} Both experimental observables rely on different interactions, but both can be used to probe the positions of the OH groups.

In order to translate the position and orientation of the OH groups from the MD runs to experimental observables in a decent time frame, we used empirical correlations between structural elements and the ^1H chemical shift. Hereby, the main influence on the ^1H isotropic chemical shift of the hydroxyl groups is the first cation coordination sphere, which leads to a division of the experimental spectrum in a downfield region ($\delta > 6$ ppm) assigned to octahedral vacancies with OH groups in mixed Si and Mg environments and a highfield region ($\delta < 6$ ppm) resulting from Si vacancies with OH groups in pure Mg environments.²¹ Furthermore, the hydrogen bond strength leads to an additional downfield shift in each case, which is described by the following equations:²¹

$$\text{Si and Mg environments: } \delta_{\text{iso}}(^1\text{H}) = \frac{r(\text{OH} \cdots \text{O}) - 2.62}{-0.1} \quad (2)$$

$$\text{Mg environments: } \delta_{\text{iso}}(^1\text{H}) = \frac{r(\text{OH} \cdots \text{O}) - 2.33}{-0.1} \quad (3)$$

For the chemical shift anisotropy (Fig. S1, ESI†), which is essential for the evaluation of DQ buildup curves, we now derived an empirical correlation to the hydrogen bond length (Fig. 2) by evaluating the chemical shift anisotropy (CSA) of the protons within 477 representative snapshots of the MD DFT runs for all four hydrous defect types (Fig. 1b–e). For these the chemical shift tensors were additionally calculated at the DFT level. The resulting relation is given in eqn (4).

$$\delta_{\text{aniso}}(^1\text{H}) = a \cdot r(\text{OH} \cdots \text{O})^b + c \quad (4)$$

$$(a = -150 \pm 24(1), b = -5.79 \pm 0.355(1), c = -9.49 \pm 0.231(1)).$$

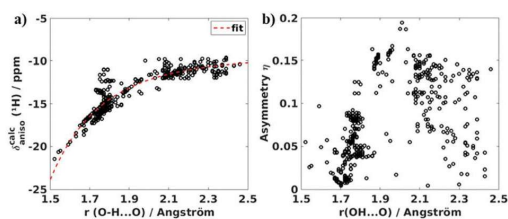


Fig. 2 (a) Correlation between calculated chemical shift anisotropy (Haebleren–Mehring–Spiess convention as implemented in SIMPSON^{50–52}) and hydrogen bond length of an OH group in ringwoodite. (b) Calculated asymmetry and the corresponding hydrogen bond length for 477 different models revealing no obvious correlation.

The calculated asymmetry of the CSA for all models is below 0.2 and shows no obvious dependency on the hydrogen bond strength (Fig. 2b). Therefore, it is assumed that the asymmetry will only have minor influence and was set to 0 for the evaluation of DQ buildup curves (Fig. S2 and Table S1, ESI[†]). The orientation of the *z* component of the CSA tensors was found to be aligned along the O–H bond.

First, we determined for each proton of each step of the MD simulations the ¹H isotropic chemical shift by eqn (2) and (3), respectively. In order to transfer these values to observable lineshapes for each calculated shift, individual ¹H resonances were convoluted using a pseudo-Voigt lineshape, a half width of 0.3 ppm and a Gaussian-to-Lorentzian ratio (*G/L*) of 0.5. By summing these over all 10 000 MD steps, the final lineshape of the individual ¹H signal for each defect type is obtained

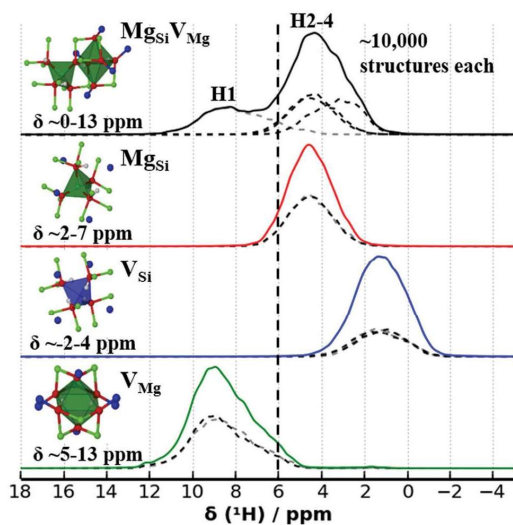


Fig. 3 Simulated ¹H signals of 10 000 MD steps for all OH groups of each hydrous defect type in ringwoodite. The calculated spectra are divided into downfield ($\delta > 6$ ppm) and highfield ($\delta < 6$ ppm) regions according to OH groups in mixed Mg and Si and pure Mg environments, respectively. Exemplary proton positions from the MD runs for all defect types are given in Fig. S3 (ESI[†]).

Table 1 Summary of minimum and maximum simulated hydrogen bond lengths, calculated isotropic chemical shift regions, and maxima for each of the different hydrous defect types in ringwoodite

Model	Min. $r(\text{O}\cdots\text{HO})$ (Å)	Max. $r(\text{OH}\cdots\text{O})$ (Å)	Shift region (ppm)	Max. intensity (ppm)
V_{Mg}	1.32	2.19	4.3 to 12.4	9.0
V_{Si}	1.73	2.62	-2.5 to 5.2	1.3
Mg_{Si}	1.48	2.22	1.0 to 7.4	4.6
$\text{Mg}_{\text{Si}}V_{\text{Mg}}$	1.34	2.56	0.6 to 12.1	4.3/8.7

(Fig. 3 and Table 1). The isolated Mg and Si defects show strongly overlapping shift areas, each with a well-defined shape with a half width of ~ 7 ppm and a maximum intensity at 9.0 ppm (V_{Mg} , Fig. 3 green), 1.3 ppm (V_{Si} , Fig. 3 blue) and 4.6 ppm (Mg_{Si} , Fig. 3 red). In contrast, the mixed coupled defect ($\text{Mg}_{\text{Si}}V_{\text{Mg}}$, Fig. 3 black) exhibits high- and downfield shift regions with maxima at 4.3 (H2–H4) and 8.7 ppm (H1), respectively, due to the different cation environments of the OH groups within the defect. The hydroxyl group (H1) in the octahedral vacancy is bound to Mg and Si, while the other three (H2–H4) are in pure Mg environments (Fig. S3, ESI[†]).

In the following, the summed lineshape of the individual ¹H signals will be used in a refinement of the experimental 1D ¹H MAS NMR spin echo ($\tau = 2 \nu_{\text{rot}}^{-1} = 50 \mu\text{s}$) of ringwoodite (Fig. 4, black). This is reasonable, since the broad components of the experimental spectrum show similar lineshapes as function of the interpulse distance of spin-echo excitation (Fig. S4, ESI[†]). Therefore, we expect similar spin–spin relaxation times for all defect resonances.

For the second cost function, we used the ¹H–¹H distances of the MD run of each defect type by first simulating the individual average DQ buildup curve and a subsequent comparison to experimental findings. The experimental ¹H–¹H DQ buildup curves of ringwoodite (Fig. 5a and b, grey dots) were obtained using the R18_s⁵ sequence with an S_0S_π supercycle.

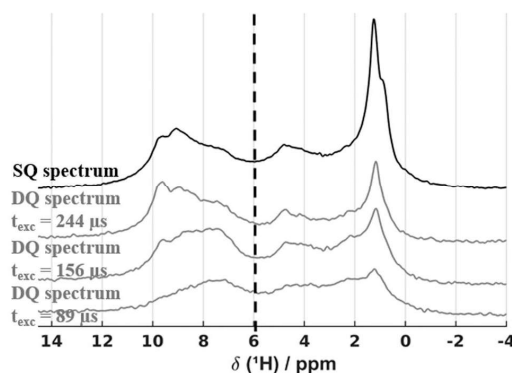


Fig. 4 Comparison of the 1D ¹H SQ MAS spin echo ($\tau = 2 \nu_{\text{rot}}^{-1} = 50 \mu\text{s}$, black) to 1D ¹H DQ MAS spectra (multiplied by a factor of 8 in comparison to the SQ spectrum) at excitation times t_{exc} of 89 μs , 156 μs and 244 μs (grey) of ringwoodite. The boundary at 6 ppm between the two isotropic chemical shift regions for the mixed Si and Mg environment ($\delta > 6$ ppm) and the pure Mg environment ($\delta < 6$ ppm) is depicted as a black dashed line. The DQ efficiencies of the two chemical shift regions are reported in Fig. 5 and 6.

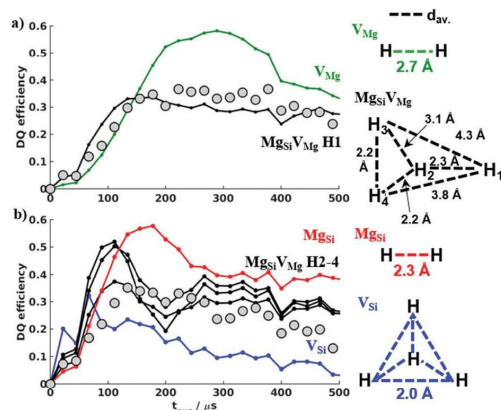


Fig. 5 (a) Experimentally measured ^1H - ^1H DQ buildup curve for the shift area above 6 ppm (grey dots) and the simulated ^1H - ^1H DQ buildup curves of an isolated Mg vacancy (V_{Mg} , green), as well as for the OH group in mixed Si and Mg environments (H1) of the mixed coupled defect ($V_{\text{Mg}}\text{MgSi}$, black). (b) Experimentally measured ^1H - ^1H DQ buildup curve for the shift area below 6 ppm (grey dots) and the simulated ^1H - ^1H DQ buildup curves of an isolated Si vacancy charge balanced by four protons (V_{Si} , blue), as well as the charge balanced by one Mg^{2+} and two protons (MgSi , red) and for the three OH groups in pure Mg environments (H2-H4) of the mixed coupled defect ($V_{\text{Mg}}\text{MgSi}$, black). The ^1H connectivities of each defect type and the corresponding ensemble average ^1H - ^1H distances (d_{av} , Table 2) of the MD runs are additionally depicted on the right side.

With this sequence, curves with a fast sampling with time increments of 22.22 μs could be recorded, which is mandatory to measure short distances, with a pulse power of ~ 100 kHz (MAS rate of 40 kHz). Additionally, the sequence exhibits a relatively small amount of second-order CSA cross terms promising a good CSA compensation.⁴³ The strong overlap of the ^1H signals of the defect types observed in the 1D ^1H SQ and DQ spectra (Fig. 4) in combination with a distribution of ^1H - ^1H distances results in averaging of 1D ^1H - ^1H DQ buildup curves. We rely on the previously established down- and highfield chemical shift regions²¹ with the boundary at 6 ppm to measure integral symmetric 1D ^1H - ^1H DQ buildup curves of protons around Mg and Si vacancies, respectively. The two resulting experimental curves are normalized according to eqn (1) and show maxima at t_{exc} of about 200 μs ($\delta > 6$ ppm) and 133 μs ($\delta < 6$ ppm), respectively. Both curves are strongly dampened to a maximum DQ efficiency below 0.4 (Fig. 5).

For each step of the MD simulations, the corresponding ^1H - ^1H DQ buildup curves were calculated including the full proton chemical shift tensors and all dipolar couplings of each proton in the model. In this way, the simulated ^1H - ^1H DQ buildup curves including the influence of possible second-order CSA and ICS terms were generated by creating the ensemble average by summing and normalizing over all 10 000 MD steps (Fig. S5-S7, ESI[†] and Table 2) for each defect type. Oscillations of the simulated curves, expected for isolated spin pairs, are averaged and as a consequence the curves are dampened (Fig. 5a and b). The simulated ^1H - ^1H DQ buildup curve of isolated Mg vacancies (Fig. 5a, green) increases to almost

Table 2 Summary of the minimum, maximum and average-simulated ^1H - ^1H distances, as well as the maximum of simulated ^1H - ^1H DQ buildup curves for each of the different hydrous defect types in ringwoodite

Model	Min. ^1H - ^1H distance (\AA)	Max. ^1H - ^1H distance (\AA)	Av. ^1H - ^1H distance (\AA)	Maximum (μs)
V_{Mg}	2.2	3.1	2.7	300
V_{Si}	1.5	2.7	2.0	67
MgSi	1.7	3.5	2.3	178
$\text{MgSi}V_{\text{Mg}}$ (H2-H4)	2.3 (H2-H3)	3.7 (H2-H3)	3.1 (H2-H3)	111
	1.7 (H2-H4)	3.0 (H2-H4)	2.2 (H2-H4)	
	1.6 (H3-H4)	2.7 (H3-H4)	2.2 (H3-H4)	
$\text{MgSi}V_{\text{Mg}}$ (H1)	1.7 (H1-H2)	2.9 (H1-H2)	2.3 (H1-H2)	156
	3.3 (H1-H3)	5.1 (H1-H3)	4.3 (H1-H3)	
	2.8 (H1-H4)	4.9 (H1-H4)	3.8 (H1-H4)	

0.6 in DQ efficiency with a broad maximum at $t_{\text{exc}} \sim 300$ μs , while the curve corresponding to the one OH group (H1) in mixed cation environments of the mixed coupled model ($\text{MgSi}V_{\text{Mg}}$, Fig. 5a, black) shows a faster buildup (maximum at $t_{\text{exc}} \sim 156$ μs) but is dampened to roughly 0.3 DQ efficiency due to dipolar truncation^{33,56} by other stronger dipolar couplings within the defect. The simulated ^1H - ^1H DQ buildup curves resulting from OH groups in pure Mg environment are shown in Fig. 5b. The isolated MgSi defect type gives a single simulated ^1H - ^1H DQ buildup curve with a maximum at $t_{\text{exc}} \sim 178$ μs and a maximum DQ efficiency close to 0.6 (Fig. 5b, red). For the mixed coupled defect ($\text{MgSi}V_{\text{Mg}}$), three curves for each OH group (H2/H3/H4) in Mg environments were calculated (Fig. 5b, black). They show a fast DQ buildup with maxima at $t_{\text{exc}} \sim 111$ μs dampened to DQ efficiencies of ~ 0.5 ($2 \times \text{H2/H4}$) and 0.4 (H3). In the case of the isolated Si vacancy charge balanced by four protons, all OH groups have the same cation environment, which allows not only to ensemble average over all MD steps but also over the four protons (Fig. 5b, blue). Here, the four-spin proton configuration leads to a simulated DQ buildup curve rising to a DQ efficiency of ~ 0.3 and then dropping rapidly below 0.1. However, none of the simulated individual ^1H - ^1H DQ buildup curves alone (Fig. 5a and b) fits the experimental data.

From the MD DFT simulations we derived the individual lineshapes of the ^1H signals (Fig. 3) and the individual ^1H - ^1H DQ buildup curves (Fig. 5) of the four OH defect types (V_{Mg} , V_{Si} , MgSi , and $\text{MgSi}V_{\text{Mg}}$). We now combine both observables in one approach to fit the experimental 1D ^1H SQ MAS NMR spectrum together with the experimental ^1H - ^1H DQ buildup curves using a joint cost function in order to gain a quantitative description of ringwoodite's defect chemistry.

In the first step, the experimental ^1H SQ spectrum \bar{S}^{exp} is fitted by the sum of the simulated ^1H signals \bar{S}_i^{sim} of all defect types i scaled by a variable factor v_i (eqn (5)).

$$\bar{S}^{\text{sum}} = \sum_i v_i \cdot \bar{S}_i^{\text{sim}} \quad (5)$$

Based on the scaling v_i of the ^1H signals, the relative integrals r_i of each defect type can be calculated (eqn (6)).

$$r_i = \frac{v_i \int \bar{S}_i^{\text{sim}} d\omega}{\sum_i v_i \int \bar{S}_i^{\text{sim}} d\omega} \quad (6)$$

Then, the relative integrals r_i are divided by the corresponding number of protons n_i in the defect type i and normalized. This results in the defect ratios d_i (eqn (7)).

$$d_i = \frac{r_i n_i^{-1}}{\sum_i r_i n_i^{-1}} \quad (7)$$

The quality parameter m_{spc} for the optimization is based on the squared 2-norm of the residual compared to the experimental data divided by the squared 2-norm of the experimental spectrum (eqn (8)).

$$m_{\text{spc}} = \frac{\sum_j \left[(\vec{S}^{\text{sum}})_j - (\vec{S}^{\text{exp}})_j \right]^2}{\sum_j (\vec{S}^{\text{exp}})_j^2} = \frac{\|\vec{S}^{\text{sum}} - \vec{S}^{\text{exp}}\|_2^2}{\|\vec{S}^{\text{exp}}\|_2^2} \quad (8)$$

Since the simulated ^1H - ^1H DQ buildup curves $\overrightarrow{\text{DQ}}_i^{\text{indiv.}}$ (Fig. 5) are inherently normalized for the individual defect types, but the experimental curves are averaged and normalized over the shift regions (eqn (1)) and thus contain DQ intensities of more than one defect type, scaling factors D_i^x of the individual ^1H - ^1H DQ buildup curves $\overrightarrow{\text{DQ}}_i^{\text{indiv.}}$ are calculated from the defect ratios d_i for the high shift (D_i^{HS} , $\delta > 6$ ppm) and low shift (D_i^{LS} , $\delta < 6$ ppm) regions (eqn (9) and (10)).

$$D_i^{\text{HS}} = \frac{d_i}{\sum_{i \in \text{HS}} d_i} \quad (9)$$

$$D_i^{\text{LS}} = \frac{d_i}{\sum_{i \in \text{LS}} d_i} \quad (10)$$

The sum of the scaled individual buildup curves yields the summed DQ curves $\overrightarrow{\text{DQ}}_{\text{sim}}^x$ ($x \in \{\text{HS}, \text{LS}\}$) for each shift region.

$$\overrightarrow{\text{DQ}}_{\text{sim}}^x = \sum_{i \in x} D_i^x \cdot \overrightarrow{\text{DQ}}_i^{\text{indiv.}} \quad (11)$$

Similarly to eqn (8), the final summed DQ curves are fitted against the corresponding experimental data, *i.e.* the DQ curves $\overrightarrow{\text{DQ}}_{\text{exp}}^x$ ($x \in \{\text{HS}, \text{LS}\}$), based on the squared 2-norm of the residual divided by the squared 2-norm of the experimental data returning a quality parameter m_{DQ}^x .

$$m_{\text{DQ}}^x = \frac{\|\overrightarrow{\text{DQ}}_{\text{sim}}^x - \overrightarrow{\text{DQ}}_{\text{exp}}^x\|_2^2}{\|\overrightarrow{\text{DQ}}_{\text{exp}}^x\|_2^2} \quad (12)$$

To yield the optimal overall configuration, a joint function of all residuals is minimized. The relative weight is implemented by a scaling factor *scal*, expressing the influence of the DQ curves with respect to the spectrum.

$$m_{\text{tot}} = m_{\text{spc}} + \text{scal}[m_{\text{DQ}}^{\text{HS}} + m_{\text{DQ}}^{\text{LS}}] \quad (13)$$

The best joint fit of the experimentally observed ^1H MAS NMR spectrum and the ^1H - ^1H DQ buildup curves for the high and low shift regions is obtained with a relative weighting *scal*

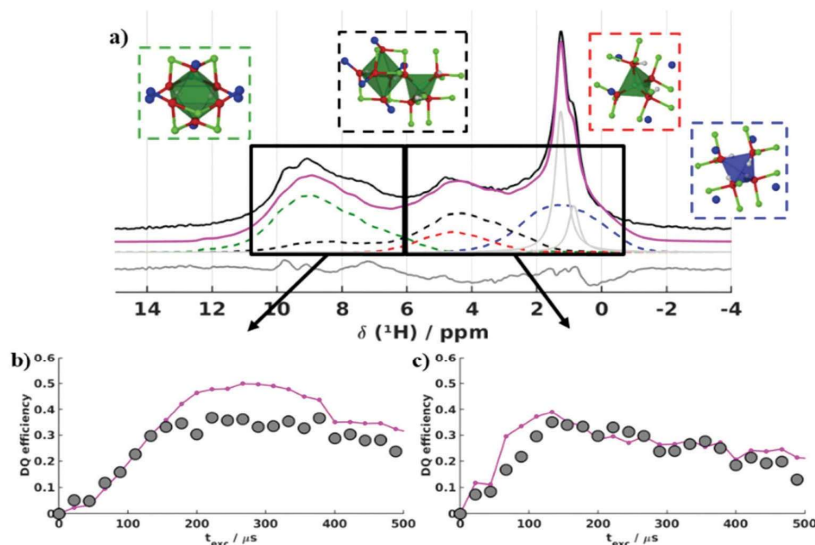


Fig. 6 (a) Experimentally observed ^1H MAS NMR spin echo ($\tau = 2 \nu_{\text{rot}}^{-1} = 50 \mu\text{s}$, black) of hydrous ringwoodite containing 0.1 wt% H_2O fitted by the sum of the ^1H signals (pink) calculated of the MD simulations of the defect types V_{Mg} (green dashed), V_{Si} (blue dashed), Mg_{Si} (red dashed) and $\text{Mg}_{\text{Si}}\text{V}_{\text{Mg}}$ (black dashed). The two resonances depicted in gray are assigned to proton species on the surface. The difference between experiment and simulation is shown in gray below the spectrum. The areas used for the ^1H - ^1H DQ buildup curves are indicated by black rectangles. (b and c) Combination of the simulated ^1H - ^1H DQ buildup curves of the corresponding models shown in Fig. 5(a) and (b), respectively, with the defect ratio observed in the 1D ^1H spectrum (pink) in comparison to the appropriate experimental curve (gray dots). The experimental error of the ^1H - ^1H DQ buildup curves is estimated from the S/N ratio to 5–10%.

Table 3 Summary of the relative integrals, the scaling factors of the individual ^1H - ^1H DQ buildup curves and the defect ratio of the hydroxyl defect types in ringwoodite determined by the fit of the individual ^1H signals and DQ buildup curves to the corresponding experiments using a joint cost function with a relative weighting of 0.5

Model	Relative integral	Scaling factor	Defect ratio (%)
V_{Mg}	0.36	0.71	49.0(7)
V_{Si}	0.29	0.35	17.9(6)
Mg_{Si}	0.10	0.26	13.1(10)
$\text{Mg}_{\text{Si}}V_{\text{Mg}}$	0.26	0.39 (H2-H4)/0.29 (H1)	19.9(11)

of 0.5. Since the individual quality parameters are normalized, a scaling of 0.5 expresses that the weight for the lineshape is twice as high as for the DQ cost function. This can be explained by the fact that the deviations of the spectrum are smaller than in the case of the DQ buildup curves, which is expected by the higher number of secondary disturbances in both the experimental and the simulated curves, such as ^1H probe background, imperfect pulses or second-order cross terms.

The comparison of the experimentally observed ^1H MAS NMR spectrum to the simulated summed spectrum S^{sum} of all defect types is shown in Fig. 6a, while the summed simulated ^1H - ^1H DQ buildup curves $\overrightarrow{\text{DQ}}_{\text{sim}}^{\text{v}}$ for the high and the low shift area are shown in Fig. 6b and c. Both the lineshape of the simulated spectrum (Fig. 6a, pink) and the trend of the DQ efficiency, as well as the overall shape of the combined simulated ^1H - ^1H DQ buildup curves (Fig. 6b and c, pink), show a very good agreement with the corresponding experiment. This not only provides further proof for the previously assigned hydrous defect types, but also allows for determining the quantitative ratio between these (Table 3). Through the simulated ^1H signal area and shape, it is possible to separate the broad experimental spectrum to the different defect types: isolated Mg vacancies ($V_{\text{Mg}}^{\text{v}} + 2\text{H}^{**}$) account for 49%, while isolated, hydrogarnet-like, Si vacancies ($V_{\text{Si}}^{\text{v}} + 4\text{H}^{****}$) account for 18%. The defects involving the replacement of a Si by an Mg on the tetrahedral site, isolated $\text{Mg}_{\text{Si}}^{\text{v}} + 2\text{H}^{**}$ and coupled $\text{Mg}_{\text{Si}}V_{\text{Mg}}^{\text{v}} + 4\text{H}^{****}$ defects, amount to 13% and 20%, respectively. The accuracy as obtained from the joint refinement is on average 5% (Table 3).

Conclusions

We used MD DFT simulations to model the orientational disorder of the OH groups within four well-defined hydrous defect types in ringwoodite resulting in distributions of hydrogen bond configurations and ^1H - ^1H distances within the defects. By using empirical correlations of the isotropic and the anisotropic chemical shift to structural elements, we were able to predict the full signature of the defects with respect to the 1D ^1H signals and the summed and normalized ^1H - ^1H DQ buildup for two characteristic shift regions. These results match both, the broad and structured lineshape of the experimental ^1H SQ MAS NMR spectrum and the experimentally observed ^1H - ^1H DQ buildup curves, excellently.

Based on these data, we finally reach a quantitative description of the defect concentrations with an average accuracy of about 5% for each hydrous defect type in ringwoodite: isolated Mg vacancies ($V_{\text{Mg}}^{\text{v}} + 2\text{H}^{**}$) account for \sim 49%, while isolated Si defects, $V_{\text{Si}}^{\text{v}} + 4\text{H}^{****}$ and $\text{Mg}_{\text{Si}}^{\text{v}} + 2\text{H}^{**}$, amount to 18% and 13%. The contribution of mixed coupled defects, $V_{\text{Mg}}V_{\text{Si}}^{\text{v}} + 4\text{H}^{****}$, is roughly 20%. Our quantitative assessment of ringwoodite's defect chemistry is the basis to understand its thermodynamics, such as the extraction of equilibrium constants or reaction enthalpies of the water incorporation mechanisms, if more hydroxyl concentrations are evaluated. Since ringwoodite is a main component of the Earth's mantle, quantifying its defect chemistry will also have an impact on understanding the transport properties of the mantle, such as viscosity⁵⁷ and thermal conductivity,⁵⁸ which are of great importance for understanding mantle convection.

Furthermore, the excellent agreement between experiment and simulation for two independent observables, ^1H chemical shift, thus hydrogen bond strength, as well as ^1H - ^1H distances, confirm that our simulations are able to scan the full range of orientations and hydrogen bonding for OH groups within constrained defect sites. Consequently, we show that MD DFT simulations are well suited to predict the potential energy surface for local disorder in point defects. We expect that our approach will be valuable for related issues, where heavy overlap within MAS NMR spectra prevents straightforward quantification.

Conflicts of interest

There are no conflicts to declare.

Acknowledgements

H. G. acknowledges the "Fonds der Chemischen Industrie" for financial support in the form of the "Chemiefonds Fellowship" and C. Tschense for programming scripts used for the analysis of the MD trajectories in Python.

References

- 1 D. W. Bolen and G. D. Rose, *Annu. Rev. Biochem.*, 2008, **77**, 339–362.
- 2 G. A. Jeffrey and W. Saenger, *Hydrogen Bonding in Biological Structures*, Springer, Berlin, Heidelberg, 1991.
- 3 C. Schmuck and W. Wienand, *Angew. Chem., Int. Ed.*, 2001, **40**, 4363–4369.
- 4 K. Kreuer, *Solid State Ionics*, 2000, **136–137**, 149–160.
- 5 L. Glasser, *Chem. Rev.*, 1975, **75**, 21–65.
- 6 K. D. M. Harris, M. Tremayne and B. M. Kariuki, *Angew. Chem., Int. Ed.*, 2001, **40**, 1626–1651.
- 7 K. D. M. Harris and E. Y. Cheung, *Chem. Soc. Rev.*, 2004, **33**, 526–538.
- 8 G. A. Jeffrey, *An Introduction to Hydrogen Bonding*, Oxford University Press, Oxford, 1997.
- 9 T. Steiner, *Angew. Chem., Int. Ed.*, 2002, **41**, 49–76.

- 10 C. Martineau, J. Senker and F. Taulelle, *Annu. Rep. NMR Spectrosc.*, 2014, **82**, 1–57.
- 11 R. K. Harris, R. E. Wasylshen and M. J. Duer, *NMR-Crystallography*, Wiley, Chichester, 2009.
- 12 L. Seyfarth and J. Senker, *Phys. Chem. Chem. Phys.*, 2009, **11**, 3522.
- 13 M. B. Mesch, K. Bärwinkel, Y. Krysiak, C. Martineau, F. Taulelle, R. B. Neder, U. Kolb and J. Senker, *Chem. – Eur. J.*, 2016, **22**, 16878–16890.
- 14 D. H. Brouwer, R. J. Darton, R. E. Morris and M. H. Levitt, *J. Am. Chem. Soc.*, 2005, **127**, 10365–10370.
- 15 D. D. Laws, H.-M. L. Bitter and A. Jerschow, *Angew. Chem., Int. Ed.*, 2002, **41**, 3096–3129.
- 16 S. P. Brown and H. W. Spiess, *Chem. Rev.*, 2001, **101**, 4125–4156.
- 17 J. Xu, V. V. Terskikh, Y. Chu, A. Zheng and Y. Huang, *Chem. Mater.*, 2015, **27**, 3306–3316.
- 18 G. N. M. Reddy, A. Huqi, D. Iuga, S. Sakurai, A. Marsh, J. T. Davis, S. Masiero and S. P. Brown, *Chem. – Eur. J.*, 2017, **23**, 2235.
- 19 R. F. Moran, D. McKay, C. J. Pickard, A. J. Berry, J. M. Griffin and S. E. Ashbrook, *Phys. Chem. Chem. Phys.*, 2016, **18**, 10173–10181.
- 20 J. M. Griffin, A. J. Berry, D. J. Frost, S. Wimperis and S. E. Ashbrook, *Chem. Sci.*, 2013, **4**, 1523.
- 21 H. Grüninger, K. Armstrong, D. Greim, T. Boffa-Ballaran, D. J. Frost and J. Senker, *J. Am. Chem. Soc.*, 2017, **139**, 10499–10505.
- 22 L. Seyfarth, J. Sehnert, N. E. a. El-Gamel, W. Milius, E. Kroke, J. Breu and J. Senker, *J. Mol. Struct.*, 2008, **889**, 217–228.
- 23 T. Charpentier, *Solid State Nucl. Magn. Reson.*, 2011, **40**, 1–20.
- 24 S. R. Chaudhari, J. M. Griffin, K. Broch, A. Lesage, V. Lemaury, D. Dudenko, Y. Olivier, H. Sirringhaus, L. Emsley and C. P. Grey, *Chem. Sci.*, 2017, **8**, 3126–3136.
- 25 X. Filip, I.-G. Grosu, M. Miclăuş and C. Filip, *CrystEngComm*, 2013, **15**, 4131.
- 26 A. Hofstetter and L. Emsley, *J. Am. Chem. Soc.*, 2017, **139**, 2573–2576.
- 27 M. Baias, A. Lesage, S. Aguado, J. Canivet, V. Moizan-Basle, N. Audebrand, D. Farrusseng and L. Emsley, *Angew. Chem., Int. Ed.*, 2015, **54**, 5971–5976.
- 28 A. Samoson, T. Tuhern, J. Past, A. Reinhold, T. Anupöld and I. Heinmaa, *Top. Curr. Chem.*, 2005, **246**, 15–31.
- 29 I. Schnell and H. W. Spiess, *J. Magn. Reson.*, 2001, **151**, 153–227.
- 30 P. K. Madhu, X. Zhao and M. H. Levitt, *Chem. Phys. Lett.*, 2001, **346**, 142–148.
- 31 C. J. Pickard and R. J. Needs, *J. Phys.: Condens. Matter*, 2011, **23**, 53201.
- 32 S. Kirkpatrick, C. D. Gelatt and M. P. Vecchi, *Science*, 1983, **220**, 671–680.
- 33 J. C. Schön, K. Doll and M. Jansen, *Phys. Status Solidi B*, 2010, **247**, 23–39.
- 34 H. Eckert, J. P. Yesinowski, L. A. Silver and E. M. Stolper, *J. Phys. Chem.*, 1988, **92**, 2055–2064.
- 35 S. C. Kohn, R. A. Brooker, D. J. Frost, A. E. Slesinger and B. J. Wood, *Am. Mineral.*, 2002, **87**, 293–301.
- 36 X. Xue and M. Kanzaki, *J. Am. Ceram. Soc.*, 2009, **92**, 2803–2830.
- 37 P. Lorente, I. G. Shenderovich, N. S. Golubev, G. S. Denisov, G. Buntkowsky and H.-H. Limbach, *Magn. Reson. Chem.*, 2001, **39**, S18–S29.
- 38 T. Emmmler, S. Gieschler, H. H. Limbach and G. Buntkowsky, *J. Mol. Struct.*, 2004, **700**, 29–38.
- 39 D. Marx and J. Hutter, in *Modern Methods and Algorithms of Quantum Chemistry*, ed. J. Grotenrost, NIC-Directors, FZ Jülich, 2000, pp. 301–449.
- 40 S. Rauei, P. L. Silvestrelli and M. Parrinello, *Phys. Rev. Lett.*, 1999, **83**, 2222–2225.
- 41 S. K. Estreicher, J. L. Hastings and P. a. Fedders, *Phys. Rev. B: Condens. Matter Mater. Phys.*, 1998, **57**, R12663–R12665.
- 42 P. E. Kristiansen, M. Carravetta, J. D. van Beek, W. C. Lai and M. H. Levitt, *J. Chem. Phys.*, 2006, **124**, 234510.
- 43 P. E. Kristiansen, D. J. Mitchell and J. N. S. Evans, *J. Magn. Reson.*, 2002, **157**, 253–266.
- 44 K. Saalwächter, *ChemPhysChem*, 2013, **14**, 3000–3014.
- 45 S. J. Clark, M. D. Segall, C. J. Pickard, P. J. Hasnip, M. J. Probert, K. Refson and M. C. Payne, *Z. Krist.*, 2005, **220**, 567–570.
- 46 C. Pickard and F. Mauri, *Phys. Rev. B: Condens. Matter Mater. Phys.*, 2001, **63**, 245101.
- 47 J. R. Yates, C. J. Pickard and F. Mauri, *Phys. Rev. B: Condens. Matter Mater. Phys.*, 2007, **76**, 24401.
- 48 M. Profeta, F. Mauri and C. J. Pickard, *J. Am. Chem. Soc.*, 2003, **125**, 541–548.
- 49 J. P. Perdew, K. Burke and M. Ernzerhof, *Phys. Rev. Lett.*, 1996, **77**, 3865–3868.
- 50 M. Bak, J. T. Rasmussen and N. C. Nielsen, *J. Magn. Reson.*, 2000, **147**, 296–330.
- 51 Z. Tosner, T. Vosegaard, C. Kehlet, N. Khaneja, S. J. Glaser and N. C. Nielsen, *J. Magn. Reson.*, 2009, **197**, 120–134.
- 52 Z. Tošner, R. Andersen, B. Stevansson, M. Edén, N. C. Nielsen and T. Vosegaard, *J. Magn. Reson.*, 2014, **246**, 79–93.
- 53 J. P. Bradley, C. Tripon, C. Filip and S. P. Brown, *Phys. Chem. Chem. Phys.*, 2009, **11**, 6941–6952.
- 54 J. P. Bradley, C. J. Pickard, J. C. Burley, D. R. Martin, L. P. Hughes, S. D. Cosgrove and S. P. Brown, *J. Pharm. Sci.*, 2012, **101**, 1821–1830.
- 55 S. P. Brown, *Prog. Nucl. Magn. Reson. Spectrosc.*, 2007, **50**, 199–251.
- 56 M. J. Bayro, M. Huber, R. Ramachandran, T. C. Davenport, B. H. Meier, M. Ernst and R. G. Griffin, *J. Chem. Phys.*, 2009, **130**, 114506.
- 57 J. Hustoft, G. Amulele, J. I. Ando, K. Otsuka, Z. Du, Z. Jing and S. I. Karato, *Earth Planet. Sci. Lett.*, 2013, **361**, 7–15.
- 58 S.-M. Thomas, C. R. Bina, S. D. Jacobsen and A. F. Goncharov, *Earth Planet. Sci. Lett.*, 2012, **357–358**, 130–136.

Supporting Information
for
**Quantitative description of ^1H SQ and DQ coherences for the
hydroxyl disorder within hydrous ringwoodite**

Helen Grüninger,^a Adrian Schmutzler,^a Renée Siegel,^a Katherine Armstrong,^b Daniel J. Frost^b
and Jürgen Senker*^a

^a Anorganische Chemie III, University of Bayreuth, Universitätsstr. 30, 95447 Bayreuth,
Germany.

^b Bayerisches Geo-Institut, University of Bayreuth, Universitätsstr. 30, 95447 Bayreuth,
Germany.

*juergen.senker@uni-bayreuth.de

Contents

1. Influence of the CSA on experimental spectra and simulations	2
2. Defect models	4
3. Comparison of 1D ^1H MAS spin echos of ringwoodite	4
4. Simulated ^1H - ^1H DQ buildup curves	5
5. Convergence of ^1H signal and average ^1H - ^1H DQ buildup curves	6
6. SIMPSON input for the simulation of DQ buildup curves	9

1. Influence of the CSA on experimental spectra and simulations

The occurrence of spinning sidebands as shown in Fig. S1 indicate a significant contribution of the chemical shift anisotropy. We observe a slightly poorer resolution in the spinning sidebands, which is a common phenomenon for MAS NMR spectroscopy. In our case a likely explanation is a higher spin correlation in some defect types, as previously described by Schnell and Spiess¹ and Zorin *et al.*².

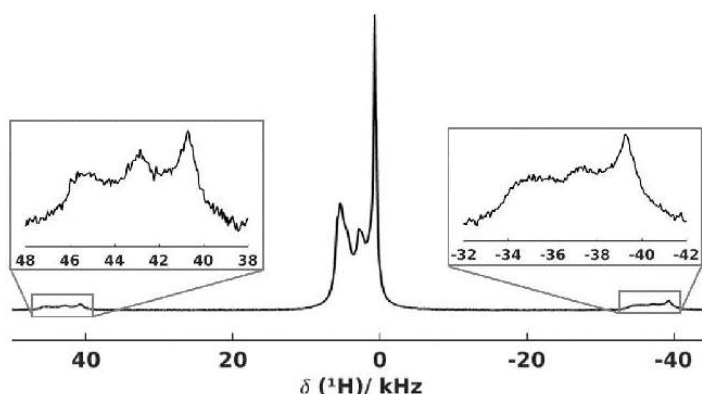


Fig. S1: ^1H MAS spin-echo of hydrous ringwoodite with two visible spinning sidebands (ν_{rot} 40 kHz) highlighted as insets. The presence of two spinning sidebands with comparable lineshapes indicates a CSA of significant strength for all defect types and emphasizes the necessity to consider the CSA interaction in the simulations of experimental observables.

Two different two-spin systems of an isolated Mg vacancy ($\text{V}_{\text{Mg}}^{\bullet\bullet} + 2\text{H}^{*}$) with varying strength of the CSA were used (Table S1) to test the influence of the asymmetry η ($\eta = 0.0, 0.1, 0.2$) on ^1H - ^1H DQ buildup curves (Fig. S2). The resulting curves of both spin systems (SS1, SS2 Fig. S2) for the different values of η are overlapping and reveal that the asymmetry has no or negligible influence on the behaviour of the DQ curves.

¹ I. Schnell, H. W. Spiess, J. Magn. Reson., 2001, **151**, 153–227.

² V. E. Zorin, S. P. Brown, P. Hodgkinson, Mol. Phys. 2006, **104**, 293–304.

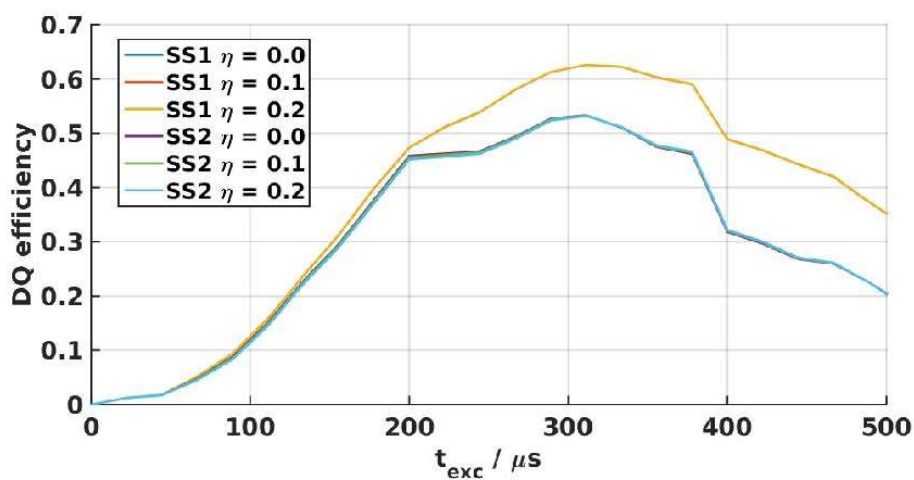


Fig. S2: Simulated ^1H - ^1H DQ buildup curves ($R18g^5$ sequence with an S_0S_π supercycle) of the spin systems SS1 and SS2 (Table S1) of an isolated Mg vacancy in ringwoodite with varying asymmetry η .

Table S1: Spin systems SS1 and SS2 of an isolated Mg vacancy in ringwoodite.

Model $V_{Mg}'' + 2H^{**}$	^1H - ^1H distance	$\delta_{iso}(H1/H2)$	$\delta_{aniso}(H1/H2)$
Spin system 1 (SS1)	2.8 Å	9.1 / 8.5 ppm	-17.4 / -15.7 ppm
Spin system 2 (SS2)	2.7 Å	11.4 / 10.3 ppm	-29.2 / 21.9 ppm

2. Defect models

100 exemplary proton positions of the OH groups of each defect type extracted from the MD runs are depicted in Fig. S3. Proton H1 of the coupled defect $\text{Mg}_{\text{Si}}\text{V}_{\text{Mg}}$ “hops” after roughly 4,100 MD steps.

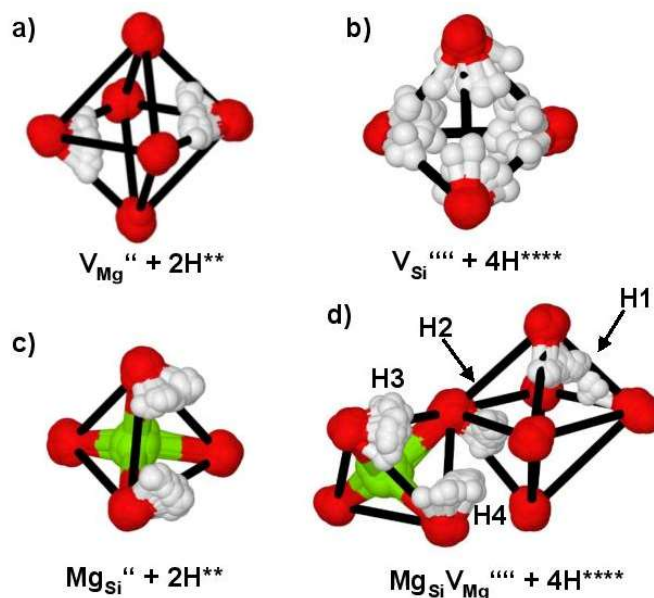


Fig. S3: 100 exemplary proton positions from the MD runs of a) an isolated Mg vacancy, b) an isolated Si vacancy charge balanced by four protons, c) an isolated Si vacancy charge balanced by an Mg^{2+} and two protons and d) a coupled defect with an octahedral vacancy and one Mg^{2+} on a Si site. In d) the four different OH groups (H1-H4) are specified. H1 has a mixed Si and Mg coordination sphere, while H2-4 are solely in Mg environment.

3. Comparison of 1D ^1H MAS spin echos of ringwoodite

The three 1D ^1H MAS spin echos of ringwoodite (Fig. S4) with interpulse delays of $25\ \mu\text{s}$ ($1\ \nu_{\text{rot}}^{-1}$), $50\ \mu\text{s}$ ($2\ \nu_{\text{rot}}^{-1}$, scaled by 1.15) and $75\ \mu\text{s}$ ($3\ \nu_{\text{rot}}^{-1}$, scaled by 1.31) reveal that the broad components of the spectrum exhibit spin-spin relaxation times (T_2) of similar magnitude, while the sharper resonances at 1.2 and 0.8 ppm, which have previously been assigned to surface species, show slightly longer relaxations times. This behaviour allows for a quantitative description of the spectrum, since the ratio of the broad components remains virtually constant and the surface species are not considered in the description of ringwoodites defect chemistry.

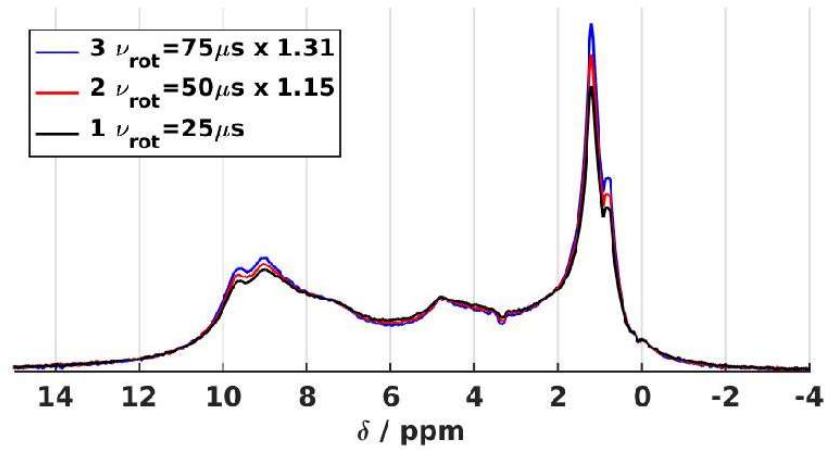


Fig. S4: Comparison of three 1D ^1H MAS spin echos of ringwoodite with interpulse delays of $25\ \mu\text{s}$ ($1\ \nu_{\text{rot}}^{-1}$, black), $50\ \mu\text{s}$ ($2\ \nu_{\text{rot}}^{-1}$, scaled up by 1.15, red) and $75\ \mu\text{s}$ ($3\ \nu_{\text{rot}}^{-1}$, scaled up by 1.31, blue).

4. Simulated ^1H - ^1H DQ buildup curves

The simulated individual, as well as average ^1H - ^1H DQ buildup curves for the four hydrous defect types are shown in Figs. S5-S7.

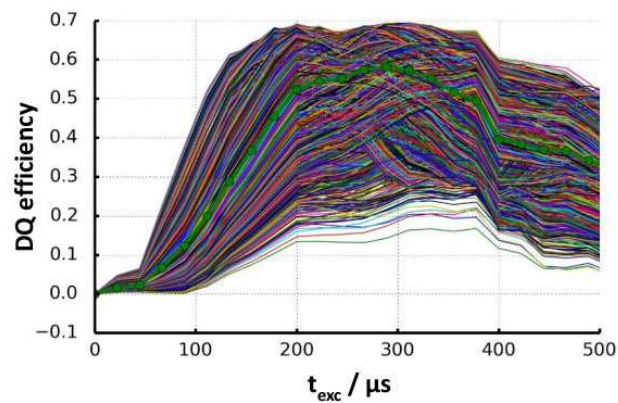


Fig. S5: Individual and averaged (green) ^1H - ^1H DQ buildup curve of an isolated Mg vacancy (V_{Mg}) for the 10,000 structures of the MD run.

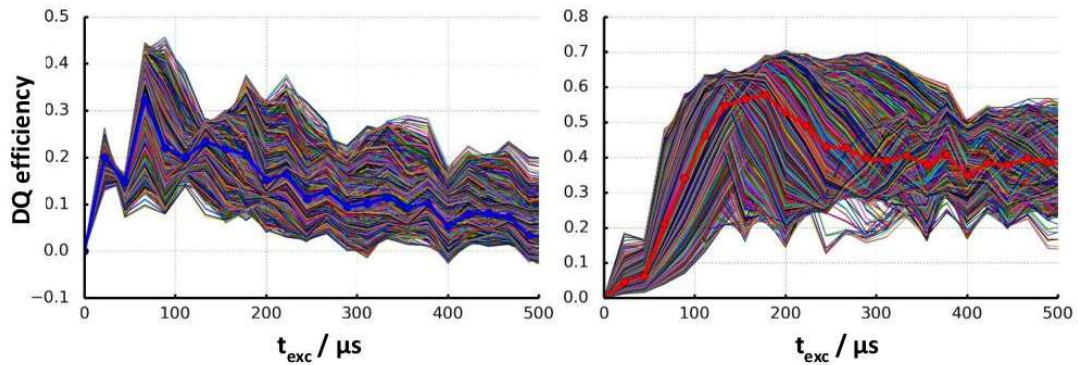


Fig. S6: Individual and averaged ^1H DQ buildup curve of an isolated Si vacancy charge balanced by either four protons (V_{Si} , left blue) or one Mg^{2+} and two protons (Mg_{Si} , right red) for the 10,000 structures of the MD runs.

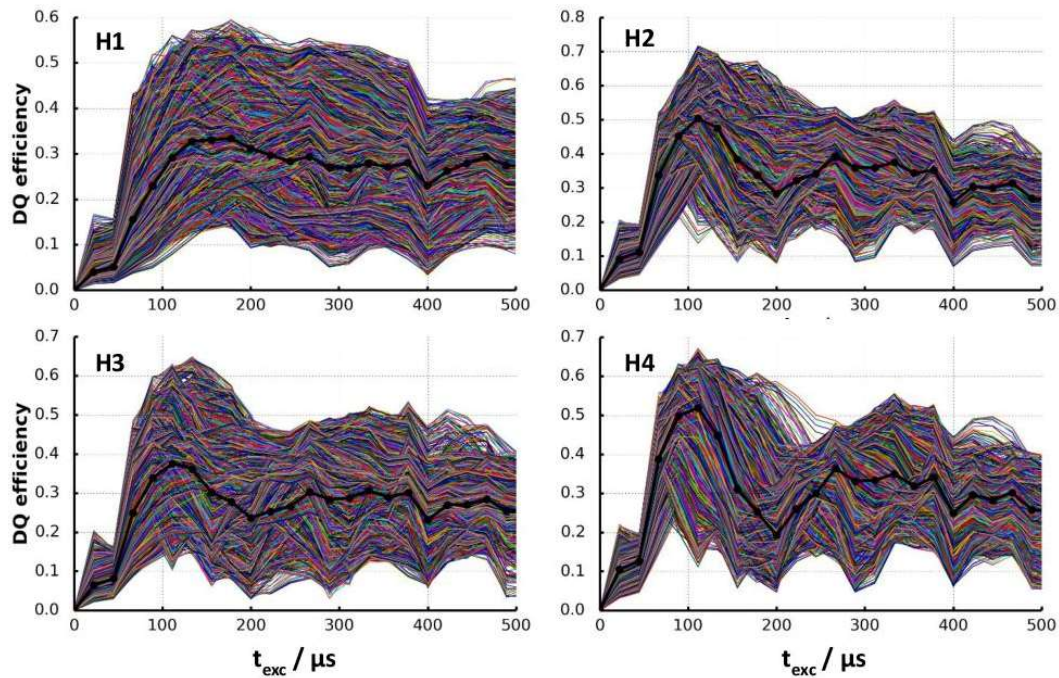


Fig. S7: Individual and averaged (black) ^1H - ^1H DQ buildup curve for each OH group (H1-H4, Fig. S2) of a mixed coupled defect $\text{Mg}_{\text{Si}}\text{V}_{\text{Mg}}$ for the 10,000 structures of the MD run.

5. Convergence of ^1H signal and average ^1H - ^1H DQ buildup curves

Figs. S8-11 show the convergence of the two experimental observables – lineshape of the ^1H signal and average ^1H - ^1H DQ buildup curves. In each Fig. the expected ^1H signal or ^1H - ^1H DQ build up curve is shown for increments of 1,000 MD steps. The lineshape of the ^1H signal (Fig. S7) for each defect type converges within 10,000 MD steps.

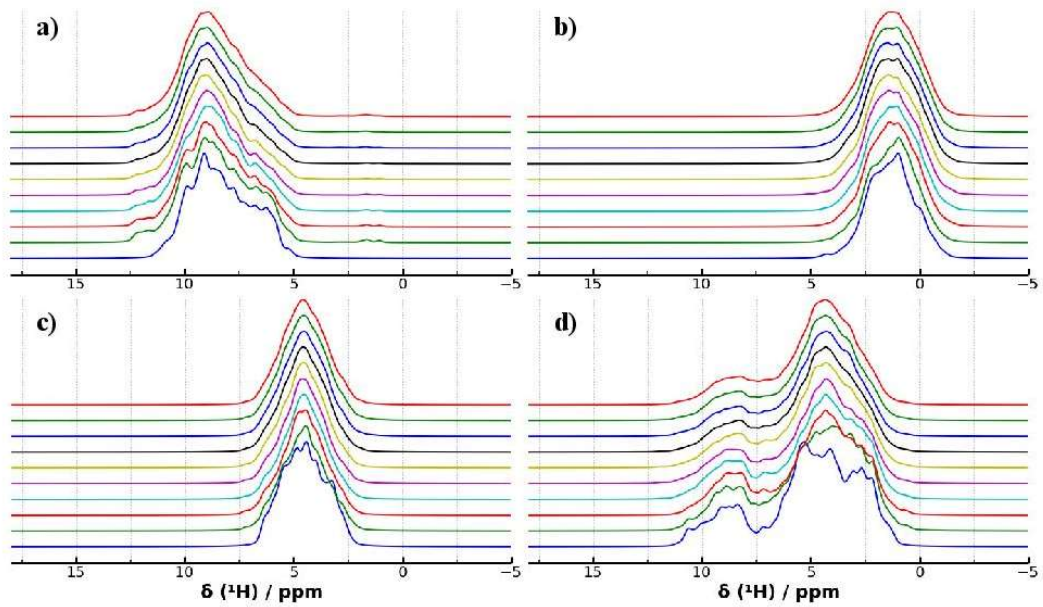


Fig. S8: Convergence of the calculated ^1H signal in steps of 1,000 structures for an isolated Mg vacancy (a); an isolated Si vacancy charge balanced by four protons (b) or one Mg^{2+} and two protons (c) and the mixed coupled defect (d).

The average ^1H - ^1H DQ buildup curves of the isolated defect types, V_{Mg} (Fig. S9), V_{Si} and Mg_{Si} (Fig. S10) already converge after roughly 4,000 steps.

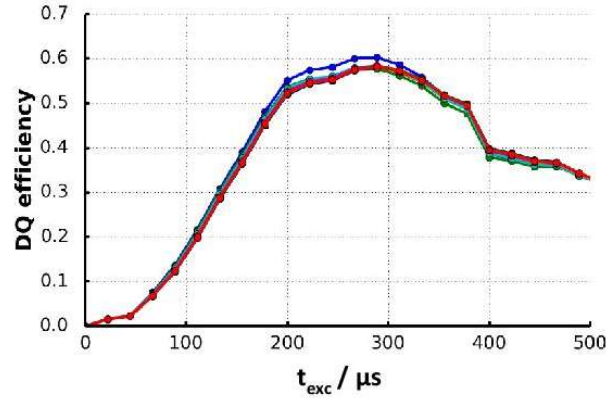


Fig. S9: Convergence of the calculated average ^1H - ^1H DQ buildup curve in increments of 1,000 MD steps for an isolated Mg vacancy. The averaged curve over the first 1,000 steps is shown in blue, while the curve averaged over 10,000 structures is shown in red. Convergence of the ^1H - ^1H DQ buildup curve is already reached after roughly 4,000 MD steps.

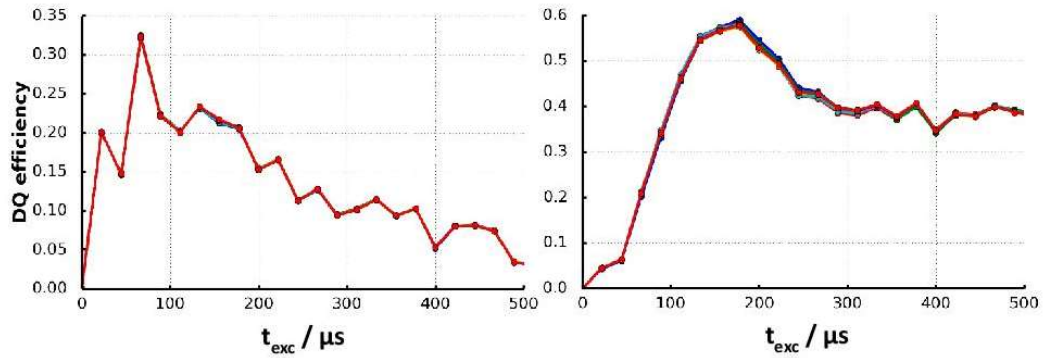


Fig. S10: Convergence of the calculated average ^1H - ^1H DQ buildup curve in increments of 1,000 MD steps for an isolated Si vacancy charge balanced by four protons (left) and by one Mg^{2+} and two protons (right). The averaged curve over the first 1,000 steps is shown in blue, while the curve averaged over 10,000 structures is shown in red. Convergence of the ^1H - ^1H DQ buildup curves is already reached after roughly 4,000 MD steps.

The convergence of the average ^1H - ^1H DQ buildup curves of the mixed coupled defect type $\text{Mg}_{\text{Si}}\text{V}_{\text{Mg}}$ are depicted in Fig. S11. The curves take more steps ($\sim 9,000$) to reach convergence since proton H1 “hops” to a neighbouring oxygen after roughly 4,100 MD steps in the simulation run.

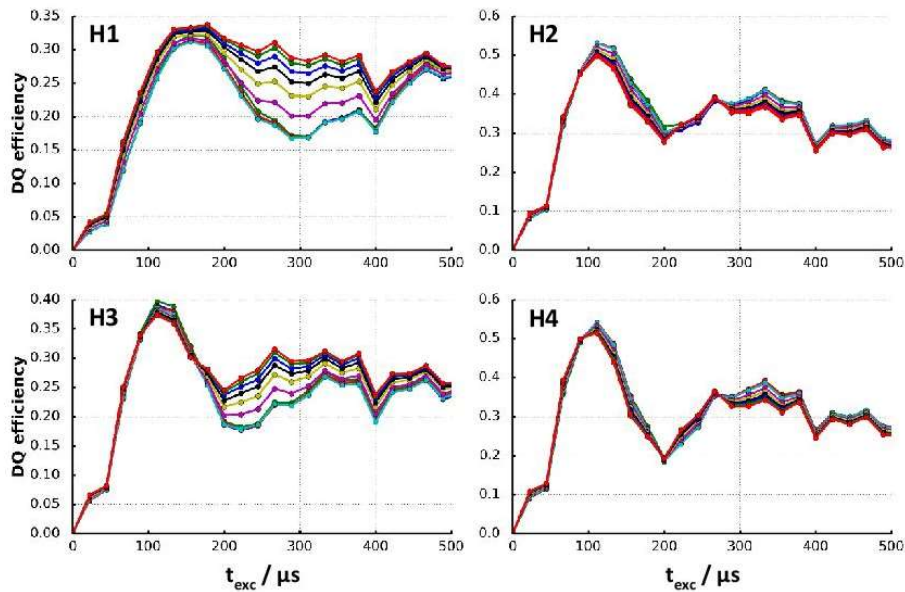


Fig. S11: Convergence of the calculated average ^1H - ^1H DQ buildup curves in increments of 1,000 MD steps for the four OH groups of the mixed coupled defect $\text{Mg}_{\text{Si}}\text{V}_{\text{Mg}}$.

6. SIMPSON input for the simulation of DQ buildup curves

In the following section a representative SIMPSON input-file of one proton configuration of a $V_{Mg}'' + 2H^{**}$ and a one proton configuration of a $Mg_{Si}V_{Mg}'''' + 4H^{****}$ defect model is provided. Due to the necessity to calculate points after each RR' block of the $R18_8^5$ sequence the use of propagators is not possible.

Exemplary spin-system for the $V_{Mg}'' + 2H^{**}$ defect model:

```
spinsys {
channels 1H
nuclei 1H 1H
shift 1 9.13519460534p -17.442954149273753p 0.0 -180.0 147.112680258 -96.0999976466
shift 2 8.45403012623p -15.721046143694831p 0.0 89.5128851082 33.9049512299 90.5869044213
dipole 1 2 -5637.1164636 0.0 31.6851345727 -78.1078876858
}
```

Exemplary spin-system for the $Mg_{Si}V_{Mg}'''' + 4H^{****}$ defect model:

```
spinsys {
channels 1H
nuclei 1H 1H 1H 1H
shift 1 7.65570538667p -14.230231427794791p 0.0 9.56652519022e-16 89.9053170479
116.107581184
shift 2 4.83390111118p -14.91842233233166p 0.0 2.39509235681e-13 75.7896442027
145.827201686
shift 3 3.68098859231p -13.067138872028291p 0.0 180.0 72.0379085765 -115.290718781
shift 4 4.09971035372p -13.637849624820266p 0.0 -180.0 65.4909116727 -176.770801038
dipole 1 2 -9979.71504354 -0.0 90.890156288 -132.673633621
dipole 1 3 -2207.9376203 -0.0 126.834801466 -133.940698073
dipole 1 4 -1309.36099235 -0.0 121.542103199 -165.605453363
dipole 2 3 -9180.32699327 -0.0 161.606622851 -137.848273934
dipole 2 4 -3461.074725 0.0 135.429867105 161.424835593
dipole 3 4 -14279.8642363 0.0 92.4715817321 142.809597446
}
```

General Parameters and pulse program:

```
par {
variable      N 18.
variable      n 8.
variable      nu 5.
start_operator Inz
detect_operator I1p
spin_rate     40000
gamma_angles  5
crystal_file  zcw232
np            50
sw            spin_rate/$n
```

```

proton_frequency 600e6
verbose          11110
}

proc pulseseq {} {
  global par
  maxdt 1.0

  #
  set rf [expr $par(spin_rate)*$par(N)/$par(n)]
  set p90 [expr 0.25e6/$rf]
  set p270 [expr 0.75e6/$rf]

  # Phase: phi, phi+pi, -phi, -phi+pi

  set ph10 [expr 180.00*$par(nu)/$par(N)]
  set ph11 [expr 180.00*$par(nu)/$par(N)+180.00]
  set ph12 [expr (-1)*180.00/$par(N)*$par(nu)+360.00]
  set ph13 [expr (-1)*180.00/$par(N)*$par(nu)+180.00]

  # Calculation of buildup curve
  # 1. Point of Buildup
  reset
  acq

  # 2. Point of buildup
  reset

  pulse $p90 $rf $ph10
  pulse $p270 $rf $ph11

  pulse $p90 $rf $ph12
  pulse $p270 $rf $ph13

  matrix set 1 totalcoherence {-2 2}
  filter 1

  pulse $p90 $rf $ph10
  pulse $p270 $rf $ph11

  pulse $p90 $rf $ph12
  pulse $p270 $rf $ph13

  matrix set 2 totalcoherence {0}
  filter 2
  pulseid 1 250000 -y

```

```
        acq
.... et cetera

        }

proc main {} {
global par
set f [fsimpson]
fexpr $f {$re} {$Sim}
fsave $f $par(name).dat -xreim
}
```


4.3 On the feasibility of ^1H NMR on hydrous defects within nanoliter ringwoodite crystals

This manuscript is the result of a cooperation between the Inorganic Chemistry III, the Bavarian Research Institute of Experimental Geochemistry and Geophysics (BGI) and the Inorganic Chemistry I of the University of Bayreuth and the Solid-State NMR group of Radboud University in Nijmegen (Netherlands).

My contributions are:

- conception and main authorship of the manuscript
- conduction of ^1H MAS NMR measurements using a standard Bruker probe
- support of NMR measurements using a piggy-back μMAS probe
- evaluation of all NMR data
- conduction and evaluation of XRD measurements
- conduction and evaluation of all DFT calculations

The contribution of all other authors are:

- conception and co-authorship of the manuscript
- high-pressure synthesis of the ringwoodite crystals
- measurement and evaluation of FTIR spectra
- support in conduction and evaluation of XRD measurements
- conduction of ^1H MAS NMR measurements using a piggy-back μMAS probe

On the feasibility of ^1H NMR on hydrous defects within nanoliter ringwoodite crystals

Helen Grüninger^a, Zhaodong Liu^b, J. Ole Brauckmann^c, Thomas Martin,^d Tiziana Boffa Ballaran^b, Renée Siegel^a, Arno P. M. Kentgens^{c*}, Daniel J. Frost^{b*}, Jürgen Senker^{a*}

^a Anorganische Chemie III, University of Bayreuth, Universitätsstr. 30, 95447 Bayreuth, Germany.

^b Bayerisches Geo-Institut, University of Bayreuth, Universitätsstr. 30, 95447 Bayreuth, Germany.

^c Institute for Molecules and Materials / Solid State NMR, Radboud University, Heyendaalseweg 135, 6525 AJ Nijmegen, Netherlands.

^d Anorganische Chemie I, University of Bayreuth, Universitätsstr. 30, 95447 Bayreuth, Germany.

Introduction

Recently, we could qualitatively and quantitatively solve the surprisingly rich OH defect chemistry of one ringwoodite ($\gamma\text{-Mg}_2\text{SiO}_4$) sample containing ~ 0.1 wt% of water by a combination of ^1H solid-state NMR spectroscopy with computational methods on Density Functional Theory (DFT) level.^[1,2] As such we could show, that four different defect motifs are formed in the spinel-type crystal structure of ringwoodite consisting of isolated SiO_4 tetrahedra and edge-sharing MgO_6 octahedra. Additionally to the expected isolated low-valent Mg^{2+} vacancies charge balanced by two protons ($\text{V}_{\text{Mg}}'' + 2\text{H}^{**}$), also isolated Si^{4+} defects charge balanced by either four protons ($\text{V}_{\text{Si}}'''' + 4\text{H}^{****}$) or two protons and one Mg^{2+} on the Si site ($\text{Mg}_{\text{Si}}'' + 2\text{H}^{**}$) are formed. Furthermore, a coupled defect type with an Mg^{2+} on a Si site coupled to an octahedral vacancy ($\text{Mg}_{\text{Si}}\text{V}_{\text{Mg}}'''' + 4\text{H}^{****}$) makes up a significant proportion.^[1] By modelling the experimentally observed OH group disorder within the point defects, we were able to determine characteristic chemical shift footprints and characteristic ensemble-average ^1H - ^1H DQ buildup curves for each defect motif. By applying a joint cost function we could reproduce the strongly overlapping experimental ^1H MAS NMR spectrum and ^1H - ^1H double-quantum (DQ) buildup curves simultaneously leading to a quantitative determination of defect motifs to $\sim 50\%$ V_{Mg} , 18% V_{Si} , $\sim 13\%$ Mg_{Si} and 20% coupled $\text{Mg}_{\text{Si}}\text{V}_{\text{Mg}}$.^[2]

Since the high-pressure magnesium silicate ringwoodite is the main mineral phase of the transition zone of the Earth's mantle in depth between ~ 530 km and 660 km,^[3] the OH defects will not only account for a large fraction of the Earth's entire water budget,^[4] which was

enforced by the recent discovery of natural ringwoodite containing the equivalent of ~1 wt% H₂O,^[5] but significantly alter the physical and chemical properties of the mineral and thus also influence transport properties of the mantle, such as viscosity^[6] and thermal conductivity^[7]. Therefore, it is essential to fully understand ringwoodites OH defect chemistry, i.e. its thermodynamics, such as the extraction of equilibrium constants or reaction enthalpies, and to model its impact on mantle properties. This can only be accomplished by evaluating the behaviour of OH defect formation, i.e. the ratio of the OH defect motifs within the ringwoodite structure, systematically as function of hydration level up to an equivalent of 3wt% H₂O. However, synthesizing suitably large and pure powder samples for ¹H NMR spectroscopy is challenging due to the demanding pressure and temperature requirements in the synthesis. Furthermore, identifying the water concentrations accurately is difficult from powdered samples since it is usually measured by polarized FTIR or secondary ion mass spectroscopy (SIMS) on single-crystals.

Therefore, in this study we investigate the feasibility of ¹H solid-state NMR spectroscopy on three hydrous nanoliter ringwoodite crystals containing intrinsically small amounts of protons as OH defects with varying water concentrations between roughly 0.1 and 2 wt% estimated from FTIR spectroscopy. We use the previously determined individual ¹H chemical shift footprints for each defect type^[2] to fit each of the experimental ¹H MAS NMR lineshapes and to determine the ratio of the four above mentioned defect motifs within each sample. Furthermore, we use X-ray diffraction on the same crystals to measure the volume expansion of the spinel-type crystal structure upon hydration and to allow for a comparison to earlier results revealing substantial differences.

Experimental Details

Synthesis

Nanoliter crystals of hydrous ringwoodite were synthesized in two synthesis runs at 19 GPa and 1350°C and 1400°C, respectively, using the 1000 and 5000 ton press at the Bayerisches Geoinstitut. Starting materials were oxide mixture of Mg₂SiO₄ and Mg₂SiO₄ plus 11.3 wt% H₂O from the reagent oxide MgO, Mg(OH)₂ and SiO₂. The starting materials were sealed in a welded Pt capsule, and then put into a high pressure 18/8 (edge length of Cr₂O₃-doped MgO octahedral and truncation edge length of tungsten carbide anvils) cell assembly. The run duration was approximately 6-8 hours and to enhance the crystal growth, the *P-T* conditions

appropriate for partial melting in the system $\text{Mg}_2\text{SiO}_4\text{-H}_2\text{O}$, i.e. just above the wet solidus, were selected.

Table 1. Synthesis conditions, starting composition and run products of synthesis run 1 and 2.

Run (run number)	Starting composition of MgO , $\text{Mg}(\text{OH})_2$ and SiO_2	Synthesis conditions	Run products
Run 1 (Z1584)	Mg_2SiO_4	19 GPa / 1350 °C / 6 h	Rw
Run 2 (H4672)	Mg_2SiO_4 + 11.3 wt% H_2O (H_2O saturated)	19 GPa / 1400 °C / 8 h	Rw + melt + trace Sti

FTIR spectroscopy

Double-polished thin sections of one crystal of run 1 (70 μm thick) and run 2 (50 μm thick) were analysed by Fourier transform infrared spectroscopy (FTIR) using unpolarized radiation and a minimum spot size of 30 μm . The water content of the ringwoodite crystals is calculated from the OH stretching region (wavenumber range 4000–2400 cm^{-1}) in the two FTIR spectra (Figure 1), which are normalized and baseline-corrected with a linear background, using the method by Koch-Müller and Rhede.^[8] The basis of this method applies the Beer–Lambert law in the form of:

$$A_{i \text{ tot}} = \varepsilon_i \cdot C_{\text{H}_2\text{O}} \cdot t$$

where $A_{i \text{ tot}}$ is the integrated absorbance (A_i) multiplied by 3, ε_i is the extinction coefficient in $\text{l}(\text{mol H}_2\text{O})^{-1} \text{cm}^{-2}$, $C_{\text{H}_2\text{O}}$ is the concentration in mol l^{-1} and t is the sample thickness. The conversion to p.p.m. H_2O is achieved by multiplying the concentration of H_2O (mol l^{-1}) with the conversion factor K:

$$C_{(\text{p.p.m. H}_2\text{O})} = C_{(\text{H}_2\text{O})} \cdot K = \frac{3 \cdot A_{i \text{ tot}}}{\varepsilon_i \cdot t} \cdot K$$

where $A_{i \text{ tot}}$ is the integrated OH absorption normalized to 1 cm thickness; ε_i is the absorption factor, which for an Mg endmember ringwoodite is estimated to be 100,000;^[8] and $t = 1 \text{ cm}$.

The conversion factor K is given by:

$$K = \frac{1000 \cdot M(\text{H}_2\text{O})}{\rho}$$

where $M(\text{H}_2\text{O})$ is the molar weight of water (18 gmol^{-1}) and ρ is the density of the ringwoodite Mg endmember (3.90 gcm^{-3}). The factor 1000 arises from the conversion of l to cm^3 .

Solid-state NMR spectroscopy

Solid-state ^1H MAS NMR spin echo measurements of the ringwoodite crystal B were performed using a Bruker Avance III spectrometer operating at a magnetic field strength of 23.5 T corresponding to a ^1H Larmor frequency of 1 GHz. The ^1H MAS spectrum was recorded using a Bruker 1.3 mm double-resonance probe at an MAS frequency of 62.5 kHz.

Solid-state ^1H MAS spin-echo measurements of the ringwoodite crystals A and C were performed using a Varian VNMRs spectrometer operating at a magnetic field strength of ~ 20 T corresponding to a ^1H Larmor frequency of 850 MHz. The ^1H MAS spectra was recorded using the μMAS probe-head (sample volume up to 50 nL), described in ref. [9] at an MAS frequency of 20 kHz.

In any setup the crystals were positioned with teflon inserts in the center of the fused silica capillaries of the sample tip (outer and inner diameter are 320 μm and 250 μm , respectively) or the Bruker 1.3 mm MAS rotor to ensure that the crystals are placed in the middle of the radiofrequency coil. In order to reduce the background of the probe and the MAS rotors we used spin-echo measurements. It was previously shown that although spin-echos are used, the resulting ^1H spectra are quantitatively refinable, because the defect resonances exhibit similar spin-spin relaxation times.^[2] For crystal B an interpulse delay of 32 μs ($2 \nu_{\text{rot}}^{-1}$ at 62.5 kHz MAS), a B_1 field of ~ 110 kHz and recycle delay of 20 s was used and 4096 averages were recorded. For crystal A and C an interpulse delay of 50 μs ($1 \nu_{\text{rot}}^{-1}$ at 20 kHz MAS), a B_1 field of ~ 110 kHz and a recycle delay of 20 s (crystal A) and 5 s (crystal C) was used. For crystal A 10240 averages and for crystal C 18432 averages were recorded.

Due to the low the proton concentrations of the ringwoodite samples, it is necessary to subtract remaining proton background, which originates most probably from the Kel-F sample holder, which mounts the capillary onto the 1.6 mm rotor in the μMAS setup, and the caps/bottoms of the 1.3mm MAS rotor as well as the stator. Therefore, in the case of crystal B a background measurement of the same empty 1.3 mm MAS rotor with the same teflon inserts was recorded with similar parameters and length as the corresponding crystal spectrum. The sample tip used for crystal C was measured empty to determine the background of the μMAS setup with a recycle delay of 5 s and 12488 averages were recorded. Unfortunately the sample-tips cannot be reused and therefore for crystal A, the same background was assumed. The μMAS background spectrum was scaled for the number of scans of the crystal spectra A and C, respectively, before subtraction.

X-ray Diffraction

The crystals A-C were mounted on top of a 0.1 mm glass capillary and the unit cell parameters of each crystal were measured in transmission geometry using a STOE STADI P diffractometer with Cu $K\alpha_1$ radiation equipped with a fast, high-resolution silicon strip detector (DECTRIS Mythen1K). Instrument parameters for Pawley refinements were determined by analysing Si. For Pawley refinements^[10] the software TOPAS Academic^[11] was used. The background was fitted using a 16th-order Tchebyshev polynomial.

DFT calculations

Geometry-optimizations of the four different OH defect motifs in ringwoodite were carried out using the CASTEP DFT code (version 8.0).^[12] For all calculations, the generalized gradient approximation (GGA) Perdew–Burke–Ernzerhof (PBE)^[13] functional with the semi-empirical dispersion correction Grimme06^[14] was employed and a planewave energy cutoff of 800 eV and a k-point spacing of 0.015 \AA^{-1} over the Brillouin zone was used.

For anhydrous ringwoodite, the initial atomic positions and unit cell parameters were taken from ref. [15]. Different hydrous ringwoodite defect structures (Table 2) were introduced by removing Mg or Si atoms from the anhydrous structure and adding the corresponding number of H atoms around the resulting vacancies. To isolate the defects in the models from their periodic images, $2 \times 1 \times 1$ supercells were used, and the defects were placed with maximum distance within the cells. Hydration levels of 1.6 wt% H_2O and 3.2 wt% H_2O were calculated for each defect motif (Table 2). The optimized unit cell volumes and the resulting slope of a linear volume-hydration level trend are summarized in Table 2.

Table 2. Hydration level, number of cation defect sites, optimized unit cell volume and corresponding slope of a linear volume-hydration level trend of anhydrous ringwoodite and each hydrous defect motif in ringwoodite.

Model	Hydration level / wt% H_2O	No. of defects per 2 1 1 supercell	Optimized unit cell volume	slope
anhydrous	0	0	528.96	-
$V_{\text{Mg}}''+2\text{H}^{**}$	1.6	2	529.99	0.72
	3.2	4	531.29	
$\text{Mg}_{\text{Si}}''+2\text{H}^{**}$	1.6	2	534.15	9.6
	3.2	4	559.69	
$V_{\text{Si}}''''+4\text{H}^{****}$	1.6	1	534.15	3.3
	3.2	2	539.52	
$\text{Mg}_{\text{Si}}V_{\text{Mg}}''''+4\text{H}^{****}$	1.6	1	536.32	4.8
	3.2	2	544.35	
Mixed $V_{\text{Mg}}''+2\text{H}^{**}$ and $\text{Mg}_{\text{Si}}''+2\text{H}^{**}$	1.6	2	536.88	

Results and Discussion

We have synthesized hydrous nanoliter (nL) ringwoodite crystals in two different synthesis runs using a multi-anvil apparatus at 19 GPa and 1350°C and 1400°C, respectively, starting from MgO, SiO₂ and brucite (Mg(OH)₂) as water source to give a composition of Mg₂SiO₄ (run 1) and Mg₂SiO₄ + 11.3wt% H₂O (run 2).

First, the approximate hydration level of the ringwoodite crystals of run 1 and run 2 was estimated by unpolarised FTIR spectroscopy on double-polished thin sections of one crystal of each synthesis run to 0.3 wt% H₂O (run 1, Figure 1 black) and 2.0 wt% H₂O (run 2, Figure 1 blue), respectively. We assume that the crystals within each run have hydration levels within a similar region of 0.3±0.2 wt% H₂O for run 1 and 2.0±0.5 wt% H₂O for run 2. We then have picked a total of three other crystals, crystal A from run 1 and crystals B and C from run 2, with volumes ranging from ~6 to 18 nL (Table 3) and measured preliminary X-ray diffraction patterns in Debye-Scherrer geometry (Figure 2) to check the mineral phase of the crystals on the one hand and on the other hand to evaluate the volume of the unit cell upon hydration, which can then be compared to literature^[16] data.

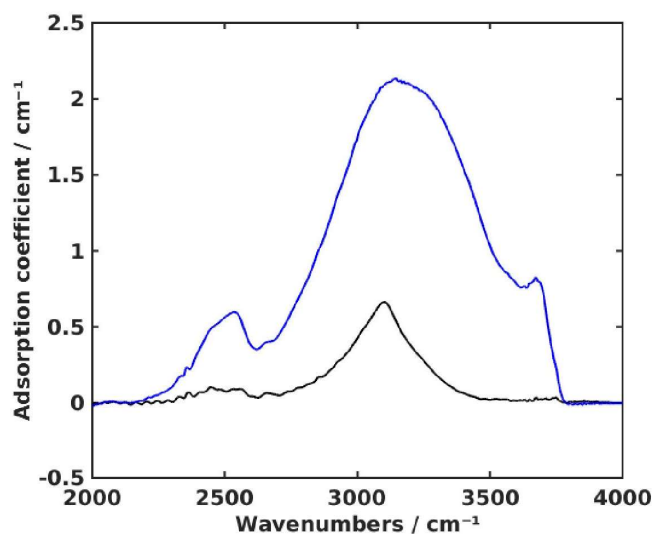


Figure 1. Unpolarised FTIR spectrum (background corrected) of a double-polished hydrous ringwoodite crystal of run 1 (black) and run 2 (blue) normalized to 100 μm thickness. The spectra exhibit the for ringwoodite typical broad OH adsorption features in the range from 2400 cm^{-1} to 3800 cm^{-1} ,^[17,18] arising from the presence of four different defect motifs with additional orientational OH group disorder. From the adsorption coefficient we estimate a hydration level of 0.3(2) and 2.0(5) wt% H₂O for the crystals of run1 and run 2, respectively.

Due to the intrinsic preferred orientation of the crystals A-C some reflections are extinguished and the intensities of the remaining reflections are altered in the XRD patterns of the crystals measured on a powder XRD machine in Debye-Scherrer geometry (Figure 2). This is preventing a full structural refinement, but all observed reflections of the crystals A-C can clearly be assigned to ringwoodite except the broader reflections at 71.24° and 80.90° 2θ , which arise from the diffractometer and are also present in background measurements (Figure 2, indicated by grey dashed lines).

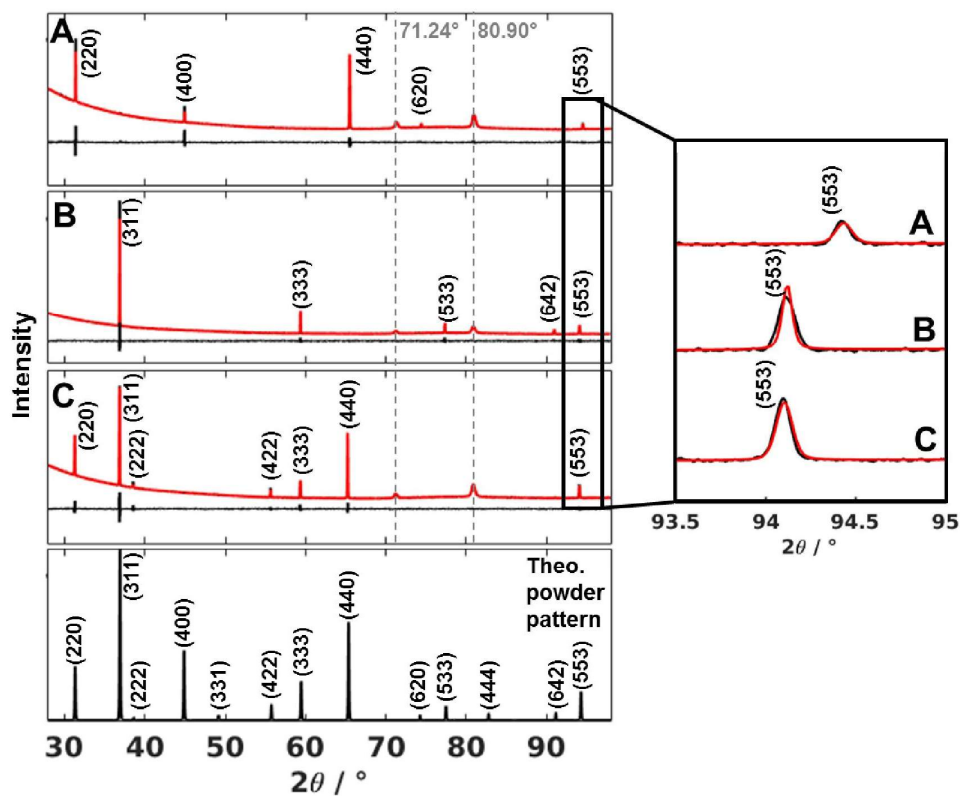


Figure 2. Right: XRD patterns (black) and corresponding Pawley refinements (red) of the hydrous ringwoodite crystals A to C. Below each pattern the difference between refinement and experiment is depicted (grey). For comparison also the expected theoretical powder pattern of ringwoodite with the Miller indices of the reflections is depicted. The grey dashed lines represent the position of the intrinsic background reflections of the XRD machine. Left: Zoom on the 5 5 3 reflex at ~ 94 - 94.5° 2θ for the crystals A to C revealing the slight shift in reflex position representing the expansion of ringwoodites unit cell upon hydration.

The lattice parameters of the spinel-type crystal structure of ringwoodite can be extracted from the 2θ positions of the remaining reflections by applying Pawley refinements^[10]. However, the presence of OH defects within the structure only slightly alter the lattice parameters of ringwoodite. Therefore, the instrument parameters, especially the zero error, of the XRD

machine has to be carefully evaluated on a reference sample, typically Si, and consistent refinement parameter sets have to be used throughout the crystals to yield comparable data. From crystal A to B+C we do observe a significant increase in unit cell volume (Table 3, Figure 5, red) supporting the principal trend of estimated hydration level of 0.3(2) and 2.0(5) wt% for crystals A and B+C, respectively. A comparison of this data with literature of the unit cell volume expansion and OH defect formation mechanisms will be combined with ^1H NMR data and the end of the Results and Discussion section.

Table 3. Volume, hydration level, zero-pressure unit-cell volume and estimated amount of ^1H spins of the three hydrous ringwoodite crystals A-C.

Sample	Volume	Hydration level from FTIR / wt%	No. of ^1H spins	Unit cell volume / \AA^3
A	~ 6 nL	0.3(2)	$\sim 1 \times 10^{15}$	524.3(4)
B	~ 18 nL	2.0(5)	$\sim 8 \times 10^{16}$	528.4(4)
C	~ 9 nL	2.0(5)	$\sim 4 \times 10^{16}$	528.5(4)

We used the same crystals A-C to investigate the feasibility of ^1H solid-state NMR spectroscopy on these small samples allowing for a direct quantification of ringwoodites hydrous defect chemistry. Two of the ringwoodite crystals A+C with less than 10 nL volume were measured using a special piggy-back μMAS setup^[9,19] using a micro-coil leading to enhanced signal due to a higher filling factor of the coil. The number of ^1H spins is estimated to $\sim 1 \times 10^{15}$ (crystal A) and $\sim 4 \times 10^{16}$ (crystal C) from their volume and their hydration levels of 0.3(2) wt% and 2.0(5) wt% H_2O estimated from unpolarised FTIR spectroscopy on unpolished crystals of the same runs, respectively. The other crystal B with a volume of ~ 18 nL (8×10^{16} ^1H spins) was measured using a standard *Bruker* 1.3 mm MAS set-up.

In any case, special attention in the set-up of the ^1H NMR measurements is needed, since any proton containing contamination will significantly contribute to the resulting spectra due to the low amount of sample with intrinsically low amounts of proton spins. Therefore, the MAS rotors were carefully cleaned and dried with air (dry) before placing the crystals on top of teflon inserts in the rotors ensuring that the crystals are placed in the middle of the radio-frequency coil of the probe. Handling of the rotors was accomplished with carefully cleaned tools and/or wearing gloves to avoid any proton-containing contamination or grease of the hands. Still, in any set-up, the ^1H background of the probe and the MAS rotors contribute significantly to the crystal spectra (Figure 3). Therefore, we have measured ^1H background spectra of carefully

cleaned empty MAS rotors for each NMR setup with similar parameters and comparable length as the corresponding ^1H MAS NMR spin-echo of the crystal. Hereby it is favourable to use the same rotor/microtip if possible as for the crystal, including rotor caps and bottoms in the case of a standard probe setup, respectively, since already small changes may lead to severe difficulties in the background correction. Subtracting the background spectrum from the crystal spectrum resulted in the final background-corrected ^1H MAS NMR spectra of the crystals (Figure 3). Hereby, it is important to process, i.e. phase, line-broadening etc., the crystal spectrum similarly and if necessary to scale the background and the crystal spectrum to the similar number of scans. A reasonable background-corrected ^1H MAS NMR spectrum exhibits an even baseline, as well as a clear, but smooth transition between signal and baseline.

Measurement times needed to record reasonable 1D ^1H MAS NMR spectra including background spectra ranged from ~ 2 d for crystals B and C up to ~ 4 d for crystal A. Considering the different sample volume and the measurement times needed to record reasonable spectra, we can qualitatively estimate a trend in hydration level: from crystal A to C the water concentration is expected to increase, whereby the concentration for crystal B and C (from the same run) should be in a similar region, but pressure and temperature gradients within the capsule during the synthesis run can cause a difference in hydration level. This trend agrees also with the hydration levels estimated from unpolarised FTIR spectroscopy on double-polished crystals of run 1 (crystal A) and run 2 (crystals B+C) and the trend of unit cell volume of the crystals A-C.

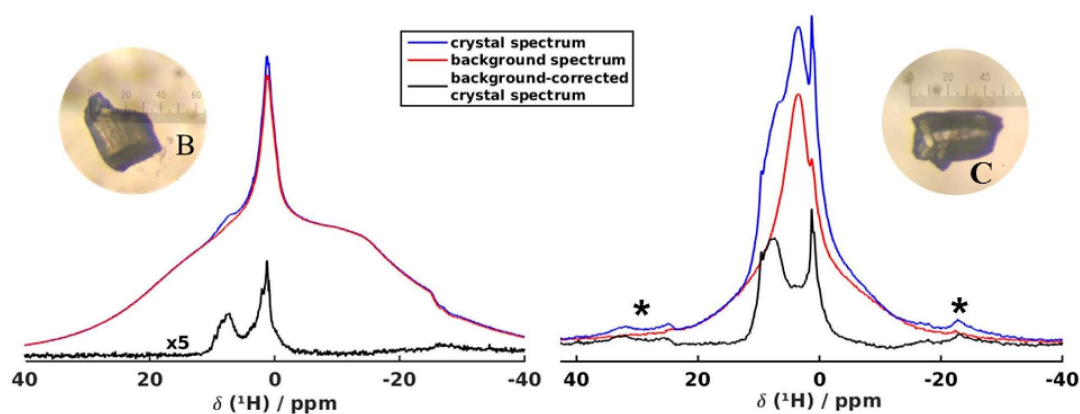


Figure 3. Comparison of the ^1H MAS NMR spectrum (blue) of crystal B (~ 18 nL, left, 62.5 kHz MAS) recorded using a standard Bruker 1.3 mm MAS probe, the ^1H MAS NMR spectrum (blue) of crystal C (~ 9 nL, right, 20 kHz MAS) recorded using a piggyback μMAS probe^[9] and the corresponding ^1H MAS background spectra (red). Subtracting the background from the spectrum of the crystal spectrum yields the background-corrected crystal spectrum (black, right multiplied by factor 5 for crystal B). Small spinning sidebands are observed at 20 kHz MAS (left) and marked by stars.

The experimental ^1H lineshapes of the background-corrected spectra were each fitted by the previously determined individual ^1H chemical shift footprints of the four defect types^[2] (Figure 4). Additionally, two sharper signals at low chemical shift ($\delta(^1\text{H}) = 1.2$ and 0.8 ppm, Figure 4 grey) were fitted manually and are expected to arise from proton species, i.e. Si-OH groups on the surface of the crystals.^[1,2,20] Furthermore, two additional sharp signals are observed at high shifts ($\delta(^1\text{H}) = 9.6$ and 9.1 ppm, Figure 4 grey), which haven't been discussed in previous studies.^[1,2] Due to the high observed shift and narrow half width of these signals, we expect a strong hydrogen bond without considerable distribution of these OH groups. Therefore, it is conceivable that the signals arise from Mg defects, where at least one proton resides outside the vacant octahedron which would lead to a higher energy compared to models with protons inside the vacant octahedron and a strong hydrogen bond.^[21]

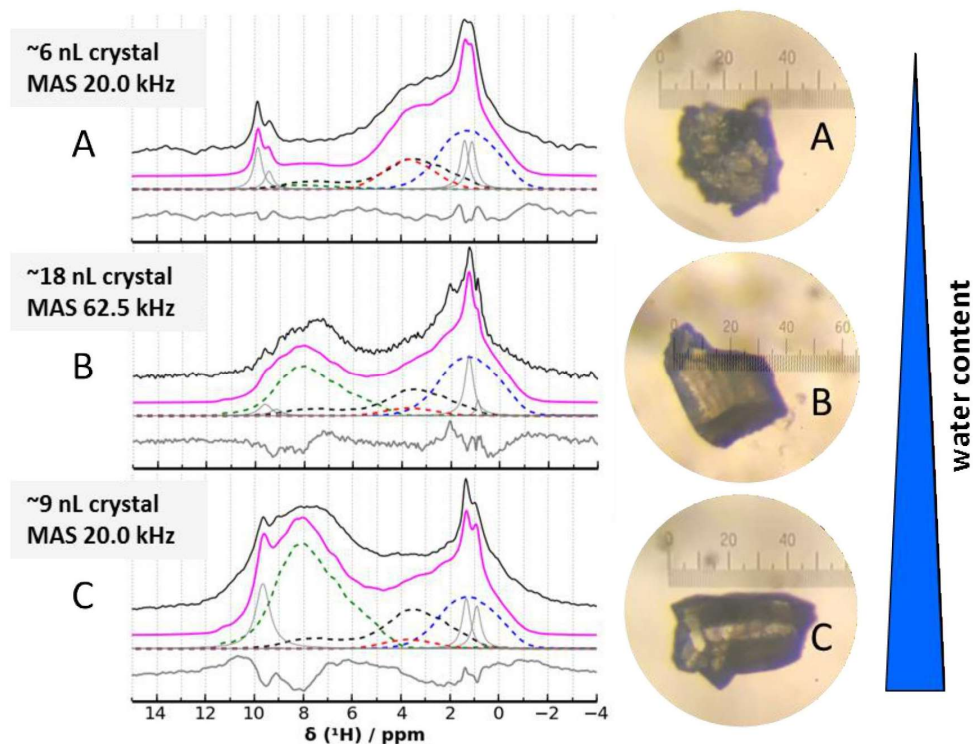


Figure 4. Left: Background-corrected experimental ^1H MAS NMR spectra (black) of hydrous ringwoodite crystals A-C and the corresponding refinements (pink) with the individual ^1H chemical shift footprints for each OH defect motif, V_{Mg} (green dashed), V_{Si} (blue dashed), Mg_{Si} (red dashed) and the coupled $\text{Mg}_{\text{Si}}V_{\text{Mg}}$ (black dashed). Right: Photos of the four crystals A-C with illumination with polarized light from below (transmission). The scale shown can be used to calculate the size of the crystals, whereby 1 digit corresponds to $7\ \mu\text{m}$.

The good agreement between experimental and simulated lineshape for each crystal (Figure 4) additionally shows that the background correction must have worked fairly well and allows to

quantitatively determine the ratio of the four different defect motifs for each crystal sample (Table 4). Here, a clear trend in the ratio of defect motifs is observed: for the crystals A-C the proportion of isolated Mg vacancies (V_{Mg}) is continuously increasing (Figure 4, green dashed), while the proportion of isolated Si defects (V_{Si} blue dashed, Mg_{Si} red dashed), as well as the coupled defect type ($Mg_{Si}V_{Mg}$, black dashed) decreases (Table 4). This would imply an opposite effect than expected from a correlation between unit cell volume and hydration level in literature^[16] which is indicating that up to a hydration level of 2 wt% H_2O mainly isolated Mg vacancies are formed and only at even higher hydration levels ($> 2wt\% H_2O$) significant amounts of Si defects occur.

Table 4. Approximate crystal volumes, defect type ratios and approximate hydration levels for the for hydrous ringwoodite crystals A-C. The error expected for the defect ratio is 5-10%.

Crystal	Crystal volume	$V_{Mg}'' + 2H^{**}$	$V_{Si}'''' + 4H^{****}$	$Mg_{Si}'' + 2H^{**}$	$Mg_{Si}V_{Mg}'''' + 4H^{****}$	water content / wt%
A	~ 6 nL	5.8 %	36.7 %	32.1 %	25.4 %	0.3(2)
B	~ 18 nL	51.2 %	26.8 %	6.0 %	16.0 %	2.0(5)
C	~ 9 nL	66.5 %	14.4 %	4.4 %	14.7 %	2.0(5)

We can now combine the experimentally observed volume cell expansion with the observed trend of OH defect type formation in 1H NMR spectra of the ringwoodite crystals A-C (Figure 2 and 4, Table 3 and 4) and compare our findings with earlier results. Therefore, the correlation between unit cell volume and water concentration, which Ye *et al.*^[16] have found, is reproduced in blue in Figure 5, while two more data points (10 and 11) from literature,^[22,23] which don't fit to this correlation, are depicted in pink. Furthermore, the unit cell volume of the crystals A-C and the ringwoodite powder sample of our previous 1H NMR crystallographic studies^[1,2] (data point 9) are depicted in red. To link defect formation mechanisms with unit cell volumes additionally theoretical volume trends of each defect motif predicted by DFT calculations of anhydrous ringwoodite, as well as of each individual defect motif at ~1.6 and 3.2 wt% hydration level (Table 2), are depicted in Figure 5 as black solid lines. At these OH concentrations each OH defect motif remains isolated in the structure and the zero-pressure unit cell volume show a linear increase of 0.45% (V_{Mg}), 2.0% (V_{Si}) 5.9% (Mg_{Si}) and 2.9% ($Mg_{Si}V_{Mg}$) per 0.5 H pfu each. The calculated zero-pressures volumes were referenced, i.e. linearly shifted, to fit the experimentally determined anhydrous unit cell volume.

Crystal A from this study and sample 2 from literature^[16], which contains approximately 0.15 wt% H₂O,^[16] show a smaller unit cell volume than the anhydrous reference volume chosen from the single-crystal X-ray study of Sasaki *et al.*^[24] indicating that their crystal might have contained a small amount of water and the “true” anhydrous unit cell is indeed a little smaller. For crystals B+C we do observe a significant increase in unit cell volume (Figure 5, red) supporting the principal trend of higher estimated hydration level of 2 wt% for these crystals, but compared to literature (Figure 5, blue) is more pronounced. This could either be due to an offset in the estimation of absolute water contents of the crystals B+C, or due to the formation of a higher proportion of isolated or coupled Si defects compared to the previous results (blue).

However, from the defect ratios observed in the ¹H NMR spectra (Figure 4, Table 4) and the slope of the predicted volume trends extracted from DFT calculations of each defect motif (Figure 5, black solid lines), we calculate the expected slope of the volume expansion for each crystal A-C and data point 9^[1,2]. Since the defect motifs remain isolated in this hydration region (max. 3.2 wt% H₂O), an additive behaviour of the unit-cell volume expansion upon mixing of defect motifs is reasonable. This is also supported by the DFT-predicted volume expansion of a model structure including one isolated Mg vacancy and one isolated Mg_{Si} defect, which is the exactly average value of the corresponding isolated defects (Table 2). From the expected slopes and the experimental unit cell volumes we can then predict the hydration level, which we would expect from the ratio of ¹H NMR experiments (Figure 5, green dots).

For crystal C the hydration level estimated from FTIR, and defect ratio with corresponding volume expansion fits very well, while for crystal B a clear offset is observed (Figure 5, green and red dots). Still the hydration level calculated from the defect ratio could be valid, since the water content was estimated by FTIR on another crystal of the same run and pressure and temperature gradients within the capsule during the synthesis can easily lead to variations in hydration level for crystals growing at different locations in the capsule. For crystal A even a lower hydration level would be expected from NMR due to the high proportion of Si defect observed, but in this low hydration area high uncertainties arise due to a weakly constrained anhydrous unit cell volume.

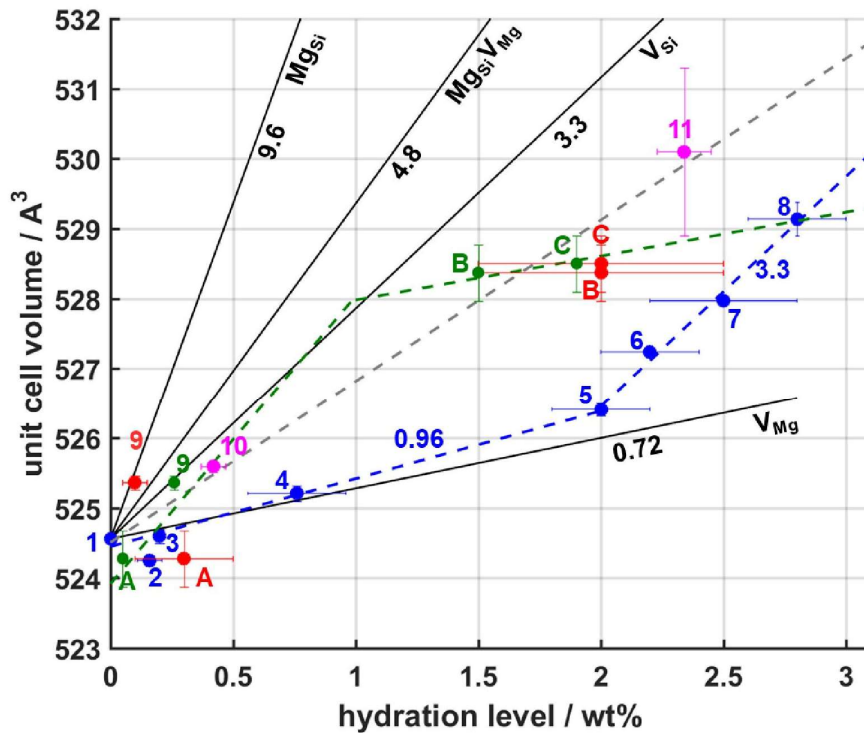


Figure 5. Correlation between unit cell volume and hydration level of hydrous ringwoodite crystals. In blue the correlation published by Ye *et al.*^[16] is indicated for comparison, while red shows the experimental volumes and estimated water concentrations for the crystals A-C of the current study and sample 9 of our previous ¹H NMR study^[1,2]. Pink data points are from literature (Table 5), which don't agree with the trend observed by Ye *et al.*^[16] Black solid lines show the volume trends and slopes predicted for the four hydrous defect types by DFT calculations, which are in well agreement with earlier results by Panera^[25]. Green dots represent the experimental volumes and predicted water concentrations of the crystals A-C (current study) and sample 9 (previous ¹H NMR study) calculated from the ratios of defect types in ¹H NMR spectra (Table 4) and predicted volume trends from DFT. The two possible hydration-volume trends fitting to our data are depicted in grey dashed and green dashed, respectively. The first would be a linear correlation between hydration level and unit cell volume over the whole range (grey dashed) implying a constant defect ratio. The other possibility is a discontinuous trend with a strong slope (~4.1, dark green dashed) up to 1 wt% H₂O indicating the formation of Si defects and at higher hydration levels a linear trend with a weaker slope (0.63) indicating the formation of Mg vacancies in significant proportions.

Our model (Figure 5, green dots), as well as some other volume-hydration data points observed in recent literature (points 10+11, magenta) are quite far off the trend observed by Ye *et al.*^[16] (Figure 5, blue). Therefore, we believe that the ratio and thus the formation of the different defect types in ringwoodite is different. In principal the green and magenta coloured data points can be fitted by a linear correlation (grey dashed), which would imply that the defect ratios should stay constant. However, we do observe a different trend in the ¹H NMR spectra of the crystals (A-C) with a higher proportion of Si defects at low hydration levels and higher proportions of Mg defects at higher hydration levels. For this reason also a discontinuous

volume-hydration behaviour would be conceivable with a strong slope (~ 4.1) up to ~ 1 wt% equivalent of H_2O due to the formation of mainly Si defects and a linear trend with a weaker slope (0.63) at higher hydration levels due to the formation of Mg vacancies (Figure 5, green dashed). Up to now, this hypothesis is weakly constrained and the defect ratio of our powder ringwoodite sample (data points 9^[1,2]) with roughly 50% Mg defects at a low water content wouldn't fit here. However, the synthesis conditions for this sample were different since SiO_2 excess was used, which may render the formation of a higher proportion of Mg vacancies more likely. Furthermore, since it is a powdered sample it may also be slightly inhomogeneous in hydration levels over the crystallites. Anyhow, for unambiguous proof of any hydration-defect formation trend, though, the water concentrations for each crystal need to be accurately determined and more data points, especially in the area of 0.7-1.1 wt% water concentration have to be added to the current results. Furthermore it would be desirable to develop solid models of configurational entropy for the four defect motifs and their mixing in order to model the thermodynamics of the defect formation mechanisms and compare it to experimental results.

Table 5: Unit cell volume, hydration level, as well as calculated hydration level from the defect ratios obtained by ^1H NMR spectroscopy for hydrous ringwoodite samples (Mg endmember) and the corresponding synthesis conditions and starting materials.

Data point	unit cell volume / \AA^3	hydration level / wt%	Calc. hydration level / wt%	synthesis conditions	Starting materials	Reference
A	524.3	0.3(2)	0.05	19 GPa / 1350 °C	MgO+ Mg(OH) ₂ +SiO ₂ (Mg ₂ SiO ₄)	this study
B	528.4	2.0 (5)	1.48	19 GPa / 1400 °C	MgO+ Mg(OH) ₂ +SiO ₂ (Mg ₂ SiO ₄ + 11.3wt% H ₂ O)	this study
C	528.5	2.0 (5)	1.90	19 GPa / 1400 °C	MgO+ Mg(OH) ₂ +SiO ₂ (Mg ₂ SiO ₄ + 11.3wt% H ₂ O)	this study
1	524.56	0	-	22 GPa / 1000°C	-	[16,24]
2	524.25 (7)	0.16 (5)	-	21 GPa / 1500°C	MgO+ Mg(OH) ₂ +SiO ₂ (Mg ₂ SiO ₄ + 4wt% H ₂ O)	[16,26]
3	524.60 (10)	0.200 (4)	-	23 GPa / 1680°C	α -Mg ₂ SiO ₄ + Mg(OH) ₂ +SiO ₂ (5 wt% H ₂ O)	[16,27]
4	525.21 (11)	0.76 (20)	-	22 GPa / 1500°C	MgO+ Mg(OH) ₂ +SiO ₂	[16,26]

5	526.41 (9)	2.0 (2)	-	20 GPa / 1300°C	(Mg ₂ SiO ₄ + 4wt% H ₂ O) α-Mg ₂ SiO ₄ + Mg(OH) ₂ +SiO ₂ (11wt% H ₂ O)	[16,18]
6	527.24 (3)	2.2 (2)	-	19 GPa / 1300 °C	MgO+ Mg(OH) ₂ +SiO ₂ (Mg ₂ SiO ₄ + 11.3wt% H ₂ O)	[16,28]
7	527.97 (7)	2.5 (3)	-	20 GPa / 1250°C	α-Mg ₂ SiO ₄ + Mg(OH) ₂ +SiO ₂ (2.8wt% H ₂ O)	[16]
8	529.14 (24)	2.8 (3)	-	19 GPa / 1300°C	MgO+ Mg(OH) ₂ +SiO ₂ (Mg ₂ SiO ₄ + 11.3wt% H ₂ O)	[16,29]
9	525.36	0.10(5)	0.26	21 GPa / 1100°C	α-Mg ₂ SiO ₄ + 2wt% H ₂ O (liq.) +SiO ₂	[1]
10	525.59(8)	0.42(5)	-	19 GPa / 1500°C	α-Mg ₂ SiO ₄	[22]
11	530.1(1.2)	2.34(11)	-	19 GPa / 1300°C	MgO+ Mg(OH) ₂ +SiO ₂ (Mg ₂ SiO ₄ + 11.3wt% H ₂ O)	[23]

Conclusion and Outlook

Here, we have demonstrated the feasibility of ¹H NMR spectroscopy on trace amounts of protons within nL crystal samples. Though being time consuming, hydrous ringwoodite crystals ≥ 18 nL containing $\geq 8 \times 10^{16}$ ¹H spins (~ 2 wt% H₂O), can be measured using a standard *Bruker* MAS 1.3mm probe, while crystals between 5 and 10 nL containing $\geq 1 \times 10^{15}$ ¹H spins could be measured using piggyback μ MAS techniques^[9]. With any set-up ¹H background treatment is a critical issue, and this problem can only be overcome by measuring and subtracting exact background spectra for each sample setup. The ¹H lineshapes of the background-corrected spectra could be fitted each by our previously established characteristic ¹H chemical shift footprints of each of the four defect motifs^[2] giving access to the defect ratios of each crystal.

Through a combination of the unit cell volume of the same hydrous crystals extracted from preliminary X-ray diffraction measurements in Debye-Scherrer geometry (PXRD machine) with DFT calculations to predict the unit cell volume trends of each defect motif and our NMR data on the ratio of hydrous defect motifs for each crystal we derive a trend of unit cell volume and hydration mechanisms. Currently, our preliminary XRD data and ¹H NMR data suggest that up to ~ 1 wt% mainly Si defects ($V_{Si}'''' + 4H^{****}$, $Mg_{Si}'' + 2H^{**}$, $Mg_{Si}V_{Mg}'''' + 4H^{****}$)

form, while at higher hydration levels the formation of Mg vacancies is favoured ($V_{\text{Mg}}^{2+} + 2\text{H}^{*}$). However, for unambiguous conclusions, it is necessary to determine the water concentration of each crystal accurately, which has not been accomplished yet within this study, and to add more data points especially in the range of 0.8 to 1.1 wt% hydration level.

These results demonstrate the feasibility to comprehensively study ringwoodites defect chemistry on certainly homogenous samples combining ^1H solid-state NMR spectroscopy allowing for direct quantitative analysis of defect motifs, X-ray diffraction to extract the influences of defects on the crystal structure, as well as the possibility to accurately quantify water concentrations by FTIR on double-polished crystals or even by secondary ion mass spectroscopy (SIMS) in the future. Furthermore, for a full understanding of ringwoodites defect chemistry it would be desirable to model the thermodynamics of each hydration mechanism, as well as their mixing, and to compare the results with systematic experimental findings from comprehensive studies. Finally, this could lead to a reasonable model of the impact of ringwoodites defect chemistry on the transport properties of the transition zone of the Earth's mantle.

Acknowledgements

H. G. acknowledges the “Fonds der Chemischen Industrie” for financial support in form of the ‘Chemiefonds-Fellowship’.

References

- [1] H. Grüninger, K. Armstrong, D. Greim, T. Boffa-Ballaran, D. J. Frost, J. Senker, *J. Am. Chem. Soc.* **2017**, *139*, 10499–10505.
- [2] H. Grüninger, A. Schmutzler, R. Siegel, K. Armstrong, D. J. Frost, J. Senker, *Phys. Chem. Chem. Phys.* **2018**, *20*, 15098–15105.
- [3] D. J. Frost, *Elements* **2008**, *4*, 171–176.
- [4] T. Inoue, H. Yurimoto, Y. Kudoh, *Geophys. Res. Lett.* **1995**, *22*, 117–120.
- [5] D. G. Pearson, F. E. Brenker, F. Nestola, J. McNeill, L. Nasdala, M. T. Hutchison, S. Matveev, K. Mather, G. Silversmit, S. Schmitz, et al., *Nature* **2014**, *507*, 221–4.
- [6] J. Hustoft, G. Amulele, J. I. Ando, K. Otsuka, Z. Du, Z. Jing, S. I. Karato, *Earth Planet. Sci. Lett.* **2013**, *361*, 7–15.
- [7] S.-M. Thomas, C. R. Bina, S. D. Jacobsen, A. F. Goncharov, *Earth Planet. Sci. Lett.* **2012**, *357–358*, 130–136.
- [8] M. Koch-Müller, D. Rhede, *Am. Mineral.* **2010**, *95*, 770–775.

- [9] J. O. Brauckmann, J. W. G. (Hans) Janssen, A. P. M. Kentgens, *Phys. Chem. Chem. Phys.* **2016**, *18*, 4902–4910.
- [10] G. S. Pawley, *J. Appl. Crystallogr.* **1981**, *14*, 357–361.
- [11] A. A. Coelho, **2012**.
- [12] S. J. Clark, M. D. Segall, C. J. Pickard, P. J. Hasnip, M. J. Probert, K. Refson, M. C. Payne, *Z. Krist.* **2005**, *220*, 567–570.
- [13] J. P. Perdew, K. Burke, M. Ernzerhof, *Phys. Rev. Lett.* **1996**, *77*, 3865–3868.
- [14] S. Grimme, *J. Comput. Chem.* **2006**, *27*, 1787–1799.
- [15] W. H. Baur, *Am. Mineral.* **1972**, *57*, 709–31.
- [16] Y. Ye, D. A. Brown, J. R. Smyth, W. R. Panero, S. D. Jacobsen, Y.-Y. Chang, J. P. Townsend, S.-M. Thomas, E. H. Hauri, P. Dera, et al., *Am. Mineral.* **2012**, *97*, 573–582.
- [17] W. R. Panero, J. R. Smyth, J. S. Pigott, Z. Liu, D. J. Frost, *Am. Mineral.* **2013**, *98*, 637–642.
- [18] Y. Kudoh, T. Kuribayashi, H. Mizobata, E. Ohtani, *Phys. Chem. Miner.* **2000**, *27*, 474–479.
- [19] A. Brinkmann, S. K. Vasa, H. Janssen, A. P. M. Kentgens, *Chem. Phys. Lett.* **2010**, *485*, 275–280.
- [20] J. M. Griffin, A. J. Berry, D. J. Frost, S. Wimperis, S. E. Ashbrook, *Chem. Sci.* **2013**, *4*, 1523.
- [21] L. Li, J. Brodholt, D. Alfè, *Phys. Earth Planet. Inter.* **2009**, *177*, 103–115.
- [22] K. Schulze, H. Marquardt, T. Kawazoe, T. Boffa Ballaran, C. McCammon, M. Koch-Müller, A. Kurnosov, K. Marquardt, *Earth Planet. Sci. Lett.* **2018**, *498*, 9–16.
- [23] J. Wang, S. V Sinogeikin, T. Inoue, J. D. Bass, *Geophys. Res. Lett.* **2006**, *33*, L14308.
- [24] S. Sasaki, C. T. Prewitt, Y. Sato, E. Ito, *J. Geophys. Res.: Solid Earth* **1982**, *87*, 7829–7832.
- [25] W. R. Panero, *J. Geophys. Res.* **2010**, *115*, B03203.
- [26] J. R. Smyth, C. M. Holl, D. J. Frost, S. D. Jacobsen, F. Langenhorst, C. A. McCammon, *Am. Mineral.* **2003**, *88*, 1402–1407.
- [27] Y. Kudoh, T. Kuribayashi, H. Mizobata, E. Ohtani, S. Sasaki, M. Tanaka, *J. Mineral. Petrol. Sci.* **2007**, *102*, 8–11.
- [28] T. Inoue, D. J. Weidner, P. A. Northrup, J. B. Parise, *Earth Planet. Sci. Lett.* **1998**, *160*, 107–113.
- [29] H. Yusa, T. Inoue, Y. Ohishi, *Geophys. Res. Lett.* **2000**, *27*, 413–416.

4.4 Detection of oxygen vacancy ordering in aluminous bridgmanite in the Earth's lower mantle

This work is the result of a cooperation between the Inorganic Chemistry III and the Bavarian Research Institute of Experimental Geochemistry and Geophysics (BGI) of the University of Bayreuth.

H. Grüninger and Z. Liu contributed equally.

My contributions are:

- conception and main-authorship of the article
- measurement of all 1D ^{27}Al MAS NMR spectra and the 2D ^{27}Al STMAS NMR spectrum
- set-up of DFT simulations of various Al defect models in bridgmanite
- evaluation of all NMR data and DFT simulations

The contribution of all other authors are:

- conception and co-authorship of the article
- high-pressure synthesis of the bridgmanite samples
- EPMA, XRD, SEM and Raman analysis of the samples
- support of NMR measurements

Detection of oxygen vacancy ordering in aluminous bridgmanite in the Earth's lower mantle

Helen Grüninger^a, Zhaodong Liu^{b*}, Renée Siegel^a, Tiziana Boffa Ballaran^b, Tomoo Katsura^b, Jürgen Senker^{a*}, Daniel J. Frost^{b*}

To be submitted to Nature Geoscience

^aInorganic Chemistry III, University of Bayreuth, Universitätsstr. 30, 95447 Bayreuth, Germany.

^bBayerisches Geoinstitut, University of Bayreuth, Universitätsstr. 30, 95447 Bayreuth, Germany.

*zhaodong.liu@uni-bayreuth.de; *juergen.senker@uni-bayreuth.de; *dan.frost@uni-bayreuth.de

The formation of oxygen vacancies in MgSiO₃ bridgmanite due to Al substitution will have a major impact not only on the physical and elastic properties of this mineral, but also on the solubility of volatile components such as water and noble gases, which should have important consequences for the Earth's deep volatile cycle. A key aspect in the role of oxygen vacancies in bridgmanite, however, is their structure and distribution, which remain entirely unexplored. Here we present ²⁷Al magic angle spinning nuclear magnetic resonance (MAS NMR) spectra collected for six aluminous bridgmanite samples that were also characterized by X-ray diffraction (XRD) and electron-probe microanalysis (EPMA). Moreover, 2D ²⁷Al satellite-transition (ST) MAS spectroscopy was employed to enhance the resolution. In the

resulting spectra four-, five- and six-fold coordinated Al species are resolved, in addition to an Al coordination higher than eight. In combination with Density Functional Theory (DFT) calculations the quantitative analysis of the 1D NMR spectra revealed that both the charge-coupled (CC) and the oxygen vacancy (OV) substitution mechanisms are present. OV defects seem to be favored in Mg-rich compositions and at low defect concentrations. Additionally, OV defects tend to form clusters due to the high mobility of defects in the perovskite structure.

Cation substitution in minerals affects their physical and elastic properties as well as their transport properties (Kurnosov et al. 2017). For this reason the substitution of trivalent cations in the MgSiO_3 bridgmanite structure, the dominant mineral of the Earth's lower mantle, has been the focus of several studies (e.g., McCammon 1997; Navrotsky 1999; Brodholt 2000). MgSiO_3 bridgmanite has an orthorhombic perovskite-type structure with Si in octahedral coordination (B site) and Mg occupying a larger dodecahedral site (A site). Al, together with Fe^{3+} , is the most abundant trivalent cation substituting into bridgmanite. Its incorporation may occur by two competing mechanisms: one involving the substitution of Si by Al with consequent formation of oxygen vacancies and one involving the coupled substitution of Mg and Si by 2 Al. The former mechanism, hereafter referred as OV, is characterized by the stoichiometric component $\text{MgAlO}_{2.5}$. The solid solution $\text{MgSiO}_3 -$

$\text{MgAlO}_{2.5}$ is expected to be favored in a bulk pyrolitic mantle composition where the presence of ferropicicase ((Fe,Mg)O) in equilibrium with bridgmanite gives rise to a Mg/Si ratio larger than 1 (Irifune et al., 1994). The latter mechanism, hereafter referred as CC, is represented by a solid solution in the system $\text{MgSiO}_3 - \text{Al}_2\text{O}_3$ and is expected to be the dominant mechanism in SiO_2 -rich systems as well as at the highest pressures of the Earth's lower mantle (Liu et al. 2017). The two mechanisms are expected to have different impacts on the elastic properties, diffusivity, conductivity and rheology of bridgmanite, for example OV-rich bridgmanite can store water in a manner similar to ceramic perovskites (Navrotsky et al. 2003) in contrast with a vacancy free bridgmanite which can accommodate only negligible amount of OH (Bolfan-Casanova et al. 2000). Any change in the physical and transport properties of bridgmanite will depend on the local distribution of Al and OV in its structure. However, attempts at characterizing the OV distribution in Al-bearing bridgmanite have been so far unsuccessful. Both X-ray absorption- and NMR-spectroscopy studies of the local structure around the Al atoms in bridgmanite have resulted in spectra consistent with Al in 6-fold or higher coordination (Andrault et al. 1998; Stebbins et al. 2001, 2003, 2006; Palke et al. 2012). The bridgmanite samples investigated in these previous studies, however, appeared to have slightly inhomogeneous compositions, or coexisted with stishovite or contained Fe^{3+} which charged balanced the Al incorporation.

In this study we have taken a number of measures to provide optimal samples for the characterization of OV-bearing bridgmanite; we synthesized chemically homogeneous Al-bearing bridgmanite from vitreous starting materials with different compositions; we have buffered the Si and Al activities in these samples through the presence of additional phases such as periclase (OV) or corundum (CC); we have recovered the samples from the synthesis runs in the form of well-sintered pellets, which have then been accurately characterized without being ground in order to avoid the formation of amorphous material. We have collected ^{27}Al MAS NMR spectra for all samples and additionally acquired a 2D ^{27}Al STMAS spectrum for one sample to derive representative parameters for the isotropic chemical shift and the quadrupolar interaction for each Al environment in order to guide the deconvolution of the 1D spectra. The 2D STMAS experiment provides increased resolution by separating the signals according to their isotropic interaction components, i.e. isotropic chemical shifts and the isotropic part of the second order quadrupolar effect. Finally, we have performed DFT calculations to generate NMR parameters for different CC and OV defect configurations to be compared with the experimental results in order to identify the possible Al defect and oxygen vacancies distributions in the bridgmanite structure.

Al-bearing bridgmanites

Six Al-bearing bridgmanite samples have been investigated in this study: three samples were synthesized along the join $\text{MgSiO}_3\text{--MgAlO}_{2.5}$ and two along the join $\text{MgSiO}_3\text{--Al}_2\text{O}_3$ (Table 1) from glassy starting materials using a multi-anvil apparatus (see methods and Tables S1 and S2). Moreover, a further bridgmanite sample was synthesized using 70 wt% of enstatite containing 5 mol% of Al_2O_3 and 30 wt% of MgO (sample F). All samples were recovered from the high-pressure high-temperature runs in the form of well-sintered pellets. These were characterized by means of scanning electron microscope (Methods, Fig. S1) and X-ray powder diffraction (Methods, Fig. 1). They consisted either of only bridgmanite or of bridgmanite plus MgO or Al_2O_3 (Table 1, Table S2). The proportions of the stoichiometric CC and OV components present in the synthesized Al-bearing bridgmanites (Table 1) were determined from their compositions, as measured by electron probe micro analyzer (EPMA, Methods and Table S3), according to the following expression:



Table 1: Al-bearing bridgmanite samples investigated in this study. Uncertainties on OV and CC contents are calculated from the microprobe analysis uncertainties reported in Table S3.

Starting materials	Synthesised products	Brg compositions	OV (mol%)	CC (mol%)
A (En ₉₅ Brm ₅)	Brg	Mg _{0.991} Al _{0.050} Si _{0.959} O _{2.984}	3.2 (9)	0.9 (1)
B (En ₉₀ Brm ₁₀)	Brg	Mg _{0.975} Al _{0.100} Si _{0.925} O _{2.975}	5.0 (8)	2.5 (5)
C (En ₈₀ Brm ₂₀)	Brg + Per	Mg _{0.937} Al _{0.161} Si _{0.902} O _{2.982}	3.5 (7)	6.3 (4)
D (En ₉₅ Cor ₅)	Brg	Mg _{0.952} Al _{0.101} Si _{0.947} O _{2.998}	0.5 (8)	4.8 (3)
E (En ₇₅ Cor ₂₅)	Brg + Cor + trace Sti	Mg _{0.884} Al _{0.235} Si _{0.881} O _{2.999}	0.3 (7)	11.6 (4)
F *	Brg + Per	Mg _{0.968} Al _{0.099} Si _{0.933} O _{2.983}	3.5 (9)	3.2 (6)

Brm = MgAlO_{2.5}; Brg = bridgmanite; Cor = Al₂O₃; Per = periclase; Sti = stishovite

*The F starting material consisted of a mixture of 70 wt.% enstatite synthesized from glass D and 30 wt.% MgO

NMR spectroscopy

The ²⁷Al MAS NMR spectra collected for the six Al-bearing bridgmanite samples A to F are depicted in Figure 1. All spectra show a sharp resonance at ~7 ppm, corresponding to Al in a symmetric octahedral environment, and a broad signal with a maximum at ~-20 ppm, indicating a larger coordination number and a distorted environment for the Al species. These signals are consistent with the NMR spectra reported in earlier studies on Al-bearing bridgmanite (Stebbins et al. 2001, 2003, 2006; Palke et al. 2012) and are, therefore, assigned to Al on the B and the A site, respectively. Both can be explained by the CC substitution mechanism. The NMR spectra of samples E and C exhibit an additional signal in the typical chemical shift range of octahedrally coordinated Al (~14.7 ppm), which is characteristic for corundum (Stebbins 2006; Palke et al. 2012), and consistent with its presence determined by XRD. Furthermore, in the spectra of samples

A-C and F broad and overlapping resonances in the typical shift range for tetra- (~50-80 ppm) and penta-coordinated (~20-50 ppm) Al are observed (Smith 1993; MacKenzie and Smith 2002; Choi et al. 2009).

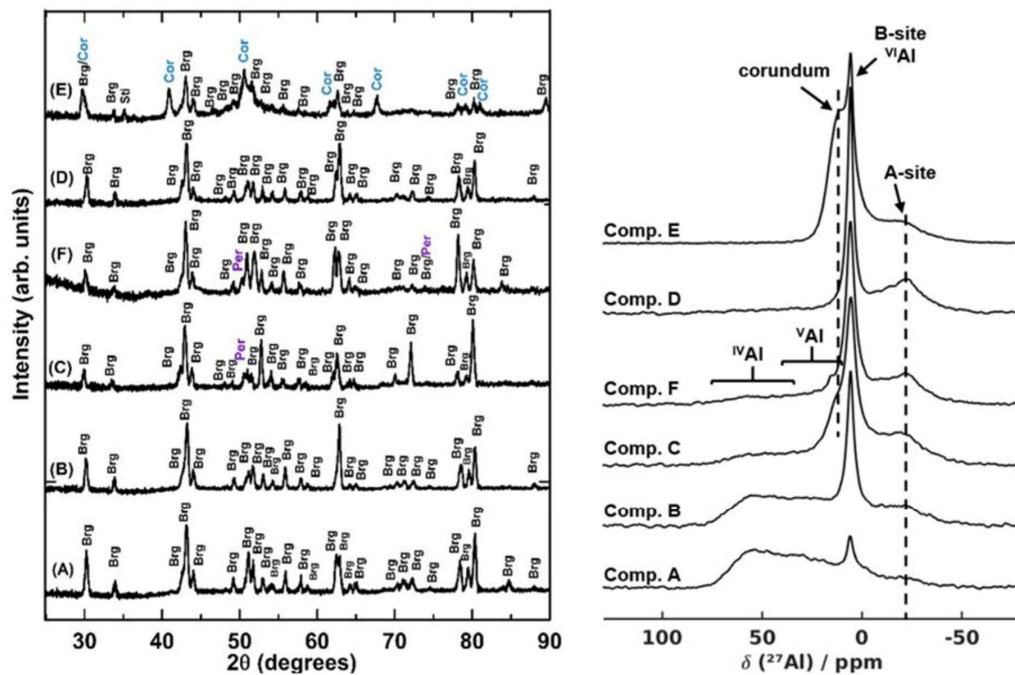


Fig. 1: XRD (left) and ²⁷Al MAS NMR (right) spectra of Al-bearing bridgmanite samples. Left: All samples are comprised predominantly of bridgmanite. In samples C and F bridgmanite coexists with periclase and sample E contains some corundum. Note that periclase does not contain any Al and, therefore, does not have an ²⁷Al NMR signature. Brg = bridgmanite; Cor = corundum; Per = periclase. Right: All ²⁷Al MAS NMR spectra exhibit resonances assigned to Al on the A and B site of bridgmanite, which arise due to the CC mechanism. Additionally, the spectra of sample A-C and F exhibit broad resonances in the typical shift range of tetra- and penta-coordinated Al species, which are expected to arise due to the OV mechanism. Corundum resonances are observed in the spectra of samples C and E.

The presence of a small amount of ^{IV}Al was observed in previous studies and attributed to the probable presence of a glassy phase left uncrystallized (Stebbins et al. 2001, 2006; Palke et al. 2012). However, significant proportion of amorphous material seems unlikely in our case, since no hints of such material are present in the XRD patterns (Figure 1). Furthermore, Raman spectra for the lattice mode region were collected for several points of each bridgmanite sample after the NMR measurements (Methods, Fig S2). The Raman spectra of sample B-F show well defined bands typical for bridgmanite's A and B modes. Only for sample A (Fig. S2) two of the five analyzed points show broad features in the Raman spectra suggesting the presence of some amorphous material. However, the intensity of the broad signals between 60-20 ppm in the NMR spectra is very pronounced rendering it very unlikely that it originates from an amorphous side phases. As a consequence, these resonances appear to be characteristic spectral features of Al-bearing bridgmanite.

Microscopic picture of the Al defect formation

In order to develop a microscopic understanding of the CC and OV incorporation mechanisms, quantitative constraints on the coordination of the observed Al sites are required and their characteristic isotropic chemical shifts δ_{iso} , quadrupolar couplings C_Q and the asymmetry

parameters η_Q need to be determined. To validate the spectral assignment and to constrain the Al distribution within bridgmanite these NMR parameters are then compared with those derived from DFT calculations of various structural models for the CC and OV mechanisms.

We used the observed Al resonances (δ_{iso} , C_Q , η_Q) of sample D as a reference for the spectral signature of the CC defects, since the EPMA analysis of this sample suggests only a minor contribution of OVs (Tab. 1). The results of the deconvolution of the ^{27}Al MAS NMR spectrum are summarized in Table 2 and Figure S3 and are consistent with earlier reports (Stebbins et al. 2003; 2006). Both the chemical shift and the quadrupolar coupling interaction show a distribution consistent with disorder of the bond distances, angles and second-neighbor cations around the Al defects in the bridgmanite structure.

EPMA analysis suggests the highest OV content for sample B (Tab. 1), which therefore serves as a reference for this defect type. Its NMR spectrum exhibits resonances covering the frequency range between -40 and 70 ppm (Fig. 1). Therefore, it is necessary to separate the Al resonances according to their isotropic interaction components, i.e. isotropic chemical shifts and scaled isotropic parts of the second order quadrupolar effect, in the indirect dimension of a 2D ^{27}Al STMAS spectrum (Fig. 2) (Gan 2000; Kwak and Gan 2003; Ashbrook and Wimperis 2004). Four signals were clearly observed (Fig. 2) confirming the presence of the following four Al environments in bridgmanite: $^{\text{IV}}\text{Al}$, $^{\text{V}}\text{Al}$, $^{\text{VI}}\text{Al}$ and Al with a higher coordination number. Each

signal has been fitted along the 1D horizontal rows (Fig. 2b) to extract their characteristic NMR parameters (Fig. 3g, Tab. 2). Whereas the shape of the signal at -20 ppm agrees well with the results obtained for sample D, the signal for ^{VI}Al at ~7 ppm is broader and requires a second component, suggesting that there is an additional octahedral environment present (Fig. 2, Tab. 2) related to the OV mechanism.

These results are corroborated by ^{27}Al MAS echo spectra recorded for samples A and B (Fig. S4) at higher magnetic field (23.5 T), which changes the ratio between influence of the chemical shift and the quadrupolar interaction on the spectral lineshape.

Table 2. Experimental isotropic chemical shift and quadrupolar parameters of the different Al resonances extracted from the 1D ^{27}Al MAS NMR spectrum of sample D and from the 2D ^{27}Al STMAS spectrum of sample B.

Sample	Al species	δ_{iso} / ppm	C_Q / MHz	η_Q^*	
D	Al (A site)	-3.9 ± 0.5	7.3 ± 0.5	0.9	MAS NMR
D	^{VI}Al (B site)	7.0 ± 0.3	2.0 ± 0.2	0.85	MAS NMR
B	Al (A site)**	-	-	-	STMAS
B	^{VI}Al	7.2 ± 0.3	1.9 ± 0.2	0.85	STMAS
B	^{VI}Al	12 ± 2	4.9 ± 0.5	0.4	STMAS
B	^{V}Al	35 ± 2	6.6 ± 0.5	0.5	STMAS
B	^{V}Al	43 ± 2	8.0 ± 0.5	0.5	STMAS
B	^{IV}Al	66 ± 2	7.7 ± 0.5	0.0	STMAS

* η_Q of the signals were chosen to fit the lineshape best, but not refined since the influence on the lineshape is weak

**Due to a very low signal to noise ratio of the Al at the A site the signal was deconvoluted with the values obtained from sample D

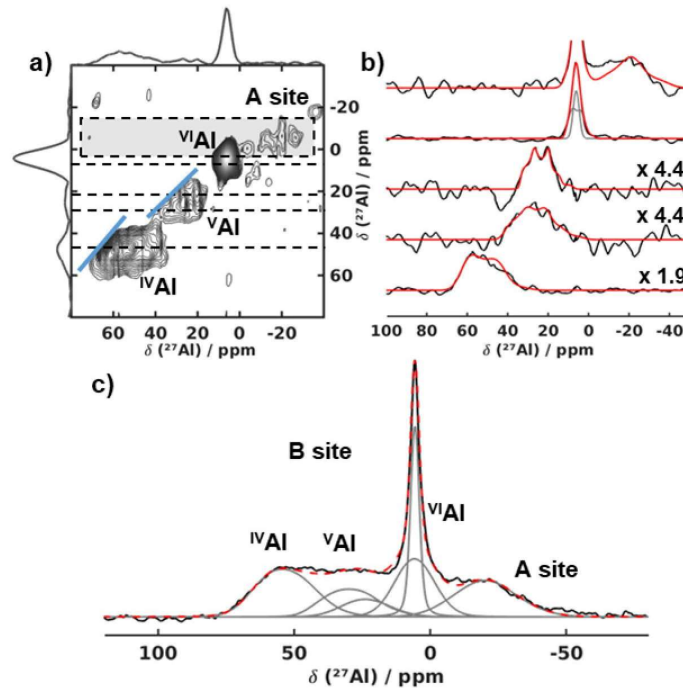


Fig. 2: (a) 2D ^{27}Al STMAS NMR spectrum, (b) fits of the 1D row signals and (c) resulting Gaussian fit of the ^{27}Al MAS NMR of sample B. a) ^{27}Al STMAS NMR spectrum of sample B revealing four distinct Al environments typical for $^{\text{IV}}\text{Al}$ and $^{\text{V}}\text{Al}$ in addition to $^{\text{VI}}\text{Al}$ and Al on the A site of bridgmanite. The blue lines highlight the effect of the distribution of isotropic chemical shifts. b) 1D rows (black) of the ^{27}Al STMAS spectrum indicated by dashed lines and the corresponding fits (red) of the quadrupolar parameters (Tab. 2). The top spectrum results from the sum of the rows in the area indicated by the translucent grey rectangle to enhance signal-to-noise ratio. c) Exemplary fit of the central transition (red dashed) of the quantitative ^{27}Al MAS NMR spectrum of sample B (black) with six Al sites (Tab. 2).

To support the assignment of the ^{27}Al NMR spectra, quantum-mechanical calculations of the NMR parameters (isotropic ^{27}Al chemical shift, quadrupolar parameters) for various structural Al defect configurations for the CC and the OV mechanisms (Table S5) were carried out.

For the CC substitution mechanism two defect models were calculated (Fig. 3a, b), in which one Mg is substituted by Al (A site) and one Si is replaced by Al either at the nearest-neighbour or at the next nearest-neighbour B site (Fig. 3a, b). For the OV substitution mechanism in total 12 models were considered in order to take into account the possible formation of isolated oxygen vacancies (Fig. 3c, Fig. S5), as well as the formation of OV dimers (Fig. 3d-f, Fig. S6 to S8). Isolated oxygen vacancies shared between two B sites result in the formation of penta-coordinated Al species (Fig 3c, Fig. S5). However, in order to form tetrahedral Al³⁺ in the bridgmanite structure, short range ordering of oxygen vacancies must occur, as previously observed for Fe-bearing CaTiO₃ perovskite (Becerro et al. 1999; McCammon et al. 2000) (Fig. 3e, Fig. S6 to S8). We also have simulated configurations similar to those reported by McCammon et al. (2000) in which two penta-coordinated sites are occupied by one Al and by one Si, with the other Al atom substituting Si on an octahedral site (Fig. 3f, Fig. S8) in order to test the possibility of vacancies not directly associated with the Al coordination, as suggested in previous studies (Stebbins et al. 2006).

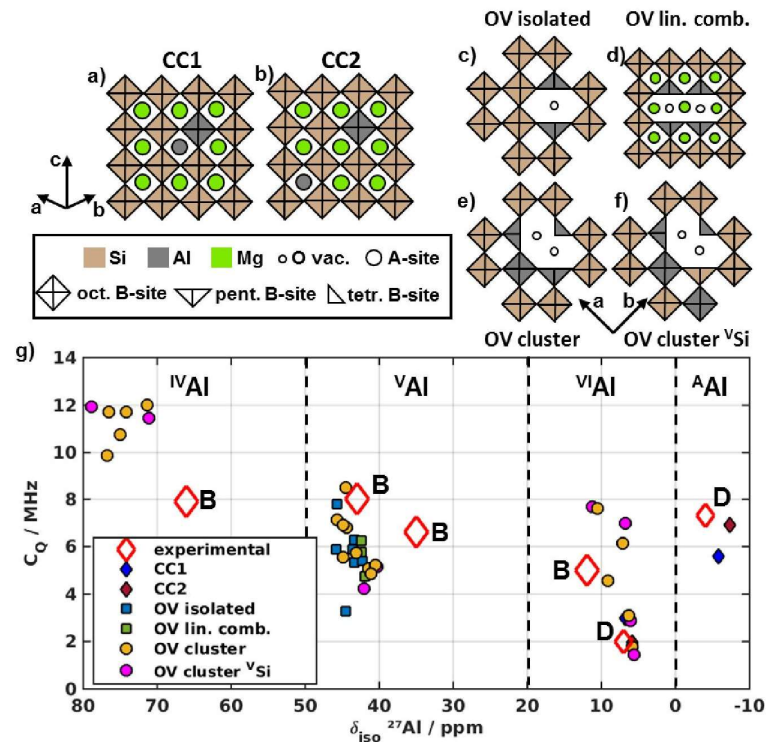


Fig. 3. Examples of potential Al defect structures in bridgmanite for the CC mechanism (a, b) and the OV mechanism (c-f) and g) corresponding calculated quadrupolar coupling C_Q and isotropic chemical shift δ_{iso} of the Al defect sites in bridgmanite in comparison to the experimental average estimates (red diamonds) of the experimental Al resonances of sample B and D. For the CC mechanism two models were calculated: a) Al on two adjacent A and B sites (CC1, blue diamonds) and b) two Al on non-neighboring A and B sites (CC2, dark red diamonds). For the OV mechanism simple oxygen vacancies of O1 and O2 (exemplary for an O2 vac. in c, blue squares), as well as a linear combinations of two O1, two O2 and O1 and O2 (exemplary for two O1 vac. in d, green squares) resulting in a solely ^VAl environment were considered to investigate possible distortions of the structure. Furthermore, partial clustering of OVs as dimers with O2 (exemplary in e, f) and a combination of O1 / O2 vacancies (orange circles) resulting in ^{IV}Al, ^VAl and ^{VI}Al environments were calculated. In this case, ^{VI}Al sites in and out of plane with the ^VAl and ^{IV}Al sites were also considered. Additionally, the ^{VI}Al site was put adjacent (e) and non-neighboring to other Al defect sites and configurations with one Al and one Si on penta-coordinated sites (f, pink) were investigated resulting in a total of 7 models for the OV dimers. A technical description of each Al defect model is given in the Supporting Information.

The calculated NMR parameters for the CC models (Fig. 3a, b) are in in very good agreement with the experimental δ_{iso} and C_Q values of the signals observed in sample D (Fig. 3g). A negative isotropic chemical shift is only predicted for Al on the A site of the perovskite structure (CC mechanism), allowing for an unambiguous assignment of the signal at -20 ppm exclusively to Al on the A site via the CC mechanism. The calculated energy of the CC model with non-adjacent Al sites (Fig. 3b, CC2) is slightly larger ($\Delta E \sim 10 \text{ kJmol}^{-1}$) than in the case with Al on adjacent sites (Fig. 3a, CC1), but the calculated NMR parameters (Table S5) of the former show a better agreement with the experimental values (Fig. 3g). Nevertheless, we consider both scenarios to be in agreement with the experimental NMR spectra.

The OV models give rise to a range of NMR parameters (Table S5) which agree well with the experimental values obtained for the $^{\text{IV}}\text{Al}$, $^{\text{V}}\text{Al}$ and $^{\text{VI}}\text{Al}$ environments (Fig. 3g). Simple oxygen vacancies even when clustering linearly (Fig. 3c+d) only lead to five-fold coordinated Al. The resulting isotropic chemical shift and quadrupolar parameters fit well to the experimental data (Fig. 3g). It is remarkable that these defects do not lead to a significant distortion of the structure.

In contrast, if two neighboring oxygen vacancies associated with one octahedron are created, tetrahedral, octahedral and two pentagonal Al environments result (Fig. 3e). Furthermore, configurations with one Al and one Si on the penta-coordinated sites (Fig. 3f) lead to the formation of an additional octahedral Al environment. The latter being slightly favored energetically (ΔE -

15 kJmol⁻¹ to -35 kJmol⁻¹). Assuming that combinations of all configurations are possible, for each tetrahedrally coordinated Al either one or two penta-coordinated and octahedral Al sites arise.

For all considered defect models the simulated isotropic chemical shift and quadrupolar coupling constants are of the same order of magnitude compared to the experimental data. For the tetrahedral site a slight overestimation of the NMR parameters is observed, which we attribute to a stronger distortion in the simulations carried out at 0 K and ambient pressure. In the case of the octahedral Al environments, the NMR parameters of those defects not directly associated with the oxygen vacancies fit the experimental data slightly better. This supports the migration of OV potentially due to a high mobility of oxygen ions at the synthesis conditions. As a consequence, they exhibit a very similar spectral signature compared to octahedral sites created by the CC substitution mechanism.

Oxygen vacancy distribution.

The 1D ²⁷Al MAS NMR spectra for all samples were deconvoluted using the characteristic parameters for each Al environment (Tab. 2) in order to derive the relative intensities of each Al coordination (Tab. S4). We use the relative integral of the A site resonance as a measure for Al incorporated due to the CC mechanism, since it is well separated from the other resonances. According to the nature of the CC mechanism the same intensity is assigned to the octahedral B

site. The DFT results imply that for the OV component, the intensities of ^{IV}Al , ^{V}Al and the remaining ^{VI}Al environments need to be summed (Tab. 3). The resulting OV/CC ratios are in excellent agreement with those obtained from the compositional analysis within analytical uncertainties (Table 3).

Table 3. Quantities (in %) of the ^{IV}Al , ^{V}Al , ^{VI}Al and ^{A}Al species assigned to the OV component and the CC component, respectively, and resulting OV/CC (%) ratio from the 1D ^{27}Al MAS NMR spectra. The OV/CC ratio obtained from the chemical compositions is reported for comparison.

Samples	Al p.f.u.	^{IV}Al %	^{V}Al %	^{VI}Al % (OV / CC)	^{A}Al %	OV/CC NMR	OV/CC EPMA
A	0.050	44	23	12 / 11	11	79 (2) / 21 (2)	78 (7) / 22 (7)
B	0.100	22	21	17 / 20	20	60 (3) / 40 (3)	67 (4) / 33 (4)
C	0.161	11	11	23 / 27	27	45 (3) / 55 (3)	36 (6) / 64 (8)
D	0.101	2	3	5 / 45	45	10 (4) / 90 (4)	9 (12) / 91 (11)
E	0.235	--	--	-- / 50	50	0 (2) / 100 (2)	2 (4) / 98 (5)
F	0.099	10	9	22 / 30	30	41 (2) / 59 (2)	49 (8) / 51 (7)

Independent of the Al content in all samples from MgO-rich syntheses five- and four-fold coordinated Al species are formed due to oxygen vacancies. The occurrence of tetrahedrally coordinated Al, in particular, demonstrates the presence of OV clusters according to Fig. 3e, f. For some samples (C, F, Tab. 3), we observed $^{VI}Al : ^{IV}Al$ ratios greater than one, which strongly hints towards a migration of OVs, leading to some ^{VI}Al not directly associated to the OV defect site.

This matches the results of the DFT calculations that indicate slightly lower energies for these configurations. However, since the migration of the OV's changes the intensity ratio between ^{IV}Al , ^{V}Al and ^{VI}Al environments, it is challenging to use these ratios for identifying the cluster configurations unambiguously. Therefore, further probes, such as ^{29}Si chemical shifts or Al connectivities, are necessary to reach a complete understanding of the exact types of OV clusters and their quantification.

Implications

The OV substitution mechanism initially dominates in Al bearing bridgmanites coexisting with MgO along the $MgSiO_3$ – $MgAlO_{2.5}$ join, and increases with Al content to a maximum in OV component at ~ 0.1 Al p.f.u. (Fig. 4a), after which the CC substitution which also increases with increasing Al content becomes dominant. Bridgmanites, on the other hand, synthesized with coexisting corundum along the $MgSiO_3$ – Al_2O_3 join, have a limited OV component and are instead dominated by the CC mechanism (Fig. 4a). The molar OV proportions obtained from the NMR spectra are in excellent agreement with those obtained from the chemical analyses (Fig. 4b). Note that the bridgmanite sample F, whose composition was created from 70 wt% $MgSiO_3$ containing 5 mol% of Al_2O_3 plus 30 wt% of MgO, contains a significantly higher OV component than sample D, which was produced from the same nominal composition in the absence of excess MgO,

proving, therefore, that the presence of MgO favours the OV substitution mechanism. In a peridotite composition lower mantle bridgmanite coexists with MgO-rich ferropericlase and the OV mechanism should, therefore, dominate in the top regions of the lower mantle.

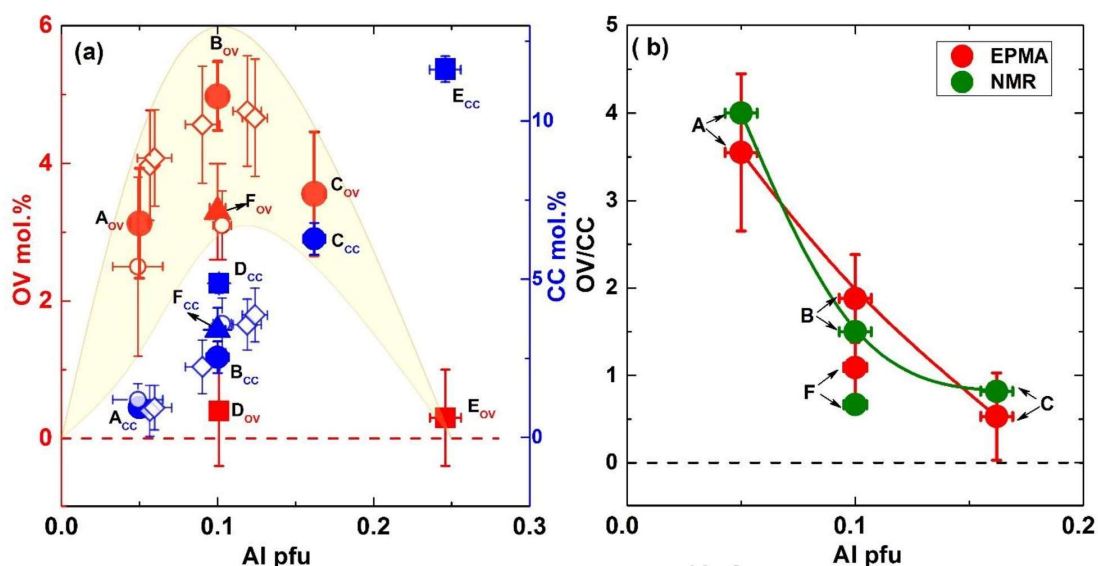


Fig. 4. (a) Solubility of OV and CC and (b) ratio of OV/CC versus Al pfu (per formula units) in bridgmanite in the systems $\text{MgSiO}_3\text{--MgAlO}_{2.5}$ (circles) and $\text{MgSiO}_3\text{--Al}_2\text{O}_3$ (squares) and in the reversal run F (triangle), respectively, in the present and previous studies. Solid symbols are the present study, while the open circle and diamond symbols are the data from Kojitani et al. (2007) and Navrotsky et al. (2003). The yellow shadow area indicates the tendency of OV component. The dashed line means the reference of zero.

The detection of short-range ordering of OVs in Al-bearing bridgmanite is of great importance for a better understanding of the crystal-chemistry of bridgmanite and its influence on the volatile cycling of noble gas and water into the mantle. Previous studies have demonstrated that noble

gases of comparable or smaller atomic-size compared to the vacancy such as neon (1.18 Å), helium (0.90 Å) and argon (1.64 Å) (Zhang and Xu 1995; Shcheka and Keppeler 2012) can be accommodated on the site, in addition to hydroxyl or water molecules (Navrotsky 1999; Murakami et al. 2012). The presence of OV ordering in Al-bearing bridgmanite under MgO-saturated mantle compositions provides a crystallographic site that is approximately two times larger and that can potentially accommodate atoms of even larger atomic radius such as, for example, xenon.

When bridgmanite forms in down welling peridotite material at the top of the lower mantle it will contain little Al, which partitions strongly into coexisting majoritic garnet at these conditions. With increasing depth garnet breaks down and the Al content of bridgmanite increases. At depths of approximately 720 km, the OV component in bridgmanite should reach a maximum which consequently should also correspond to a maximum in atoms hosted by the vacancy such as noble gases and OH species. With a further increase in pressure the OV mechanism appears to become less favorable (Brodholt, 2000; Liu et al., 2017), which should result in a gradual release in volatiles with depth. In contrast, in basaltic segments of subducting slabs the larger Al₂O₃ content with respect to the ambient mantle will suppress the OV formation and favor the CC component. OV structure may therefore be important in the deep cycling and release of volatile components.

The formation of OV clusters is somewhat surprising because local ordering lowers the configurational entropy of the component, which is an important energetic contribution to its stabilization. Similar short range ordering has been observed for perovskites along the CaTiO_3 – $\text{CaFeO}_{2.5}$ join, however, for comparable degrees of Fe^{3+} substitution (McCammon et al., 2000) in this instance rather than Al. One possibility is that the oxygen vacancies migrate through the structure but become trapped when they meet other vacancies. McCammon et al. (2000) proposed a similar process to explain high ionic conductivity for low concentrations of $\text{CaFeO}_{2.5}$ substitution in CaTiO_3 . A lowering of the conductivity is observed once dimers and longer chains of OVs form, which immobilize the OVs. Similar quite complex variations in transport properties may, therefore, also occur in bridgmanite at the top of the lower mantle as a result of changes in OV concentrations and short range ordering.

Acknowledgements

H.G. acknowledges the “Fonds der Chemischen Industrie” for financial support in the form of the Chemiefonds Fellowship.

References

- Andrault, D., Neuville, D.R., Flank, A.M., and Wang, Y. (1998) Cation sites in Al-rich MgSiO_3 perovskites. *American Mineralogist*, 83, 1045–1053.
- Ashbrook, S.E., and Wimperis, S. (2004) High-resolution NMR of quadrupolar nuclei in solids:

- The satellite-transition magic angle spinning (STMAS) experiment. *Progress in Nuclear Magnetic Resonance Spectroscopy*, 45, 53–108.
- Becerro, A.I., McCammon, C., Langenhorst, F., Seifert, F., and Angel, R. (1999) Oxygen vacancy ordering in CaTiO_3 – $\text{CaFeO}_{2.5}$ perovskites: From isolated defects to infinite sheets. *Phase Transitions*, 69, 133–146.
- Bolfan-Casanova, N., Keppler, H., and Rubie, D.C. (2000) Water partitioning between nominally anhydrous minerals in the $\text{MgO-SiO}_2\text{-H}_2\text{O}$ system up to 24 GPa: Implications for the distribution of water in the Earth's mantle. *Earth and Planetary Science Letters*, 182, 209–221.
- Brodholt, J. (2000) Pressure-induced changes in the compression mechanism of aluminous perovskite in the Earth's mantle. *Nature*, 407, 620–622.
- Charpentier, T. (2011) The PAW/GIPAW approach for computing NMR parameters: a new dimension added to NMR study of solids. *Solid state nuclear magnetic resonance*, 40, 1–20.
- Choi, M., Matsunaga, K., Oba, F., and Tanaka, I. (2009) Al NMR Chemical Shifts in Oxide Crystals: A First-Principles Study. *Journal of Physical Chemistry C*, 113, 3869–3873.
- Clark, S.J., Segall, M.D., Pickard, C.J., Hasnip, P.J., Probert, M.J., Refson, K., and Payne, M.C. (2005) First principles methods using CASTEP. *Z. Kristall.*, 220, 567–570.
- Dobson, D.P., and Jacobsen, S.D. (2004) The flux growth of magnesium silicate perovskite single crystals. *American Mineralogist*, 89, 807–811.
- Gan, Z. (2000) Isotropic NMR Spectra of Half-Integer Quadrupolar Nuclei Using Satellite Transitions and Magic-Angle Spinning. *Journal of the American Chemical Society*, 122, 3242–3243.
- Kentgens, A.P.M. (1991) Quantitative excitation of half-integer quadrupolar nuclei by a frequency-stepped adiabatic half-passage. *Journal of Magnetic Resonance (1969)*, 95, 619–625.
- Kurnosov, A., Marquardt, H., Frost, D.J., Ballaran, T.B., and Ziberna, L. (2017) Evidence for a Fe^{3+} -rich pyrolytic lower mantle from (Al,Fe)-bearing bridgmanite elasticity data. *Nature*, 543, 543–546.
- Kwak, H.-T., and Gan, Z. (2003) Double-quantum filtered STMAS. *Journal of Magnetic Resonance*, 164, 369–372.

- Liu, Z., Nishi, M., Ishii, T., Fei, H., Miyajima, N., Ballaran, T.B., Ohfuji, H., Sakai, T., Wang, L., Shcheka, S., and others (2017) Phase Relations in the System MgSiO_3 - Al_2O_3 up to 2300 K at Lower Mantle Pressures. *Journal of Geophysical Research: Solid Earth*, 122, 7775–7788.
- Liu, Z., Ishii, T., and Katsura, T. (2017) Rapid decrease of $\text{MgAlO}_{2.5}$ component in bridgmanite with pressure. *Geochemical Perspectives Letters*, 5, 12–18.
- MacKenzie, K.J.D., and Smith, M.E. (2002) *Multinuclear Solid-State NMR of Inorganic Materials*, Volume 6., 1-727 p. (R.W. Kahn, Ed.) Pergamon Materials Series. Pergamon, Oxford.
- McCammon, C. (1997) Perovskite as a possible sink for ferric iron in the lower mantle. *Nature*, 387, 694–696.
- McCammon, C.A., Becerro, A.I., Langenhorst, F., Angel, R.J., Marion, S., and Seifert, F. (2000) Short-range ordering of oxygen vacancies in $\text{CaFe}_x\text{Ti}_{1-x}\text{O}_{3-x/2}$ perovskites ($0 < x < 0.4$). *Journal of Physics: Condensed Matter*, 12, 2969–2984.
- Murakami, M., Ohishi, Y., Hirao, N., and Hirose, K. (2012) A perovskitic lower mantle inferred from high-pressure, high-temperature sound velocity data. *Nature*, 485, 90–94.
- Navrotsky, A. (1999) A Lesson from Ceramics. *Science (New York, N.Y.)*, 284, 1788–1789.
- Navrotsky, A., Schoenitz, M., Kojitani, H., Xu, H., Zhang, J., Weidner, D.J., and Jeanloz, R. (2003) Aluminum in magnesium silicate perovskite: Formation, structure, and energetics of magnesium-rich defect solid solutions. *Journal of Geophysical Research: Solid Earth*, 108, ECV2-1–11.
- Palke, A.C., Stebbins, J.F., Frost, D.J., and McCammon, C.A. (2012) Incorporation of Fe and Al in MgSiO_3 perovskite: An investigation by ^{27}Al and ^{29}Si NMR spectroscopy. *American Mineralogist*, 97, 1955–1964.
- Perdew, J.P., Burke, K., and Ernzerhof, M. (1996) Generalized Gradient Approximation Made Simple. *Physical Review Letters*, 77, 3865–3868.
- Pickard, C., and Mauri, F. (2001) All-electron magnetic response with pseudopotentials: NMR chemical shifts. *Physical Review B*, 63, 245101.
- Profeta, M., Mauri, F., and Pickard, C.J. (2003) Accurate first principles prediction of ^{17}O NMR parameters in SiO_2 : Assignment of the zeolite ferrierite spectrum. *Journal of the American Chemical Society*, 125, 541–548.

- Shcheka, S.S., and Keppler, H. (2012) The origin of the terrestrial noble-gas signature. *Nature*, 490, 531–534.
- Siegel, R., Rocha, J., and Mafra, L. (2009) Combining STMAS and CRAMPS NMR spectroscopy: High-resolution HETCOR NMR spectra of quadrupolar and ^1H nuclei in solids. *Chemical Physics Letters*, 470, 337–341.
- Smith, M.E. (1993) Application of ^{27}Al NMR Techniques to Structure Determination in Solids. *Applied Magnetic Resonance*, 4, 1–64.
- Stebbins, J.F. (2006) Aluminum substitution in stishovite and MgSiO_3 perovskite: High-resolution ^{27}Al NMR. *American Mineralogist*, 91, 337–343.
- Stebbins, J.F., and Kroeker, S. (2001) The mechanism of solution of aluminium oxide in MgSiO_3 perovskite. *Geophysical Research Letters*, 28, 615–618.
- Stebbins, J.F., Kojitani, H., Akaogi, M., and Navrotsky, A. (2003) Aluminum substitution in MgSiO_3 perovskite: Investigation of multiple mechanisms by ^{27}Al NMR. *American Mineralogist*, 88, 1161–1164.
- Yates, J.R., Pickard, C.J., and Mauri, F. (2007) Calculation of NMR chemical shifts for extended systems using ultrasoft pseudopotentials. *Phys. Rev. B*, 76, 24401.
- Zhang, Y., and Xu, Z. (1995) Atomic radii of noble gas elements in condensed phases. *American Mineralogist*, 80, 670–675.

Methods

Here we describe the experimental set ups used to synthesize and characterize the samples, as well as the strategy for modelling possible Al defect structures based on density functional theory. For Tables and more detailed discussion, we refer the reader to the main text as well as to the Supplementary Information.

Sample syntheses

Five bridgmanite samples have been synthesized from glassy starting materials prepared from fine-grained oxide mixtures from reagent grade chemicals: MgO, SiO₂, and Al₂O₃, fused at 2000 K for one hour ground for a total of three times, and finally quenched into water. The compositions of the glassy starting materials were measured by means of an electron probe microanalyzer (conditions are described in the next section) and are reported in Table S1.

The starting materials were put into platinum capsules, and heated at 800 K for one hour in order to minimize the amount of adhesive water before putting them into the high-pressure cell assemblies made of Cr₂O₃-doped MgO octahedra with 7-mm edge length and LaCrO₃ sleeves as heating elements. All syntheses have been performed at 27 GPa and at 2000 K for periods ranging between 3 to 26 hours using tungsten carbide cubes with 3-mm truncated edge lengths in a Kawai-type multi-anvil apparatus (IRIS-15) at the Bayerisches Geoinstitut, University of Bayreuth (Ishii et al., 2016) (Table S2). Pressures at 2000 K were calibrated based on the solubility of Al₂O₃ in bridgmanite in equilibrium with corundum (Liu et al. 2017a, 2017b). Pressure uncertainties of these quench experiments are approximately ± 0.5 GPa.

One reversed experiment was performed at the same pressure and temperature conditions using a mixture of 70 wt.% enstatite synthesized from glass D at 3 GPa and 1400 K for 5 hours and 30 wt.% MgO which is referred hereafter as sample F.

Sample characterization

The recovered synthesis runs were mounted in epoxy resin, ground to expose the centered portion, and then polished using 0.25 μm diamond paste. Textural observations of the recovered samples were performed using a LEO1530 scanning electron microscope (SEM). Back-scattered electrons (BSE) images for the different samples are reported in Figure S1. The chemical compositions of the run products were obtained by means of a JEOL JXA-8200 electron probe microanalyzer (EPMA) operating at an acceleration voltage of 15 kV and a beam current of 5 nA using enstatite and forsterite as standard for Mg and Si, respectively, and corundum as standard for Al. We also measured with the same settings a pure MgSiO_3 bridgmanite crystal (Liu et al., 2017a) as benchmark analysis obtaining a Mg/Si ratio of 1.002 ± 0.004 . Therefore, we expect the cation ratios of the bridgmanites investigated in this study to have a similar accuracy. The chemical compositions of the six bridgmanite samples are reported in Table S2.

The samples were then recovered from the epoxy and extracted from the platinum capsule and resulted in well sintered pellets. Phase identification was performed on these pellets using a micro-focused X-ray diffractometer (MF-XRD), a Bruker D8 DISCOVER equipped with a two-dimensional solid state detector (VANTEC500) and a micro-focus source ($1\mu\text{S}$) with $\text{Co-K}\alpha$ radiation operated at 40 kV and 500 μA . The X-ray beam was focused to less than 100 μm using a IFG polycapillary X-ray mini-lens. XRD profiles were collected for three hours.

Solid-state NMR spectroscopy

^{27}Al solid-state NMR spectroscopic experiments were performed using a Bruker Avance III 600 MHz, as well as 1 GHz spectrometer operating at a magnetic field strength of 14.1 T and 23.5 T, respectively. AlCl_3 solution adjusted to pH of one with hydrochloric acid was used as a frequency reference (156.3 MHz and 260.57 MHz). All experiments were performed using Bruker

1.3 mm double resonance probes spinning the samples at an MAS frequency of 60.0 kHz for 1D and at 62.5 kHz for 2D experiments.

The sintered bridgmanite pellets were loaded in the 1.3mm ZrO₂ rotors on top of a Teflon spacer in order to position the samples in the center of the radio-frequency coil. The 1D ²⁷Al MAS NMR spectra were recorded at the 600 MHz spectrometer for ~ 24 h using a single-pulse acquisition sequence with flip angles of ~3° and a pulse duration of 1 μs to ensure quantitative spectra (Kentgens 1991). A recycle delay of 0.75 s gave fully relaxed spectra.

²⁷Al MAS NMR echo spectra with an interpulse delay of 16.7 μs ($1 \nu_{\text{rot}}^{-1}$) were recorded to suppress background signals of the probe of the 1 GHz spectrometer. The recycle delay was set to 1 s and selective pulses with radio frequency fields of ~40 kHz was used to increase the sensitivity for resonances with stronger quadrupolar coupling.

The 2D ²⁷Al STMAS spectrum was recorded for ten days at the 600 MHz spectrometer using the DQF-STMAS-split-t1 pulse sequence (Kwak and Gan 2003; Siegel et al. 2009) with an extended 768-step phase cycle in combination with an echo / antiecho scheme for the indirect dimension to suppress CT-CT transitions and other possible artefacts in the spectrum.

DFT calculations

DFT calculations were performed using the CASTEP DFT code (version 8) (Pickard and Mauri 2001; Profeta et al. 2003; Clark et al. 2005; Yates et al. 2007) employing the GIPAW algorithm (Charpentier 2011). For all calculations the generalized gradient approximation (GGA) Perdew-Burke-Ernzerhof functional (PBE) (Perdew et al. 1996) with the semiempirical dispersion correction Grimme06 (Grimme 2006) was employed. Initial atomic positions and unit cell parameters of bridgmanite were taken from published single-crystal X-ray diffraction data (Dobson and Jacobsen 2004). Different Al defect types were introduced by replacing one Si and

one Mg atom by two Al atoms according to the CC substitution mechanism, as well as replacing 4 Si with Al atoms while removing 2 O atoms according to the OV substitution mechanism. Two types of bridgmanite supercells were used in order to isolate the Al defects from their periodic images, a $2 \times 2 \times 1$ supercell for the CC substitution mechanism (2 Al atoms) and a $2 \times 2 \times 2$ supercell for the OV substitution mechanism (4 Al atoms). In the OV models, simple vacancies as well as linear combination of O vacancies and partial clustering of O vacancies were considered. In total 14 different Al defect models (described in detail in the Supplementary Information) were fully geometry optimized within space group P1 allowing the unit-cell to relax prior to calculating the NMR parameters. Geometry-optimizations and NMR parameters (chemical shielding and the electric field gradient (EFG) tensors) were calculated using a plane wave energy cut-off of 800 eV and a Monkhorst-Pack grid k-point spacing of 0.03 \AA^{-1} over the Brillouin zone. The calculation of NMR parameters generates the absolute shielding tensor σ in the crystal frame. The isotropic shielding σ_{iso} is given by $1/3 \text{ Tr}\{\sigma\}$. The isotropic chemical shift δ_{iso} is given by $-1 \cdot (\sigma_{\text{iso}} - \sigma_{\text{ref}})$, where σ_{ref} is a reference shielding. For ^{27}Al a reference shielding $\sigma_{\text{ref}} = 557.3 \text{ ppm}$ was determined by comparison to the experimentally observed isotropic ^{27}Al chemical shift of Al at the octahedral B-sites ($\delta_{\text{iso}} \sim 6 \text{ ppm}$, Stebbins et al. 2001, 2003, 2006; Palke et al. 2012) of bridgmanite.

Raman spectroscopy

In order to check whether some amorphisation of the bridgmanite samples occurred, the bridgmanite pellets were recovered after the NMR measurements and further examined by Raman spectroscopy using a Horiba LabRAM HR UV spectrometer equipped with an argon ion laser ($\lambda = 514.5 \text{ nm}$) as excitation source. The output laser power was set to 10 mW to avoid amorphization of bridgmanite during the Raman measurements and a confocal hole of $100 \text{ }\mu\text{m}$ in diameter combined with a 50 times magnifying objective were used. High-quality Raman spectra were

collected for all samples (Fig. S2) in the wavenumber region between 150 and 1000 cm^{-1} using an acquisition time of 30 minutes for each sample point.

Supplementary Information

Table S1. Chemical compositions of the glasses used as starting material for the Al-bearing bridgmanites. Oxide analyses are reported in wt%. The total number of cations is normalized to two. Number in parentheses represents standard deviations.

Glasses	A	B	C	D	E
Nr. of point analyses	20	15	12	15	12
Oxides wt%					
MgO	40.31 (56)	39.49 (18)	40.41 (12)	38.42 (29)	29.86 (22)
Al ₂ O ₃	2.45 (8)	5.11 (5)	10.16 (9)	5.10 (5)	25.47 (10)
SiO ₂	57.27 (41)	55.08 (37)	48.91 (22)	57.47 (48)	44.28 (33)
Total	100.02 (83)	99.68 (40)	99.48 (29)	100.99 (52)	99.61 (33)
Compositions (mol%)	En ₉₅ Brm ₅	En ₉₀ Brm ₁₀	En ₈₀ Brm ₂₀	En ₉₅ Cor ₅	En ₇₅ Cor ₂₅
Ions					
Mg	0.999 (6)	0.981 (4)	0.995 (2)	0.950 (7)	0.749 (6)
Al	0.049 (2)	0.100 (1)	0.198 (2)	0.099 (2)	0.505 (2)
Si	0.953 (5)	0.918 (4)	0.808 (2)	0.951 (6)	0.745 (7)
O	2.977 (6)	2.968 (4)	2.906 (2)	3.001 (7)	2.998 (6)

En = MgSiO₃; Brm = MgAlO_{2.5}; Cor = Al₂O₃

Table S2. High-pressure and high-temperature synthesis conditions and resulting runs products

Starting materials	Run Nr.	time (h)	Phases
A	IRIS361	3	Brg
B	IRIS356	5	Brg
C	IRIS522	3	Brg + Per
D	IRIS450	5	Brg
E	IRIS428	20	Brg + Cor + trace Sti
F	IRIS514	24	Brg + Per

Note: syntheses were performed at 27 GPa and 2000 K

Brg = bridgmanite; Cor = corundum; Per = periclase; Sti = stishovite

The F starting material consisted of a mixture of 70 wt.% enstatite synthesized from glass D and 30 wt.% MgO

Table S3. Chemical compositions of the Al-bearing bridgmanites synthesized in this study. Oxide analyses are reported in wt%. The total number of cations is normalized to two. Number in parentheses represents standard deviations.

Samples	A	B	C	D	E	F
Nr. of point analyses	20	18	15	26	15	40
Oxides wt%						
MgO	39.60 (38)	39.29 (23)	38.21 (40)	37.93 (22)	35.46 (33)	39.74 (43)
Al ₂ O ₃	2.54 (33)	5.12 (18)	8.31 (35)	5.11 (12)	11.95 (48)	5.15 (29)
SiO ₂	57.17 (57)	55.58 (42)	54.79 (46)	56.31 (30)	52.70 (49)	57.09 (51)
Total	99.30 (67)	99.99 (49)	101.3 (8)	99.35 (55)	100.04 (8)	101.99 (8)
Elements (p.f.u.)						
Mg	0.991 (4)	0.975 (4)	0.937 (4)	0.952 (5)	0.884 (4)	0.968 (5)

Al	0.050 (6)	0.100 (5)	0.161 (7)	0.101 (2)	0.235 (9)	0.099 (6)
Si	0.959 (5)	0.925 (4)	0.902 (59)	0.947 (4)	0.881 (7)	0.933 (5)
O	2.984 (5)	2.975 (4)	2.982 (3)	2.998 (3)	2.999 (3)	2.983 (6)
OV (mol%)*	3.2 (9)	5.0 (8)	3.5 (7)	0.5 (8)	0.3 (7)	3.5 (9)
CC (mol%)*	0.9 (1)	2.5 (5)	6.3 (4)	4.8 (3)	11.6 (4)	3.2 (6)

* The OV and CC contents have been calculated according to expression (1)

Table S4. Integrated area of the peaks of the different ^{27}Al coordinations signals obtained from the fits of the ^{27}Al MAS NMR spectra and the resulting OV to CC ratio. The Al signal assigned to the A-site has been taken as normalizing factor (see text).

sample	$^{\text{IV}}\text{Al}$	$^{\text{V}}\text{Al}$	$^{\text{VI}}\text{Al}$	$^{\text{A}}\text{Al}$	NMR
					OV % : CC %
A	4.37	2.29	2.18	1	79±2 : 21±2
B	1.18	1.05	1.85	1	60±3 : 40±3
C	0.41	0.35	1.82	1	45±3 : 55±3
D	0.04	0.06	1.11	1	9±4 : 91±4
E	-	-	4.34 (*1.01 CC)	1	0±2 : 100±2
F	0.33	0.31	1.78	1	41±2 : 59±2

*The integrated area of the $^{\text{VI}}\text{Al}$ signal assigned to the CC component in sample E was obtained after subtraction of the integrated area of the $^{\text{VI}}\text{Al}$ species assigned to corundum.

Table S5. Calculated isotropic chemical shift, δ_{iso} , quadrupolar coupling, C_Q , and asymmetry parameter, η_Q , for the different Al sites of the 14 DFT-optimized Al defect models in Al-bearing bridgmanite.

Model	Energy / kJmol ⁻¹	Cellsize / N (Al)	Al	Coord.	δ_{iso} ppm	C_Q MHz	η_Q	O Vac.
CC1	0 (Reference CCM)	221 / 2	1	A-site	-5.8	5.6	0.87	-
			2	B-site	6.8	3.0	0.76	-
CC2	10.6	221 / 2	1	A-site	-7.3	6.9	0.87	-
			2	B-site	5.9	2.0	0.67	-
OV_O1	50.8	222 / 4	1-4	AlO ₅	2 x 42.4	2 x 5.8	2 x 0.43	2 x O1
OV_O2	29.5	222 / 4	1+3	AlO ₅	2 x 41.9	2 x 4.7	2 x 0.46	2 x O2
			2+4	AlO ₅	2 x 42.4	2 x 6.2	2 x 0.33	
OV_O1_lin	0 (Reference OVM)	222 / 4	1+2	AlO ₅	2 x 43.4	2 x 6.3	1.0	2 x O1
			3+4	AlO ₅	2 x 42.8	2 x 5.4	0.64	
OV_O2_lin	18.2	222 / 4	1+4	AlO ₅	2 x 43.3	2 x 5.3	0.84	2 x O2
			2+3	AlO ₅	2 x 43.6	2 x 5.9	0.93	
OV_O1O2_lin	54.4	222 / 4	1	AlO ₅	41.9	5.9	0.87	O1 O2
			2	AlO ₅	45.7	7.8	0.57	
			3	AlO ₅	42.3	5.4	0.44	
			4	AlO ₅	44.6	3.3	0.48	
OV_O1O2_clus	29.6	222 / 4	1	AlO ₄	74.1	11.7	0.42	O1 O2
			2	AlO ₅	44.6	8.5	0.39	
			3	AlO ₅	45.7	7.1	0.69	
			4	AlO ₆	10.5	7.6	0.77	
OV_O2_clus_1	28.8	222 / 4	1	AlO ₄	68.6	12.1	0.45	2x O2
			2	AlO ₅	44.6	8.4	0.65	
			3	AlO ₅	45.7	7.8	0.28	
			4	AlO ₆	12.8	10.6	0.64	
OV_O2_clus_2	21.4	222 / 4	1	AlO ₄	76.6	11.7	0.99	2x O2
			2	AlO ₅	40.5	5.2	0.44	
			3	AlO ₅	44.9	6.9	0.25	
			4	AlO ₆	6.3	3.0	0.69	
OV_O2_clus_3	46.9	222 / 4	1	AlO ₄	75.0	10.8	0.75	2x O2

			2	AlO ₅	41.1	4.9	0.44	
			3	AlO ₅	44.8	5.5	0.96	
			4	AlO ₆	9.1	4.6	0.13	
OV_O2_clus_4	28.4	222 / 4	1	AlO ₄	71.1	11.4	0.68	2x O2
			2	AlO ₅	40.2	5.2	0.48	
			3	AlO ₅	44.4	6.8	0.19	
			4	AlO ₆	5.8	1.8	0.52	
OV_O2_clus_5	4.9	222 / 4	1	AlO₄	71.3	12.0	0.52	2x O2
			2	AlO₅	44.3	6.4	0.32	
			3	AlO₆	5.6	1.5	0.91	
			4	AlO₆	6.8	7.0	0.33	
OV_O2_clus_6	-13.5	222 / 4	1	AlO₄	78.9	11.9	0.83	2x O2
			2	AlO₅	42.1	4.2	0.67	
			3	AlO₆	6.0	2.9	0.90	
			4	AlO₆	11.1	7.7	0.16	

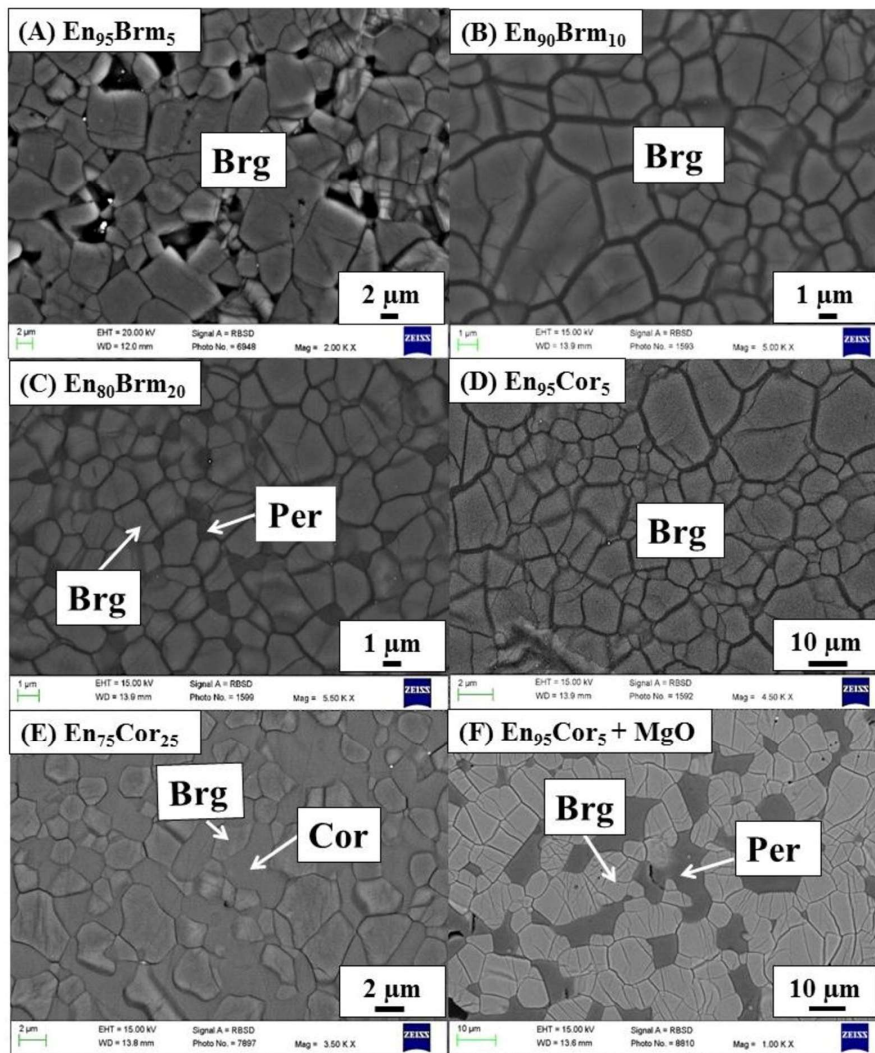


Figure S1. Representative BSE images of the six different run products. Note the presence of a single bridgmanite phase obtained from the A B and D starting materials and the presence of an extra phase in the run products obtained from the C E and F starting materials. Abbreviations: Brg = bridgmanite; Cor = corundum; Per = periclase.

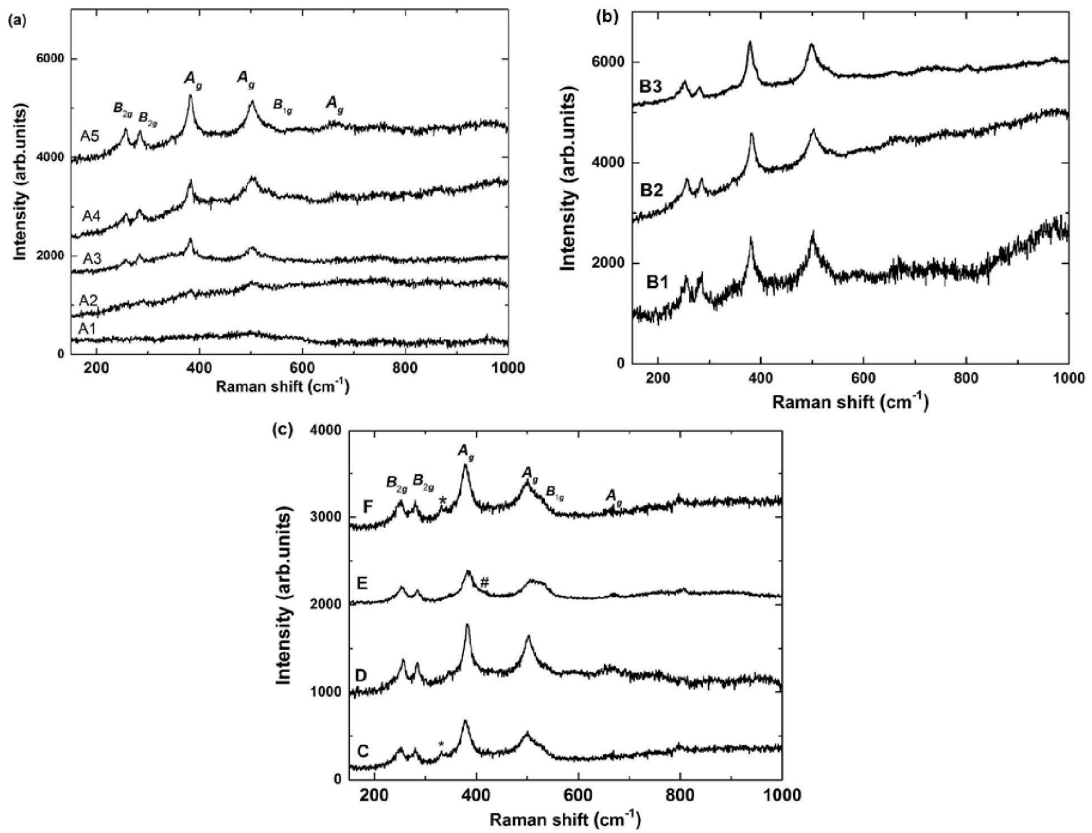


Figure S2. (a) Raman spectra of sample A for 5 different points (b) Three different points for sample B, and (c) sample C-F. The star symbol represents the peak from periclase, while the pound symbol represents that from corundum. It's found that some amorphization occurs in sample A and B, especially for sample A, because no Raman signals or very weak signals are detected for Raman spectra A1-A3 and B3. Strong Raman peak form sample C-F are clearly observed, suggesting that no amorphization occurs for these sample after NMR measurement.

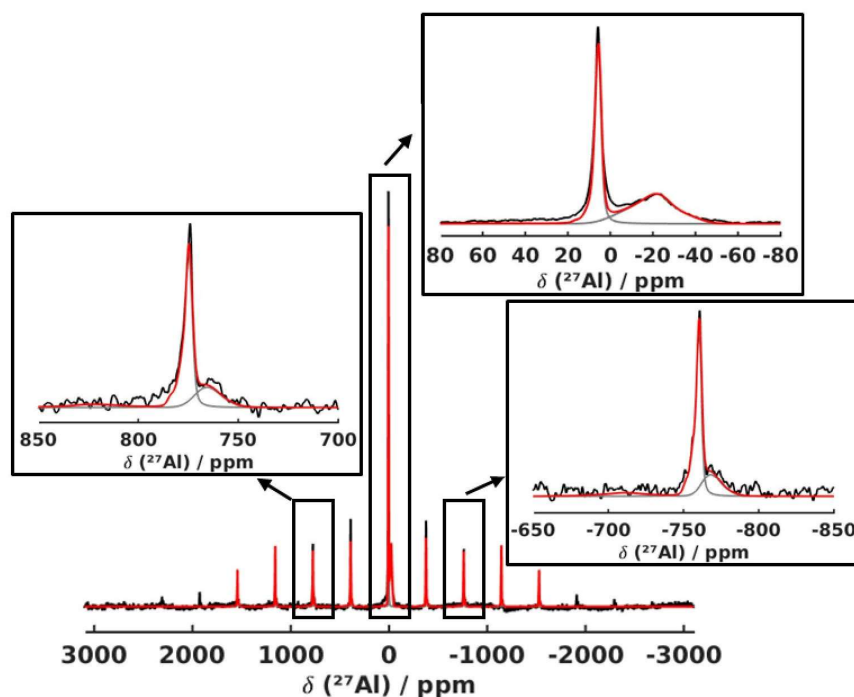


Figure S3. Deconvolution of the 1D ^{27}Al MAS NMR spectrum of sample D with two Al resonances to extract the isotropic chemical shift and quadrupolar parameters (C_Q and η_Q) for Al on the A and B site of bridgmanite resulting from the CC mechanism. Gaussian broadening was needed to account for a distribution of NMR parameters, which is indicated by the broadening of the experimental signal at a maximum of -20 ppm and the broader tail of the signal at 7 ppm suggesting disorder of bond distances, angles and second-neighbor cations around the Al defects in the bridgmanite structure. The isotropic chemical shifts and quadrupolar parameters of the two experimentally observed ^{27}Al sites are summarized in Table 2.

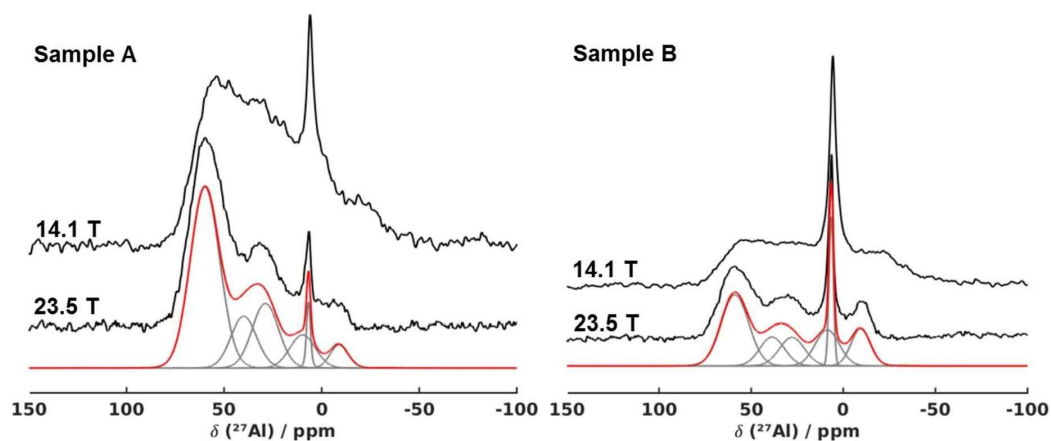


Figure S4. ^{27}Al MAS NMR spectra and ^{27}Al MAS echo spectra of sample A (left) and B (right) recorded at magnetic fields of 14.1 T and 23.5 T. The same sets of isotropic chemical shift and quadrupolar parameters as used for the fits of the spectra recorded at 14.1 T (Tab. 2) can be used to refine the echo spectra recorded at 23.5 T (red), but Gaussian broadening needs to be increased by a factor of ~ 1.6 - 1.7 arising from the increase of the magnetic field ($^{23.5\text{ T}}/^{14.1\text{ T}}$) due to the effects of chemical shift distribution observed also in the 2D ^{27}Al STMAS spectrum of sample B (Fig. 2, blue lines).

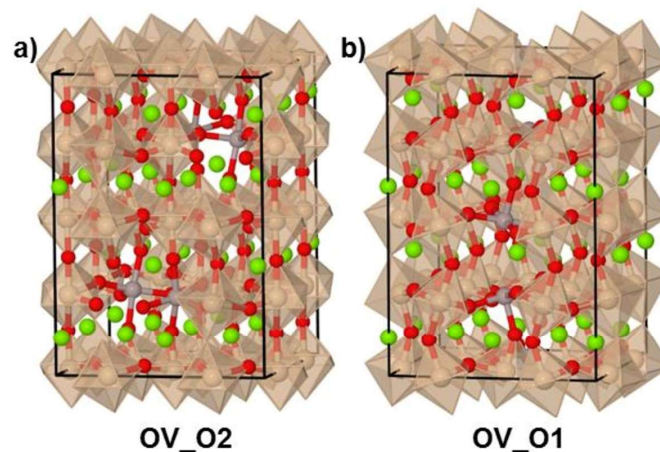
DFT OV structural models

Figure S5. a) Two isolated O2 vacancies and b) two isolated O1 vacancies were created by replacing two Si by Al on adjacent B sites and removing the bridging O atom resulting in two penta-coordinated Al sites. To allow for a comparison of energies of the OV models two of such defects were placed in a $2 \times 2 \times 2$ supercell. The formation of isolated O2 vacancies (OV_O2) is energetically favored compared to isolated O1 vacancies ($\Delta E(\text{OV_O1} - \text{OV_O2}) \sim 21 \text{ kJmol}^{-1}$), but has a higher energy than a linear combination of two O1 vacancies ($\Delta E(\text{OV_O2} - \text{OV_O1_lin}) \sim 30 \text{ kJmol}^{-1}$, Fig. S6); Si octahedra in front of the Al defects were removed for the sake of clarity. In b) the second defect is placed in back of the unit cell and therefore not visible. Si: brown, Mg: green, O: red, Al: grey.

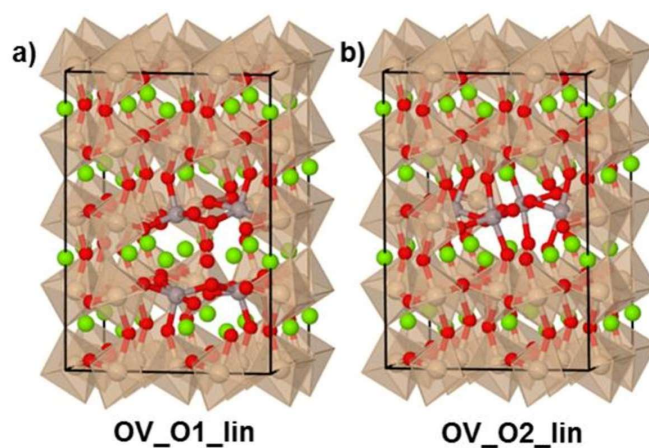


Figure S6. a) Linear combination of two O1 vacancies and b) of two O2 vacancies with Al replacing Si on adjacent B sites each resulting in penta-coordinated Al-species within a 2 x 2 x 2 supercell. A combination of two O1 vacancies (OV_O1_lin) is energetically favored compared to isolated O vacancies ($\Delta E(\text{OV_O1_lin} - \text{OV_O1}) \sim -51 \text{ kJmol}^{-1}$; $\Delta E(\text{OV_O1_lin} - \text{OV_O2}) \sim -30 \text{ kJmol}^{-1}$) and compared to a combination of two O2 vacancies ($\Delta E(\text{OV_O2_lin} - \text{OV_O1_lin}) \sim 18 \text{ kJmol}^{-1}$) or a combination of an O1 and an O2 vacancy ($\Delta E \sim 54 \text{ kJmol}^{-1}$). Therefore, the OV_O1_lin model is used as energy reference in Table S5. Si octahedra in front of the Al defects were removed for the sake of clarity. Si: brown, Mg: green, O: red, Al: grey.

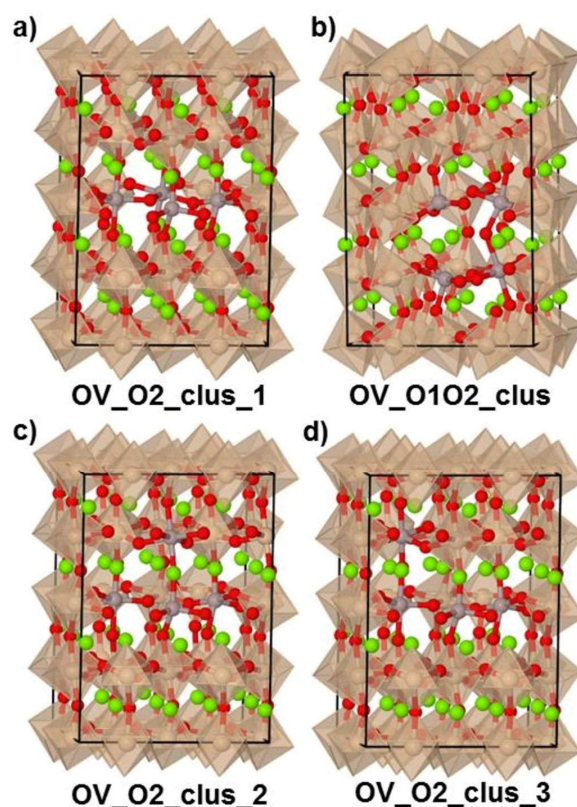


Figure S7. a) Combination of two O2 vacancies in the ab-plane and b) combination of one O1 and O2 vacancy resulting in 4-, 5- and 6-fold coordinated Al species, which are placed in plane. The energy of these models is ~ 29 kJmol⁻¹ higher compared to a linear combination of two O1 vacancies (OV_O1_lin, Fig. S6a). c+d) Combination of two O2 vacancies resulting in 4-, 5- and 6-fold coordinated Al species, but the position of the octahedral Al species was moved out of the defect plane on top of the 4-fold coordinated site (c) and on top of a 5-fold coordinated site (d), respectively. In both the resulting energies are comparable (Table S5) but the quadrupolar coupling of the ^{VI}Al site is significantly reduced due to smaller distortions (Table S5) showing a better agreement with the experimental values (Fig. 3g). Si octahedra in front of the Al defects were removed for the sake of clarity. Si: brown, Mg: green, O: red, Al: grey.

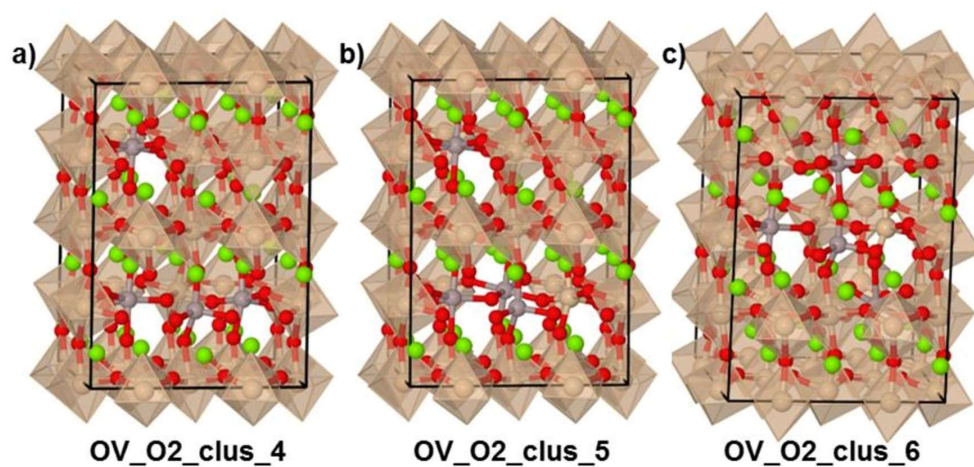


Figure S8. a) Combination of two O2 vacancies resulting in 4-, 5- and 6-fold coordinated Al species with separation of the octahedral Al species resulting in comparable energy to the other OV dimer models (OV_O2_clus_1-3, Fig. S7, Tab. S5), but the ^{27}Al quadrupolar coupling of the six-fold coordinated site is further reduced (Tab. S5). (b+c) Combination of two O2 vacancies resulting in one 4-, one 5- and two 6-fold coordinated Al species and one 5-fold coordinated site occupied by Si. These OV dimer configurations lead to reduced energies of $\Delta E \sim 5$ to -14 kJmol^{-1} (Tab. S5). Si octahedra in front of the Al defects were removed for the sake of clarity. Si: brown, Mg: green, O: red, Al: grey.

Erklärung

Hiermit versichere ich eidesstattlich, dass ich die Arbeit selbstständig verfasst und keine anderen als die von mir angegebenen Quellen und Hilfsmittel benutzt habe.

Hiermit erkläre ich, dass ich die Dissertation nicht bereits zur Erlangung eines akademischen Grades eingereicht habe und dass ich nicht bereits diese oder eine gleichartige Doktorprüfung endgültig nicht bestanden habe.

Hiermit erkläre ich, dass ich die Hilfe gewerblichen Promotionsberatern bzw. –vermittlern oder ähnlichen Dienstleistern weder bisher in Anspruch genommen habe noch künftig in Anspruch nehmen werde.

Hiermit erkläre ich mein Einverständnis, dass die elektronische Fassung meiner Dissertation unter Wahrung meiner Urheberrechte und des Datenschutzes einer gesonderten Überprüfung unterzogen werden kann.

Hiermit erkläre ich mein Einverständnis, dass bei Verdacht wissenschaftlichen Fehlverhaltens Ermittlungen durch universitätsinterne Organe der wissenschaftlichen Selbstkontrolle stattfinden können.

Helen Grüninger, Bayreuth, der 27. September 2018